

Optical Magnetometry Using Multiphoton Transitions

by

Skyler M. Degenkolb

A dissertation submitted in partial fulfillment
of the requirements for the degree of
Doctor of Philosophy
(Physics)
in the University of Michigan
2016

Doctoral Committee:

Professor Timothy E. Chupp
Professor Alex Kuzmich
Professor Wolfgang B. Lorenzon
Professor Theodore B. Norris
Professor Aaron T. Pierce

natura valde simplex est et sibi consona
– Sir Isaac Newton

© Skyler M. Degenkolb

2016

ACKNOWLEDGEMENTS

Tim Chupp receives the customary place of honor at the top of this page; his support went beyond what is ordinarily expected of an advisor. He accommodated a very independent working style, and remained enthusiastic about research that evolved well outside the usual scope of his group. Forays into atomic beam spectroscopy, ultrafast lasers, cleanroom fabrication, and technical glass working substantially enriched the content of this dissertation, as well as the experience of producing it. Tim is also responsible for cultivating an extremely productive and enjoyable collaboration with Peter Fierlinger's group at TUM (the Technische Universität München), in which it has been a great privilege and pleasure to participate.

Aaron Leanhardt was, in effect, a second advisor for close to four years. I am grateful for his persistence and patience, and for the example set by his rapid and incisive style of problem solving. Aaron also deserves much of the credit for formulating an experimental approach to two-photon magnetometry, and the impact of his contributions – both material and intellectual – cannot be overstated.

The Fierlinger group at TUM has been a vibrant source of collaborative energy. Peter himself is a superlative friend and colleague whose energy, enthusiasm, and generosity defy comprehension. In addition to providing some of the data presented in section 3.5.1, Bernd Taubenheim repeatedly volunteered components of his mercury experiment for cooption into the xenon two-photon effort, and joined me in the search for a minute signal with admirable resourcefulness and tenacity. (That our rapid success with mercury was not repeated in xenon does not diminish my gratitude.) Jaideep Singh and Florian Kuchler also deserve special mention for coordinating the xenon EDM (HeXe) experiments at TUM, which provided the primary means of testing and characterizing new vapor cells.

The entire nEDM and HeXe teams, besides setting a very high bar for collaborative science, have reliably provided useful input on this work, which falls outside the main thrust of our collaboration. It is impossible to provide a comprehensive list of contributors, but I am particularly grateful to Earl Babcock and Wolfgang Kilian for discussions and measurements relating to polarized xenon.

Roy Wentz has provided inestimable material contributions to this work in the form of technical glassblowing, repairs, and cell design input. He has singlehandedly produced in

the neighborhood of one hundred cells for me personally, in addition to countless others from which I benefited indirectly. Besides enthusiastically experimenting at our request and iteratively improving designs, he has on several occasions visited our lab to perform particularly touchy pieces of work or to repair delicate apparatus *in situ*.

The Lurie Nanofabrication Facility at the University of Michigan was extremely efficient and helpful in all matters relating to the cleanroom and hydroxide-catalysis bonding. In particular, Nadine Wang and Pilar Herrera-Fierro invested considerable time and energy training me and assisting in the development of several processes that are decidedly non-standard for the facility. Our initial efforts were so successful that the first trial prototypes went immediately into experiments, and optimization of the recipes awaits a future generation of students.

Steve Katnik has repeatedly assisted with the optimization, re-optimization, and repair of several lasers that were crucial to this dissertation. His intimate knowledge of specific commercial systems has saved time and money on numerous occasions, and my own facility with cavity alignment rests largely upon his tutelage.

I am indebted to Alex Kuzmich for the loan of the picosecond Ti:sapphire oscillator that was used for experiments discussed in chapter 4, for graciously sharing other equipment, and for useful input on certain aspects of the ytterbium experiments. Nils Walter kindly lent our lab the LBO frequency doubler for use with the picosecond laser, and John Whittaker generously supplied the electronics module for active modelocking. Georg Raithel rescued the experiment with the loan of a Verdi pump laser after the magnet on our 15-year-old Ar-ion laser abruptly failed on a particularly memorable morning.

Steve Cundiff and Bacha Lomsadze deserve special thanks for allowing me to use their femtosecond Ti:sapphire laser, and for collaborating on the experiments that followed. They devoted more time, energy, and resources than I had any right to ask, and continued to graciously provide useful input even as the measurements dragged on beyond our most pessimistic projections.

Jaideep Singh has been a supportive friend and collaborator since his first visit to TUM in 2013. After moving to Michigan State in 2014, he has also made heroic efforts to support our xenon spectroscopy experiments under severe constraints of time, equipment, and personnel; these ultimately led to our first two-photon data from xenon. I am extremely grateful for his mentorship, generosity, and persistence.

I would be remiss not to acknowledge Cheng Chin and Nate Gemelke, whose unusually dedicated mentorship during my undergraduate years played a significant role in the decision to continue studying physics in graduate school. It is unfortunate that such high standards for both science and advising do not coincide more frequently. For similar rea-

sons, I owe an earlier debt to Vince Ferlini, Sue Steiner, Fred Marin, and (earliest of all) my parents Charles and Martha.

It is also a pleasure to acknowledge those who made life more pleasant while this work was being performed; of these, Jack Kearney and Alex Fisher deserve special mention for repeatedly going above and beyond the call of friendship. I also have fond memories of working alongside Jeongwon Lee during a few years of overlap in the Leanhardt lab, trading thoughts and practical tips on different experiments that shared a lot of equipment. Matt Bales was an excellent officemate, and remains a reliable source of stimulating conversation. I offer my best wishes to the next generation of Chupp students, and my apologies for the numerous and inevitable omissions; many others, too numerous to list, have greatly enriched both work and leisure.

Finally, to Connie, for enduring it all.

TABLE OF CONTENTS

Acknowledgments	ii
List of Figures	viii
List of Tables	xxi
List of Appendices	xxii
List of Abbreviations	xxiii
List of Symbols	xxv
Abstract	xxvi
Chapter	
1 Introduction	1
1.1 Broad Motivation: Searches for New Physics	3
1.2 Precision Measurements in Low-Energy Atomic Systems	5
1.3 Approaches to Optical Magnetometry with Warm Vapors	5
1.3.1 The Common Optical Magnetometer	12
1.3.1.1 One-Photon Electric Dipole Transitions	15
1.3.2 Spatial Averaging	18
1.3.3 Optical Pumping	20
1.3.3.1 Direct Optical Pumping: Depopulation and Repopulation	21
1.3.3.2 Spin-Exchange Optical Pumping (SEOP)	21
1.4 Features of Continuous-Wave Lasers	22
1.5 Atomic Species: Alkaline-Earth-Like Metals and Noble Gases	25
1.6 Permanent Electric Dipole Moments (EDMs)	27
1.6.1 Generic Experimental Protocol	28
1.6.2 Limitations and Representative Systematics	28
1.7 Outline of this Dissertation	29
2 Theory of Multiphoton Excitation	31
2.1 Notation and Definitions	32
2.1.1 Expansions of the Density Operator	36
2.2 Equations of Motion, Approximations, and Analytic Solutions	39
2.2.1 Single Beam, CW Two-Photon Excitation	39

2.2.2	Two Beam, CW Two-Photon Excitation	43
2.2.3	Angular Momentum Coupling in Two-Photon Excitation	46
2.2.4	N-Photon Excitation	48
2.2.5	Polarization Rotation	49
2.3	Pulsed Optical Fields	52
2.4	Temporal Sensitivity	55
2.5	Spatial Sensitivity	56
2.6	Diffusive Motion and Geometric Phases	57
2.6.1	Systematic Effects in EDM Experiments	60
2.7	Summary	61
3	Experiments with Ytterbium and Continuous-Wave Lasers	62
3.1	Atomic Beam Apparatus	64
3.2	Optical Pumping (One-Photon Transitions)	74
3.2.1	Zeeman Splittings in a Homogeneous Field	79
3.3	Two-Photon Spectroscopy	83
3.3.1	Probe Polarization and Allowed Transitions	84
3.3.2	Analysis of Overlapping Resonance Lines	85
3.3.3	Nuclear Polarization Dependence	91
3.4	Further Thoughts and Improvements	91
3.5	CW Lasers and Vapor Cell Spectroscopy	94
3.5.1	Mercury	94
3.5.2	Xenon	96
4	Experiments with Pulsed Lasers	101
4.1	Scaling of Excitation Efficiency with Pulse Parameters	102
4.2	Ytterbium Atomic Beam: Picosecond Pulses	105
4.3	Rubidium Vapor Cell	109
4.4	Ytterbium Atomic Beam: Femtosecond Pulses	114
4.5	Further Thoughts and Improvements	121
4.5.1	Stabilization of the Picosecond Pulsed Spectrum at 808nm	123
4.5.2	Modelocked Picosecond Pulses for Xenon	125
4.5.3	Radon EDM	126
5	Cells and EDM Applications	129
5.1	Requirements for Optical Magnetometry	130
5.2	EDM Measurements: the HeXe Experiment	130
5.3	Glass Design and Vacuum Filling Station	135
5.4	Survey of Some Bonding Methods Relevant to Cell Fabrication	139
5.4.1	Hydroxide-Catalysis Bonding	139
5.4.2	Diffusion Bonding	141
5.4.3	Anodic Bonding of Glass to Silicon	142
5.5	Cell Materials	142
5.6	Silicate Assisted Hydroxide-Catalysis Bonding	144
5.6.1	Polishing	145

5.6.2	Surface Cleaning and Wafer Preparation	145
5.6.3	Bonding	146
5.6.4	Sapphire and Quartz Bonding for Spectroscopy Cells	147
5.7	Further Thoughts and Improvements	148
6	Conclusions	149
6.1	Theoretical Material	149
6.2	Experiments with CW Laser Sources	150
6.3	Experiments with Pulsed Laser Sources	151
6.4	Cell Development and EDM Experiments	151
	Appendices	153
	Bibliography	168

LIST OF FIGURES

1.1	Optical E1 excitation from a ground state with $J=0, I=\frac{1}{2}$ to an excited state with $J=1, I=\frac{1}{2}$. If the optical field is circularly polarized, then each photon carries one unit (\hbar) of angular momentum and only transitions with $\Delta m_F=1$ are possible. Spectroscopic terms are shown at left, and eigenvalues of total angular momentum ($\mathbf{F} = \mathbf{I} + \mathbf{J}$) at right; both $F'=\frac{1}{2}$ and $F''=\frac{3}{2}$ belong to the 1P_1 term. We have assumed that the hyperfine splitting is large compared to the bandwidth of the optical field, such that only the lower hyperfine component of 1P_1 is resonantly excited.	8
1.2	Schematic illustration of a conventional all-optical magnetometer. The atoms are optically pumped along the axis of a static field $\mathbf{B} = B\hat{z}$, after which the spins are rotated into the xy plane to initiate free precession. The precession is detected via the transmitted component of a probe beam along \hat{x}	13
1.3	Electronic structure of an idealized alkali without nuclear spin, including Zeeman sublevels. The solid arrow indicates D1 excitation with left circularly polarized ($\hat{\sigma}^+$) light, and dashed arrows show allowed decay pathways for spontaneous emission. The numbers $\frac{1}{3}$ and $\frac{2}{3}$ are branching fractions due to angular momentum coupling for E1 transitions.	14
1.4	Isosurfaces defining the effective interrogation volume. Blue represents the envelope of a Gaussian beam with wavelength 256nm, focused to a $2\mu\text{m}$ waist. Red is the $1/e^2$ surface of constant I^2 , and in the top figure green shows the volume from which atoms can diffuse into the exact focal center (during a characteristic timescale that depends on \bar{n}). In the bottom figure, the green surface represents the $1/e^2$ isosurface of a convolution between the red and green surfaces of the top figure, which is the effective interrogation volume V . The horizontal full scale is approximately $200\mu\text{m}$	20

1.5	Some low-lying electronic excited states labeled by their spectroscopic terms, in alkaline-earth-like atoms. The states are labeled as for pure LS -coupling, but in heavier atoms spin-orbit mixing of the pure LS -eigenstates allows intercombination transitions such as the green arrow in (a). For Yb the shown transitions occur at wavelengths 399nm (blue), 556nm (green), and 808nm (red; two-photon). An isotope with $I = \frac{1}{2}$ such as ^{171}Yb is assumed for (b), and the same two-photon transition is shown with hyperfine and Zeeman structure included. The upper hyperfine level $F'' = \frac{5}{2}$ (shown in gray) is assumed to lie outside the bandwidth of the optical field; neither of the intermediate levels is resonantly excited. In atoms with this electronic structure, the most convenient wavelengths for detection of laser-induced fluorescence usually turn out to be the same ones that are used for direct optical pumping (e.g., 556nm in ytterbium). As discussed below, this produces background noise that is avoidable in the noble gases.	26
2.1	Absorption and dispersion... the complex index of refraction, plotted in dimensionless units for the case of two-photon excitation where only the two-photon detuning is allowed to vary.	50
2.2	An optical pulse train with phase coherence between successive pulses. The frequency spectrum of such a field quite generally takes the form shown in figure 2.3, where the quasi-discrete modes shown in red are fully determined by two frequency parameters. These are the repetition rate, $f_r = \omega_r/2\pi = T^{-1}$ (which corresponds to the inverse of the round-trip time in the resonator producing the pulses), and the carrier-envelope offset frequency $f_0 = \Delta\phi_{ce}/T$ (which describes the rate of phase slip between the carrier wave and the field envelope maximum). The pulse duration τ determines the bandwidth of the frequency spectrum, $\Delta\omega \sim \tau^{-1}$, and thus also how many modes of the resonator are excited.	53
2.3	Calculated frequency “comb” resulting from a periodically repeated envelope function. The blue curve represents the spectral envelope of a series of Gaussian pulses, whose phase coherence from pulse to pulse leads to the interferometric pattern shown in red. We will often suppose that an atomic resonance line (green) overlaps one of the modes in such a spectrum.	54
3.1	Vapor pressure and equivalent number density of ytterbium gas in thermal equilibrium with solid ytterbium metal, as a function of temperature. The values are calculated from a model equation with coefficients according to [1], and should represent the actual vapor pressure to within $\pm 5\%$	64
3.2	Some low-lying electronic transitions and excited states of ytterbium, labeled with spectroscopic term symbols. The states are labeled as for pure LS -coupling, but spin-orbit mixing of the pure LS -eigenstates allows intercombination transitions such as the $^1S_0 \rightarrow ^3P_1$ intercombination line (green arrow). For magnetic level structure of the spin- $\frac{1}{2}$ isotope ^{171}Yb , refer to figure 1.5(b).	65

3.3	Ytterbium atomic beam vacuum chamber and associated optics. The red external field coils are clearly visible in the upper picture, and the optics just left of center guide the pump and probe beams into the chamber. External detection optics and the photomultiplier tube are contained in the light-shielded box under the vacuum chamber. The pictures below left and right show detail of the normal-incidence flange adapter for the pump beam windows (see also figure 3.4).	66
3.4	The normal-incidence flange adapter, designed and installed to eliminate polarization dependent backgrounds resulting from the pump beam. A stainless steel connector tube is welded between bored holes in standard 2-3/4" blank ConFlat flanges, one at normal incidence and one at 45°. The offset from center on the 45° flange is to position the beam in the center of the clear aperture for transmission through the spherical octagon.	67
3.5	Block diagram of the cw atomic beam experiment, showing major equipment connections and key optical elements. Only one of the two possible probe beams is used at one time.	67
3.6	Tantalum oven for ytterbium atomic beam source, showing copper leads and ConFlat flange with electrical feedthrough. The beam emerges to the reader's right.	68
3.7	Internal Components of Ytterbium Atomic Beam Chamber	69
3.8	The Toptica TA-SHG 110 used to produce 556 nm light resonant with the $^1S_0 \rightarrow ^3P_1$ transition in ytterbium. The top half contains (A) the grating-feedback seed laser of 1112 nm wavelength, (B) and (D) optical isolators, and (C) anamorphic beam-shaping prisms. The lower half contains mode-matching optics (E) and (F), which prepare the beam for injection into the resonant doubling cavity (H). An optical error signal from the cavity is recorded on a photodiode (G) for Pound-Drever-Hall locking of the cavity resonance. The 556 nm beam produced by the BBO crystal in the cavity is coupled out and filtered (I) before being shaped with an additional set of anamorphic prisms (not shown).	71
3.9	Detail of the resonant frequency doubling cavity. The four mirrors of the "bowtie" cavity are visible, and the doubling crystal is mounted in the small metallic temperature-stabilized platform between the lower two mirrors.	72
3.10	Typical fluorescence spectrum at 539.384 THz (~ 556 nm) as a function of probe frequency, showing resonance lines (from left to right) of ^{173}Yb , ^{171}Yb , and ^{176}Yb . Their relative spacing is due to hyperfine and isotope shifts.	73
3.11	Measured retardance curve for liquid crystal variable waveplate at $\lambda = 556$ nm. The vertical axis shows the relative delay in wavelengths between linear polarization components along the fast and slow axes, i.e. $d\Delta n/\lambda$ where d is the waveplate thickness, Δn is the difference in index of refraction between the fast and slow axes, and λ is the wavelength. At drive voltages of 3.375 V and 1.5 V, the waveplate functions respectively as a quarter-wave plate and a three-quarter-wave plate. By switching between these values with a linearly polarized input beam, the sense of pump polarization can be changed from $\hat{\sigma}^-$ to $\hat{\sigma}^+$ without moving any optics.	74

3.12	Magnetic field strength in the region between the pump beam (left limit) and the probe beam (right limit), calculated from a numerical model of the internal coils. Note that the field strength changes by roughly 50% between 5 cm and 7 cm (i.e., in $\sim 70 \mu\text{s}$ for an atom in the beam). The calculated field corresponds to 15 amp-turns applied to the coils shown in figure 3.7.	75
3.13	Calculated contours of magnetic field strength in the region around the atomic beam, which is represented by the red line. The field is produced by external coils visible in figure 3.3, shown here in blue. Field lines in each plane are spaced by $50 \mu\text{T}$	76
3.14	The upper two figures show the off-resonance effect of 556 nm optical pumping with various light polarizations on ^{171}Yb , as measured with a fixed probe polarization. The amplitude of the sinusoidal fit corresponds to the degree of measurable ground-state nuclear spin polarization. The bottom two figures show the same measurement performed on ^{176}Yb , which has no nuclear spin and therefore cannot be polarized in the $J=0$ ($F=0$) electronic ground state. The lack of a polarization signal in the $I=0$ isotopes provides an important systematic check in the two-photon case; in this case the fit function is a constant. (Note that for two-photon excitation there are significant qualitative differences in the Zeeman spectra of isotopes with and without nuclear spin. This phenomenon is illustrated in figure 3.19.)	78
3.15	Zeeman splittings measured in a homogeneous external field. (a) Frequency splitting between the $m'_F = \pm\frac{1}{2}$ sublevels of $ ^3P_1, F' = \frac{1}{2}\rangle$ as a function of coil current, measured by fitting a range of spectra like those shown in (b)-(d). The transition is probed with linear $\hat{\sigma}$ -polarized light, such that both peaks can be observed in the same dataset. The Zeeman splitting is extracted via a fit (see table 3.2) to the sum of two Lorentzian functions and a constant background (equation 3.7). The fit determines the individual line centers and the center of gravity. The two resonance peaks are constrained by the fit to have the same amplitudes and widths; see figure 3.16 for an alternative analysis with an additional free parameter. (b) Corresponds to the case of no applied field (and therefore no measurable splitting), while (c) and (d) illustrate the effect of slightly different applied fields on the measured spectra.	80
3.16	The same data sets shown in figure 3.15(b)-(d), now analyzed with the fit function equation 3.8. In this case the two peaks are allowed to have different amplitudes, which accommodates asymmetries due to optical pumping or elliptical probe polarization. See table 3.3 for the fit parameters; most of these agree well with the values in table 3.2. The most notable difference is in figure (c), which has a noticeable asymmetry of approximately 2% between the left- and right-hand peaks. Asymmetries of this magnitude correspond to a fraction of a degree in the alignment of the probe waveplate, and must be characterized in detail for optical pumping and magnetometry.	81

- 3.17 Raw data showing two-photon excitation of ^{174}Yb and the $F = \frac{1}{2} \rightarrow F'' = \frac{3}{2}$ hyperfine transition in ^{171}Yb , in a 1 mT magnetic field. **Blue:** A linearly polarized probe excites all allowed transitions in both isotopes (see figure 3.19). **Red:** A $\hat{\sigma}^-$ probe excites only $m_J = 0 \rightarrow m'_J = -2$ in ^{174}Yb and $m_F = +\frac{1}{2} \rightarrow m''_F = -\frac{3}{2}$ in ^{171}Yb . **Green:** A $\hat{\sigma}^+$ probe excites only $m_J = 0 \rightarrow m'_J = +2$ in ^{174}Yb and $m_F = -\frac{1}{2} \rightarrow m''_F = +\frac{3}{2}$ in ^{171}Yb . For each isotope the excited state Zeeman structure is clearly resolved, but note that at this magnetic field strength the peak for ^{171}Yb , $m''_F = -\frac{3}{2}$ overlaps with the one for ^{174}Yb , $m''_F = +2$. The relative line strengths (in the absence of optical pumping) are determined by the Clebsch-Gordan coefficients for each transition; these in turn are observed more or less efficiently according to the square of the optical intensity that satisfies the corresponding selection rules. 85
- 3.18 Zeeman structure of the $^{172}\text{Yb } 5d6s \ ^3D_2$ state in a magnetic field, where the probe polarization is $\hat{\epsilon} = a\hat{\sigma}^- + b\hat{\sigma}^+$: (a) nearly linear probe polarization with $a \gtrsim b$, (b) pure linear probe polarization ($a = b$ within experimental limitations), (c) nearly linear probe polarization with $a \lesssim b$. Only three of the five 3D_2 magnetic sublevels are excited, since angular momentum conservation cannot be satisfied for a $\Delta m = \pm 1$ transition where two circularly polarized photons are absorbed. When the probe polarization has no $\hat{\pi}$ component, there is no two-photon E1 amplitude that connects the state $m_J = 0$ with any of $m'_J = 0$ or $m''_J = \pm 1$ (see figure 3.19). Since the even isotopes of ytterbium have no nuclear spin, these spectra provide a reference baseline in which optical pumping has no effect on the ground state. As such, they are a sensitive means of calibrating the effects of imperfect probe polarization. Green lines show a fit to the function $g(\omega)$ defined in equation 3.9 (see table 3.4 for the fit parameters). Red lines show the $m''_F = -2$ component, i.e. $g(\omega)|_{A_2=A_3=0}$. Blue lines show the $m''_F = 0$ component, i.e. $g(\omega)|_{A_1=A_3=0}$. Pink lines show the $m''_F = +2$ component, i.e. $g(\omega)|_{A_1=A_2=0}$. The horizontal-axis frequency offset is measured with respect to 371.022 THz. 86
- 3.19 Two-photon excitation pathways in ytterbium from $6s^2 \ ^1S_0 \rightarrow 5d6s \ ^3D_2$ with light propagating along the quantization axis, in isotopes with (right) and without (left) nuclear spin. The transition can be driven driven by $\hat{\sigma}^-$ (red) or $\hat{\sigma}^+$ (green) polarization, or any superposition of the two – such as the linear polarization $\hat{\sigma} = (\hat{\sigma}^- + \hat{\sigma}^+)/\sqrt{2}$ shown in blue – but the polarization determines which Zeeman states can participate, through selection rules resulting from conservation of angular momentum. In the $I = 0$ isotope shown at left, the levels which do not participate in any of these pathways are dashed; to involve these requires a finite component of $\hat{\pi}$ polarization, which is impossible when the probe wave vector is parallel to the quantization axis. Note that all Zeeman sublevels can be involved when the nuclear spin is nonzero, but that each excited sublevel can only be reached from one ground state sublevel. 87

3.20	The upper figures (a) and (b) show fluorescence spectra in the absence of an optical pumping field, with an arbitrary probe polarization and at two relatively large (different) magnetic field strengths. The signal-to-noise ratio is high enough that the isotopes ^{174}Yb (compound peak between 30MHz and 70MHz) and ^{171}Yb (smaller peaks near 90 MHz) can be readily distinguished, and their Zeeman structure analyzed in some detail; the green line represents a fit to the function $h(\omega)$ defined in equation 3.10 (see table 3.5 for the fit parameters). The lower figures (c) and (d) show the same data, with the fit function for the ^{174}Yb peaks subtracted off; the green lines show $h(\omega)$ evaluated with $A_0 = A_1 = A_2 = A_3 = 0$, and the other parameters as in table 3.5.	89
3.21	The upper figures show fluorescence spectra of ^{174}Yb and ^{171}Yb , with an optical pumping field of (a) $\hat{\sigma}^+$ polarization and (b) $\hat{\sigma}^-$ polarization applied to the atoms before they enter the probe region. The signal-to-noise ratio is considerably worse than in figure 3.20, owing largely to light from the pump beam entering the PMT. The lower figures (c) and (d) show the same data with the contribution from ^{174}Yb subtracted using the fit, as in figure 3.20. Fit parameters are given in table 3.6, according to the function $h(\omega)$ defined in equation 3.10.	90
3.22	Normalized amplitude of the ^{171}Yb $F = \frac{1}{2} \rightarrow F' = \frac{3}{2}$ resonance peak, as a function of pump beam polarization (normalized to the amplitude of the neighboring ^{174}Yb resonance peak). (a) Probe polarization is $\hat{\sigma}^-$, corresponding to the red data series in figure 3.17, which is a good representation of the type of data sets that were averaged to produce the present plot. (b) Probe polarization is $\hat{\sigma}^+$, corresponding to the green data series in figure 3.17, which is a good representation of the type of data sets that were averaged to produce the present plot. The horizontal axes show the voltage applied to the liquid crystal waveplate in the pump beam (see figure 3.11). The three data points on each plot correspondingly show ($\hat{\sigma}^-, \hat{\sigma}^+, \hat{\sigma}$) pump polarizations from left to right.	92
3.23	Error signal resulting from circular dichroism in ^{199}Hg (left) and ^{201}Hg (right) in a vapor cell, as a function of the offset voltage applied to an intracavity piezoelectric transducer. Two photodiodes are used to monitor the intensities of transmitted $\hat{\sigma}^+$ and $\hat{\sigma}^-$ light, which are normalized to the total power and subtracted. The ~ 1 MHz width results from an applied magnetic field along the probe axis; the dispersive lineshape arises from subtracting two nearly-overlapping absorption peaks. The laser frequency can be locked to either zero crossing, and the slope at the lock point determines the bandwidth of the lock. The blue curve is a fit that assumes Gaussian absorption lineshapes. (Data and figure produced in collaboration with Bernd Taubenheim.)	95
3.24	Differential transmission signal through a mercury vapor cell ($\hat{\sigma}^+$ compared to $\hat{\sigma}^-$): (a) without and (b) with a Doppler-free DAVLL system providing active frequency stabilization. The intensity modulation in (a) is a result of free-running frequency drift near resonance. (Data and figure produced in collaboration with Bernd Taubenheim.)	96

3.25	Level structure of atomic xenon, showing two possible two-photon transitions for magnetometry. The measurements reported here focus exclusively on the 256.0 nm transition and the 905 nm decay branch, but analogous measurements are possible using other wavelengths.	97
3.26	Measured doubling efficiencies as a function of temperature, in the second- and fourth-harmonic generation stages of a Toptica TA-FHG pro laser designed for mercury spectroscopy at 253.7 nm. For these data the laser is tuned to operate ~ 2 THz away from the design wavelength, in order to search for the 256 nm two-photon resonance in xenon. The red curve shows temperature dependence of the conversion efficiency in the first doubling stage, and the green data points show the same measurement performed on the second doubling stage (after optimizing the first doubler). For comparison, the blue curve shows a repeated measurement of the green data with the doubling cavity rapidly scanning; this averages out large fluctuations in the vicinity of certain problematic frequencies, and provides some indication of the phase-matching efficiency.	98
3.27	Simplified block diagram of the cw xenon experiment, in the configuration used to produce figure 3.28. Magnetic field coils (not shown) are mounted around the cell and blackout box.	100
3.28	Xenon fluorescence signal at 905 nm, as a function of excitation wavelength. The cell used to obtain these data contained approximately 1.5 bar of natural xenon. Approximately 200 mW of power at 256 nm was used; the nearly constant background is due to laser light entering the PMT through the 905 nm bandpass filter. Weak modulation of the background is attributable to a molecular oxygen resonance at 764.5 nm, which reduces the Ti:sapphire power available to produce 256 nm light.	100
4.1	Intensity spectrum of the optical field, atomic absorption lineshape, and frequency parameters appearing in the overlap integral used to estimate the two-photon absorption rate. We can consider the integration parameters to be ω_1 and ω_2 , or (alternatively) ω and Δ	103

4.2	Block diagram of the experimental configuration used for picosecond two-photon spectroscopy of ytterbium; the atomic beam and 556 nm laser are discussed in chapter 3. The 808 nm probe beam is produced by a commercial Ti:sapphire oscillator (Spectra-Physics Tsunami), pumped by 10 W at 532 nm (Coherent Verdi V-12). The beam passes through a LBO frequency doubler, optical isolator, and optical chopper wheel. Pick-off beams are used to monitor the pulse train (on an APD) and the power spectrum (on a CCD spectrometer), while the intensity of the 404 nm second harmonic is used to evaluate modelocking stability. (Future experiments will use an error signal generated by the second harmonic beam to stabilize the fundamental frequency; see section 4.5.1). The optical isolator is required for stable modelocking since back-reflections from normal-incidence optics tend to destabilize the resonator. A monitor photodiode behind the chamber is used to track the phase of the optical chopper for gated photon counting, and a lens in front is used to increase the intensity incident on the atomic beam.	106
4.3	Schematic diagram of the Spectra-Physics Tsunami 3960-X1BB cavity. Pump light at 532 nm (9-10 W) is coupled into the cavity with a Brewster window and steering and focusing mirrors. The cavity is a folded linear configuration, with a Gires-Tournois interferometer (GTI) at one end and the output coupler mirror providing the second boundary. The GTI can be adjusted to change the amount of negative group velocity dispersion (GVD), thereby regulating the pulse length within approximately a factor of two. The carrier frequency is adjusted by rotating a three-plate birefringent filter about its optical axis. External adjustment knobs for the GTI, birefringent filter, and output coupler are provided for optimization without opening the cavity’s protective cover. Active modelocking is accomplished using an acousto-optic modulator driven near the repetition rate of ~ 80 MHz, and an error signal is produced using the output of a fast photodiode monitor whose alignment can be adjusted by opening the cavity. The control electronics is a Spectra-Physics Model 3955 driver, which provides coarse and fine adjustments of the modelocker phase (required for compensation when cable lengths are changed).	107
4.4	Two-photon fluorescence signal from the Yb atomic beam, excited by 2 ps pulses at 808 nm. Seven 100 ms bins are averaged for each data point, and the signal-to-background ratio is approximately 10. When the atomic beam current is switched off, exponential decay of the fluorescence signal due to the oven cooling down is observed with a time constant of $\tau \approx 2.9$ s (fit line to $f(t) = A + Be^{-(t-t_0)/\tau}$ shown in red). No chopper wheel was used for the measurement shown here, so the residual count rate during the “off” intervals is indicative of the level of background light light entering the PMT.	109
4.5	Level structure of the 778 nm $5s\ ^2S_{1/2} \rightarrow 5d\ ^2D_{5/2}$ two-photon transition, including the 420 nm fluorescence line used for detection.	110

4.6	Spectrum of the picosecond Ti:sapphire oscillator, tuned to the 778 nm two-photon resonance in rubidium. The green line indicates the nominal transition wavelength, but the laser spectrum is centered at the observed fluorescence maximum (the discrepancy is likely due to error in the spectrometer calibration). The spectral bandwidth corresponds to approximately 0.5 nm or ~ 250 GHz, near the transform limit of 220 GHz for 2 ps Gaussian pulses. . . .	111
4.7	Diagram of the rubidium vapor cell experiment, in a configuration similar to that envisioned for noble gas vapor cells. A room-temperature rubidium vapor cell is mounted inside a light-blocked “blackout” box, and probed with a focused probe beam at 778 nm produced by the picosecond Ti:sapphire oscillator. A focusing lens and recycling mirror maximize the intensity at the center of the cell, which is also the focal point for the high-numerical-aperture collection optics for the 420 nm fluorescence light. Two antiparallel fluorescence paths are collected, and both are directed through a bandpass filter into a photon-counting PMT head, similar to that used for the ytterbium experiments. The fluorescence and excitation wavelengths are discriminated by a 420 nm bandpass filter, and detection is synchronized to an optical chopper wheel for background subtraction.	112
4.8	Modulation of fluorescence signal with probe polarization. The x -axis indicates the angular orientation of a quarter-waveplate’s fast axis; the angles 0° , 90° , 180° , 270° , and 360° correspond to the same linear polarization. The angles 45° and 225° correspond to right-hand circular polarization, while 135° and 315° correspond to left-hand circular polarization. Note that the sense of circular polarization does not affect the signal, but the degree of ellipticity does. The green line is fit to the function $q(\theta)$ defined in equation 4.12; the period of the sinusoidal modulation is approximately 90° , as expected.	113
4.9	Diagram of the femtosecond Ti:sapphire (Ti:S) resonator, showing the tuning degrees of freedom δL and $\delta\theta$ that respectively stabilize the repetition rate f_r and the carrier-envelope offset frequency f_0 . The angular parameter θ is modulated by a split piezo-electric transducer mounted on the end mirror of the double-pass prism compressor, providing a fine adjustment of the cavity dispersion. The repetition rate is determined by the optical path length L of the cavity, and adjusted by translating the output coupler with another piezo. The prism compressor consists of two fused silica prisms in double pass configuration; the interprism distance, where the beam is diverging, determines the amount of negative dispersion introduced to compensate for normal dispersion in other cavity components. This regulates the pulse length, which can be as low as 15-20 fs at the output of the resonator. The acousto-optic modulator (AOM) is used to modulate the intensity of pump light entering the cavity, and can be used to tune the cavity dispersion via the intensity-dependent refractive index of the Ti:sapphire crystal. The curved cavity mirrors focus the beam into the Ti:sapphire crystal, increasing the intensity to further exploit the Kerr nonlinearity for modelocking.	115

4.10	Representative spectrum of the femtosecond Ti:sapphire oscillator, with a center wavelength near 808 nm. The frequency bandwidth is approximately 15 THz, corresponding to a pulse length of ~ 30 fs for a transform-limited Gaussian pulse. The central frequency is $f_c \approx 371$ THz and the repetition rate is $f_r \approx 93.2$ MHz, so that an adjustment of f_r by 1 Hz produces a change of ~ 4 MHz in f_c	116
4.11	Diagram of the experimental configuration used for femtosecond two-photon spectroscopy of the ytterbium atomic beam. The picosecond oscillator shown in figure 4.2 has been replaced by the femtosecond oscillator shown in figure 4.9. The monitors for repetition rate and power spectrum are similar, but a pulse compressor and autocorrelator have been added in place of the LBO frequency doubler. The pulse length at the cavity output is 25-30 fs (inferred from the power spectrum), but this broadens to ~ 250 fs due to propagation through dispersive optical media. Prisms (shown) or chirped mirrors are used in the compression stage to precompensate for dispersion, and their effect can be measured by redirecting the beam into a BBO autocorrelator with a flip mirror. Pulses as short as 60 fs were observed in autocorrelation, using either chirped mirrors or fused silica prisms.	117
4.12	Pulse width measured by autocorrelation, as a function of the number of reflections on a set of chirped mirrors. Without chirped mirrors, the pulse width was measured to be 242.5 fs; blue points show measurements. The green line is a linear fit to these data, which indicates a reduction in pulse length by approximately 5.5 fs per reflection. The shortest pulse length achievable with chirped mirrors was 60 fs; additional reflections on the chirped mirrors seem to introduce higher-order dispersion that leads to pulse broadening.	119
4.13	Fluorescence data showing the presence/absence of a femtosecond ytterbium signal, and its dependence on the position of a focusing lens for the probe beam. (a) Red data points correspond to both the probe laser and atomic beam on and intersecting; the first green data point has the laser blocked (atomic beam on) and the second has the atomic beam blocked (laser on). (b) Variation of the measured fluorescence intensity as the probe focusing lens is moved, thereby scanning the highest-intensity region through the atomic beam. The peak around 25 mm is the global maximum; the smaller maximum near 17 mm may result from a subsidiary density maximum in the atomic beam, or from diffracted laser light entering the PMT. The green data point on the right-hand plot was recorded with the lens in the same position as the corresponding blue data point, but with the atomic beam turned off. The red data point at the same position was recorded after the oven was turned back on, but not fully warmed up. The full signal, consistent with the blue data point, was recovered when the oven was allowed to warm up completely.	120

- 4.14 (a) Detected count rate as a function of carrier frequency (blue points), which is extrapolated from the measured repetition rate f_r under the assumption that drifts in the carrier-envelope offset frequency f_0 are negligible. The red line shows a fit to a constant “off-resonant” average signal of 43 Hz, corresponding to the situation where no single transition makes a dominant contribution to the measured count rate. The peak visible near -1000 MHz is a resonantly enhanced transition, but the signal-to-background ratio is not high enough to conclusively identify it. (b) Drift of the laser spectrum during the nine hours when the data in plot (a) were collected. Note that a majority of the recorded frequencies are in the range of -1500 MHz to -1000 MHz, so the error bars are correspondingly larger in the range of -500 MHz to 500 MHz. 121
- 4.15 Stabilization scheme for the picosecond ytterbium experiment. A cw diode laser at 404.5 nm is locked to a potassium reference cell, and its heterodyne beat frequency with the second harmonic beam from the Ti:sapphire is measured with an avalanche photodiode (APD). The beat frequency is stabilized by adjusting the drive frequency of an acousto-optic modulator (AOM) in the original 808 nm beam. The cavity length can be separately stabilized with a piezoelectric transducer, by separately locking a harmonic of the repetition rate f_r to a RF reference oscillator. The AOM thus feeds back to a combination of f_0 and f_r , but the spectral bandwidth of a picosecond pulse is sufficiently narrow that this distinction is not important. 124
- 4.16 The scheme envisioned for producing stable picosecond pulses at 256 nm for two-photon spectroscopy of xenon. Most features of the laser stabilization are similar to those detailed in figure 4.15, with the difference that the potassium D-line resonance at 766.7 nm or 770.1 nm is used as an absolute reference to stabilize the 768 nm fundamental output of the Ti:sapphire. The stabilized 768 nm beam is frequency-doubled to produce 384 nm, followed by a sum-frequency stage in BBO to produce 256 nm. The experimental apparatus for xenon spectroscopy is similar to the one described for rubidium in section 4.3. 127
- 4.17 Some excited states and intermediate levels relevant to two-photon excitation of radon. The red wavelengths are close to the xenon transition at 256 nm and could therefore be obtained from a xenon experiment with minimal adjustments. 128

5.1	<p>Block diagram of central components in the HeXe EDM experiment. A spin-exchange optical pumping cell containing rubidium, N₂ buffer gas, ³He, and ¹²⁹Xe is contained in a calcium silicate oven and heated to 150°C by flowing air. A magnetic field along the beam axis of approximately 4 mT is produced by coils outside the oven (not shown). The rubidium vapor is maintained at nearly 100% polarization by D1 optical pumping using a 100 W circularly polarized beam (produced by a 795 nm laser diode array); this polarization is collisionally transferred to the noble gas nuclei over a period of several hours. The polarized gas is introduced to an evacuated EDM cell using manually actuated valves, and the cell is transported into a magnetically shielded room whose walls include an aluminum layer for RF shielding and two layers of μ-metal (Krupp Magnifer) for passive magnetic shielding. The cell's silicon electrodes are connected to high voltage leads to produce an internal electric field, and it is placed directly underneath a nonmagnetic liquid helium dewar containing a six-channel LTc SQUID sensor (not shown). The grounded silicon wafer serves as a protective barrier for the SQUIDS in case of high voltage breakdown. A magnetic field of approximately 1 μT is supplied by three-axis Helmholtz coils within the room (not shown), and spin precession is initiated either by rapidly changing the direction of this applied field, or by using one pair of coils to produce a resonant NMR pulse.</p>	132
5.2	<p>(a) Spin precession signals of ³He and ¹²⁹Xe at frequencies of 40.8 Hz and 14.8 Hz, respectively, detected by the LTc SQUID sensor (Z1) at a distance of about 110 mm to the center of the EDM cell. (b) Free precession decays of ³He (red) and ¹²⁹Xe (blue) (signals were filtered by a software FIR bandpass filter of 4 Hz width centered at the corresponding Larmor frequencies) (c) EDM cell mounted on the transport system. (Reproduced from [2] with permission of Springer; figure and caption © Springer International Publishing Switzerland 2016.)</p>	133
5.3	<p>Gradiometer signals recorded from the SQUID sensor, following a series of NMR pulses (ordered in time from top to bottom). Note that the transverse relaxation time increases with each successive $\frac{\pi}{4}$ pulse; this effect may be due to the diminution of a large longitudinal magnetization component, which is assumed to produce rapid relaxation of the precessing spins. When a $\frac{\pi}{2}$ pulse is applied instead, most of this longitudinal magnetization is rotated into the precession plane and the transverse relaxation time increases substantially. The small signal resulting from application of a second $\frac{\pi}{2}$ pulse is consistent with the assumption that little longitudinal polarization remains after the first $\frac{\pi}{2}$ pulse.</p>	134

5.4	Typical layout of a three cell manifold prepared for filling on the vacuum system shown in figure 5.5. The connection to the vacuum system is made with a standard 1-1/3" ConFlat flange, which is attached to the glass manifold via a Kovar joint. The open apertures (including the sidearm for alkali-loading) are used for cleaning, and sealed with an oxygen-propane torch when the manifold is attached to the vacuum system. Virtually any cell with a glass stem can be attached to this type of manifold for filling, but a thermal-expansion-matching layer may be necessary for certain glass types. The manifold – apart from the cells – is almost always made of pyrex, or occasionally quartz.	136
5.5	Layout of the vacuum system used for cell filling. All tubing is stainless steel.	138
5.6	(Left) GE-180 components prepared for a sealed two-chamber EDM cell. The bent tube is intended to regulate diffusion between the chambers and prevent metallic rubidium from migrating into the cylindrical chamber where high voltage is applied. (Right) Finished cell installed in an experiment.	144
5.7	Schematic illustration of the first silicon wafer being bonded to an EDM cylinder. The bond area of about 1.5 cm ² is determined by the wall thickness of the glass tubing, which is polished to an optical finish by hand. Whetting at the interface is visible through the glass when bonding solution is applied to the edge and the pieces are pressed together. Once pressed together, the pieces should not be allowed to move until the bond has cured, and may be weighted to maintain good contact.	147
B.1	Two pulse resonance experiment, where a constant-amplitude oscillating field acts for a duration τ starting at $t=0$ and again at $t=\tau + T$	166

LIST OF TABLES

1.1	Isotopes with 1S_0 ground states and nuclear spin [3]	7
1.2	Wavelengths for low-energy optical transitions from a 1S_0 ground state to selected excited states [3]. Note that the “spin forbidden” $^1S_0 \rightarrow ^3P_1, ^3D_2$ transitions are strongly suppressed in light atoms; they are shown to illustrate the scaling of excitation wavelength with atomic number. In practice a 1D_2 level exists at a similar energy above the ground state, and this could be used instead for multiphoton magnetometry with light atoms. For the cases of Sr, Ba, and Ra it would probably be more convenient to choose a higher electronic level for multiphoton excitation.	24
3.1	Naturally occurring isotopes of ytterbium [4]	63
3.2	Fit parameters for the data shown in figure 3.15 (b)-(d). The fit constants are defined by the function $f_1(\omega)$ given in equation 3.7.	82
3.3	Fit parameters for the data shown in figure 3.16 (a)-(c). The fit constants are defined by the function $f_2(\omega)$ given in equation 3.8.	82
3.4	Fit parameters for the data shown in figure 3.18 (a)-(c). The fit constants are defined by the function $g(\omega)$ given in equation 3.9.	84
3.5	Fit parameters for the data shown in figure 3.20; the fit constants are defined by the function $h(\omega)$ given in equation 3.10. It should be noted that $\omega'_0 - k\Delta$ (not ω'_0) is the center of gravity for the ^{171}Yb transition, since only the $m_F = +\frac{1}{2}, +\frac{3}{2}$ components are included in the fit.	88
3.6	Fit parameters for the data shown in figure 3.21; the fit constants are defined by the function $h(\omega)$ given in equation 3.10. It should be noted that $\omega'_0 - k\Delta$ (not ω'_0) is the center of gravity for the ^{171}Yb transition, since only the $m_F = +\frac{1}{2}, +\frac{3}{2}$ components are included in the fit.	88
3.7	Naturally occurring isotopes of mercury [4]	94
3.8	Naturally occurring isotopes of xenon [4]	97

LIST OF APPENDICES

A The Two Level Problem	153
B Ramsey Interferometry	162

LIST OF ABBREVIATIONS

APD	Avalanche Photodiode
BBO	β -BaB ₂ O ₄ (beta Barium Borate)
BSM	Beyond Standard Model
cw	Continuous Wave
DAVLL	Dichroic Atomic Vapor Laser Lock
E1	(Single-Photon) Electric Dipole
EDM	(Permanent) Electric Dipole Moment
FWHM	Full Width at Half Maximum
GTI	Gires-Tournois Interferometer
ITO	Indium Tin Oxide
LBO	LiB ₃ O ₅ (Lithium Triborate)
LIAD	Light-Induced Atomic Desorption
LIF	Laser Induced Fluorescence
LTc	Low T_c (low critical temperature)
MPOP	Multiphoton Optical Pumping
MSR	Magnetically Shielded Room
NMR	Nuclear Magnetic Resonance
OTS	CH ₃ (CH ₂) ₁₇ SiCl ₃ (Octadecyltrichlorosilane)
PPLN	Periodically-Poled Lithium Niobate
PMT	Photomultiplier Tube
RF	Radio Frequency

RGA Residual Gas Analyzer

RWA Rotating Wave Approximation

SEOP Spin-Exchange Optical Pumping

SHG Second Harmonic Generation

SQUID Superconducting Quantum Interference Device

TPOP Two-Photon Optical Pumping

UVFS Ultraviolet-Grade Fused Silica

LIST OF SYMBOLS

B magnetic field

C charge conjugation operator, or integration contour

d electric dipole moment

E electric field

F total atomic angular momentum (vector operator **F**)

g_K Landé *g*-factor associated with the angular momentum *K*

I nuclear spin (vector operator **I**)

J total electronic angular momentum (vector operator **J**)

$\mathbf{k} = k\hat{\mathbf{k}}$ vector with magnitude *k*, parallel to the unit vector $\hat{\mathbf{k}}$

L total electronic orbital angular momentum (vector operator **L**)

$\boldsymbol{\mu}$ magnetic dipole moment

μ_B Bohr magneton, $\approx 9.274 \times 10^{-24}$ J/T

μ_N nuclear magneton, $\approx 5.051 \times 10^{-27}$ J/T

m_e electron mass, $\approx 5.486 \times 10^{-4}$ u

m_p proton mass, ≈ 1.007 u

P parity inversion operator

S total electronic spin (vector operator **S**), or surface of integration

T time reversal operator

u atomic mass unit, $\approx 1.661 \times 10^{-27}$ kg

ABSTRACT

Optical magnetometry plays a critical role in low-energy precision measurements and numerous other applications. In particular, permanent electric dipole moment (EDM) searches impose strict requirements on magnetic field sensitivity of the underlying atomic or molecular species. Other magnetometer properties – such as chemical reactivity, dielectric strength, and interaction cross-sections with other species – also impose limitations on experimental conditions.

Here, we explore a novel approach to optical magnetometry, using multiphoton transitions of diamagnetic atoms to detect Larmor precession of polarized nuclei. Resonant probes are possible at moderate ultraviolet wavelengths, and hyperfine structure couples spin precession to fluorescence transitions with negligible backgrounds; paramagnetic rotation due to intensity-dependent dispersion may also be detectable. Nuclear spins and nonlinear optical excitation introduce new degrees of freedom, and evade limitations arising from rapid electronic decoherence.

This dissertation reports progress towards two-photon optical magnetometry using ytterbium, rubidium, and xenon. We characterize the influence of probe polarization and magnetic fields on fluorescence spectra, for one- and two-photon continuous-wave (cw) excitation of ytterbium. Resolved hyperfine and isotope structure allow us to use spin-zero isotopes for diagnostics and normalization, and we develop analysis for overlapping two-photon resonances. We also report measurements of two-photon excitation in ytterbium and rubidium using picosecond laser pulses, and in xenon using a cw laser. Although hyperfine structure is unresolved, the rubidium measurements are sensitive to probe field polarization. Fluorescence spectra from two-photon excitation of ytterbium with femtosecond pulses show modulation when the repetition rate changes.

Although techniques for polarizing noble gas nuclei are mature, existing cell designs are incompatible with two-photon magnetometry. We describe development of silicate-assisted hydroxide-catalysis bonding for both aluminosilicate EDM cells with silicon electrodes, and sapphire-windowed cells that transmit ultraviolet excitation light. Progress in measuring the ^{129}Xe nuclear EDM is discussed. Absolute referencing of the picosecond laser to potassium transitions is proposed for two-photon spectroscopy of ytterbium and xenon, and a compatible frequency-tripling method is outlined to produce excitation light

for xenon. Novel possibilities including spatial resolution and multiphoton optical pumping of nuclear spins are considered.

CHAPTER 1

Introduction

This thesis presents progress in the development of a fundamentally new type of precision measurement technique: multiphoton nuclear spin magnetometry. Optical magnetometry, in which light is used to measure the coupling of quantized angular momenta to magnetic fields, plays a critical role in low-energy precision measurements. It is also important in numerous other applications such as medicine, electromagnetic compatibility testing, geophysics and seismology, space science, and magnetic microscopy. The magnetic field sensitivity required by these applications can impose severe restrictions on the underlying atoms or molecules (resulting from the magnitude of the magnetic moment, available number density, or experimentally achievable signal-to-noise ratio), with the result that only a few atomic species have been employed as optical magnetometers. Other properties of the magnetometer – such as chemical reactivity, dielectric strength, and interaction cross-sections with other species – also impose limitations on the experimental conditions in which it can be usefully employed, which can conflict with an application’s technical requirements. The experimental techniques described here offer the possibility to perform optical magnetometry with a number of desirable but previously impractical atomic species, thus potentially evading previous limitations. The multiphoton optical interaction further promises a new set of tools for broader applications, including spatially resolved magnetometry and direct optical pumping of noble gases from their ground states.

Previous methods of optical magnetometry rely on single photon electric dipole (E1) transitions, which can be used to determine the strength of an external magnetic field by optically measuring the Larmor precession frequency of electronic spin angular momenta. Nuclear spin precession is also used for atomic magnetometry; in this case the Larmor frequency is usually measured using conventional methods of nuclear magnetic resonance (NMR), superconducting quantum interference devices (SQUIDs), or an auxiliary optical magnetometer to detect the precessing magnetization of a polarized ensemble. Optical magnetometry has also been demonstrated with nuclear spins – by exploiting the hyperfine interaction, which couples nuclear spin dynamics to E1 electronic transition amplitudes –

but in most cases relatively high E1 transition energies result in prohibitively short probe wavelengths.

However, optical magnetometry based on the nuclear spins of diamagnetic atoms affords several advantages in comparison to alternative methods based on electronic angular momentum or inductive detection. These mainly result from weaker coupling to the external environment, which considerably reduces the impact of noise sources and systematic shifts that limit other magnetometers. At the same time, this means that nuclear spins are more challenging to optically polarize and interrogate than their electronic counterparts; our goal is to establish a reasonable compromise between technical complexity of a new method, and the advantages it offers.

In particular, the long coherence times and small spin-flip cross-sections of polarized nuclei contribute to improvements in statistical sensitivity. Moreover, a large dynamic range in both field strength and temperature opens up the possibility to perform magnetometry in many environments where existing optical magnetometers cannot be used. Diamagnetic atoms (and the noble gases in particular) are nonreactive in comparison to alkali metals, and therefore suitable for a wider range of applications. Many diamagnetic atoms are also interesting for fundamental physics experiments, in particular those in which nuclear structure leads to large expected enhancements in sensitivity to CP -violating physics. Next-generation experiments searching for permanent electric dipole moments (EDMs) will rely heavily on magnetometry with polarized nuclear spins, and new techniques for optical magnetometry will be key to controlling systematic errors in this type of measurement.

By using multiphoton (and especially two-photon) transitions, atoms such as xenon and radon can be excited from the ground state with existing laser light sources. In comparison to the excitation wavelengths for single-photon electric dipole transitions (which lie in the vacuum ultraviolet), the deep ultraviolet wavelengths required for two-photon transitions can be manipulated with relatively conventional optical methods. For higher-order transitions, the wavelength requirements are further relaxed at the expense of reduced excitation rates. Another important feature of multiphoton spectroscopy is that fluorescence detection can use wavelengths that are far removed from the excitation wavelength, due to cascaded radiative relaxation through states that were not directly excited. Spectral filtering thus allows us to perform essentially background-free measurements, where small excitation rates can be detected by photon counting or coincidence measurements at the fluorescence wavelength.

The optical probe must be sensitive to hyperfine structure in the excited electronic spectrum, since this provides the mechanism that couples nuclear spin polarization to optical

excitation. Narrow bandwidth continuous-wave (cw) lasers can easily resolve hyperfine structure in the excited state, and the polarization of the exciting light determines which Zeeman sublevels are probed. Pulsed lasers (whose bandwidth may greatly exceed the hyperfine splitting) can also provide the required spectral resolution, provided that the carrier wave is phase-coherent between pulses and that the excited state lifetime is greater than the interpulse time delay. The frequency spectrum of a modelocked pulsed laser is fully constrained by two radio-frequency parameters, which can be measured and experimentally stabilized or modulated.

Pulsed lasers provide an easier path to high power deep ultraviolet light sources, since resonant cavities are not generally required for nonlinear frequency mixing (as they are in the cw case). They also provide a means to alleviate certain technical limitations, such as multiphoton ionization (which can lead to high-voltage breakdown in EDM experiments) and photodegradation of ultraviolet optical components. The excitation rate is comparable to that obtained from a cw laser of the same average power, and may be enhanced by certain pulse shapes and excitation geometries.

In the following sections we summarize the motivations and methods for multiphoton magnetometry with nuclear spins, and survey similarities and differences to existing techniques. The application to EDM searches is highlighted, and impact on leading systematics briefly discussed. This chapter concludes with an outline of the dissertation, and the remaining chapters discuss in detail several experiments with cw and pulsed lasers that probe nuclear spin polarization with two-photon transitions in diamagnetic atoms, as well as the underlying theory.

1.1 Broad Motivation: Searches for New Physics

Precision measurements at low energy have stringently tested the extremely successful Standard Model of particle physics [5–8], and currently provide some of the most definitive experimental constraints on theories that seek to extend it [9–11] – as well as some of the most intriguing open questions [12–14]. Broadly speaking, experimental searches for physics Beyond the Standard Model (BSM) can be approached in two complementary ways: via direct searches for new particles or interactions at high center-of-mass energies (where the Standard Model’s deficiencies may be relatively significant), or by careful analysis of known low-energy interactions with the aim of identifying or constraining small contributions from new sources. The former category includes high-energy collider experiments, and observational studies of high-energy particles from other sources; the latter includes a broad spectrum of experiments in atomic/nuclear and low-energy particle sys-

tems, which are mainly concerned with precisely quantifying radiative corrections to Standard Model processes, or with somehow isolating the relatively weak signature of a new particle or coupling from a large Standard Model “background”.

A generic feature of low-energy experiments concerned with BSM physics is that the energy scale of new physics must be somehow coupled to experimental apparatus in which Standard Model physics overwhelmingly dominates. (The Standard Model quite adequately accounts for the essential features of existing experimental methods.) Such experiments therefore require exquisitely detailed knowledge of the Standard Model background, such that BSM effects can be unambiguously identified and distinguished from it. Background characterization is confounded by two classes of effects: statistical limits relating to the quantity and precision of obtainable data, and systematic effects in which some Standard Model contribution has an experimental signature indistinguishable from the prospective BSM signal. Experimental improvements are largely driven by technological advances that minimize the impact of systematic correlations (in addition to technological advances that increase the rate of data production).

A corresponding problem occurs in the theoretical interpretation of experimental results. Since the fundamental BSM physics is not probed directly, it may couple to experiments through subtle and quite complex mechanisms. Even an unequivocal experimental signature may not be straightforwardly connected to parameters in the fundamental theory; this obviously motivates a great deal of theoretical work seeking to elucidate the coupling of fundamental parameters to experimental observables, but it also highlights the need for multiple measurements in complementary systems. Generally speaking, it is possible to jointly constrain parameters in an effective field theory (or even the fundamental BSM source) by combining results from systems in which the mechanisms of intermediate coupling differ [15].

Although experimental techniques and their underlying technologies are diverse and continually evolving, two early themes remain consistently present: control and stabilization of electromagnetic fields,¹ and frequency-based metrology.² The two naturally go hand-in-hand, and indeed were crucial to the most numerically precise determinations of Standard Model parameters (see [6] for the most conspicuous example). Interestingly, the basic approaches to magnetic field control and frequency metrology have not substantially

¹Qualitatively, we can explain this circumstance by the fact that electromagnetic interactions dominate everyday physics. In practice, they are by far the most easily manipulable of the four “fundamental” Standard Model forces.

²It is unofficial canon that, “in experimental physics a precision measurement is almost always a frequency measurement, and the easiest way to study an effect with precision is to find an observable frequency that is sensitive to that effect” [16].

changed in recent decades. The work presented here aims to expand the set of atomic systems that can be probed and manipulated at a level of precision useful for modern BSM searches, by introducing a novel technique for measuring the coupling of atoms to magnetic fields.

1.2 Precision Measurements in Low-Energy Atomic Systems

Atomic and molecular systems provide unique experimental opportunities to investigate the low-energy signature of BSM physics, since the test systems of interest are relatively stable and abundant. Probing many identical (albeit composite) particles for a long time is necessary for statistical precision, and doing so under stable and adjustable external conditions allows a careful experimenter to mitigate the leading systematic effects. In these systems, the known interactions of the Standard Model background are very well described by the interactions of classical electromagnetic fields with charged particles, with and without spin. These interactions are understood in exquisite detail, and numerous highly refined techniques for controlling them experimentally are now commonplace.

Searches for permanent electric dipole moments (EDMs), spin-mass couplings, violations of local Lorentz invariance, and other BSM physics are readily accomplished via techniques borrowed from precision laser and NMR spectroscopies. The metrological precision of optical magnetometers, along with the fact that many of these searches depend on the response of a system to a magnetic field, imply that modern precision measurements almost invariably rely upon optical magnetometry. It should, of course, be mentioned that the techniques of precision measurement also find ready application outside the search for new physics (see, for example, Part II of [17] for a relatively comprehensive survey relating specifically to optical magnetometers).

1.3 Approaches to Optical Magnetometry with Warm Vapors

The essential feature of optical magnetometry is that polarization moments of an ensemble density matrix³ couple both to an external magnetic field, and to optical radiation. Suppose

³Strictly speaking, of the density *operator* – see section 2.1.1.

an ensemble of atoms with magnetic structure is prepared in a polarized state⁴ (e.g., by optical pumping) and subjected to an external magnetic field. The energy splittings between different eigenstates include terms due to the linear or nonlinear Zeeman effects, which couple the field to the atomic (magnetic) dipole moment. Therefore, the dynamical phases associated with time evolution in this field depend on the field strength. Optical radiation can induce a new coupling between particular eigenstates, thereby permitting an experimental determination of their relative phase. Under suitably controlled conditions, this phase is directly related to the absolute field strength through fundamental constants and good quantum numbers, and optical magnetometers thus readily achieve “calibration-free” field measurements.

Optical magnetometers currently provide the most sensitive means of measuring magnetic field strengths, with demonstrated sensitivities well below $1 \text{ fT}/\sqrt{\text{Hz}}$ [18]. Although great variety exists in the detailed schemes of individual systems and applications,⁵ some universal themes are surprisingly restrictive. Chief among these is the use of single-photon electric dipole (E1) transitions, followed closely by the overwhelming prominence of alkali metals and metastable helium as the atomic species of choice.⁶ The reason for this pattern is obvious: these are by far the most technologically mature and experimentally convenient choices, but specific measurements impose specific requirements that need not be compatible with mature or convenient technologies. Indeed, we have reached a stage where precision measurements (for example, [9]) can be limited by systematic effects in a reference magnetometer, rather than in the system nominally under investigation.

Next-generation precision measurements require fundamentally new technologies, and an optical magnetometry scheme based on nuclear spins in closed-shell⁷ atoms (see table 1.1) offers certain advantageous features unavailable in previously existing systems. Most of these advantages are associated with the lack of unpaired electrons in the ground state, since such atoms tend to be less chemically reactive than the alkalis, and the nuclear spin is well shielded from residual perturbing interactions. The resulting long coherence times and small spin-flip cross sections are well known in the context of NMR with hyperpolarized diamagnetic atoms [19–21], but for the most part these atoms have not been explored as optical magnetometers – and even the exceptions (e.g., [22–24]) frequently still rely on E1

⁴We will sometimes use the term *polarized state* to indicate any density matrix with nonvanishing moments higher than the monopole (rank zero). Somewhat confusingly, the term *polarization* is also commonly used to denote the magnitude of the dipole (rank 1) moment. See section 2.1.1 for a brief discussion of nomenclatural conventions.

⁵See, e.g., the variety of topics covered in [17].

⁶The most notable exception is mercury [9, 10], which also deserves special mention as the most prominent example of an optical magnetometer based on *nuclear* rather than electronic spin.

⁷By which we often really mean closed *sub*-shell, e.g. the np^6 configuration of the noble gases.

Table 1.1: Isotopes with 1S_0 ground states and nuclear spin [3]

Atomic Number	Isotopes	Electron Configuration	Nuclear Spin I
2	^3He	$1s^2$	$1/2+$
4	^9Be	$2s^2$	$3/2$
10	^{21}Ne	$2s^2 2p^6$	$3/2$
12	^{25}Mg	$3s^2$	$5/2$
18	Ar^a	$3s^2 3p^6$	0
20	^{43}Ca	$4s^2$	$7/2$
30	^{67}Zn	$3d^{10} 4s^2$	$5/2$
36	^{83}Kr	$3d^{10} 4s^2 4p^6$	$9/2$
38	^{87}Sr	$5s^2$	$9/2$
48	$^{111,113}\text{Cd}$	$4d^{10} 5s^2$	$1/2, 1/2$
54	$^{129,131}\text{Xe}$	$4d^{10} 5s^2 5p^6$	$1/2, 3/2$
56	$^{135,137}\text{Ba}$	$6s^2$	$3/2, 3/2$
70	$^{171,173}\text{Yb}$	$4f^{14} 6s^2$	$1/2, 5/2$
80	$^{199,201}\text{Hg}$	$4f^{14} 5d^{10} 6s^2$	$1/2, 3/2$
86	$^{211,219,221,223}\text{Rn}^b$	$4f^{14} 5d^{10} 6s^2 6p^6$	$1/2-, 5/2+, 7/2+, 7/2$
86	^{223}Ra	$7s^2$	$1/2$
102	No^b	$5f^{14} 7s^2$	

^aAll stable isotopes of argon have $I = 0$

^b unstable isotopes

excitation of alkali atoms.⁶

The disadvantages of a magnetometer based on closed-shell atomic species are fairly obvious: 1) the nuclear spin does not couple directly to the electric dipole operator, and 2) electrons in closed sub-shells tend to be tightly bound, with the result that relatively short wavelengths are required for optical excitation. Whereas for all alkalis the unpaired electron can be excited with photon energies less than about 2 eV,⁸ the lowest-lying dipole-allowed excited state of mercury (in some sense the best case for a nuclear spin magnetometer) is nearly 5 eV above the 1S_0 ground state. The corresponding transition wavelength of 254 nm actually is commercially available, but remains far removed in convenience, cost, and versatility from the diode laser systems that are readily available for alkali metals. For the noble gases the situation is considerably worse, with all wavelengths for E1 transitions from the ground state lying in the vacuum ultraviolet.

To address the first point, we observe that the hyperfine interaction mixes eigenstates of \mathbf{I} and \mathbf{J} (the total nuclear and electronic spin operators, respectively). Since the ground state has no electronic angular momentum, hyperfine structure occurs only in the excited state. An optical field of narrow bandwidth can excite a single hyperfine component of the excited state, and is therefore sensitive to nuclear spin moments. For example, figure 1.1 illustrates a situation in which only the ground state sublevel with $m_I = -\frac{1}{2}$ is excited.

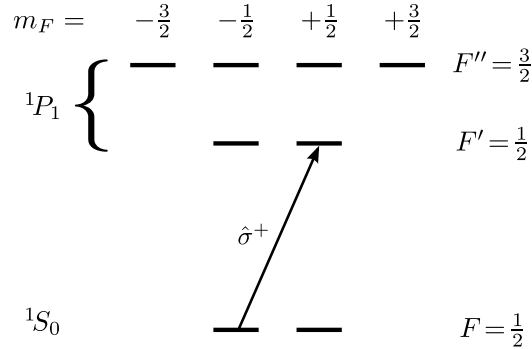


Figure 1.1: Optical E1 excitation from a ground state with $J = 0, I = \frac{1}{2}$ to an excited state with $J = 1, I = \frac{1}{2}$. If the optical field is circularly polarized, then each photon carries one unit (\hbar) of angular momentum and only transitions with $\Delta m_F = 1$ are possible. Spectroscopic terms are shown at left, and eigenvalues of total angular momentum ($\mathbf{F} = \mathbf{I} + \mathbf{J}$) at right; both $F' = \frac{1}{2}$ and $F'' = \frac{3}{2}$ belong to the 1P_1 term. We have assumed that the hyperfine splitting is large compared to the bandwidth of the optical field, such that only the lower hyperfine component of 1P_1 is resonantly excited.

The second point can be approached from two perspectives: one can either develop new light sources at extreme ultraviolet wavelengths, or alternatively find a way to make

⁸Resonant wavelengths in the range of 589 nm (sodium) to 895 nm (cesium).

do with existing sources of lower-energy photons. The first approach is an active but very challenging area of current research [25]; we shall instead focus on the use of multiphoton resonances to ease the wavelength requirements. This type of nonlinear optical process may be considered as higher-order contributions in a perturbative expansion of the atom-field interaction, where the perturbation parameter is the fine-structure constant $\alpha \approx 1/137$. The leading-order term in this series is the usual E1 interaction; we therefore expect the interaction strength to rapidly diminish as the number of participating photons increases. The perturbative scattering rate for an n -photon transition between states a and b , excited by an electric field with constant amplitude E and frequency ω (which is not resonant with any intermediate state),⁹ is given by

$$R_{ba}^{(n)} = \left| \frac{E^n}{\hbar^n} \sum_{i,j,\dots,k} \frac{d_{ai}d_{ij}\cdots d_{kb}}{\Delta_{ia}^{(n-1)}\Delta_{ja}^{(n-2)}\cdots\Delta_{ka}^{(1)}} \right|^2 2\pi\rho(\delta). \quad (1.1)$$

This result is obtained from a straightforward generalization of the perturbation theory methods described in [26]. The sum extends over all dipole-allowed intermediate states, d_{ij} is the electric dipole matrix element for the $i \rightarrow j$ transition, $\delta = \omega_{ba} - n\omega = \Delta_{ba}^{(n)}$ is the n -photon detuning from the $a \rightarrow b$ transition, and $\rho(\delta)$ is a lineshape function obtained by convolution of the probe frequency spectrum with the density of final atomic states. The energy defects $\Delta_{ia}^{(m)} = \omega_{ia} - m\omega$ express the m -photon detuning from the $a \rightarrow i$ transition, and products of these comprise the resonance denominator for each amplitude in the sum. Dependence on the field polarization and propagation vectors enters mainly through the matrix elements, while frequency dependence (including the Doppler effect) is determined by the lineshape function and resonance denominator.

Since the driving field need not be resonant with any intermediate levels, the detuning factors $\Delta_{ia}^{(m)}$ are typically large (in many cases comparable to, or even greater than, ω). Thus we see that as n increases, each term in the sum of amplitudes is suppressed by additional intermediate detunings. A few possibilities exist for enhancing the scattering rate (e.g., an intermediate resonance, or a combinatorially favorable spectrum of field frequencies and nonresonant states), but the most direct path to a high transition probability is to choose n as low as possible and then maximize the values of E and $\rho(\delta)$. Thus when E1 excitation is impractical, $n = 2$ is the obvious alternative.

We should at this point emphasize the nonlinear scaling of $R_{ba}^{(n)}$ with E for $n > 1$. For $n = 1$, a two-fold increase in optical intensity results in a two-fold increase in transition rate; this is the linear response of “linear” optics. For $n > 1$ the E^{2n} scaling makes it

⁹The “intermediate” states need not actually lie between the initial and final states, and may even include substantial contributions from the continuum.

possible to achieve a considerable increase in transition probability for a relatively modest increase of optical intensity. (In the language of nonlinear optics, this is a non-parametric process related to the imaginary components of higher-rank tensor susceptibilities.) Since most practical light sources for two-photon spectroscopy of diamagnetic atoms leave us decidedly in the perturbative regime, we can for now ignore saturation effects and expect that even small increases of output power will produce relatively large increases of signal.

Finally, we note some additional properties of the multiphoton nuclear spin magnetometer. These may be held in mind for comparison during the subsequent discussion of a generic alkali magnetometer, and will resurface later in both theoretical considerations and the exposition of experimental studies.

1. The nuclear magneton μ_N is smaller than the electronic Bohr magneton $\mu_B \approx 9.274 \times 10^{-24}$ J/T by a factor of the proton-to-electron mass ratio, $m_p/m_e \approx 1836$. The intrinsic field sensitivity is reduced by a corresponding factor, as is the Larmor precession frequency (the quantity measured in experiments).
2. NMR-based nuclear spin magnetometers have been used extensively, but typically require different readout methods at different field strengths. SQUIDs are very effective at low field, but require extensive cryogenic apparatus and extreme field stability. Inductive pickup coils work well at intermediate and high field strengths, but require large magnetization fields (i.e., high polarization¹⁰ or large samples) and have limited bandwidth. Alkali magnetometers can function across a wide range of field strengths, but require geometrical proximity to the sample (as do SQUIDs and coils). An optical probe can have a frequency measurement bandwidth from DC to GHz (fields from zero to > 100 T for a nuclear magnetic moment), and can be used remotely and in drifting fields.
3. The n -photon absorption process is followed by radiative relaxation of the excited state. This typically proceeds by cascaded E1 emission through real energy levels, and produces a fluorescence signal at wavelength(s) considerably different from the excitation light. It is therefore simple to spectrally filter the signal light from the excitation light; optical magnetometers based on E1 transitions must usually isolate the signal from a large background produced by the driving field, since the resonance and response occur at the same optical frequency. This low-background environment compensates to some degree for the low transition probabilities expected for multiphoton excitation. We also note that radiation trapping of the excitation light

¹⁰In the sense of dipole moment per unit volume.

is not a concern, and that the first fluorescence photon will typically exit the vapor unimpeded.

4. For E1 resonances, absorption and dispersion may be considered (respectively) as the imaginary and real parts of a linear susceptibility. Similarly, there is a parametric counterpart to the nonlinear process of multiphoton absorption – i.e., an intensity-dependent refractive index. Much as E1 alkali magnetometers are frequently based on off-resonant dispersive atom-field interactions, we can envision a multiphoton magnetometer based on similar effects at higher order. The experimental signal (e.g., rotation of the plane of linearly polarized light) is completely analogous, except that the refractive index now depends on intensity.
5. Existing optical magnetometers are constrained to a fairly restrictive range of operating temperatures and atomic number densities; the vapor pressures of alkali metals and mercury are strong functions of temperature, and both are incompatible with cryogenic applications. Additionally, although high number densities are required for statistical precision, they also increase the rate of depolarizing collisions and spatial averaging. Surface coatings [27,28], buffer gases [29,30], and light-induced atomic desorption (LIAD) [31,32] are partial remedies, but ultimately of limited utility when electron spins dominate the ground state magnetic field coupling. On the other hand noble gas magnetometry *is* compatible with high densities and low temperatures,¹¹ since the shielded nuclear spins are substantially less affected by depolarizing collisions with walls and other atoms or molecules. A noble gas can also act as its own buffer gas, which simultaneously limits spatial diffusion and increases the number of atoms contributing to the measurement.
6. The nonlinear scattering rate offers the possibility to spatially localize the atom-field interaction, e.g. at the focus of a laser beam. Combined with buffer-gas-restricted diffusion, this allows in principle measurements with longitudinal as well as transverse spatial resolution on length scales considerably smaller than a vapor cell (particularly in the range of $1\mu\text{m}$ to 1mm). A simple scaling argument shows that for the case of two-photon excitation, the field sensitivity is independent of the volume probed: essentially, for a focused beam the increase in intensity compensates for the reduction in atom number (see below and section 2.5).
7. Just as nuclear spins can be challenging to probe, they are difficult to polarize in the

¹¹Even, it turns out, in the liquid [33] and solid [34] states.

first place.¹² However, a sufficiently intense light source can modify the ground state population distribution by multiphoton excitation, i.e. optically pump the atoms. This is a possible means to avoid spin-exchange optical pumping, which, despite being by far the most efficient method of polarizing noble gas nuclei, considerably increases the technical complexity of an experiment and can introduce a variety of limitations and systematic errors. We shall refer to Two-Photon Optical Pumping and Multiphoton Optical Pumping, respectively, as TPOP and MPOP.

8. Pulsed lasers can more efficiently produce the short wavelengths required to excite noble gases, and with less damage to laser elements or downstream optics than their continuous-wave (cw) counterparts. The spectrum of a modelocked pulsed laser consists of many discrete modes, whose absolute amplitudes and frequencies can be regulated by a small number of experimentally accessible degrees of freedom. For multiphoton transitions, a mode spacing can usually be chosen that substantially reproduces the frequency resolution of a narrow-bandwidth cw laser without loss of signal. Since the excitation amplitudes corresponding to different paths and mode combinations add coherently, the scaling of excitation probability with n is considerably better than the cw case.

1.3.1 The Common Optical Magnetometer

The prototypical optical magnetometer is a one-electron atom with nuclear spin ignored (i.e., an alkali metal with $I = 0$).¹³ It is well described by LS coupling, with a spectroscopic term symbol ${}^2S_{\frac{1}{2}}$ for ground state and ${}^2P_{\frac{1}{2}, \frac{3}{2}}$ for the lowest-lying excited states, as shown in figure 1.3. The terms ${}^2P_{\frac{1}{2}}$ and ${}^2P_{\frac{3}{2}}$ couple to the ground state via single-photon electric dipole (E1) transitions that are commonly referred to as D1 and D2, respectively.

We suppose that the spectral bandwidth of the driving field is sufficiently narrow that D2 excitation can be neglected, and hereafter consider the atom as a two-level system. The ground state and excited state are then treated as two-level subsystems, and we are primarily concerned with the dynamical evolution of the spin $\frac{1}{2}$ ground state in a uniform external magnetic field \mathbf{B} . For a given quantization axis $\hat{\mathbf{n}}$, we represent the ${}^2S_{\frac{1}{2}}$ sublevel with $m_J = \pm \frac{1}{2}$ by the ket $|\pm\rangle_n$.

An atom initially prepared in the pure state $|\psi(0)\rangle = |+\rangle_z$ can also be represented by

¹²After all, the same physics accounts for both difficulties – and for the desirable features that originally motivated us to consider them.

¹³This is a superficially fictional object, but a pedagogically useful one; note also that several unstable isotopes fit this description. Chapter 4 discusses the extension of two-photon optical magnetometry to certain unstable species, albeit ones having finite nuclear spin.

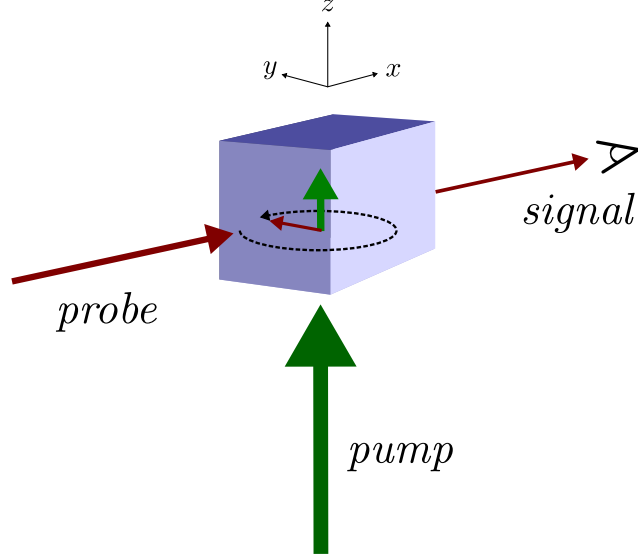


Figure 1.2: Schematic illustration of a conventional all-optical magnetometer. The atoms are optically pumped along the axis of a static field $\mathbf{B} = B\hat{z}$, after which the spins are rotated into the xy plane to initiate free precession. The precession is detected via the transmitted component of a probe beam along \hat{x} .

a coherent superposition of $|\pm\rangle_x$. If the magnetic field is applied in the direction \hat{x} , then it makes sense to discuss time-evolution in terms of the J_x eigenstates:

$$|\psi(t)\rangle = \frac{e^{-iEt/2\hbar} |+\rangle_x - e^{iEt/2\hbar} |-\rangle_x}{\sqrt{2}}, \quad (1.2)$$

where $E = \hbar\omega_0 = \sum a_n B^n$ is the energy splitting between $|+\rangle_x$ and $|-\rangle_x$ and we take the zero of energy to coincide with the twofold-degenerate energy of ${}^2S_{\frac{1}{2}}$ at $B = 0$. For weak fields and certain choices of angular momentum eigenstates (which are automatically satisfied in the present case), the power series has negligible contributions from all but the $n = 1$ term; in this case ω_0 is known as the Larmor frequency, and we typically write it in terms of a Landé g -factor and dimensionful magnetic moment (here, μ_B) as

$$\omega_0 = \frac{g_J \mu_B B}{\hbar}. \quad (1.3)$$

The superposition state in equation 1.2 clearly involves a time-dependent relative phase, regardless of the eigenbasis chosen for representation of the state kets. The probability to find the atom in, for example, $|-\rangle_z$ is

$$|\langle\psi(t)|-\rangle_z|^2 = \sin^2 \frac{\omega_0 t}{2}. \quad (1.4)$$

This can be understood as a coherent oscillation of the ground-state population (in the basis

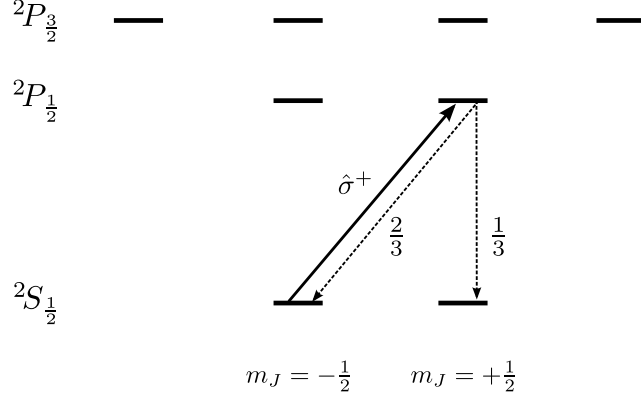


Figure 1.3: Electronic structure of an idealized alkali without nuclear spin, including Zeeman sublevels. The solid arrow indicates D1 excitation with left circularly polarized ($\hat{\sigma}^+$) light, and dashed arrows show allowed decay pathways for spontaneous emission. The numbers $\frac{1}{3}$ and $\frac{2}{3}$ are branching fractions due to angular momentum coupling for E1 transitions.

of J_z eigenstates) between $|\pm\rangle_z$, i.e. as a special case of quantum beating. A measurement that probes the instantaneous population of $m_J^{(z)} = -\frac{1}{2}$ will display a characteristic modulation at the frequency ω_0 , which is proportional to the magnetic field. Experimentally determining this modulation frequency constitutes a measurement of the magnetic field magnitude B (the other quantities in equation 1.3 are assumed to be independently known).

One possibility for such a measurement is optical excitation of the $\hat{\sigma}^+$ transition shown in figure 1.3. Both the absorptive and dispersive components of the atom-light interaction are frequency-modulated at ω_0 ; several different types of magnetometric measurement are therefore possible. In practical terms, all require an ensemble of many identically prepared atoms (although for theoretical purposes one could equally well imagine a series of repeated measurements on the same system).¹⁴

The density operator for an ensemble of these atoms can be expressed in spherical tensor components, the coefficients of which are commonly referred to as polarization moments [17, 36]. The set of polarization moments provides a quantitative measure of coherence and population distributions across the spectrum of pure states available to the atoms. A considerable advantage of the density matrix formalism is that it readily treats incoherent ensembles and decay mechanisms that are not easily expressed or motivated in a picture based on pure energy eigenstates.

Our model system has total angular momentum $J = \frac{1}{2}$, and therefore only the lowest two ranks of polarization moments can be nonvanishing: the monopole ρ^0 , which is pro-

¹⁴See [35] for an apparent exception to this principle, which is related to the geometric phase effects discussed in section 2.6.

portional to the total population; and the dipole ρ^1 , which is often referred to as *orientation* and in our spin- $\frac{1}{2}$ system relates to the polarization asymmetry or *visibility ratio*

$$P_z = \frac{|\langle\psi|+\rangle|^2 - |\langle\psi|-\rangle|^2}{|\langle\psi|\psi\rangle|^2} = \frac{|\langle\psi|+\rangle|^2 - |\langle\psi|-\rangle|^2}{|\langle\psi|+\rangle|^2 + |\langle\psi|-\rangle|^2} \quad (1.5)$$

$$= \frac{\text{Tr}[J_z\rho]}{\text{Tr}[\rho]} . \quad (1.6)$$

This vanishes for an unpolarized state, and is commonly used as a figure of merit for initial state preparation leading up to a spin precession measurement. P_z also limits the sensitivity of time-domain Larmor frequency measurements, since it is proportional to the peak-to-peak contrast resulting from modulation of the atom-light interaction probability.

1.3.1.1 One-Photon Electric Dipole Transitions

Much as alkali atoms are the workhorse of modern atomic physics, the single-photon electric dipole (E1) transition is by far the preferred means of interacting with them; this is primarily due to the relatively high scattering rates that can be achieved with commercially available diode lasers for most alkali D-lines.

The “fundamental” transition probability¹⁵ for single-photon emission from b to a is [37]

$$P_{ab}d\Omega = \frac{e^2\hbar\omega_{ba}}{2\pi m_e^2 c^3} |D_{ab}^{\mathbf{k},\epsilon}|^2 d\Omega, \quad (1.7)$$

where the wave vector \mathbf{k} of the photon field lies in the solid angle $d\Omega$, $\hbar\omega_{ba}$ is the energy separation between the two levels, and D is a matrix element that characterizes the strength of the atom-field coupling:

$$D_{ab}^{\mathbf{k},\epsilon} = i\hbar^{-1} \langle a | \sum_i e^{i\mathbf{k}\cdot\mathbf{r}_i} (\boldsymbol{\epsilon} \cdot \mathbf{p}_i) | b \rangle, \quad (1.8)$$

where the sum ranges over all electrons and \mathbf{r}_i , \mathbf{p}_i are respectively the position and momentum operators for the i th electron. When the exponent $\mathbf{k}\cdot\mathbf{r}_i \ll 1$, we can approximate the exponential by unity and cast the matrix element into the form

¹⁵This is, in fact, the probability for spontaneous emission when b lies above a in energy. It can be related to the probabilities for absorption and stimulated emission through the principle of detailed balance, which leads to the well known rate equations due to Einstein. It should be emphasized that, although these three interactions must balance each other in thermal equilibrium, the matrix elements involved are fundamental properties of the interaction, which do not depend on thermodynamics.

$$(\boldsymbol{\epsilon} \cdot \mathbf{D})_{ab} = i\hbar^{-1}(\boldsymbol{\epsilon} \cdot \mathbf{p})_{ab} = m_e\omega_{ba}\hbar^{-1}(\boldsymbol{\epsilon} \cdot \mathbf{r})_{ab}. \quad (1.9)$$

We now consider the operator \mathbf{D} to be a vector independent of \mathbf{k} , and proportional to the total electronic position or momentum operator ($\mathbf{p} = \sum_i \mathbf{p}_i$, and $\mathbf{r} = \sum_i \mathbf{r}_i$). This approximation, known as the *electric dipole approximation*, is equivalent to neglecting higher-order electromagnetic multipoles of the optical field. Qualitatively, it is valid when spatial variation of the field amplitude can be neglected on the characteristic length scale of the electronic wavefunctions.

The atom-field interaction can then be described by the matrix elements of an *electric dipole operator*,¹⁶ $\mathbf{d} = -e\mathbf{r}$. This corresponds to a term $-\mathbf{d} \cdot \mathbf{E}$ in the effective Hamiltonian for an atom interacting with an optical electric field \mathbf{E} ; the interaction strength is conveniently parameterized by the Rabi frequency,

$$\Omega_{ab} = \frac{\langle a | e\mathbf{r} \cdot \mathbf{E} | b \rangle}{\hbar}, \quad (1.10)$$

which contains information on the angular momentum coupling of the field polarization to the atomic eigenstates a and b . In particular, $\boldsymbol{\mu}$ can be expressed as a rank 1 spherical tensor operator, which accounts for the usual electric dipole selection rules required by angular momentum conservation. The relative strengths of absorption lines and radiative branching ratios can be viewed as arising from the angular momentum coupling coefficients that contribute to this matrix element.

We know from equation 1.2 that the ground state spin orientation rotates at the Larmor frequency in our model magnetometer. Now we introduce the probe coupling shown in figure 1.3; the Rabi frequency is

$$\begin{aligned} \Omega &= \hbar^{-1} \left\langle \psi(t) \left| e\mathbf{r} \cdot \mathbf{E} \right| {}^2P_{\frac{1}{2}}, m_J^{(z)} = +\frac{1}{2} \right\rangle \\ &= \hbar^{-1} \sin \frac{\omega_0 t}{2} \left\langle {}^2S_{\frac{1}{2}}, m_J^{(z)} = -\frac{1}{2} \left| e\mathbf{r} \cdot \mathbf{E} \right| {}^2P_{\frac{1}{2}}, m_J^{(z)} = +\frac{1}{2} \right\rangle \\ &= -\frac{|\mathbf{E}| \langle r \rangle}{\hbar\sqrt{3}} \sin \frac{\omega_0 t}{2}, \end{aligned} \quad (1.11)$$

where $\langle r \rangle$ is the purely radial matrix element between the two states, and we have skipped several simplifying steps involving the reduction of angular momentum coupling coefficients. Now in general the E1 scattering rate is simply

¹⁶This is an induced electric dipole moment, to be clearly distinguished from the *CP*-violating *permanent* electric dipole moments discussed later.

$$\begin{aligned}
R_{ba}^{(1)} &= \left| \frac{Ed_{ab}}{\hbar} \right|^2 2\pi\rho(\delta) \\
&\approx \frac{1}{\Gamma_b} |\Omega_{ab}|^2,
\end{aligned} \tag{1.12}$$

where Γ_b is the radiative lifetime of the upper state, and we have assumed $\delta = 0$ in the second line. In our magnetometer example, the rate of absorption from the probe beam then reduces to

$$R \approx \frac{2I \langle r \rangle^2}{3\epsilon_0 c \hbar^2 \Gamma} \sin^2 \frac{\omega_0 t}{2}. \tag{1.13}$$

It should be noted that equation 1.12 also describes the E1 optical pumping rate, and that this is the same physics typically used to initially polarize an ensemble of atoms in preparation for a spin precession measurement. In general, the optically induced polarization will relax at a characteristic rate $\Gamma_r = T_1^{-1}$, where T_1 is known as the spin lifetime or longitudinal relaxation time (this is analogous to spin-lattice relaxation in classical NMR). This rate depends on a number of physical mechanisms to be discussed later, most notably depolarizing collisions and field inhomogeneities. The effect of optical pumping on the ground state population distribution across Zeeman sublevels will be significant when the excitation rate exceeds relaxation processes, i.e. when $\kappa \gg 1$, where the dimensionless saturation parameter is defined by

$$\kappa \equiv \frac{|\Omega_{ab}|^2}{\Gamma_r \Gamma_b}. \tag{1.14}$$

Conversely, during a spin precession measurement (when we wish to introduce as little perturbation to the populations as possible) the experimental requirement is $\kappa \ll 1$. We may therefore imagine optically pumping the atoms with a static field along \hat{z} using high-intensity light, and then flipping the field¹⁷ rapidly to \hat{x} at the same time as the light intensity is reduced to a value well below the saturation threshold.

It is worth noting that many real alkali magnetometers in fact use a modulated optical field to more sensitively detect or lock to ω_0 . It is also common to base the measurement on dispersive rather than absorptive resonances, e.g. through the rotation of linear polarization. The simple example given here also extends readily to higher field strengths, where equation 1.3 breaks down and it is necessary to use the full Breit-Rabi solution for the energy eigenvalues [17],

¹⁷Or the probe wave vector and the spins.

$$E(F, m_F) = -\frac{A}{4} - g_I \mu_B m_f B \pm \frac{A}{2(2I+1)} \sqrt{1 + x^2 + \frac{4m_F x}{2I+1}}, \quad (1.15)$$

where A is the hyperfine structure constant and $x = 2(g_I + g_J)\mu_B B/A(2I+1)$ is the perturbation parameter in the intermediate coupling regime. There is immense variety to the details of individual magnetometers, even within the restrictive subset of E1 alkali transitions; our purpose at the moment is simply to give an impression of the underlying mechanisms and the capabilities that follow from them.

1.3.2 Spatial Averaging

Due to atomic motion and spatial confinement of the probe field, optical magnetometers measure a weighted average of the magnetic field strength within some characteristic volume. Several different length scales contribute to the determination of this volume, most notably: the cell's dimensions, the diffusion length over a measurement period, and the dimensions of any optical beams (if smaller than the cell). It is relatively easy to obtain information on length scales *larger* than a cell (by moving the cell, duplicating the device in another location, or building a larger cell);¹⁸ spatial resolution at small length scales is typically more challenging.

An obvious solution is to build smaller vapor cells, and indeed microfabricated alkali cells have been very successful down to millimeter dimensions [38]. There are good prospects for even smaller cells and sensor heads, but the technological requirements for producing such devices can be quite intensive. There are further limitations due to the high rate of depolarizing wall collisions, the corresponding need for high-quality antirelaxation coatings, and the competing requirement to operate at relatively high pressures to achieve a given sensitivity [39].

Yet another approach is to restrict atomic motion by introducing a non-depolarizing buffer gas [40] or cooling the ensemble [41]. The latter introduces a set of technical challenges in its own right and we will not discuss it in depth, except to mention that it has been commonly assumed that cold atoms offer the most pragmatic approach to sub-millimeter spatially resolved magnetometry. This is because for laser-cooled atoms trapped in vacuum, the entire atomic sample is typically confined to the intersection of several laser beams (a volume of order 0.5 mm^3) or optical dipole traps (of order 10^{-6} mm^3). Confinement to a fraction of a cubic micron is possible in optical lattices. In contrast, atoms in a typical

¹⁸However, there *are* significant challenges associated with measuring or precisely estimating the field in a location where it is not possible to place a magnetometer, even when multiple measurement locations surrounding the point of interest are available.

coated vacuum alkali cell can easily cross the cell many times between being polarized and probed. Therefore, even if the pump and probe light are localized to a small volume, the field is nevertheless averaged over the entire cell – whose typical dimensions are in the range of a few centimeters.

The basic difficulty associated with buffer gas restricted diffusion is that collisions with buffer gas atoms are not entirely benign, especially for a magnetometer relying on electronic spin coherence. The cross sections for spin destruction, which may be neglected at sufficiently low pressures, play an increasingly significant role in relaxation as the collision rate increases. For a nuclear spin optical magnetometer with zero ground state electronic angular momentum, the primary concern is pressure broadening of the probe transition.

Even if we concede that a nuclear spin magnetometer can operate in the “buffer gas” regime, a typical optical probe still integrates along the beam axis and so averages in at least one dimension. When driving an E1 transition, a focused beam still interacts significantly with atoms well outside its Rayleigh range. Furthermore, focusing has minimal effect on magnetometers based on polarization rotation, since the refractive index is (to leading order) independent of intensity. The situation is completely different for a multiphoton probe, due to the E^{2n} scaling mentioned above. For two-photon excitation of N atoms, now in terms of the optical intensity $I = \epsilon_0 c |\mathbf{E}|^2 / 2$, we have

$$R_{ba}^{(2)} \approx \frac{4NI^2}{\epsilon_0^2 c^2 \Gamma_b} \left| \sum_i \frac{d_{ai} d_{ib}}{\hbar^2 \Delta_{ia}^{(1)}} \right|^2, \quad (1.16)$$

where Γ_b is the homogeneous linewidth of the upper state b and we have made the simplifying assumption that the probe field is exactly resonant, allowing us to approximate $\rho(0) \approx \Gamma_b^{-1}$.

We now observe that we can write N as the product of a volumetric number density \bar{n} and an interrogation volume V (assuming that \bar{n} is uniform in space). Supposing that the probe beam has power P and is focused to a waist w_0 (the minimum $1/e^2$ beam radius), the intensity at the focus is approximately $P/\pi w_0^2$. The excitation rate drops by roughly an order of magnitude with a 3-fold decrease of intensity, so the signal will be overwhelmingly dominated by atoms close to the focal spot. We can then approximate the excitation volume by the product of the spot size with the Rayleigh range, i.e.,

$$V \approx \frac{\pi^2 w_0^4}{\lambda}, \quad (1.17)$$

and rewrite $R_{ba}^{(2)}$ in a form independent of the excitation volume and beam geometry:

$$R_{ba}^{(2)} \approx \frac{4\bar{n}P^2}{\epsilon_0^2 c^2 \Gamma_b \lambda} \left| \sum_i \frac{d_{ai}d_{ib}}{\hbar^2 \Delta_{ia}^{(1)}} \right|^2. \quad (1.18)$$

Thus we see that although the region where atoms are excited can be extensively controlled by the size and location of the beam focus, the number of excitations per unit time (and thus the signal amplitude of a magnetometer) depends only on the atomic number *density*. Figure 1.4 shows a quantitative calculation of the effective interrogation volume, including diffusion effects.

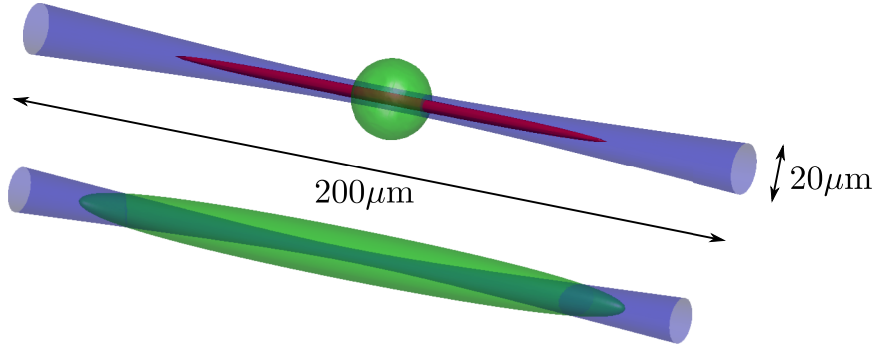


Figure 1.4: Isosurfaces defining the effective interrogation volume. Blue represents the envelope of a Gaussian beam with wavelength 256nm, focused to a $2\mu\text{m}$ waist. Red is the $1/e^2$ surface of constant I^2 , and in the top figure green shows the volume from which atoms can diffuse into the exact focal center (during a characteristic timescale that depends on \bar{n}). In the bottom figure, the green surface represents the $1/e^2$ isosurface of a convolution between the red and green surfaces of the top figure, which is the effective interrogation volume V . The horizontal full scale is approximately $200\mu\text{m}$.

1.3.3 Optical Pumping

Since the magnitude of spin precession signal typically scales with the ground state orientation P , methods for increasing it as close as possible to unity have become a standard element of magnetometry schemes. The equilibrium thermal polarization at room temperature is typically quite small due to the small energy splittings between populated state, and a variety of specialized optical methods for enhancing it have become standard tools in many laboratories. Reference [29] provides a comprehensive review of optical pumping theory and methods (as of 1972), and reference [36] provides a more recent overview of optically-induced polarization, with a great deal of detailed pedagogical material. The timeless article [42] by Kastler, which started it all, invariably rewards inspection.

1.3.3.1 Direct Optical Pumping: Depopulation and Repopulation

We mentioned optical pumping above in section 1.3.1; here we make a few remarks concerning the two principle mechanisms of direct optical pumping. These are “depopulation”, where the population asymmetry arises due to removal of atoms from certain states by excitation; and “repopulation”, in which case where it arises from decay out of a polarized excited state [43]. Hyperfine structure of the excited state plays an important role in optically pumping the nuclear spin of a 1S_0 ground state, which is substantially different for depopulation and repopulation pumping. In both cases the hyperfine splitting must exceed the natural linewidth of the excited state, in order that the excited state survives long enough to couple the electronic and nuclear degrees of freedom.

Depopulation pumping is typically effective only when the excited state’s hyperfine structure is resolved. If the spectral bandwidth of the pump light is not sufficiently narrow, then the all hyperfine components are excited with equal probability and no nuclear spin polarization can result. This is analogous to the situation where spin-orbit coupling in an alkali is not resolved, and both D-lines are excited with equal probability; in that case no electronic spin polarization can be produced.

In contrast, repopulation pumping can occur whether or not the pump field bandwidth is narrower than the hyperfine splitting. In this case the polarization of the excited state matters, and the population asymmetry is communicated to the ground state via radiative decay. We require only that the homogeneous lifetime of the excited state exceed the hyperfine period, such that polarization can be transferred from electron to nucleus before the population decays.

The above considerations apply mainly to cw E1 transitions, and must be reconsidered when we discuss multiphoton optical pumping (MPOP). They remain essentially valid for cw multiphoton excitation, but for pulsed excitation apply only under the additional assumption that the atoms are not interacting with multiple, phase-coherent pulses. A phase-coherent pulsed optical field exhibits periodic frequency structure due to inter-pulse interference, with the result that it is possible to excite only one hyperfine component, even when the total bandwidth exceeds the hyperfine splitting. This violates the apparent restriction on depopulation pumping described above, and constitutes a unique feature of MPOP as compared to conventional E1 optical pumping.

1.3.3.2 Spin-Exchange Optical Pumping (SEOP)

As an alternative to direct optical pumping, the electronic spin polarization of an optically pumped alkali vapor is transferable to other electronic or nuclear spins. During a collision,

when the wavefunction of an alkali electron has a significant overlap with that of another electron or nucleus, there is a finite amplitude for them to exchange angular momentum. In the event that this exchange takes place, the now depolarized alkali atom can be repolarized by direct optical pumping; the timescale for optical pumping of alkali atoms is typically orders of magnitude shorter than that for T_1 relaxation of the species polarized by spin-exchange. The Hamiltonian describing this effect has the same structure as that for the hyperfine interaction within a single atom:

$$H_{SE} = -\frac{\mu_0}{2\pi} g_I \mu_N g_S \mu_B \sum_i \left[\frac{\mathbf{S}_i \cdot \mathbf{I} - 3(\mathbf{I} \cdot \hat{\mathbf{r}}_i)(\mathbf{S}_i \cdot \hat{\mathbf{r}}_i)}{r_i^3} - \frac{8\pi}{3} \delta(\mathbf{r}_i) \mathbf{S}_i \cdot \mathbf{I} \right], \quad (1.19)$$

where $\mathbf{r}_i = r_i \hat{\mathbf{r}}_i$ is the position of the i th electron and the sum ranges over the unpaired electron in the alkali, and all electrons in the other atom. The atom to be polarized by spin exchange has nuclear spin operator \mathbf{I} , and the Landé g -factor g_I in its ground state. The first term represents a “long-range” dipole-dipole interaction, which due to the r^{-3} denominator can nevertheless be ignored except during collisions. This is usually negligible in comparison to the second term, and particularly so in spherical cells where its total contribution vanishes due to symmetry. The second term is known as the Fermi contact interaction, which dominates when the electronic and nuclear wavefunctions overlap in space. This partly accounts for the strong dependence of spin-exchange efficiency on nuclear size, and for the well known tendency of heavy nuclei (such as ^{129}Xe) to polarize and relax much more rapidly than light nuclei (such as ^3He).

The physics of SEOP is rich and complicated [44, 45], but established techniques routinely and efficiently produce large quantities of highly polarized noble gas nuclei. These are an essential element for many precision measurements, which would be impossible using thermal polarization or prohibitively laborious if attempted with other sources of nuclear polarization.¹⁹

1.4 Features of Continuous-Wave Lasers

Continuous-wave (cw) lasers have several advantageous features for multiphoton optical magnetometry, mainly deriving from the small spectral bandwidths that are routinely achieved in actively stabilized systems. Two consequences of narrow linewidth are especially relevant here:

¹⁹E.g., metastability-exchange optical pumping.

1. The ability to perform high-resolution spectroscopy with resolved hyperfine or Zeeman structure, thus straightforwardly achieving sensitivity to the ground state nuclear spin populations via angular momentum selection rules.
2. Insensitivity to chromatic dispersion, in the sense that the dispersive phase imprinted on a sufficiently narrow optical spectrum can be approximated as constant and for most practical purposes ignored entirely. (This completely eliminates certain types of quantum interference between different excitation channels, which can substantially reduce the excitation probability for multiphoton transitions.)

The principal challenges associated with cw systems are the difficulty of producing intense sources at the wavelengths required and of maintaining them in stable operation over long periods of time. Interestingly, these technical difficulties arise due to nonlinear optical phenomena that are closely related to the process of multiphoton excitation. Deep-ultraviolet lasers are usually made by second harmonic generation (or other nonlinear frequency conversion) of a source with longer wavelength. The efficiency of the frequency mixing process that produces the ultraviolet light is thus a nonlinear function of the intensity at the fundamental wavelength, much as multiphoton absorption is a nonlinear function of the optical intensity at the excitation wavelength. In both cases, the intensity parameter \tilde{I} characterizing the strength of the interaction is much greater than the intensity available from currently existing cw light sources. Therefore the achievable ultraviolet intensity scales as $(I/\tilde{I})^n$, where $n \geq 2$ and $I \ll \tilde{I}$ is the intensity of the long-wavelength pump laser. For these reasons, efficient production of cw ultraviolet laser light typically relies on resonant cavity enhancement to achieve a significantly higher fundamental intensity than is available directly from output of the source laser.²⁰ The mixing cavity must be actively stabilized against drift, temperature and humidity regulated, and optimized for the particular frequency desired.

Optical damage mechanisms at ultraviolet wavelengths are also dominated by nonlinear processes at the cw laser powers that concern us. In particular, for the wavelength region around 250 nm, conventional optical media – including quartz, fused silica, other lens glasses, and nonlinear crystals such as BBO – become degraded over time by photochemical reactions at the surface where the light enters, and by photorefractive damage and nucleation of color centers in the bulk. Since this damage is apparently irreversible (although it can be somewhat prevented or mitigated by certain annealing procedures [46] or hydrogen-loading [47]), many optical elements become consumable components of the

²⁰ Specially designed elements such as periodically poled conversion crystals can also be employed to increase the total conversion efficiency at low intensities, removing the need for a cavity.

Atom	State:	Single-Photon				Two-Photon	
		1P_1	$^2[1/2]_1$	3P_1	$^2[3/2]_1$	3D_2	$^2[5/2]_2$
He		58.4 nm		59.1 nm		107 nm	
Be		235 nm		455 nm		322 nm	
Ne			73.6 nm		74.4 nm		133 nm
Mg		285 nm		457 nm		417 nm	
Ar			105 nm		107 nm		189 nm
Ca		423 nm		657 nm		983 nm	
Zn		214 nm		308 nm		317 nm	
Kr			116 nm		124 nm		217 nm
Sr		461 nm		689 nm		1098 nm	
Cd		229 nm		326 nm		336 nm	
Xe			130 nm		147 nm		256 nm
Ba		554 nm		791 nm		2170 nm	
Yb		399 nm		556 nm		808 nm	
Hg		185 nm		254 nm		280 nm	
Rn			145 nm		179 nm		300 nm
Ra		483 nm		714 nm		1429 nm	

Table 1.2: Wavelengths for low-energy optical transitions from a 1S_0 ground state to selected excited states [3]. Note that the “spin forbidden” $^1S_0 \rightarrow ^3P_1, ^3D_2$ transitions are strongly suppressed in light atoms; they are shown to illustrate the scaling of excitation wavelength with atomic number. In practice a 1D_2 level exists at a similar energy above the ground state, and this could be used instead for multiphoton magnetometry with light atoms. For the cases of Sr, Ba, and Ra it would probably be more convenient to choose a higher electronic level for multiphoton excitation.

system and must be regularly monitored for deterioration.

In chapter 3 we present studies of cw optical pumping and two-photon excitation in ytterbium, where it is possible to polarize the ground state nuclear spin by direct optical pumping on the 556 nm intercombination line. The 556 nm light is produced by second harmonic generation with a grating-feedback diode laser as the fundamental source. The resulting polarization is probed both by single-photon spectroscopy of the same transition, and also (in separate experiments) by two-photon spectroscopy of the 808 nm $^1S_0 \rightarrow ^3D_2$ resonance. Light to drive the 808 nm transition is more easily produced with high intensity, since that wavelength falls quite near to the center of the Ti:sapphire emission band. The laser requirements for these experiments are considerably less stringent than those for mercury or xenon, which require 254 nm or 256 nm respectively (see chapter 3).

1.5 Atomic Species: Alkaline-Earth-Like Metals and Noble Gases

For optical magnetometry we are concerned with cw and pulsed laser fields interacting with atoms that have a 1S_0 ground state and finite nuclear spin, especially $I = \frac{1}{2}$ (see table 1.1). All such atoms are interesting magnetometer candidates, and – although they vary substantially in properties such as vapor pressure, chemical reactivity, and the optical wavelengths for their strongest electronic transitions – share a number of key features in their electronic and hyperfine structure. The relevant E1 wavelengths are predominantly shorter than those commonly used for spectroscopy of alkali metals (see table 1.2), but some atoms in this set – notably, ytterbium – have single- or two-photon transitions at relatively convenient laser frequencies. Since their atom-light interactions are essentially the same as in the noble gases, the alkaline-earth-like atoms provide a natural starting place for the development of multiphoton nuclear spin magnetometry. (Indeed they are also a natural first step beyond the alkali metals, as evidenced by their relative popularity in laser-cooling and trapping experiments, and in the early literature on optical pumping and spectroscopy.)

In fact, deep-ultraviolet E1 transitions are also available in this restricted class of atoms, at wavelengths very close to those required for two-photon excitation of the heavier noble gases. In particular, the mercury intercombination line at 253.7 nm lies within 3 nm of both the xenon $^1S_0 \rightarrow ^2[5/2]_2$ resonance at 256.0 nm, and a radon resonance between the same spectroscopic terms at 250.8 nm. Lasers developed for mercury spectroscopy (see [48–50] and section 3.5) can therefore be applied with few or no modifications to the problem of two-photon magnetometry in the noble gases, with the result that laser development and magnetometer optimization are substantially decoupled. A best-case scenario for demonstrating optical magnetometry with noble gas nuclear spins is to combine two technologies that have already been separately proven in analogous systems: high-power lasers at wavelengths shorter than 300 nm, and two-photon excitation as a means of detecting nuclear spin polarization.

The excitation wavelengths for noble gases are uniformly shorter than those for the alkaline-earth-like atoms. This accounts for the practical difficulty associated with polarizing their nuclear spins, since light sources capable of efficient direct optical pumping at such extreme wavelengths are not presently available. Moreover, the wavelengths for E1 transitions out of the ground state all lie in the vacuum ultraviolet. This difficulty, specific to noble gas magnetometry, is removed in mercury and ytterbium by the possibility to polarize their nuclear spins with direct E1 optical pumping. The existing experimental

techniques for polarizing noble gas nuclear spins are relatively indirect and inefficient by comparison, and studies of nuclear spin polarization and two-photon excitation are considerably simplified by the elimination of the complex apparatus required for spin-exchange or metastability-exchange optical pumping.

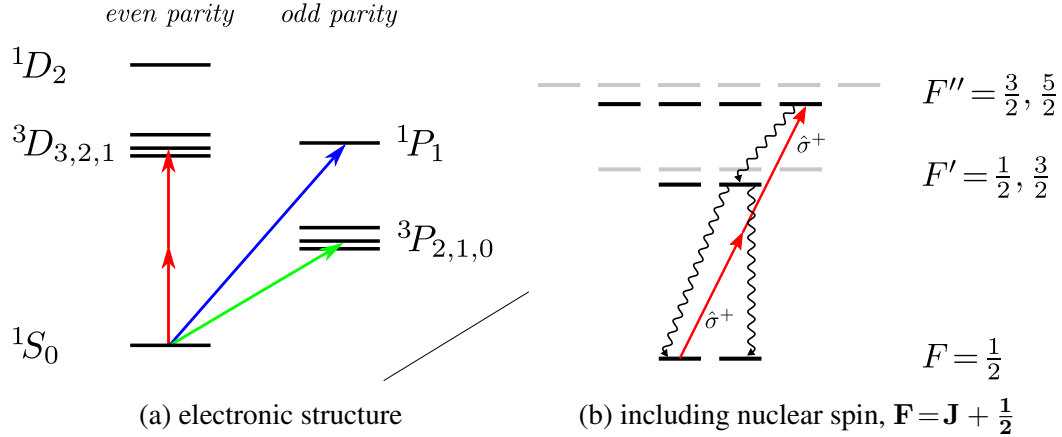


Figure 1.5: Some low-lying electronic excited states labeled by their spectroscopic terms, in alkaline-earth-like atoms. The states are labeled as for pure LS -coupling, but in heavier atoms spin-orbit mixing of the pure LS -eigenstates allows intercombination transitions such as the green arrow in (a). For Yb the shown transitions occur at wavelengths 399nm (blue), 556nm (green), and 808nm (red; two-photon). An isotope with $I = \frac{1}{2}$ such as ^{171}Yb is assumed for (b), and the same two-photon transition is shown with hyperfine and Zeeman structure included. The upper hyperfine level $F'' = \frac{5}{2}$ (shown in gray) is assumed to lie outside the bandwidth of the optical field; neither of the intermediate levels is resonantly excited. In atoms with this electronic structure, the most convenient wavelengths for detection of laser-induced fluorescence usually turn out to be the same ones that are used for direct optical pumping (e.g., 556nm in ytterbium). As discussed below, this produces background noise that is avoidable in the noble gases.

Excited electronic eigenstates of the lighter two-electron atoms are well described by LS (Russell-Saunders) coupling, and may be classified by spin multiplicity as either singlet or triplet. This is characteristic of two-electron atoms more generally (including helium), whose 1S_0 ground states arise from a ns^2 electron configuration rather than the np^6 of the heavier noble gases. For pure LS coupling, E1 transitions cannot connect states of different spin multiplicity since the electric dipole operator acts on only on the spatial component of the electronic wavefunction. Transitions between levels of the same multiplicity follow the usual selection rules, and the lowest-energy E1 transition is usually from the ground state to a low-lying 1P_1 state (see table 1.2 and figure 1.5).

In the heavier atoms, spin-orbit coupling becomes significant in comparison to the electrostatic interaction between electrons, with the result that the (total) electronic angular momentum L and spin angular momentum S are no longer good quantum numbers. In

cases where spin-orbit coupling is not too strong, the notation of LS coupling is often still used, with the understanding that due to spin-orbit mixing the LS eigenstates are not truly orthogonal. In this situation (which applies to ytterbium and mercury), E1 transitions between states of differing multiplicity *do* occur, due to the nominal admixture of singlet states into triplets and vice versa. The strong $^1S_0 - ^1P_1$ transition occurs as in the lighter species, but it is accompanied by a weaker “spin forbidden” or “intercombination” transition from the ground state to a 3P_1 level – which is invariably lower in energy than the “allowed” singlet-singlet transition. The strength of the intercombination transition (or the radiative linewidth of the 3P_1 level) is an indication of the degree of breakdown of LS coupling (or equivalently, the strength of the spin-orbit interaction), and typically grows with atomic number. In similar fashion, the 3D manifold couples both to the $^3P_{3,2,1}$ and 1P_1 levels by single-photon E1 transitions, and to the 1S_0 ground state (and other states of the same parity) by two-photon E1 transitions in which both singlet and triplet intermediate levels contribute to the excitation.

All angular momentum in the ground state is due to nuclear spin, with the result that a magnetometer based on ground state spin precession relies on the hyperfine interaction to mix eigenstates of I and J . This situation is similar to the spin-orbit mixing discussed in the previous paragraphs, since again the electric dipole operator does not act directly on spin wavefunctions. In the limit where the hyperfine interaction is weak enough to be neglected entirely (or the atom-field interaction time is significantly less than the hyperfine period), optical excitation based on E1 transitions is insensitive to the nuclear spin dynamics. We therefore require a method of spectroscopy that is sensitive to the excited state hyperfine structure, even if that structure is “finer” than the overall bandwidth of the probe field. Of course, if the laser bandwidth *is* small compared to the hyperfine splitting then it is possible to drive only one $F = \frac{1}{2} \rightarrow F' = \frac{m}{2}$ transition, where the precise value of $m = 0, \pm 1, \pm 2, \dots$ depends on the number of photons and on angular momentum selection rules. This is the situation with narrow linewidth cw lasers, which will occupy us for the remainder of the chapter. Chapter 4 discusses methods of studying nuclear spin dynamics when the probe laser’s bandwidth exceeds the excited state hyperfine splitting.

1.6 Permanent Electric Dipole Moments (EDMs)

One of several open “challenges” to the Standard Model concerns the origin and strength of CP -violating interactions in the early universe; known sources of CP -violation do not adequately account for the observed cosmological predominance of matter over antimatter. One can search for a low-energy signature of yet unknown interactions that may resolve

this situation by measuring the amplitude of P - and T -violating polarization moments in particles, nuclei, and atoms. The prototypical example of such a polarization moment is the permanent electric dipole moment (EDM), which for reasons of symmetry must lie parallel or antiparallel to the total angular momentum (and therefore also to any finite magnetic dipole moment). It is therefore in principle simple to search for an EDM: one simply measures the precession frequency of a magnetic moment in applied electric and magnetic fields, looking for a shift of the frequency that correlates linearly with the electric field amplitude but is independent of the magnetic field. In practice, of course, EDM experiments are an exercise in the detailed management of systematic errors.

1.6.1 Generic Experimental Protocol

A particle with an EDM d_{CPV} experiences an energy shift $-d_{CPV} \cdot \mathbf{E}$ and a torque $d_{CPV} \times \mathbf{E}$ when exposed to an external electric field \mathbf{E} . The interaction Hamiltonian, when a magnetic field \mathbf{B} is also present, is

$$H = -\mathbf{F} \cdot (\mu\mathbf{B} + d_{CPV}\mathbf{E}) , \quad (1.20)$$

where \mathbf{F} is the total angular momentum operator. The magnetic moment $\boldsymbol{\mu} = \mu\mathbf{F}$ and the EDM $\mathbf{d}_{CPV} = d_{CPV}\mathbf{F}$ are both constrained to lie along \mathbf{F} , but they have different transformation properties under the discrete symmetry operators C (charge conjugation), P (parity), and T (time reversal). In particular, the term involving \mathbf{B} is even under all three of C , P , and T – while the term involving \mathbf{E} is odd under P and T , and therefore (assuming CPT -invariance) must also be odd under CP .

The directions of the vector fields \mathbf{B} and \mathbf{E} can be reversed in an experiment, such that the absolute values of the magnetic and electric energy terms must be added or subtracted. When the experiment is repeated in two different field configurations (\mathbf{B} and \mathbf{E} parallel or antiparallel), the two resulting resonance frequencies can be added or subtracted to isolate the electric and magnetic contributions. The magnetic interaction is very well understood, and by characterizing it with the most sensitive magnetometers that are compatible with the experiment a bound can be placed on the magnitude of the EDM.

1.6.2 Limitations and Representative Systematics

Perhaps surprisingly, a small set of systematic effects accounts for the main limitations in all modern EDM experiments. These include “non-reversing” magnetic fields due to leakage currents, motional magnetic fields due to the $\frac{\mathbf{v}}{c} \times \mathbf{E}$ term arising from relativity,

and a geometric phase associated with particle motion (typically involving an “interference term” that couples magnetic field gradients and the motional magnetic field). The solutions for managing these effects frequently involve characterization by magnetometry, a situation which is complicated by the stringent requirements of EDM apparatus with regard to high voltage, magnetic and material purity, and long-term stability. New tools are clearly needed, and this was the original motivation for pursuing two-photon optical magnetometry in xenon. It now appears that this may be incompatible with the on-line high voltage requirements of the experiments in question, but off-line measurements can still provide a wealth of information, particularly about spatial field structure and geometric phases.

A useful reference for theoretical and experimental issues relating to EDM searches is [51]. A recent survey of the status of theory and experiment, which places an emphasis on the joint constraints obtainable from multiple independent measurements is provided in [15].

1.7 Outline of this Dissertation

In chapter 2, we lay the theoretical groundwork for multiphoton optical magnetometry. The connections between cw and pulsed excitation are emphasized, in order to clearly distinguish their respective features and elucidate which degrees of freedom are experimentally useful in each case. We also discuss some details of electronic pair-coupling and atomic structure, which are particularly important for heavy atoms where LS -coupling fails due to spin-orbit term mixing. Finally, we examine practical magnetometry schemes in more detail, estimate the ultimate sensitivity in some illustrative cases, and list some extant challenges in theoretical approaches to these issues.

In chapter 3 we present the details and results of experiments using cw lasers for optical pumping and probing of nuclear spins. An ytterbium atomic beam in vacuum was used for both single- and two-photon excitation, as a test system for optical readout of optically polarized nuclear spins in a 1S_0 ground state. Vapor cell measurements involving mercury and xenon are also presented; unlike ytterbium, these require lasers at deep ultraviolet wavelengths – as do many species of interest listed in table 1.1.

Chapter 4 turns the focus to pulsed lasers, and reports further studies using the same ytterbium atomic beam system. Two-photon excitation of ytterbium is demonstrated with both picosecond and femtosecond pulses, although no results showing sensitivity to nuclear spin polarization are yet available. The scaling of signal with pulse width is analyzed, and reveals some surprising features that may indicate room for improvement in the laser system. The picosecond laser system was also used to drive two-photon excitation of rubidium

in a vapor cell, in a configuration substantially similar to that envisioned for xenon. Laser developments toward the wavelengths required for xenon and radon are presented, and a scheme for controlling the absolute excitation frequency in ytterbium is proposed.

Chapter 5 discusses some work related to an ongoing measurement of the ^{129}Xe nuclear EDM, one of the many precision measurements reliant on polarized nuclear spins. A novel approach to vapor cell bonding developed for this experiment also promises to simplify the task of inserting deep ultraviolet excitation light into vapor cells without prohibitive losses. Transverse relaxation times in excess of 4000 s are demonstrated for both ^{129}Xe and ^3He , simultaneously, in a cell with silicon end caps bonded to an aluminosilicate glass cylinder. We also discuss prospective applications of spatially resolved multiphoton magnetometry using ^{129}Xe , to mitigate systematic errors associated with geometric phases in EDM searches.

Chapter 6 enumerates some promising directions for future research, which while outside the scope of experiments reported in this thesis, are nevertheless worthy of consideration. These include the possibilities of magnetometry based on polarization rotation, multiphoton magnetometry with $n > 2$, direct spin-polarization by TPOP/MPOP, details of a search for a nuclear EDM in Rn isotopes which will rely on two-photon optical magnetometry, and other (perhaps more ambitious) ideas.

Chapter 7 summarizes the content of this dissertation, and mentions the next steps required to improve upon the experiments reported here.

The appendices include some additional derivations and calculations; results derived in them are used elsewhere, and referred to in the main text.

CHAPTER 2

Theory of Multiphoton Excitation

This chapter explores results from the theory of multiphoton excitation that are relevant for optical magnetometry, and discusses some additional physics that impacts magnetometer sensitivity and systematic errors. A brief survey of the irreducible tensor formalism and polarization moments is presented first in section 2.1, including some consideration of nomenclature and phase conventions. This is followed by explicit calculations of two-photon excitation amplitudes for continuous wave (cw) laser fields in section 2.2, in which it is assumed that the intermediate states are far from resonance so that their amplitudes can be adiabatically eliminated from the calculation. (An analogous treatment using the density matrix formalism can be found in references [52, 53].) Angular momentum coupling, selection rules for two-photon transitions, multiphoton absorption, and paramagnetic rotation are then briefly discussed; this completes the theoretical apparatus required for model calculations and analysis relating to optical interrogation of nuclear spins using cw lasers and multiphoton transitions. The data presented in chapter 3 are discussed and analyzed entirely within this framework.

The following sections discuss pulsed excitation (section 2.3), figures of merit for magnetometer sensitivity (sections 2.4 and 2.5), and a class of systematic effects arising from geometric phases (section 2.6); each of these subjects has an extensive literature of its own, and we only present a brief summary of their most relevant features. Pulsed excitation is considered again in section 4.1, and the remainder of chapter 4 reports on experiments using pulsed lasers (whose interpretation relies upon these results). The magnetometer sensitivity estimates derived in sections 2.4 and 2.5 can be applied to either pulsed or cw excitation. The discussion of geometric phases in section 2.6 is somewhat general, and we consider how such phases can produce systematic effects in experimental searches for a permanent electric dipole moment (EDM).

Some results associated with the dynamics of a two-level quantum system in a time-harmonic potential are presented in appendix A; these are used freely throughout this chapter. The closely related “Ramsey method” of interference by separated oscillatory fields is

discussed in appendix B. A recurring theme is that the spectrum of an ideal modelocked laser can be considered from two complementary points of view: a periodic time-domain envelope function modulating a single-frequency carrier wave, or a superposition of cw modes with fixed relative phases. This, together with the close analogy connecting optical excitation of effective two-level systems and radio frequency (RF) excitation in classical NMR, is a powerful tool for comparing results in qualitatively different experiments.

2.1 Notation and Definitions

Several different conventions exist for the nomenclature and definitions that specify optical polarization, transition matrix elements, and angular momentum coupling coefficients. This section clarifies which conventions are used here, and illustrates some basic results associated with complex conjugation and transitions involving circularly polarized light. More comprehensive presentations can be found in textbooks such as [36, 54–58], as well as the classic references [59, 60].

We will usually express optical electric fields in the form,

$$\mathbf{E}(\mathbf{r}, t) = \frac{1}{2} \hat{\boldsymbol{\epsilon}} \mathcal{E}(\mathbf{r}, t) e^{i(\mathbf{k} \cdot \mathbf{r} - \omega t + \phi)} + \text{c.c.}, \quad (2.1)$$

where \mathcal{E} is a complex function of position and time whose variations are slow in comparison with the complex exponential phase factor. The polarization vector $\hat{\boldsymbol{\epsilon}}$ may also be complex, and we can express it in either a Cartesian basis or in terms of irreducible (spherical) tensor components:

$$\hat{\boldsymbol{\epsilon}} = \epsilon_x \hat{\mathbf{x}} + \epsilon_y \hat{\mathbf{y}} + \epsilon_z \hat{\mathbf{z}} \quad (2.2)$$

$$= \sum_{q=-1}^1 (-1)^q \epsilon_{-q} \hat{\boldsymbol{\epsilon}}_q, \quad (2.3)$$

where the (covariant) spherical components and basis vectors are related to the Cartesian ones by

$$\epsilon_{\pm 1} = \mp \frac{1}{\sqrt{2}} (\epsilon_x \pm i \epsilon_y), \quad \epsilon_0 = \epsilon_z \quad (2.4)$$

$$\hat{\boldsymbol{\epsilon}}_{\pm 1} = \mp \frac{1}{\sqrt{2}} (\hat{\mathbf{x}} \pm i \hat{\mathbf{y}}), \quad \hat{\boldsymbol{\epsilon}}_0 = \hat{\mathbf{z}}. \quad (2.5)$$

This can be done quite generally for any Cartesian vector \mathbf{a} , and it is convenient to define contravariant components with raised indices by

$$a^q = (-1)^q a_{-q}, \quad (2.6)$$

such that we can write the scalar product of two vectors \mathbf{a} and \mathbf{b} as

$$\mathbf{a} \cdot \mathbf{b} = a^q b_q = a_q b^q, \quad (2.7)$$

where repeated indices are implicitly summed. We can also write any vector in terms of the spherical basis vectors $\hat{\mathbf{e}}_q$ as

$$\mathbf{a} = a_q \hat{\mathbf{e}}^q = a^q \hat{\mathbf{e}}_q, \quad (2.8)$$

noting that complex conjugation transforms the covariant basis vectors into their contravariant counterparts, e.g. $(\hat{\mathbf{e}}_q)^* = \hat{\mathbf{e}}^q$. It is therefore important to carefully distinguish between the components $(a_q)^*$ and $(a^*)_q$, e.g. in the second term on the right-hand side of equation 2.1.

We can similarly express an arbitrary tensor T^k of rank k in terms of irreducible components T_q^k , where q takes on the $2k + 1$ values from $-k$ to k . The matrix element of a particular irreducible component can be broken into ‘‘physical’’ and ‘‘geometrical’’ factors by the Wigner-Eckart theorem:

$$\langle \alpha' j' m' | T_q^k | \alpha j m \rangle = (-1)^{j'-m'} \begin{pmatrix} j' & k & j \\ -m' & q & m \end{pmatrix} \langle \alpha' j' || T^k || \alpha j \rangle, \quad (2.9)$$

where m and m' are respectively the projections of the angular momenta j and j' along the quantization axis, and α, α' is a collective index representing any other quantum numbers required to completely specify the states. The quantity $\langle \alpha' j' || T^k || \alpha j \rangle$ is a *reduced matrix element*, which is independent of q . We can consider it to be a property of the physical observable associated with T^k , whereas the geometry-dependent part (relating to angular momentum coupling and the orientation of the quantization axis) is contained in the $3j$ symbol

$$\begin{pmatrix} j_1 & j_2 & J \\ m_1 & m_2 & -M \end{pmatrix} = \frac{(-1)^{j_1-j_2+M}}{\sqrt{2J+1}} \langle j_1 m_1, j_2 m_2 | JM \rangle. \quad (2.10)$$

In this expression, $\langle j_1 m_1, j_2 m_2 | JM \rangle$ is the Clebsch-Gordan coefficient for coupling eigenstates of $\mathbf{j}_1^2, j_{1z}, \mathbf{j}_2^2, j_{2z}$ into eigenstates of $\mathbf{J}^2 = (\mathbf{j}_1 + \mathbf{j}_2)^2$ and J_z . We will also make use of the $6j$ symbol,

$$\left\{ \begin{matrix} j_1 & j_2 & j_{12} \\ j_3 & J & j_{13} \end{matrix} \right\} = \frac{(-1)^{j_1+j_2+j_3+j}}{\sqrt{(2j_{12}+1)(2j_{23}+1)}} \langle j_{12}j_3J | j_1j_{23}J \rangle , \quad (2.11)$$

where the three angular momenta $\mathbf{j}_1, \mathbf{j}_2, \mathbf{j}_3$ are coupled to obtain \mathbf{J} in two possible ways:

$$(\mathbf{j}_1 + \mathbf{j}_2) + \mathbf{j}_3 \equiv \mathbf{j}_{12} + \mathbf{j}_3 \quad (2.12)$$

$$\mathbf{j}_1 + (\mathbf{j}_2 + \mathbf{j}_3) \equiv \mathbf{j}_1 + \mathbf{j}_{23} . \quad (2.13)$$

The expansion coefficients

$$\langle j_{12}j_3J | j_1j_{23}J \rangle = \langle j_{12}j_3J' M' | j_1j_{23}JM \rangle \quad (2.14)$$

are simply the scalar products of eigenfunctions in these two alternative coupling schemes, with the notation simplified since the product vanishes due to orthogonality unless $J = J'$ and $M = M'$.

For optical magnetometry, we are frequently concerned with transitions between specific magnetic sublevels of the eigenstates of total atomic angular momentum. Since the electric dipole operator does not act directly on spin angular momenta, in the LS -coupling scheme this usually means a transition from

$$|LSJIFm_F\rangle \rightarrow |L'SJ'IF'm'_F\rangle , \quad (2.15)$$

where \mathbf{L} is the total electronic orbital angular momentum, \mathbf{S} is the total electronic spin, $\mathbf{J} = \mathbf{L} + \mathbf{S}$ is the total electronic angular momentum, \mathbf{I} is the nuclear spin, and $\mathbf{F} = \mathbf{I} + \mathbf{J}$ is the total atomic angular momentum. When a tensor operator T^k commutes with j_2 but not j_1 , the reduced matrix element can be further simplified:

$$\begin{aligned} & \langle j'_1j_2J' || T^k || j_1j_2J \rangle \\ &= (-1)^{j'_1+j_2+J+k} \sqrt{(2J+1)(2J'+1)} \left\{ \begin{matrix} j'_1 & J' & j_2 \\ J & j_1 & k \end{matrix} \right\} \langle j'_1 || T^k || j_1 \rangle . \end{aligned} \quad (2.16)$$

By repeated use of equation 2.16 and the Wigner-Eckart theorem, we can express a general matrix element of T_q^k in terms of angular momentum coupling coefficients and reduced matrix elements. A typical example of this is

$$\begin{aligned}
& \langle L' S J' I F' m'_F | T_q^k | L S J I F m_F \rangle \\
&= (-1)^{F'-m'_F} \begin{pmatrix} F' & k & F' \\ -m'_F & q & m \end{pmatrix} \\
&\quad \times (-1)^{J'+I+F+k} \sqrt{(2F+1)(2F'+1)} \begin{Bmatrix} J' & F' & I \\ F & J & k \end{Bmatrix} \\
&\quad \times (-1)^{L'+S+J+k} \sqrt{(2J+1)(2J'+1)} \begin{Bmatrix} L' & J' & S \\ J & L & k \end{Bmatrix} \langle L' || T^k || L \rangle ,
\end{aligned} \tag{2.17}$$

such that with knowledge of $\langle L' || T^k || L \rangle$ we can compute the matrix element for any set of quantum numbers and any component T_q^k . Conversely, if the left-hand side is known for some value of q , then we can infer the value of the reduced matrix element.

We should be careful to note that the reduced matrix element $\langle j_1 || T^k || j'_1 \rangle$ still depends on position coordinates, and the purely radial factor $\langle r \rangle$ will often be used to account for this in expressions where the angular part of $\langle j_1 || T^k || j'_1 \rangle$ is evaluated explicitly (as in equation 1.11). Often the reduced matrix elements can be evaluated up to this radial factor by making use of the correspondence between spherical tensor components of rank k and the spherical harmonics Y_m^k , which have identical transformation properties.

In particular, the matrix elements of the spherical harmonics Y_m^1 are very useful since the position vector $\mathbf{r} = r^q \hat{\mathbf{e}}_q$ can be expressed in terms of them:

$$r_q = r \sqrt{\frac{4\pi}{3}} Y_q^1 . \tag{2.18}$$

The matrix element $\langle L' || Y^k || L \rangle$ is easily evaluated via the Wigner-Eckart theorem, with the result

$$\langle L' || Y^k || L \rangle = (-1)^{L'} \sqrt{\frac{(2L'+1)(2k+1)(2L+1)}{4\pi}} \begin{pmatrix} L' & k & L \\ 0 & 0 & 0 \end{pmatrix} , \tag{2.19}$$

so that

$$\langle L' || r || L \rangle = \langle r \rangle \sqrt{\frac{4\pi}{3}} \langle L' || Y^1 || L \rangle , \tag{2.20}$$

where now only $\langle r \rangle$ is undetermined.

The irreducible components of tensor products are straightforwardly related to the irreducible components of the original tensors. We are mainly concerned with vector operators such as the atomic electric dipole operator

$$\mathbf{d} = -e \sum_i \mathbf{r}_i \quad (2.21)$$

(where the sum ranges over atomic electrons), and products of vectors such as the two-photon transition operator

$$M = \sum_{k,j,j'} \mathbf{d} \cdot \hat{\boldsymbol{\epsilon}}^{(j')} \frac{|k\rangle\langle k|}{2\Delta_{kg,j}} \mathbf{d} \cdot \hat{\boldsymbol{\epsilon}}^{(j)}, \quad (2.22)$$

where $\Delta_{kg,j} = \omega_{kg} - \omega_j$ is the intermediate detuning for the j th field and the state represented by $|k\rangle$.

For E1 transitions between states α and β , we can force the matrix elements

$$\langle \alpha | \mathbf{d} \cdot \hat{\boldsymbol{\epsilon}} | \beta \rangle = -e \langle \alpha | r^q \epsilon_q | \beta \rangle \quad (2.23)$$

to be real for a given polarization $\hat{\boldsymbol{\epsilon}}$ since the absolute phase of each eigenstate is physically meaningless. The relative phase between different eigenstates can therefore be chosen to cancel the argument of $\mathbf{d} \cdot \hat{\boldsymbol{\epsilon}}$. Once this relative phase has been fixed for a given polarization $\hat{\boldsymbol{\epsilon}}$, the matrix elements corresponding to other polarizations will in general be complex. Therefore when all optical fields under consideration have the same polarization, we can take the relevant matrix elements of the dipole operator to be real without loss of generality.

2.1.1 Expansions of the Density Operator

The density operator ρ is commonly represented by its matrix elements ρ_{ij} between atomic eigenstates i and j . Its most general time evolution including dissipation is described by the Lindblad master equation [61],

$$\dot{\rho} = -\frac{i}{\hbar} [H, \rho] - \sum_{k=0}^M \left(L_k \rho L_k^\dagger - \frac{1}{2} \rho L_k^\dagger L_k - \frac{1}{2} L_k^\dagger L_k \rho \right), \quad (2.24)$$

where the dimension N of the Hilbert space is finite, and $M < N^2$. The operators L_m are a linear basis for operators on the Hilbert space; the physical interpretation is that they create and annihilate quanta, thereby inducing transitions between different states. The first term in parentheses may be viewed as a transition operator, while the second two ensure correct normalization when no transition occurs. For our purposes it is usually

adequate to consider only unitary time-evolution, in which case equation 2.24 simplifies to the Liouville equation:

$$\dot{\rho} = -\frac{i}{\hbar} [H, \rho] - \frac{1}{2} \{\Gamma, \rho\} + \Lambda, \quad (2.25)$$

where the total Hamiltonian $H = H_0 + V$ consists of the unperturbed Hamiltonian H_0 and a perturbing interaction V . The relaxation operator Γ can be parameterized somewhat generally, but is usually written in terms of phenomenological decay rates (including spontaneous emission). The repopulation operator Λ includes contributions from cascade decays involving other atomic eigenstates, atoms entering the interaction region, etc.

When the representation $\rho_{ij} = \langle i | \rho | j \rangle$ is used, equations of motion are obtained in terms of the matrix elements of the other operators in equation 2.25 (e.g., Γ_{ij}). We can also represent the density operator in terms of irreducible tensors, for which we follow normalization condition

$$\text{Tr} \left[T_q^k T_{q'}^{k'\dagger} \right] = \delta_{kk'} \delta_{qq'} \quad (2.26)$$

and phase convention

$$T_q^{k\dagger} = (-1)^q T_{-q}^k = T^{kq}. \quad (2.27)$$

of [36]. The density matrix for an atomic state with total angular momentum F has $(2F + 1)^2$ independent degrees of freedom, and coupling \mathbf{F} to \mathbf{F} we obtain a direct sum of tensors up to rank $2F$:

$$F \otimes F = T^0 \oplus T^1 \oplus \dots \oplus T^{2F}. \quad (2.28)$$

Thus, we can expand ρ over the set of T_q^k with $0 \leq k \leq 2F$:

$$\rho = \sum_{k=0}^{2F} \sum_{q=-k}^k \rho^{kq} T_q^k. \quad (2.29)$$

The expansion coefficients ρ^{kq} are known as *state multipoles* or *polarization moments*, and are related to the density matrix elements ρ_{ij} by

$$\rho^{kq} = \sum_{m, m'=-F}^F (-1)^{F-m'-q} \sqrt{2k+1} \begin{pmatrix} F & F & k \\ m & -m' & -q \end{pmatrix} \rho_{mm'}. \quad (2.30)$$

The low-rank polarization moments are commonly referred to as monopole (ρ^0), dipole (ρ^1), quadrupole (ρ^2), etc. as in other multipole expansions. Unfortunately the terms ‘‘po-

larization” and “polarized state” are less well defined than “unpolarized” or “unpolarized state”, which refer to a situation in which ρ^k vanishes for all $k > 0$. Following this usage, “polarized state” can mean a situation where *any* higher multipole is nonvanishing, but is also frequently used specifically to indicate a nonvanishing dipole moment. Where this usage may cause confusion, we will refer to the dipole moment as “orientation” and the quadrupole moment as “alignment”, but it should be noted that other conventions exist in the literature (e.g., all odd multipoles denoted by “alignment” and all even ones by “orientation”).

There is a correspondence between the nomenclature for polarization moments and the classical terminology of nuclear magnetic resonance (NMR). When the Zeeman sublevel populations $\rho_{mm'}$ are not all equal, $\rho^{k0} \neq 0$ for some $k > 0$ and the ensemble is said to be *longitudinally polarized*. In the case of dipole orientation, we find that the macroscopic polarization (dipole moment per unit volume) has a nonzero component along the quantization axis,

$$\rho^{10} \propto \langle F_z \rangle . \quad (2.31)$$

When $\rho_{mm'} \neq 0$ for some $m \neq m'$, there are coherences between different Zeeman sublevels and $\rho^{kq} \neq 0$ for some $q \neq 0$. An ensemble in this situation is traditionally referred to as having *transverse polarization*, since it corresponds to cases where the instantaneous macroscopic polarization vector has components orthogonal to the quantization axis. We follow [62] and [17] in referring to quadrupole polarization

$$\rho^{20} \propto \langle 3F_z^2 - \mathbf{F}^2 \rangle \quad (2.32)$$

as “longitudinal alignment”.

Alternatively, ρ can be expanded in a power series by treating the interaction V with perturbation theory:

$$\rho = \sum_{n=0}^{\infty} \rho^{(n)} V^n , \quad (2.33)$$

where each term corresponds to an n th-order interaction. We are concerned with light-matter interactions in which the atomic medium is (electrically) polarized by an optical field

$$\mathbf{P} = \bar{n} \text{Tr}[\rho \mathbf{d}] , \quad (2.34)$$

where \mathbf{P} is the polarization of the medium, \bar{n} in the number density of atoms, and \mathbf{d} is

the atomic electric dipole operator. The perturbation of interest in this case is the electric dipole interaction, $V = -\mathbf{d} \cdot \mathbf{E}$. Nonlinear optics most broadly includes situations where the optical properties of the atomic ensemble are modified by an optical field; these correspond to terms in the perturbation expansion with $n \geq 2$.

2.2 Equations of Motion, Approximations, and Analytic Solutions

Although all dynamics of interest can be captured in a theoretical model based on the density matrix, we begin by discussing single-beam two-photon absorption in an amplitude picture. This treatment emphasizes adiabatic elimination of the intermediate states. When those states are far from resonance, the process of two-photon excitation is formally an effective two-level problem. This allows us to rapidly generalize familiar results (see appendices A and B) for application to two-photon excitation. The related problems involving multiple fields, time- and space-dependent field amplitudes, ionization, and the density matrix are discussed later in this chapter.

The next section solves the equations of motion for a single optical field exciting two-photon transitions in a multilevel atom. See [55] for a similar discussion, in which it is assumed that two fields are present but neither one can drive the two-photon transition independently. In section 2.2.2 we modify this treatment to accommodate two-field two-photon excitation in the case where each field *can* drive the two-photon transition independently. Alternative treatments are widely available in the literature, e.g. in [26, 52, 53, 57, 63–65].

2.2.1 Single Beam, CW Two-Photon Excitation

Consider an atom with a ground state represented by $|g\rangle$ and an excited state represented by $|e\rangle$, which have the same parity. Let there also be a set of intermediate states represented by $\{|k\rangle\}$, which have the opposite parity and are coupled to each of $|g\rangle$ and $|e\rangle$ by single-photon electric dipole (E1) transitions. We will work in the interaction picture, where an arbitrary ket $|\psi\rangle$ can be expressed as a superposition

$$|\psi\rangle = \sum_m c_m(t) e^{-i\omega_m t} |m\rangle, \quad (2.35)$$

in which $\{|m\rangle\}$ are eigenstates of the atomic Hamiltonian in the absence of a radiation field:

$$H_0 |m\rangle = \hbar\omega_m |m\rangle . \quad (2.36)$$

We now include an interaction V in the Hamiltonian due to an optical electric field with amplitude \mathcal{E} , frequency ω , and polarization ϵ ,

$$\mathbf{E} = \frac{1}{2}\epsilon [\mathcal{E}e^{i(\mathbf{k}\cdot\mathbf{r}-\omega t)} + \text{c.c.}] , \quad (2.37)$$

which can drive the E1 transitions $g \leftrightarrow k$ and $k \leftrightarrow e$. Note that $g \leftrightarrow e$ is forbidden as a single-photon E1 process, since the dipole operator has odd parity. The time-dependent Schrödinger equation applied to equation 2.35 gives the equations of motion for the state amplitudes c_m :

$$i\hbar\dot{c}_m = \sum_n e^{i\omega_{mn}t} V_{mn} c_n , \quad (2.38)$$

where $\omega_{mn} = \omega_m - \omega_n$ and $V_{mn} = \langle m | V | n \rangle$. In the dipole approximation, the operator for the atom-field interaction is $V = -\mathbf{d} \cdot \mathbf{E}$, and for a given polarization we can choose the relative phases of the atomic eigenstates such that the matrix elements $\langle m | \mathbf{d} \cdot \epsilon | n \rangle$ are real. Thus we can write the matrix elements of V as

$$V_{mn} = \frac{\hbar}{2}\Omega_{mn}e^{i(\mathbf{k}\cdot\mathbf{r}-\omega t)} + \text{c.c.} , \quad (2.39)$$

where

$$\Omega_{mn} = -\hbar^{-1} \langle m | \mathbf{d} \cdot \epsilon | n \rangle \mathcal{E} \quad (2.40)$$

is the Rabi frequency, which expresses the strength of the field-induced coupling between states m and n in frequency units.

For now we also suppose that the atom is located at the origin, so that $\mathbf{r} = 0$. In this case, the amplitude equations of motion are

$$\dot{c}_m = -\frac{i}{2} \sum_n (\Omega_{mn}e^{i(\omega_{mn}-\omega)t} + \Omega_{mn}^*e^{i(\omega_{mn}+\omega)t}) c_n . \quad (2.41)$$

We will use the letters m, n to refer to an arbitrary atomic eigenstate, and k for the intermediate states that contribute to two-photon excitation; note that $V_{gm} = V_{em} = 0$ if $|m\rangle \notin \{|k\rangle\}$. Explicitly, for the ground state we have

$$\dot{c}_g = -\frac{i}{2} \sum_k (\Omega_{gk}e^{i(\omega_{gk}-\omega)t} + \Omega_{gk}^*e^{i(\omega_{gk}+\omega)t}) c_k , \quad (2.42)$$

and \dot{c}_e is given by ($g \leftrightarrow e$). For the intermediate states,

$$\dot{c}_k = -\frac{i}{2} [\Omega_{kg} e^{i(\omega_{kg}-\omega)t} + \Omega_{kg}^* e^{i(\omega_{kg}+\omega)t}] c_g + (g \leftrightarrow e). \quad (2.43)$$

Treating the intermediate levels within first-order perturbation theory, we obtain their amplitudes by integrating equation 2.43 by parts. In doing so, we assume that the field is turned on slowly with respect to the intermediate detunings $\omega_{kg} \pm \omega$ and $\omega_{ke} \pm \omega$, such that the remaining integral can be neglected. The result is

$$c_k(t) = -\frac{1}{2} \left[\frac{\Omega_{kg} e^{i(\omega_{kg}-\omega)t}}{\omega_{kg} - \omega} + \frac{\Omega_{kg}^* e^{i(\omega_{kg}+\omega)t}}{\omega_{kg} + \omega} \right] c_g + (g \leftrightarrow e), \quad (2.44)$$

which we can now substitute into equation 2.42 to obtain

$$\dot{c}_g = \frac{i}{4} \sum_k \left(\frac{\Omega_{gk} \Omega_{kg}^*}{\omega_{kg} + \omega} + \frac{\Omega_{gk}^* \Omega_{kg}}{\omega_{kg} - \omega} \right) c_g + \frac{i}{4} \left(\sum_k \frac{\Omega_{gk}^* \Omega_{ke}^*}{\omega_{ke} + \omega} \right) e^{-i\delta t} c_e. \quad (2.45)$$

In simplifying this result we have kept only the ‘‘slowly-varying’’ terms that change little in an optical period, and defined the two-photon detuning $\delta = \omega_{eg} - 2\omega$. (This corresponds to a rotating wave approximation; see appendix A. It is important to introduce this approximation *after* substituting for the amplitudes c_k , since the intermediate detunings are large and the ‘‘counter-rotating’’ terms also contribute substantially to the intermediate amplitudes. The rotating wave approximation and the two-level approximation typically enter at the same order of magnitude.) The corresponding equation for c_e is

$$\dot{c}_e = \frac{i}{4} \left(\sum_k \frac{\Omega_{ek} \Omega_{kg}}{\omega_{kg} - \omega} \right) e^{i\delta t} c_g + \frac{i}{4} \sum_k \left(\frac{\Omega_{ek} \Omega_{ke}^*}{\omega_{ke} + \omega} + \frac{\Omega_{ek}^* \Omega_{ke}}{\omega_{ke} - \omega} \right) c_e. \quad (2.46)$$

Evidently we can absorb the dependence on intermediate levels into the auxiliary quantities

$$s_g \equiv -\frac{1}{4} \sum_k \left(\frac{|\Omega_{gk}|^2}{\omega_{kg} + \omega} + \frac{|\Omega_{gk}|^2}{\omega_{kg} - \omega} \right) \quad (2.47)$$

$$s_e \equiv -\frac{1}{4} \sum_k \left(\frac{|\Omega_{ek}|^2}{\omega_{ke} + \omega} + \frac{|\Omega_{ek}|^2}{\omega_{ke} - \omega} \right), \quad (2.48)$$

and

$$\Omega_g \equiv -\frac{1}{2} \sum_k \frac{\Omega_{ek} \Omega_{kg}}{\omega_{kg} - \omega} \quad (2.49)$$

$$\Omega_e^* \equiv -\frac{1}{2} \sum_k \frac{\Omega_{gk}^* \Omega_{ke}^*}{\omega_{ke} + \omega}, \quad (2.50)$$

to write the equations of motion in the form

$$\dot{c}_g = -i s_g c_g - i \frac{\Omega_e^*}{2} e^{-i\delta t} c_e \quad (2.51)$$

$$\dot{c}_e = -\frac{i\Omega_g}{2} e^{i\delta t} c_g - i s_e c_e. \quad (2.52)$$

We now have the equations of motion for an effective two-level system, where the quantities $\hbar s_{g,e}$ represent energy shifts due to the light field (this is the two-photon *light shift* or *AC Stark shift*), and $\Omega_{g,e}$ are two-photon Rabi frequencies. These coupled first-order equations can be combined to separate the variables c_g and c_e , resulting in two second-order equations with constant coefficients:

$$\ddot{c}_g + i(s_g + s_e + \delta)\dot{c}_g + \left(\frac{\Omega_g \Omega_e^*}{4} - s_g s_e - \delta s_g \right) c_g = 0 \quad (2.53)$$

$$\ddot{c}_e + i(s_g + s_e - \delta)\dot{c}_e + \left(\frac{\Omega_g \Omega_e^*}{4} - s_g s_e + \delta s_e \right) c_e = 0. \quad (2.54)$$

Note that these equations transform into each other under the combination of ($g \leftrightarrow e$) and $\delta \rightarrow -\delta$. The full solution is most concisely expressed in terms of the *effective* two-photon Rabi frequency,

$$\Omega = \sqrt{(\delta - s_g + s_e)^2 + \Omega_g \Omega_e^*}, \quad (2.55)$$

and the *effective* detuning, $\tilde{\delta} \equiv \delta - s_g + s_e$,

$$c_g(t) = e^{\frac{i}{2}(\tilde{\delta} + 2s_g)t} \left[\left(\cos \frac{\Omega t}{2} + i \frac{\tilde{\delta}}{\Omega} \sin \frac{\Omega t}{2} \right) c_g(0) - i \frac{\Omega_e^*}{\Omega} \sin \frac{\Omega t}{2} c_e(0) \right] \quad (2.56)$$

$$c_e(t) = e^{-\frac{i}{2}(\tilde{\delta} - 2s_e)t} \left[-i \frac{\Omega_g}{\Omega} \sin \frac{\Omega t}{2} c_g(0) + \left(\cos \frac{\Omega t}{2} - i \frac{\tilde{\delta}}{\Omega} \sin \frac{\Omega t}{2} \right) c_e(0) \right]. \quad (2.57)$$

The solutions are expressed in terms of the amplitudes at $t=0$; they have exactly the same structure as the corresponding solutions for the usual two-level problem. If we assume that all population is initially in g , i.e. $c_m(0) = \delta_{mg}$, then the probabilities take a particularly simple form:

$$|c_g|^2 = \cos^2 \frac{\Omega t}{2} + \frac{\tilde{\delta}^2}{\Omega^2} \sin^2 \frac{\Omega t}{2} \quad (2.58)$$

$$|c_e|^2 = \frac{|\Omega_g|^2}{\Omega^2} \sin^2 \frac{\Omega t}{2} . \quad (2.59)$$

Note that although we have solved the equations of motion in the interaction picture, the populations are the same as in the Schrödinger picture.

2.2.2 Two Beam, CW Two-Photon Excitation

In order to highlight certain aspects of the general problem, we will assume an arbitrary superposition of monochromatic plane wave fields and derive results for the specific case of two independent fields at the end of this section. The atomic structure is the same as in the previous section, but the electric field is now

$$\mathbf{E} = \frac{1}{2} \sum_j \boldsymbol{\epsilon}^{(j)} \mathcal{E}^{(j)} e^{i(\mathbf{k}_j \cdot \mathbf{r} - \omega_j t + \phi_j)} + \text{c.c.} , \quad (2.60)$$

where we have also allowed each term in the sum to have a constant phase offset ϕ_j . The Rabi frequencies and matrix elements of V now involve the field index j :

$$\Omega_{mn}^{(j)} = -\hbar^{-1} \langle m | \mathbf{d} \cdot \boldsymbol{\epsilon}^{(j)} | n \rangle \mathcal{E}^{(j)} e^{i\phi_j} \quad (2.61)$$

$$V_{mn} = \frac{\hbar}{2} \sum_j \Omega_{mn}^{(j)} e^{i(\mathbf{k}_j \cdot \mathbf{r} - \omega_j t)} + \text{c.c.} , \quad (2.62)$$

where it is now not in general possible to choose relative phases such that all of the dipole matrix elements are real. The derivation of intermediate state amplitudes proceeds in analogy to the previous section, where each equation now involves a sum over j . The result is

$$c_k(t) = -\frac{1}{2} \sum_j \left[\frac{\Omega_{kg}^{(j)} e^{i(\omega_{kg} - \omega_j)t}}{\omega_{kg} - \omega_j} + \frac{\Omega_{kg}^{(j)*} e^{i(\omega_{kg} + \omega_j)t}}{\omega_{kg} + \omega_j} \right] c_g + (g \leftrightarrow e) , \quad (2.63)$$

where we have now assumed that each field is turned on slowly in comparison to its respective detunings $\omega_{kg} \pm \omega_j$ and $\omega_{ek} \pm \omega_j$. Substituting this amplitude into the equations of motion for c_g and c_e , we find

$$\dot{c}_g = \frac{i}{4} \sum_{j,j'} \sum_k \left[\left(\frac{\Omega_{kg}^{(j)} \Omega_{gk}^{(j')*}}{\omega_{kg} - \omega_j} e^{i(-\omega_j + \omega_{j'})t} + \frac{\Omega_{kg}^{(j)*} \Omega_{gk}^{(j')}}{\omega_{kg} + \omega_j} e^{i(\omega_j - \omega_{j'})t} \right) c_g + \left(\frac{\Omega_{ke}^{(j)*} \Omega_{gk}^{(j')*}}{\omega_{ke} + \omega_j} e^{i(-\omega_{eg} + \omega_j + \omega_{j'})t} \right) c_e \right] \quad (2.64)$$

$$\dot{c}_e = \frac{i}{4} \sum_{j,j'} \sum_k \left[\left(\frac{\Omega_{ke}^{(j)} \Omega_{ek}^{(j')*}}{\omega_{ke} - \omega_j} e^{i(-\omega_j + \omega_{j'})t} + \frac{\Omega_{ke}^{(j)*} \Omega_{ek}^{(j')}}{\omega_{ke} + \omega_j} e^{i(\omega_j - \omega_{j'})t} \right) c_e + \left(\frac{\Omega_{kg}^{(j)} \Omega_{ek}^{(j')}}{\omega_{kg} - \omega_j} e^{i(\omega_{eg} - \omega_j - \omega_{j'})t} \right) c_g \right], \quad (2.65)$$

where rapidly varying terms have been dropped. We now define the slightly modified light shift parameters,

$$\tilde{s}_{g,\pm}^{jj'} = -\frac{1}{4} \sum_k \frac{|\Omega_{kg}^{(j)} \Omega_{gk}^{(j')*}|}{\omega_{kg} \pm \omega_j} e^{\pm i\Phi_g^{jj'}} \quad (2.66)$$

$$\tilde{s}_{e,\pm}^{jj'} = -\frac{1}{4} \sum_k \frac{|\Omega_{ke}^{(j)} \Omega_{ek}^{(j')*}|}{\omega_{ke} \pm \omega_j} e^{\pm i\Phi_e^{jj'}}, \quad (2.67)$$

where $\Omega_{kg}^{(j)} \Omega_{gk}^{(j')*} = |\Omega_{kg}^{(j)} \Omega_{gk}^{(j')*}| e^{i\Phi_g^{jj'}}$ and $\Omega_{ke}^{(j)} \Omega_{ek}^{(j')*} = |\Omega_{ke}^{(j)} \Omega_{ek}^{(j')*}| e^{i\Phi_e^{jj'}}$. We similarly define two-photon Rabi frequencies for each combination of j and j' :

$$\tilde{\Omega}_e^{jj'} = -\frac{1}{2} \frac{\Omega_{ke}^{(j)*} \Omega_{gk}^{(j')*}}{\omega_{ke} + \omega_j} \quad (2.68)$$

$$\tilde{\Omega}_g^{jj'} = -\frac{1}{2} \frac{\Omega_{kg}^{(j)} \Omega_{ek}^{(j')}}{\omega_{kg} - \omega_j}, \quad (2.69)$$

and the detuning $\delta_{jj'} = \delta_{j'j} = \omega_{eg} - \omega_j - \omega_{j'}$. With these definitions, we again have an effective two-level system:

$$\dot{c}_g = -i \sum_{j,j'} \left(\tilde{s}_{g,-}^{jj'} e^{-i\omega_{jj'}t} + \tilde{s}_{g,+}^{jj'} e^{i\omega_{jj'}t} \right) c_g - \frac{i}{2} \sum_{j,j'} \tilde{\Omega}_e^{jj'} e^{-i\delta_{jj'}t} c_e \quad (2.70)$$

$$\dot{c}_e = -i \sum_{j,j'} \left(\tilde{s}_{e,-}^{jj'} e^{-i\omega_{jj'}t} + \tilde{s}_{e,+}^{jj'} e^{i\omega_{jj'}t} \right) c_e - \frac{i}{2} \sum_{j,j'} \tilde{\Omega}_g^{jj'} e^{i\delta_{jj'}t} c_g . \quad (2.71)$$

When there are only two fields, there are two particularly useful limits where the time dependence can be simplified. In the first case, $\omega_1 = \omega_2$ and we have

$$\dot{c}_g = -i \sum_{\substack{j=1,2 \\ j'=1,2}} \left(s_{g,-}^{jj'} + s_{g,+}^{jj'} \right) c_g - \frac{i}{2} \sum_{\substack{j=1,2 \\ j'=1,2}} \tilde{\Omega}_e^{jj'} e^{-i\delta t} c_e \quad (2.72)$$

$$\dot{c}_e = -i \sum_{\substack{j=1,2 \\ j'=1,2}} \left(s_{e,-}^{jj'} + s_{e,+}^{jj'} \right) c_e - \frac{i}{2} \sum_{\substack{j=1,2 \\ j'=1,2}} \tilde{\Omega}_g^{jj'} e^{i\delta t} c_g , \quad (2.73)$$

where $\delta = \delta_{12} = \delta_{11} = \delta_{22}$. In the second case, $\omega_1 - \omega_2 \gg \delta_{12}$, and we can neglect the terms that vary as $e^{\pm\omega_{12}t}$ in what amounts to a second rotating-wave approximation:

$$\dot{c}_g = -i \left(s_{g,-}^{12} + s_{g,+}^{12} + s_{g,-}^{21} + s_{g,+}^{21} \right) c_g - \frac{i}{2} \left(\tilde{\Omega}_e^{12} + \tilde{\Omega}_e^{21} \right) e^{-i\delta t} c_e \quad (2.74)$$

$$\dot{c}_e = -i \left(s_{e,-}^{12} + s_{e,+}^{12} + s_{e,-}^{21} + s_{e,+}^{21} \right) c_e - \frac{i}{2} \left(\tilde{\Omega}_g^{12} + \tilde{\Omega}_g^{21} \right) e^{i\delta t} c_g . \quad (2.75)$$

Rewriting this result with the definitions

$$S_g = s_{g,-}^{12} + s_{g,+}^{12} + s_{g,-}^{21} + s_{g,+}^{21} \quad (2.76)$$

$$S_e = s_{e,-}^{12} + s_{e,+}^{12} + s_{e,-}^{21} + s_{e,+}^{21} \quad (2.77)$$

$$\chi_g = \frac{1}{2} \left(\tilde{\Omega}_g^{12} + \tilde{\Omega}_g^{21} \right) \quad (2.78)$$

$$\chi_e = \frac{1}{2} \left(\tilde{\Omega}_e^{12} + \tilde{\Omega}_e^{21} \right) , \quad (2.79)$$

we have a formal analogy with the two-level problem for one-photon excitation:

$$\dot{c}_g = -i S_g c_g - i \chi_e e^{-i\delta t} c_e \quad (2.80)$$

$$\dot{c}_e = -i S_e c_e - i \chi_g e^{i\delta t} c_g . \quad (2.81)$$

These results can be extended to include the effects of atomic motion and relaxation

via the density matrix formalism. Because we have an effective two-level system, we can simply write down the result, which is [55]

$$\dot{\rho}_{gg} + \mathbf{v} \cdot \nabla \rho_{gg} = -i\chi_e \rho_{eg} + i\chi_g \rho_{ge} + \Lambda \rho_{ee} \quad (2.82)$$

$$\dot{\rho}_{ee} + \mathbf{v} \cdot \nabla \rho_{ee} = -i\chi_e \rho_{eg} - i\chi_g \rho_{ge} - \Gamma_e \rho_{ee} \quad (2.83)$$

$$\begin{aligned} \dot{\rho}_{ge} + \mathbf{v} \cdot \nabla \rho_{ge} = & -i\chi_e(\rho_{ee} - \rho_{gg}) - \Gamma_{eg} \rho_{eg} \\ & + i[\delta + (\mathbf{k}_1 + \mathbf{k}_2) \cdot \mathbf{v} - S_g + S_e] \rho_{eg}, \end{aligned} \quad (2.84)$$

where we have written the density matrix in a “field-interaction” representation that absorbs oscillations at the optical sum frequency $\omega_1 + \omega_2$ into the state amplitudes, i.e.,

$$\begin{pmatrix} c_g(t) \\ c_e(t) \end{pmatrix} \rightarrow \begin{pmatrix} e^{\frac{i}{2}\delta t} & 0 \\ 0 & e^{-\frac{i}{2}\delta t} \end{pmatrix} \begin{pmatrix} c_g(t) \\ c_e(t) \end{pmatrix}. \quad (2.85)$$

The point is that the lineshape function for the transition arises from the factor

$$- \Gamma_{eg} + i[\delta + (\mathbf{k}_1 + \mathbf{k}_2) \cdot \mathbf{v} - S_g + S_e] \quad (2.86)$$

in equation 2.84 (since the dipole operator has odd parity, diagonal elements of the density matrix cannot contribute to $\text{Tr}[\rho \mathbf{d}]$ in equation 2.34). This depends on the sum of the wave vectors for the two optical fields, which gives rise to a Doppler-broadened spectrum whose characteristic width is $|\mathbf{k}_1 + \mathbf{k}_2|$. It is immediately apparent that in a counter-propagating geometry where $\hat{\mathbf{k}}_1 = -\hat{\mathbf{k}}_2$, the Doppler effect is precisely canceled and we observe a resonance whose width is the radiative linewidth Γ_e of the excited state, and whose center frequency is shifted by the differential light shift $S_e - S_g$. In the copropagating geometry where $\hat{\mathbf{k}}_1 = \hat{\mathbf{k}}_2$, the Doppler width attains its maximal value $2|\mathbf{k}_1|$ and the light shift is the same. Doppler-free multiphoton excitation is discussed in [64].

2.2.3 Angular Momentum Coupling in Two-Photon Excitation

The steady-state probability per unit time for a two-photon transition from $g \rightarrow e$, induced by two statistically independent optical fields is [57, 65]

$$P_{ge}^{(2)} = \frac{2\pi}{\hbar^4} \frac{I_1 I_2}{4\epsilon_0 c^2} |M_{eg}|^2 G(\omega), \quad (2.87)$$

where I_1 and I_2 are the intensities of the two fields and $G(\omega)$ is a lineshape function that corresponds to the density of atomic states that can couple to the field. The lineshape

function is often taken to be a Lorentzian,

$$G(\omega) = \frac{\frac{\Gamma}{2\pi}}{\delta^2 + \frac{\Gamma^2}{4}}, \quad (2.88)$$

in which the detuning $\delta = \omega_{eg} - \omega_1 - \omega_2$ is defined as before. The radiative linewidth of any atomic state m is denoted by Γ_m , and $\Gamma = \Gamma_e + \Gamma_g$. The matrix element of the two-photon transition operator M is given by

$$M_{eg} = \sum_k \left[\frac{\langle e | \hat{\epsilon}^{(1)} \cdot \mathbf{d} | k \rangle \langle k | \hat{\epsilon}^{(1)} \cdot \mathbf{d} | g \rangle}{\omega_{kg} - \omega_1 + i\frac{\Gamma_k}{2}} + \frac{\langle e | \hat{\epsilon}^{(1)} \cdot \mathbf{d} | k \rangle \langle k | \hat{\epsilon}^{(2)} \cdot \mathbf{d} | g \rangle}{\omega_{kg} - \omega_2 + i\frac{\Gamma_k}{2}} \right] + (1 \leftrightarrow 2), \quad (2.89)$$

where again $\hat{\epsilon}^{(1)}$ and $\hat{\epsilon}^{(2)}$ are the polarization vectors of the optical fields. We have previously neglected the linewidths Γ_k in the resonance denominators that appear in the expression for M_{eg} ; this is a good approximation when they are small in comparison with detunings $\omega_{kg} - \omega_1$ and $\omega_{kg} - \omega_2$, as they are for all cases considered in this dissertation. When the detunings are additionally large in comparison with all of the fine and hyperfine structure splittings, the projection operator

$$P_k = \sum_k \left[\frac{|k\rangle \langle k|}{\omega_{kg} - \omega_1} + \frac{|k\rangle \langle k|}{\omega_{kg} - \omega_2} \right] \quad (2.90)$$

is rotationally invariant due to the sum over all possible quantum numbers [56]. In this case the structure of angular momentum coupling arises solely due to the tensor products $(\hat{\epsilon}^{(i)} \cdot \mathbf{d})(\hat{\epsilon}^{(j)} \cdot \mathbf{d})$, which can be factored into a product of terms in which the optical and atomic vectors are completely separated:

$$(\hat{\epsilon}^{(i)} \cdot \mathbf{d})(\hat{\epsilon}^{(j)} \cdot \mathbf{d}) = \sum_{k,q} (-1)^{k-q} [\epsilon^{(i)} \otimes \epsilon^{(j)}]_q^k [\mathbf{d} \otimes \mathbf{d}]_{-q}^k, \quad (2.91)$$

where k runs from zero to two. In terms of Cartesian components, the spherical polarization tensor $[\epsilon^{(i)} \otimes \epsilon^{(j)}]^k$ and dipole tensor $[\mathbf{d} \otimes \mathbf{d}]^k$ can be decomposed in the usual way for a dyadic product of two vectors. That is,

$$[\boldsymbol{\epsilon}^{(i)} \otimes \boldsymbol{\epsilon}^{(j)}]_0^0 = -\frac{1}{\sqrt{3}} \boldsymbol{\epsilon}^{(i)} \cdot \boldsymbol{\epsilon}^{(j)} \quad (2.92)$$

$$[\boldsymbol{\epsilon}^{(i)} \otimes \boldsymbol{\epsilon}^{(j)}]_q^1 = \frac{i}{\sqrt{2}} (\boldsymbol{\epsilon}^{(i)} \times \boldsymbol{\epsilon}^{(j)}) \cdot \hat{\mathbf{e}}_q \quad (2.93)$$

$$[\boldsymbol{\epsilon}^{(i)} \otimes \boldsymbol{\epsilon}^{(j)}]_0^2 = \frac{1}{\sqrt{6}} (3\epsilon_z^{(i)}\epsilon_z^{(j)} - \boldsymbol{\epsilon}^{(i)} \cdot \boldsymbol{\epsilon}^{(j)}) \quad (2.94)$$

$$[\boldsymbol{\epsilon}^{(i)} \otimes \boldsymbol{\epsilon}^{(j)}]_{\pm 1}^2 = \mp \frac{1}{2} [(\epsilon_z^{(i)}\epsilon_x^{(j)} + \epsilon_x^{(i)}\epsilon_z^{(j)}) \pm i(\epsilon_z^{(i)}\epsilon_y^{(j)} + \epsilon_y^{(i)}\epsilon_z^{(j)})] \quad (2.95)$$

$$[\boldsymbol{\epsilon}^{(i)} \otimes \boldsymbol{\epsilon}^{(j)}]_{\pm 2}^2 = \frac{1}{2} [(\epsilon_x^{(i)}\epsilon_x^{(j)} - \epsilon_y^{(i)}\epsilon_y^{(j)}) \pm i(\epsilon_x^{(i)}\epsilon_y^{(j)} + \epsilon_y^{(i)}\epsilon_x^{(j)})] , \quad (2.96)$$

and similarly for $\mathbf{d} \otimes \mathbf{d}$. These tensors are entirely responsible for the structure of angular momentum coupling in two-photon transitions, and using the Wigner-Eckart theorem we find [56, 65]

$$|M|^2 = \left| \sum_k \sum_{J=0}^2 \langle \alpha F_e \| [\boldsymbol{\epsilon}^{(i)} \otimes \boldsymbol{\epsilon}^{(j)}]^J [\mathbf{d} \otimes \mathbf{d}]^J \| \beta F_g \rangle (-1)^{F_e+2J} \sqrt{2J+1} \right. \\ \left. \times \sum_{\mu, \nu=-1}^1 \sum_M (-1)^{-M_e} \begin{pmatrix} F_e & J & F_g \\ -M_e & M & M_g \end{pmatrix} \begin{pmatrix} J & 1 & 1 \\ -M & \mu & \nu \end{pmatrix} \right|^2, \quad (2.97)$$

where α and β represent the additional quantum numbers that are required to fully specify the initial and final states, and μ, ν index the spherical components of $\hat{\boldsymbol{\epsilon}}^{(i)}, \hat{\boldsymbol{\epsilon}}^{(j)}$. This expression can be further reduced through use of equation 2.16, and the reduced matrix element can be explicitly factored into a form depending on the reduced matrix elements of \mathbf{d} . (This is useful in cases where pure LS -coupling does not apply, and a $6j$ symbol involving the expansion coefficients of the physical eigenstates in terms of pure LS wavefunctions then modifies the line strength.) However, we have already obtained in the product of the two $3j$ symbols, all that is required to infer the selection rules for two-photon excitation. For example, $\hat{\sigma}^+$ polarization of both fields corresponds to $\mu = \nu = +1$, and we find that the transition probability vanishes unless $J = M = 2$ and $M_e = M_g + 2$.

2.2.4 N-Photon Excitation

The n -photon excitation rate for a weak cw laser beam can be calculated via n th-order perturbation theory applied to the density matrix (see, e.g. [26] for explicit calculations of the first few terms). The result is

$$R_{ba}^{(n)} = \left| \frac{E^n}{\hbar^n} \sum_{i,j,\dots,k} \frac{d_{ai}d_{ij}\dots d_{kb}}{\Delta_{ia}^{(n-1)}\Delta_{ja}^{(n-2)}\dots\Delta_{ka}^{(1)}} \right|^2 2\pi\rho(\delta), \quad (2.98)$$

where the sum extends over all dipole-allowed intermediate states, d_{ij} is the electric dipole matrix element for the $i \rightarrow j$ transition, $\delta = \omega_{ba} - n\omega = \Delta_{ba}^{(n)}$ is the n -photon detuning from the $a \rightarrow b$ transition, and $\rho(\delta)$ is a lineshape function obtained by convolution of the probe frequency spectrum with the density of final atomic states. The energy defects $\Delta_{ia}^{(m)} = \omega_{ia} - m\omega$ express the m -photon detuning from the $a \rightarrow i$ transition, and products of these comprise the resonance denominator for each amplitude in the sum. Dependence on the field polarization and propagation vectors enters mainly through the matrix elements, while frequency dependence (including the Doppler effect) is determined by the lineshape function and resonance denominator.

2.2.5 Polarization Rotation

Since multiphoton absorption is a nonparametric process, we can view the scattering rate as the absorptive (imaginary) component of a complex refractive index. The corresponding real part gives rise to dispersive phase shifts, which are straightforward to calculate in the case of two-photon transitions by exploiting the formal analogy between one-photon and two-photon excitation of two-level systems (see [36, 62] for detailed reviews of nonlinear magneto-optics in the one-photon case). The result is

$$n_{ba}^{(2)} \approx 1 + \frac{\bar{n}I\hbar}{\epsilon_0^2 c \Gamma_b} \left| \sum_i \frac{d_{ai}d_{ib}}{\hbar^2 \Delta_{ia}^{(1)}} \right|^2 \frac{\frac{\delta}{\Gamma_b}}{1 + \left(\frac{\delta}{\Gamma_b}\right)^2}, \quad (2.99)$$

where we have explicitly included a dispersive Lorentzian lineshape function that depends on the excited state linewidth Γ_b as well as the detuning δ . The volumetric number density of atoms is \bar{n} , and the optical intensity is I ; the other quantities that appear here are defined following equation 2.98. Figure 2.1(a) shows the real and imaginary components of a Lorentzian lineshape, which is usually an appropriate description of absorption and dispersion for E1 atomic resonances. In the case of two-photon electric dipole resonances, this lineshape function remains a good approximation when the two-photon detuning is small compared to the intermediate detunings, i.e. when $\delta \ll \Delta_{ia}^{(1)}$.

Since the atomic energy levels are shifted by interaction with an external magnetic field, the resonance frequencies for transitions between states that have different magnetic quantum numbers (or g -factors) also shift. A simple and illustrative example is the case of *circular birefringence*, where we consider $\hat{\sigma}^+$ and $\hat{\sigma}^-$ polarization, and consider the atomic

quantization axis to be parallel with the wave vector of the light.

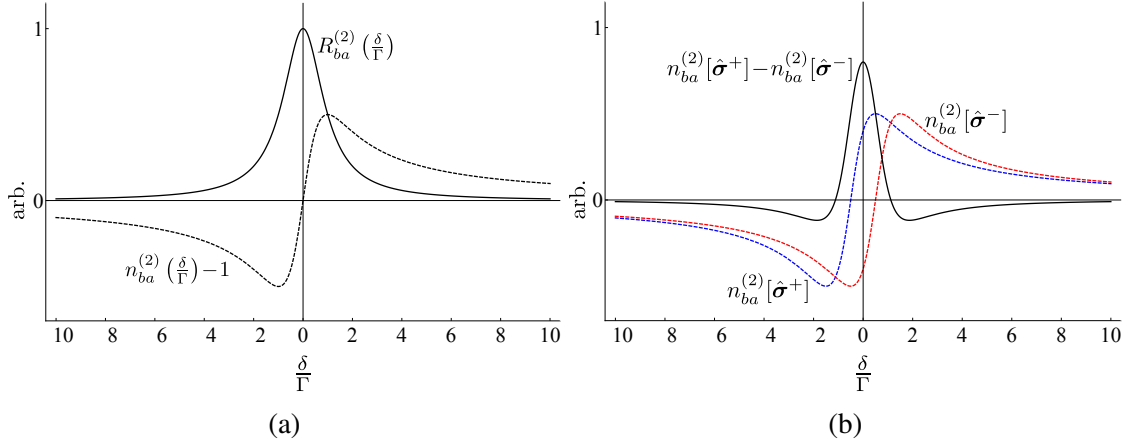


Figure 2.1: Absorption and dispersion... the complex index of refraction, plotted in dimensionless units for the case of two-photon excitation where only the two-photon detuning is allowed to vary.

The resonance frequency for $\hat{\sigma}^\pm$ radiation is shifted by an amount

$$\pm \Delta\omega = \pm(g_b\mu_b - g_a\mu_a)B_z, \quad (2.100)$$

where B_z is the magnetic field component along the quantization axis. The g -factors associated with the total angular momentum of levels a and b are g_a and g_b , respectively; the corresponding magnetic moments are μ_a and μ_b . (We are often interested in the situation where the initial state has no electronic angular momentum, in which case $\mu_b \gg \mu_a$ and $\Delta\omega \approx g_b\mu_b B_z$.) Thus the zero crossing of $n_{ba}^{(2)} - 1$ is also shifted away from $\delta = 0$, and in opposite directions for opposite polarizations. In effect the atomic gas becomes optically active in a magnetic field, to a degree that depends on the magnetic field strength. The difference in refractive index when we compare $\hat{\sigma}^+$ to $\hat{\sigma}^-$ is

$$n_{ba}^{(2)}[\hat{\sigma}^+] - n_{ba}^{(2)}[\hat{\sigma}^-] = \frac{\bar{n}I\hbar}{\epsilon_0^2 c \Gamma_b} \left| \sum_i \frac{d_{ai}d_{ib}}{\hbar^2 \Delta_{ia}^{(1)}} \right|^2 \frac{\frac{2\Delta\omega}{\Gamma_b} \left[1 - \left(\frac{\delta}{\Gamma_b} \right)^2 + \left(\frac{\Delta\omega}{\Gamma_b} \right)^2 \right]}{\left[1 - \left(\frac{\delta}{\Gamma_b} \right)^2 + \left(\frac{\Delta\omega}{\Gamma_b} \right)^2 \right]^2 + \left(\frac{2\delta}{\Gamma_b} \right)^2}, \quad (2.101)$$

which has a maximum at $\delta = 0$ as shown in figure 2.1(b). (The symmetry of the excitation probability for unpolarized atoms under $\hat{\sigma}^- \longleftrightarrow \hat{\sigma}^+$ was used to include the absolute square of the matrix elements in coefficient of the lineshape function.)

We now recall that linearly polarized light is equivalent to a coherent superposition of

$\hat{\sigma}^-$ and $\hat{\sigma}^+$, in which the relative phase determines the angle of linear polarization with respect to a fixed reference axis. Suppose we start with a linear polarization $\hat{\sigma}$ that has a relative phase of zero between the $\hat{\sigma}^-$ and $\hat{\sigma}^+$ components; the optical path difference for the two circular polarizations after propagating a distance L results in a relative phase

$$\phi = \frac{\omega L}{c} \left(n_{ba}^{(2)}[\hat{\sigma}^+] - n_{ba}^{(2)}[\hat{\sigma}^-] \right) . \quad (2.102)$$

The axis of linear polarization is rotated through an angle $\phi/2$ after propagating through a cell of length L ; note that the rotation angle is the same if the beam is retroreflected through the cell, so that the acquired phase in a double-pass configuration is 2ϕ and not zero. This ‘‘paramagnetic rotation’’ of the probe beam polarization is usually measured by dividing the exiting beam on a polarizing beam splitter and recording the ratio of intensities for two orthogonal linear components. When the rotation angle is small this means that the visibility ratio, i.e. the contrast of the rotation signal, scales as ϕ^2 .

Suppose now that we are probing a polarized ensemble of atoms using a two-photon $F = \frac{1}{2} \rightarrow F'' = \frac{3}{2}$ transition, and let the optical wave vector \mathbf{k} and magnetic field now be perpendicular. We choose the quantization axis along \mathbf{k} ; in this case the $\hat{\sigma}^-$ and $\hat{\sigma}^+$ resonances occur at the same frequency, but the strength of the atom-field coupling for each (optical) polarization depends orientation of the (atomic) polarization vector $\boldsymbol{\mu}$. If $\hat{\boldsymbol{\mu}} \cdot \hat{\mathbf{k}} = +1$, then $|n_{ba}^{(2)}[\hat{\sigma}^+] - 1|$ is maximized; $\hat{\sigma}^-$ radiation decouples from the atoms with the result that $n_{ba}^{(2)}[\hat{\sigma}^-] - 1 = 0$, since in this orientation the only excited state allowed by angular momentum conservation has $F'' = \frac{3}{2}, m_{F''} = +\frac{3}{2}$. If $\hat{\boldsymbol{\mu}} \cdot \hat{\mathbf{k}} = -1$, then we have the opposite case: $n_{ba}^{(2)}[\hat{\sigma}^+] - 1 = 0$ and $|n_{ba}^{(2)}[\hat{\sigma}^-] - 1|$ is maximal. Note that $n_{ba}^{(2)}[\hat{\sigma}^+] = n_{ba}^{(2)}[\hat{\sigma}^-] = 1$ when $\delta = 0$, since the magnetic field does not shift the two-photon resonance frequency in this configuration. The rotation angle is maximized when $\delta = \Gamma$.

If the atomic polarization vector is now allowed to precess about the magnetic field, then the index contrast (and thus the rotation angle $\phi/2$) is sinusoidally modulated at the precession frequency. In this ‘‘perpendicular’’ geometry the rotation signal does not depend on the excited state Zeeman splittings, as it does in the case where $\hat{\mathbf{k}}$ is parallel to the magnetic field. The modulation is due to an amplitude asymmetry between the refractive indices for $\hat{\sigma}^-$ and $\hat{\sigma}^+$ radiation, rather than a shift of the actual resonance frequency. (We can imagine using polarization rotation in the ‘‘parallel’’ configuration to detect oscillating magnetic fields.)

2.3 Pulsed Optical Fields

The frequency spectrum of a periodically repeated time-domain electric field such as

$$E^{(N)}(t) = \sum_{n=0}^{N-1} E(t - nT) \quad (2.103)$$

(e.g., the pulse train depicted in figure 2.2) is [66]

$$E_{\omega}^{(N)}(\omega) = \frac{1 - e^{iN\omega T}}{1 - e^{i\omega T}} E_{\omega}(\omega) , \quad (2.104)$$

where $E_{\omega}(\omega)$ is the Fourier transform of $E(t)$. The corresponding intensity spectrum is

$$I_{\omega}^{(N)}(\omega) = \frac{1 - \cos N\omega T}{1 - \cos \omega T} I_{\omega}(\omega) , \quad (2.105)$$

which displays the characteristic “comb” structure shown in figure 2.3. Although the spectral bandwidth of a pulse can be much larger than the linewidth of an atomic resonance, this comb structure allows spectroscopy to be performed with a resolution limited by the width of an individual tooth, rather than the width of the entire spectrum. This technique, known as *direct frequency comb spectroscopy*, is surveyed in detail in reference [67]. It is also the underlying principle for the experiments using pulsed lasers reported in chapter 4.

The narrow teeth under the pulse envelope correspond to excited axial modes of the laser resonator, and interpulse phase coherence is the time-domain result of phase-locking their relative frequencies. Thus there are two complementary time-domain pictures: one in which many cw modes oscillate simultaneously with fixed relative phases, and one in which a single carrier frequency is amplitude-modulated by a time-varying envelope function. Both pictures correspond to equivalent frequency spectra, provided the overall power and power per mode are normalized correctly.

Although the relative phases of the various modes are obviously critical to a correct description of the optical field, there is an interesting sum rule that roughly relates the total average power to the power per mode. If we consider the frequency spectrum to be centered at $\omega = 0$, then the average power $\langle P \rangle$ can be represented as

$$\langle P \rangle = P_0 \sum_{m=-\infty}^{\infty} e^{-m^2 \omega_r^2 / \Delta^2} , \quad (2.106)$$

where P_0 is the power of the central mode, m is the (shifted) mode index, ω_r is the (angular) repetition frequency, and Δ is the width of the (field) frequency spectrum. This representation can be used to express the power in each mode in terms of a Jacobi θ function,

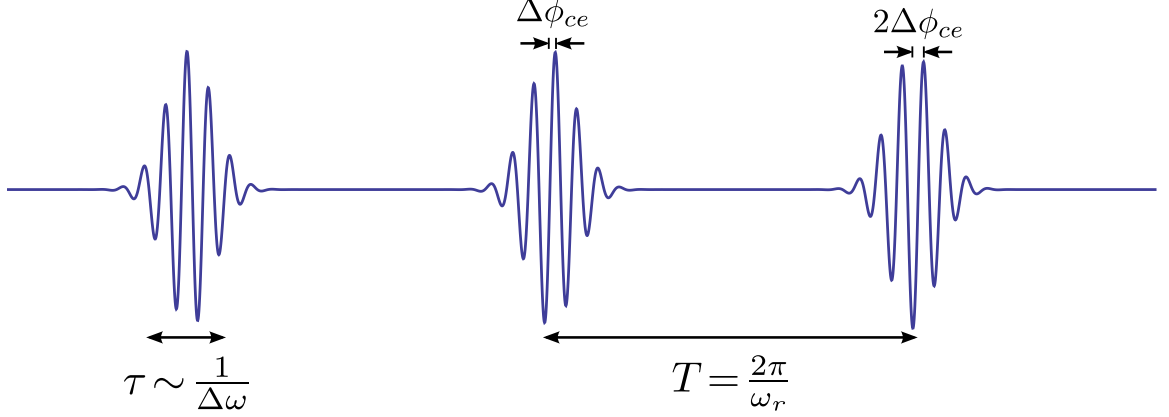


Figure 2.2: An optical pulse train with phase coherence between successive pulses. The frequency spectrum of such a field quite generally takes the form shown in figure 2.3, where the quasi-discrete modes shown in red are fully determined by two frequency parameters. These are the repetition rate, $f_r = \omega_r/2\pi = T^{-1}$ (which corresponds to the inverse of the round-trip time in the resonator producing the pulses), and the carrier-envelope offset frequency $f_0 = \Delta\phi_{ce}/T$ (which describes the rate of phase slip between the carrier wave and the field envelope maximum). The pulse duration τ determines the bandwidth of the frequency spectrum, $\Delta\omega \sim \tau^{-1}$, and thus also how many modes of the resonator are excited.

$$\theta_3(0, r) = \sum_{m=-\infty}^{\infty} r^{-m^2}. \quad (2.107)$$

Thus, $\langle P \rangle = P_0 \theta_3(0, e^{-\omega_r^2/\Delta^2})$, and we have an analytic expression to relate the power of any given mode to the average power, for any pulse width and repetition rate.

We note that, for multiphoton excitation, the atomic lineshape function (green curve in figure 2.3) need not overlap with any axial mode to resonantly excite an atom. If for example it falls symmetrically between two comb teeth, then for two-photon excitation the positive detuning of one tooth is exactly canceled by the negative detuning of the other one. Similarly, any two modes that are symmetrically detuned from the atomic resonance will produce a resonant contribution to the excitation amplitude: similar to the case of Doppler-free multiphoton excitation, any combination of modes can resonantly excite an atom via a multiphoton transition if the *total* detuning vanishes. For higher-order multiphoton transitions, the number of resonant excitation pathways grows rapidly.

If we represent the laser field spectrum by

$$E_\omega(\omega) \sim \sum_m A_m e^{-i[(\omega_c + m\omega_r)t - \phi_m]}, \quad (2.108)$$

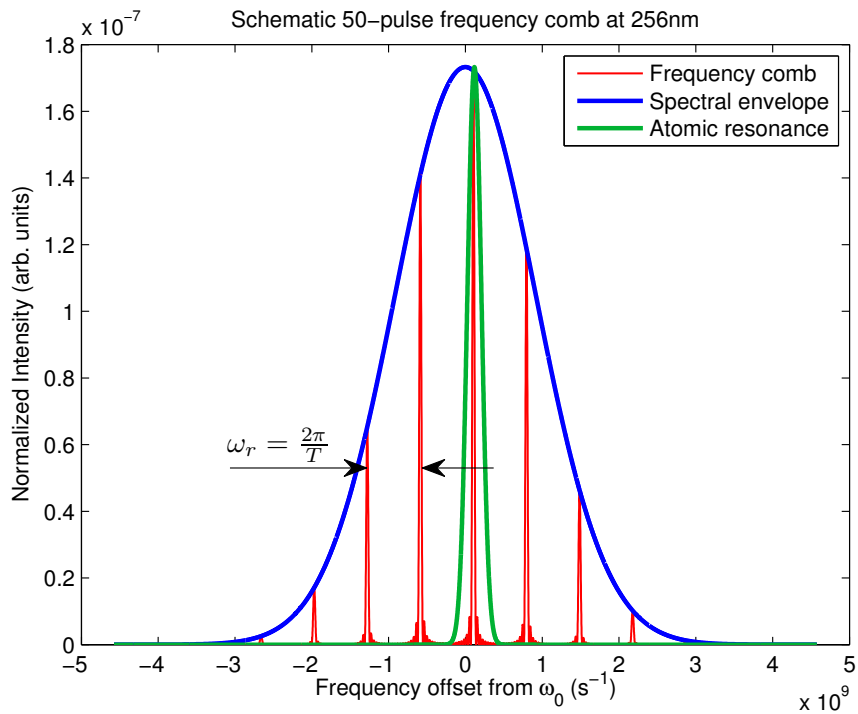


Figure 2.3: Calculated frequency “comb” resulting from a periodically repeated envelope function. The blue curve represents the spectral envelope of a series of Gaussian pulses, whose phase coherence from pulse to pulse leads to the interferometric pattern shown in red. We will often suppose that an atomic resonance line (green) overlaps one of the modes in such a spectrum.

where ω_c is the carrier frequency, A_m the amplitude of the m th mode, and ϕ_m a constant phase, then the excitation amplitude for a two-photon resonance at optical frequency ω_0 has the structure

$$\langle e|M|g\rangle \sim e^{-2i(\omega_0-\omega_c)t} \sum_k A_k A_{-k} e^{i(\phi_k-\phi_{-k})}, \quad (2.109)$$

where we have assumed that ω_c is resonant with the atomic transition at ω_0 and kept only the correspondingly resonant contributions from other modes. Note that we must take the absolute square of this amplitude to obtain the transition probability, which opens up the possibility for different terms in the sum to interfere. The situation is simplest if the spectral phase is odd, that is if $\phi_m = -\phi_{-m}$ for every m . In that case the phases cancel term-by-term and there is no interference. If the spectral phase is even ($\phi_m = \phi_{-m}$), then every term has a finite complex argument and (unless they are all the same) some degree of interference is guaranteed.

This situation accounts for the substantial concern paid to group velocity dispersion (GVD) in experiments with modelocked lasers, including those presented in chapter 4. GVD is a second-order spectral phase, and the different phases acquired by different modes can reduce the excitation probability through this type of interference between different optical excitation channels. Experimentally, GVD also broadens the pulse by introducing chirp; we have not discussed the various parameterizations of time- and frequency-chirp that can be used to characterize non-transform-limited pulses. We only remark that a transform-limited pulse (one with a minimal time-bandwidth product) has no chirp, and that experimental sources of GVD tend to produce chirp that can be observed as pulse broadening in the time domain via autocorrelation measurements.

2.4 Temporal Sensitivity

The “true” sensitivity of a magnetometer depends in excruciating detail on the experimental configuration – and must in general be considered on a case-by-case basis – but we can go a long way in the right direction by pursuing some naive scaling arguments. When the field is measured through Larmor precession at a frequency ω , we have $\hbar\omega = g_F\mu B$, where g_F is the total angular momentum Landé g -factor, μ is the appropriate magnetic moment (usually the Bohr or nuclear magneton), and B is the strength of the field giving rise to spin precession. A dimensional estimate for the frequency uncertainty of a single precessing spin is $\delta\omega \sim \tau^{-1}$, where τ is the measurement time. Scaling for m repetitions, N spins, and a signal-to-noise ratio η (assuming white frequency noise),

$$\delta\omega \sim \frac{1}{\tau\eta\sqrt{mN}} = \frac{1}{\eta\sqrt{NT\tau}}, \quad (2.110)$$

where we have assumed that the m measurements of duration τ are performed in a total time interval T . The single-measurement timescale τ is usually constrained by relaxation rates Γ_r such that $\tau \sim \Gamma_r^{-1}$, so assuming this and converting the frequency to a magnetic field we have

$$\delta B \sim \frac{\hbar}{g_F\mu\eta} \sqrt{\frac{\Gamma_r}{NT}}. \quad (2.111)$$

This is in fact the uncertainty due to atomic shot noise, and a very practical figure of merit for the intrinsic field sensitivity. We immediately notice that a factor of ~ 1800 is lost by going from electronic spins to nuclear spins; fortunately Γ_r is much less in nuclear systems, in some cases by enough to more than offset the factor of 1800.

To properly quote a magnetic field *sensitivity*, we should use the field uncertainty per unit bandwidth $\delta B/\sqrt{\Delta\nu}$, where $\Delta\nu \sim (2T)^{-1}$ is the frequency bandwidth resulting from the temporal average

$$\langle B \rangle = \frac{1}{T} \int_{t-\frac{T}{2}}^{t+\frac{T}{2}} B(t) dt. \quad (2.112)$$

2.5 Spatial Sensitivity

The figure of merit for spatially resolved measurements can be viewed as arising from a spatial frequency bandwidth, in analogy to the usual detection bandwidth that arises from averaging a time-varying field over a finite interaction time. Each spatial dimension l thus has an associated spatial frequency bandwidth $\delta k \sim l^{-1}$. Following [41], we can therefore generalize the usual magnetic field sensitivity by explicitly including spatial dimensions in the figure of merit 2.111. An optical magnetometer that consists of an atomic gas with number density $\bar{n} = N/V$ occupying a volume $V = l_x l_y l_z$ thus has a field uncertainty of

$$\delta B \sim \frac{\hbar}{g_F\mu\eta} \sqrt{\frac{\Gamma_r}{\bar{n}T l_x l_y l_z}}, \quad (2.113)$$

and a sensitivity of $\delta B/\sqrt{\Delta\nu\Delta\kappa_x\Delta\kappa_y\Delta\kappa_z}$, where $\Delta\kappa_i \sim (2l_i)^{-1}$ for $i = x, y, z$. Evidently the ‘‘spatiotemporal sensitivity’’ (which has units of $\text{T}/\sqrt{\text{Hz} \cdot \text{m}^3}$) scales as $\sqrt{\Gamma_r/\bar{n}}$.

2.6 Diffusive Motion and Geometric Phases

The atomic Hamiltonian may depend on parameters such as position and local field strength that (from the point of view of an atom) change in time. If this time variation is sufficiently slow, then the spectrum of eigenstates and eigenvalues – which in general depend on these parameters – evolves smoothly in time. A system initially prepared in an eigenstate thus evolves with the usual dynamical phase, but also according to the time dependence of the instantaneous eigenbasis. The Schrödinger equation requires that each eigenstate develop an additional, nondynamical phase factor, which depends on the details of its parametric variation [68]. Perhaps surprisingly, this “geometric” phase has important physical implications and (although it can be expressed as the line integral of a vector potential) cannot in general be eliminated by a gauge transformation. In fact, geometric phases associated with field inhomogeneities comprise an important class of systematic effects for magnetometers and EDM searches.

Suppose we have an instantaneous eigenbasis that depends on time through the values of the parameters $\mathbf{R}(t) = (x(t), y(t), \dots)$:

$$H(\mathbf{R}) |n(\mathbf{R})\rangle = E_n(\mathbf{R}) |n(\mathbf{R})\rangle . \quad (2.114)$$

The dynamical phase associated with a given eigenstate is thus

$$\theta_n(t) = -\hbar^{-1} \int_0^t dt' E_n(\mathbf{R}(t')), \quad (2.115)$$

and a state given by $|\psi(0)\rangle = \sum_n a_n(0) |n(\mathbf{R}(0))\rangle$ at $t = 0$ will evolve to

$$|\psi(t)\rangle = \sum_n a_n(t) e^{i\theta_n(t)} |n(\mathbf{R}(t))\rangle \quad (2.116)$$

at a later time t . We can show from the time-dependent Schrödinger equation that

$$\dot{a}_n(t) = - \sum_m a_m \langle n | \dot{m} \rangle e^{i(\theta_m - \theta_n)} , \quad (2.117)$$

where the time dependence on the right hand side is left implicit for notational simplicity. If we now differentiate 2.114 with respect to time, we can show that (for $n \neq m$)

$$\langle n | \dot{m} \rangle = \frac{\langle n | \dot{H} | m \rangle}{E_m - E_n} , \quad (2.118)$$

and so

$$\dot{a}_n = -a_n \langle n | \dot{n} \rangle - \sum_{m \neq n} \frac{\langle n | \dot{H} | m \rangle}{E_m - E_n} c_m e^{i(\theta_m - \theta_n)}. \quad (2.119)$$

For sufficiently slow variation of H , the sum can be neglected and we have

$$a_n(t) = a_n(0) e^{-\int_0^t dt' \langle n | \dot{n} \rangle} \equiv a_n(0) e^{i\gamma_n(t)}, \quad (2.120)$$

where we have defined the geometric phase $\gamma_n = i \int_0^t dt' \langle n | \dot{n} \rangle$. The time evolution of $|\psi\rangle$ is now given by

$$|\psi(t)\rangle = \sum_n a_n(0) e^{i\theta_n(t)} e^{i\gamma_n} |n\rangle. \quad (2.121)$$

We now note that $|n\rangle$ depends on t only through \mathbf{R} , so in fact we can write $|\dot{n}\rangle = |\nabla_{\mathbf{R}} n\rangle \cdot \dot{\mathbf{R}}$, and defining the *Berry potential* $\mathbf{A}_n(\mathbf{R}) = i \langle n | \nabla_{\mathbf{R}} n \rangle$, the integral becomes

$$\gamma_n = i \int_{\mathbf{R}(0)}^{\mathbf{R}(t)} \langle n | \nabla_{\mathbf{R}} n \rangle \cdot d\mathbf{R} = \int_{\mathbf{R}(0)}^{\mathbf{R}(t)} d\mathbf{R} \cdot \mathbf{A}(\mathbf{R}). \quad (2.122)$$

If for some time $t = T$, $\mathbf{R}(0) = \mathbf{R}(T)$, then we have a closed line integral about some circuit C , which depends only on the geometry in parameter space (i.e., not on the dynamics of how the path is followed):

$$\gamma_n = \oint_C d\mathbf{R} \cdot \mathbf{A}(\mathbf{R}). \quad (2.123)$$

Now if we make a local gauge transformation $|n\rangle \rightarrow e^{i\beta(\mathbf{R})} |n\rangle$, then $\mathbf{A}_n \rightarrow \mathbf{A}_n + \nabla_{\mathbf{R}}\beta$, and so from equation 2.122

$$\gamma_n \rightarrow \gamma_n + \beta(\mathbf{R}(t)) - \beta(\mathbf{R}(0)). \quad (2.124)$$

Thus, over a closed path the geometric phase factor $e^{i\gamma_n}$ is *absolutely* gauge-invariant, and the geometric phase itself is gauge-invariant up to $2\pi m$ for integer m .

Applying these results to spins moving in a magnetic field, we consider the three field components B_x , B_y , and B_z as parameters in the Hamiltonian $H = \mu \mathbf{F} \cdot \mathbf{B}$, where \mathbf{F} is the total angular momentum operator and μ the magnetic moment. Since we now have a simple three-dimensional parameter space, we can use Stokes' theorem to transform equation 2.122 into a surface integral:

$$\gamma_n = \iint_S d\mathbf{S} \cdot \nabla \times \mathbf{A}(\mathbf{B}) \quad (2.125)$$

$$= -\text{Im} \iint_S d\mathbf{S} \cdot \langle \nabla_{\mathbf{B}} n | \times | \nabla_{\mathbf{B}} n \rangle, \quad (2.126)$$

where S is a surface bounded by C . The cross product can be expanded by inserting a complete set of states $\sum_m |m\rangle \langle m|$, and observing that $\langle m | \nabla_{\mathbf{B}} E_n(\mathbf{B}) | n \rangle$ must vanish, we can exclude the $m = n$ terms from the sum. The matrix elements with $m \neq n$ are obtained from 2.114, and we find

$$\langle \nabla_{\mathbf{B}} n | \times | \nabla_{\mathbf{B}} n \rangle = \frac{1}{\mu^2 B^2} \sum_{m \neq n} \frac{\langle n | \nabla_{\mathbf{B}} H | m \rangle}{n - m} \times \frac{\langle m | \nabla_{\mathbf{B}} H | n \rangle}{m - n}, \quad (2.127)$$

where we have used $E_n = \mu B n$. Now $\nabla_{\mathbf{B}} H = \mu \mathbf{F}$, and so we need to evaluate the matrix elements $\langle n | \mathbf{F} | m \rangle$. These are readily obtained from the raising and lowering operators $F_{\pm} = F_x \pm iF_y$ and F_z , in a basis where $\mathbf{B} = B\hat{\mathbf{z}}$. Following [68], we rotate into such a coordinate system to evaluate the cross product before rotating back to obtain the general result. In the rotated coordinate system, we use

$$F_{\pm} |n\rangle = \sqrt{F(F+1) - n(n \pm 1)} |n \pm 1\rangle \quad (2.128)$$

$$F_z |n\rangle = n |n\rangle \quad (2.129)$$

to obtain

$$\langle n \pm 1 | F_x | n \rangle = \frac{1}{2} \sqrt{F(F+1) - n(n \pm 1)} \quad (2.130)$$

$$\langle n \pm 1 | F_y | n \rangle = \mp \frac{i}{2} \sqrt{F(F+1) - n(n \pm 1)}. \quad (2.131)$$

Only the $\hat{\mathbf{z}}$ component of the cross product is nonvanishing in this coordinate system, and the only nonvanishing matrix elements are between pairs of states where $m = n \pm 1$. Thus,

$$\begin{aligned} \langle \nabla_{\mathbf{B}} n | \times | \nabla_{\mathbf{B}} n \rangle &= \frac{-i}{2B^2} [-n(n-1) + n(n+1)] \\ &= \frac{in}{B^2}, \end{aligned} \quad (2.132)$$

and rotating back to the original coordinate system we have

$$\langle \nabla_{\mathbf{B}} n | \times | \nabla_{\mathbf{B}} n \rangle = in \frac{\mathbf{B}}{B^3}. \quad (2.133)$$

Finally,

$$\gamma_n = -n \iint_S d\mathbf{S} \cdot \frac{\mathbf{B}}{B^3}, \quad (2.134)$$

which we recognize as $-n$ multiplied by the solid angle subtended by S at $\mathbf{B} = 0$. Thus, a geometric phase arises due to the degeneracy in eigenvalues that occurs when the magnetic field vanishes, and is proportional to the solid angle subtended at the degeneracy point in parameter space by the path C .

2.6.1 Systematic Effects in EDM Experiments

In EDM experiments, static external electric and magnetic fields (\mathbf{E} and \mathbf{B}_0 , respectively) are applied to a precessing ensemble of spatially confined spins. Geometric phases arise both from magnetic field gradients ($\partial \mathbf{B}_0 / \partial z \neq 0$, where $\hat{\mathbf{z}}$ is the quantization axis), and from motional magnetic fields ($\mathbf{B}_m = \mathbf{v} \times \mathbf{E}/c$, where \mathbf{v} is the translational velocity of a particle in the ensemble).

As discussed above, a particle trajectory that follows a closed path in the parameter space of magnetic field components will produce a finite geometric phase. When \mathbf{B}_0 is completely uniform in space and the particles are stationary, no geometric phase is acquired since the trajectories reduce to a single point in parameter space. However, real experiments inevitably produce changes in the motional field due to changes in particle velocity, as well as field gradients due to the finite extent of magnetic sources.

When the particle velocity is small, the magnitude of the total effective magnetic field $\mathbf{B} = \mathbf{B}_0 + \mathbf{B}_m$ includes terms that depend on B_m :

$$B \approx B_0 + \hat{\mathbf{B}}_0 \cdot \mathbf{B}_m + \frac{B_m^2}{2B_0}. \quad (2.135)$$

These produce a shift of the precession frequency with respect to the case where \mathbf{B}_m vanishes, which is given by [51]

$$\begin{aligned} \Delta\omega &\approx \frac{\mu}{\hbar c} \hat{\mathbf{B}}_0 \cdot (\mathbf{v} \times \mathbf{E}) + \frac{\mu}{2\hbar c^2} \frac{(\mathbf{v} \times \mathbf{E})^2}{B_0} \\ &\approx \frac{\mu v}{\hbar c} \theta_{EB} E + \frac{\mu v^2}{2\hbar c^2} \frac{E^2}{B_0}, \end{aligned} \quad (2.136)$$

where θ_{EB} is the angle between \mathbf{B}_0 and \mathbf{E} in the plane perpendicular to \mathbf{v} . (We have assumed in the second line that \mathbf{B}_0 and \mathbf{E} are nearly parallel.) The term proportional to θ_{EB} is linear in E and independent of B_0 ; it therefore has the same correlation with $\mathbf{B} \cdot \mathbf{E}$ as a permanent electric dipole moment. It is not, however, a signature of CP -violating physics: the particle velocities \mathbf{v} also change sign under T , and so simply changing the relative direction of \mathbf{B}_0 with respect to \mathbf{E} does not produce the true time-reversed Hamiltonian [51].

Geometric phases also arise from “cross-terms” that include contributions from both gradients and motional fields, and indeed these can dominate the systematic error budget of EDM experiments that rely on a cohabiting reference magnetometer. Geometric phase effects in a mercury co-magnetometer were one of the most severe systematic limitations in the most recent measurement of the neutron EDM [9]. Such effects are quantitatively discussed in the literature, see for example [69, 70]. Recent numerical simulations also indicate that they can lead to asymmetrical phase distributions, a result that is consistent with nonextensive statistics [35].

Geometric phases that mimic an EDM can be minimized by using particles with a very low mean velocity (this is a notable advantage of ultracold neutrons and laser cooled atoms), and by confining the sample to a region of space where the applied fields are highly uniform and parallel. In this respect, species whose spatial diffusion can be restricted by buffer gas present a novel advantage [71, 72]. Magnetometry with spatial resolution would be a particularly useful tool for diagnosing geometric phase systematics.

2.7 Summary

We have now laid the groundwork for discussing multiphoton electronic transitions excited by cw and pulsed lasers. The scaling of excitation rate with optical intensity, intermediate state detunings, and atomic density of states has a significant impact on the experimentally achievable signal-to-noise ratio. These results are employed to interpret experimental data, and to extrapolate the potential of future experiments in chapters 3 and 4. We have also seen the origin of two-photon light shifts, and of the high spectral resolution that can be achieved with modelocked pulsed lasers; these will play more important roles in future experiments with improved laser stability. The discussion of geometric phases is particularly relevant in EDM experiments, such as the one discussed in section 5.2.

CHAPTER 3

Experiments with Ytterbium and Continuous-Wave Lasers

This chapter mainly discusses experiments with atomic ytterbium, which has one- and two-photon transitions from the ground state at relatively convenient laser wavelengths. Its electronic structure is representative of other diamagnetic atoms, corresponding to a case intermediate between helium and the heavier noble gases. These properties make ytterbium an excellent candidate for studying two-photon excitation and nuclear spin polarization, in an atom that can also be polarized and probed using more conventional one-photon E1 transitions. The naturally abundant isotopes include several with nuclear spin $I = 0$ and one, ^{171}Yb , with $I = \frac{1}{2}$; this provides a useful opportunity to cross-check experiments with ^{171}Yb by repeating them using isotopes whose nuclei cannot be polarized. An atomic beam and narrowband cw lasers are used to investigate the features of these transitions that are influenced by nuclear spin, in a configuration where the excited state Zeeman splittings are resolved (as are the hyperfine and isotope shifts).

In section 3.5 we present data from cw vapor cell spectroscopy of one-photon transitions in mercury at 253.7 nm, and two-photon transitions in xenon at 256.0 nm.

Ytterbium ($Z = 70$) is the only lanthanide whose ground state electronic configuration consists entirely of filled subshells. Seven stable isotopes occur naturally, of which ^{171}Yb and ^{173}Yb have nonzero nuclear spin (see table 3.1). Chemically and spectroscopically it is similar to the alkaline-earth metals, and it shares with them the electronic level structure shown in figures 1.5 and 3.2. The natural linewidth of the $^1S_0 - ^1P_1$ transition (~ 1.2 MHz) is about 167 times less than for $^1S_0 - ^3P_1$ (~ 200 MHz) [3]. The corresponding radiative lifetimes are $\tau_{^3P_1} \approx 850$ ns and $\tau_{^1P_1} \approx 5$ ns [73].

Ytterbium is a relatively heavy atom, and the finite single-photon electric dipole (E1) transition rate for the “spin forbidden” $^1S_0 - ^3P_1$ transition is a signature of the expected breakdown of LS coupling in its electronic excited states (see section 1.5). It is nevertheless conventional to designate the excited states by an electron configuration and approximate

Table 3.1: Naturally occurring isotopes of ytterbium [4]

Isotope	Abundance (%)	Nuclear Spin	Nuclear Magnetic Moment (μ_N)
^{168}Yb	0.13	0+	
^{170}Yb	3.05	0+	
^{171}Yb	14.3	1/2-	+0.4919
^{172}Yb	21.9	0+	
^{173}Yb	16.12	5/2-	-0.6776
^{174}Yb	31.8	0+	
^{176}Yb	12.7	0+	

LS spectroscopic term symbols, where it is understood that the pure LS eigenstates are mixed by the spin-orbit interaction. In the usual parameterization, the physical wavefunctions are written in terms of pure LS components as

$$\psi(^3P_1) = \alpha\psi^0(^3P_1) + \beta\psi^0(^1P_1) \quad (3.1)$$

$$\psi(^1P_1) = \alpha\psi^0(^1P_1) - \beta\psi^0(^3P_1), \quad (3.2)$$

where ψ^0 denotes a pure LS eigenstate and $\alpha^2 + \beta^2 = 1$. The coefficients have been experimentally determined [74] to be $\alpha = 0.991$ and $\beta = -0.133$. Neglecting decay channels other than spontaneous E1 emission, these values account reasonably well for the difference in observed linewidth:

$$\frac{\Gamma_{^1P_1}}{\Gamma_{^3P_1}} \approx \left(\frac{556 \text{ nm}}{399 \text{ nm}}\right)^3 \left(\frac{\alpha}{\beta}\right)^2 \approx 150, \quad (3.3)$$

where $\Gamma_{^1P_1} = \tau_{^1P_1}^{-1}$ and $\Gamma_{^3P_1} = \tau_{^3P_1}^{-1}$ are the reciprocals of the radiative lifetimes for the indicated states.

Similarly, the 3D_2 and 1D_2 states are not pure LS coupled states and we can write

$$\psi(^3D_2) = \sqrt{1 - \xi^2}\psi^0(^3D_2) - \xi\psi^0(^1D_2) \quad (3.4)$$

$$\psi(^1D_2) = \sqrt{1 - \xi^2}\psi^0(^1D_2) + \xi\psi^0(^3D_2), \quad (3.5)$$

where the mixing parameter ξ has been determined to be $\xi = 0.13(1)$ [75]. The lifetimes are $\tau_{^3D_2} \approx 460$ ns and $\tau_{^1D_2} \approx 380$ ns [75].

Before addressing magnetometry, we first describe the experimental apparatus and present measurements that characterize the interaction of ytterbium atoms with cw lasers and static magnetic fields.

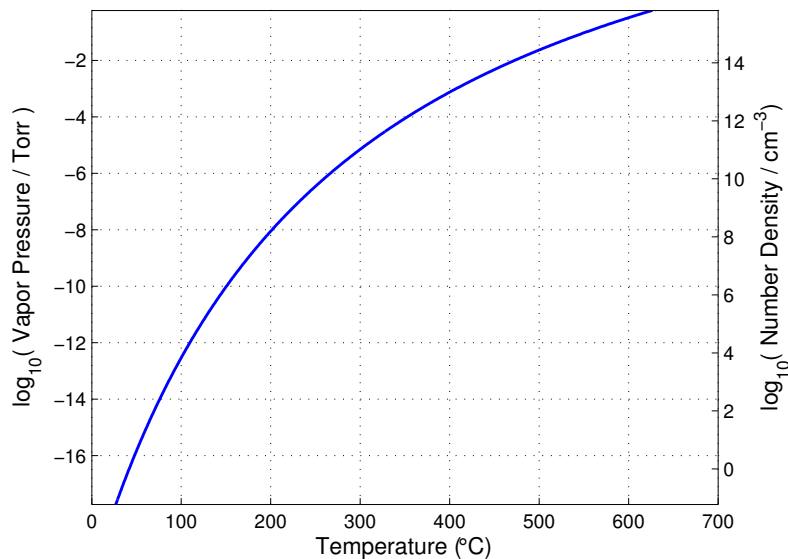


Figure 3.1: Vapor pressure and equivalent number density of ytterbium gas in thermal equilibrium with solid ytterbium metal, as a function of temperature. The values are calculated from a model equation with coefficients according to [1], and should represent the actual vapor pressure to within $\pm 5\%$.

3.1 Atomic Beam Apparatus

The experiments involving optical spectroscopy of ytterbium were performed with the atomic beam apparatus shown in figures 3.3 and 3.5. The choice of an atomic beam rather than a vapor cell is dictated by the low pressure of ytterbium vapor in thermal equilibrium with ytterbium metal (see figure 3.1), and by the hot gas's propensity for destructively reacting with glass and other optically transmissive materials. Experiments relying on ytterbium vapor cells typically use metallic heat pipe ovens, with differential heating to avoid ytterbium condensation on optical surfaces.

The atomic beam operates in vacuum to achieve a long mean free path for its constituent atoms, and to prevent unwanted chemical reactions from disrupting the optical and magnetic interactions under investigation. It is collimated by passing through apertures and the atoms are optically excited by laser beams along a transverse axis to minimize Doppler broadening. This has the result that Zeeman structure in the excited state can be resolved by tuning the excitation frequency, which provides a useful systematic check when determining the effect of optical pumping (since a given Zeeman level can be addressed either by polarization or by frequency).

The vacuum chamber consists of an eight-inch spherical octagon (Kimball MCF800-

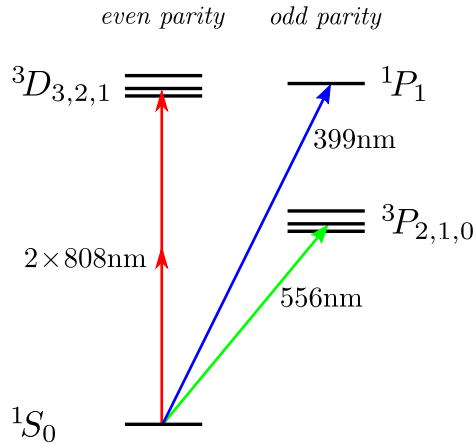


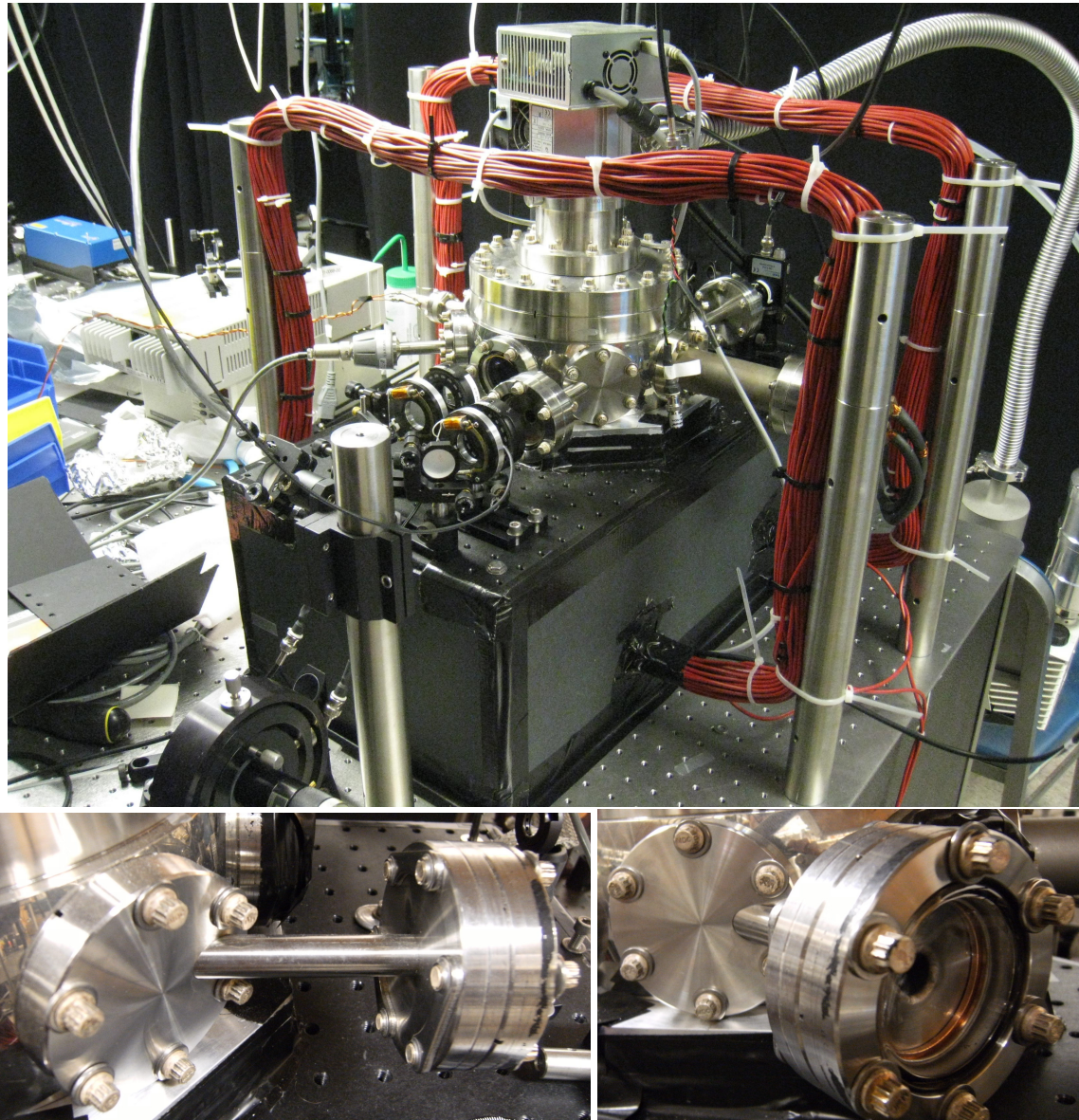
Figure 3.2: Some low-lying electronic transitions and excited states of ytterbium, labeled with spectroscopic term symbols. The states are labeled as for pure LS -coupling, but spin-orbit mixing of the pure LS -eigenstates allows intercombination transitions such as the $^1S_0 \rightarrow ^3P_1$ intercombination line (green arrow). For magnetic level structure of the spin- $\frac{1}{2}$ isotope ^{171}Yb , refer to figure 1.5(b).

SO2000800), with a 6.3-inch (~ 16 cm) bore and two standard 8" ConFlat flanges. The upper flange connects to a turbo pump and mechanical pump in series, which maintain a base vacuum of $\sim 1 \times 10^{-6}$ Torr. The lower flange is sealed to a stainless steel plate, which has an optical window in the center to couple fluorescence light out of the chamber and into a photomultiplier tube (PMT). A machined recess around the window is used to seat the 3" aluminum "spectroscopy box" (described below and shown in figure 3.7). Standard 2-3/4" ConFlat flanges on each of the eight faces of the spherical octagon are used for optical windows, electrical feedthroughs, a vacuum gauge, and the effusive ytterbium oven.

The source for the atomic beam is the effusive oven shown in figure 3.6, which consists of a tantalum shell containing natural-abundance ytterbium metal (see table 3.1 for isotopic abundances). Metallic ytterbium is placed in the tubular tube, and a steel washer is spot-welded over the open end to hold it in place. The hole at the center of the washer provides an aperture through which the beam effuses. The oven and electrical feedthrough are mounted into a ConFlat nipple, which is connected to a flange on one octagonal face so that the beam crosses the center of the chamber. It is resistively heated by an externally supplied current of ~ 60 A, producing a thermal beam with volumetric number density $\bar{n} \sim 10^8 \text{ cm}^{-3}$ and mean velocity $v_{th} \sim 300$ m/s under normal operating conditions.

The oven output is quite stable after a warm-up period of one hour, and fluctuations in the fluorescence signal, after adequate warm-up, usually indicate that the ytterbium needs to be replenished. The oven has a useful lifetime of several months per loading cycle, and the atomic beam flux can be increased to compensate for this gradual decay (or for a measure-

Figure 3.3: Ytterbium atomic beam vacuum chamber and associated optics. The red external field coils are clearly visible in the upper picture, and the optics just left of center guide the pump and probe beams into the chamber. External detection optics and the photomultiplier tube are contained in the light-shielded box under the vacuum chamber. The pictures below left and right show detail of the normal-incidence flange adapter for the pump beam windows (see also figure 3.4).



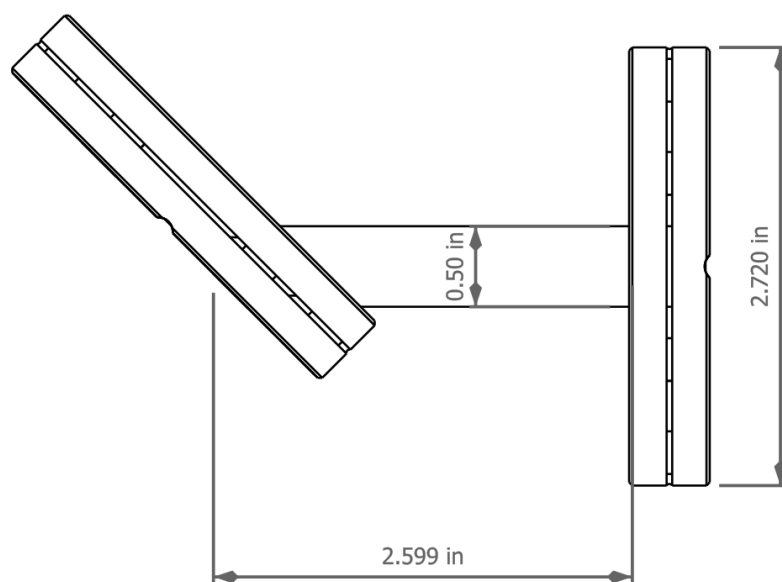


Figure 3.4: The normal-incidence flange adapter, designed and installed to eliminate polarization dependent backgrounds resulting from the pump beam. A stainless steel connector tube is welded between bored holes in standard 2-3/4" blank ConFlat flanges, one at normal incidence and one at 45°. The offset from center on the 45° flange is to position the beam in the center of the clear aperture for transmission through the spherical octagon.

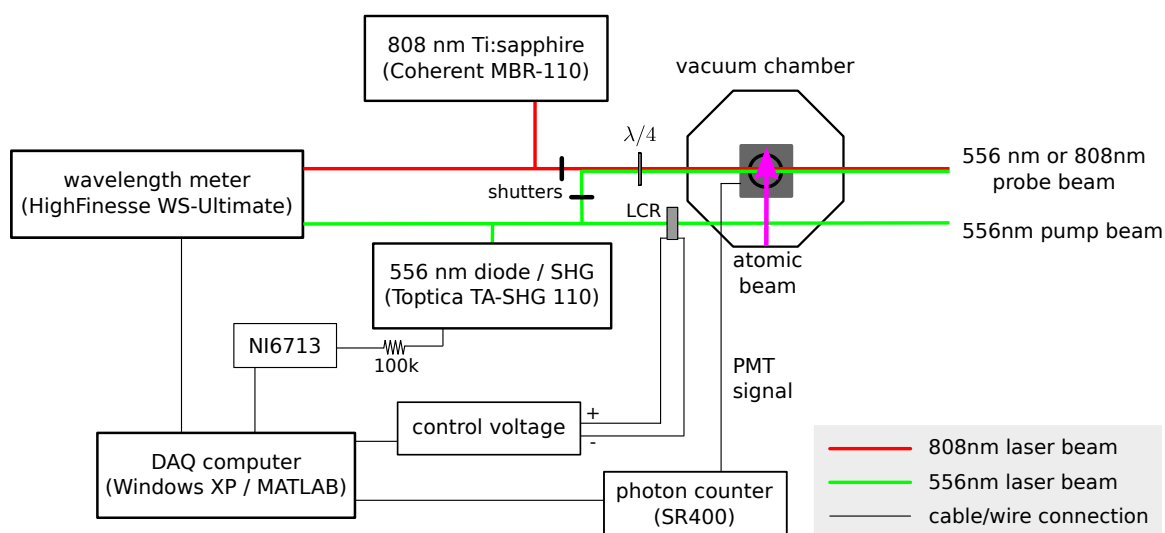


Figure 3.5: Block diagram of the cw atomic beam experiment, showing major equipment connections and key optical elements. Only one of the two possible probe beams is used at one time.

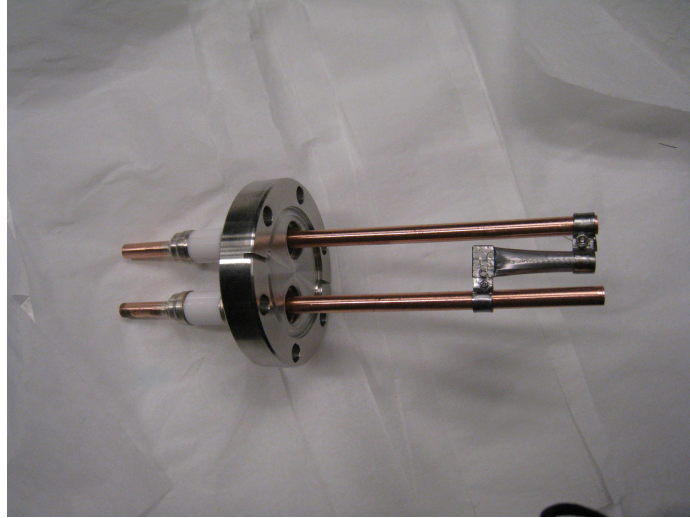


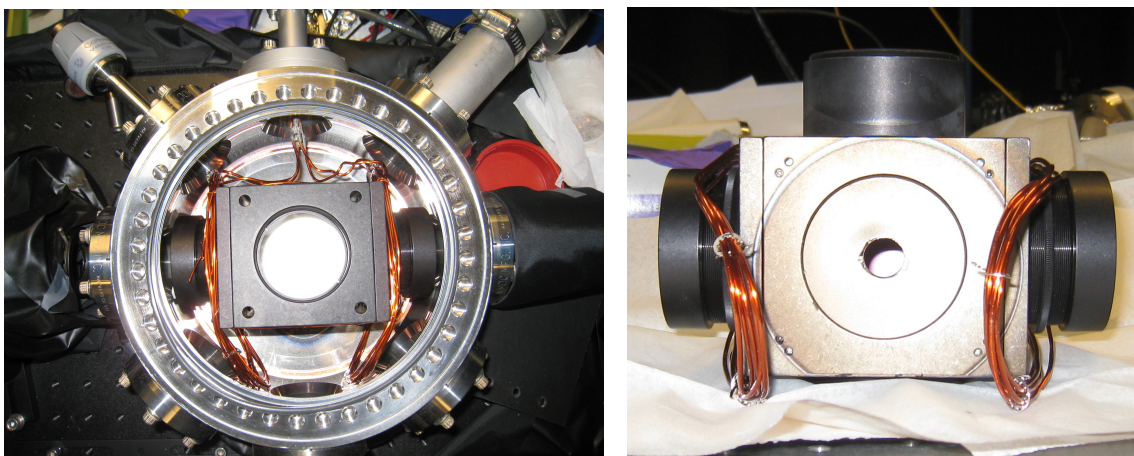
Figure 3.6: Tantalum oven for ytterbium atomic beam source, showing copper leads and ConFlat flange with electrical feedthrough. The beam emerges to the reader’s right.

ment requiring a larger signal) by increasing the oven current. Since the oven is operated in fixed-current mode, a slow increase over time in the supplied voltage can be monitored to estimate the remaining lifetime (ytterbium depletion changes the total resistance of the oven). The amplitude of the fluorescence signal from the 556nm ^{171}Yb , $F = \frac{1}{2} \rightarrow F' = \frac{1}{2}$ transition is also used as a benchmark for fluctuations in oven performance.

The 2-3/4" ConFlat flanges on either side of the oven are used to hold windows for an optical pumping beam resonant with the 556 nm $^1S_0 - ^3P_1$ intercombination transition. In order to mount the windows normal to the pump beam (and thereby maintain the polarization of the transmitted beam), the adapting connectors shown in figures 3.3 and 3.4 were custom-made by boring a 45° hole through a blank ConFlat flange, and welding a stainless steel connector tube between it and another flange at 90° to the beam axis. With this configuration, the polarization-dependent background that limited early beam experiments was completely eliminated. (The probe beam transects the chamber on a diameter, and so naturally enters the windows at normal incidence.)

The spectroscopy box at the center of the chamber surrounds the region where the atomic beam interacts with the probe light, a distance of approximately 7.4 cm from the the pump beam. (This distance corresponds to $\sim 250 \mu\text{s}$ time of flight at the estimated mean thermal velocity). It consists of a 60 mm cage cube (Thorlabs LC6W), with a 12 mm circular aperture mounted in the front face that serves as the second collimating constriction for the atomic beam. Condenser lenses are mounted confocally above and below the box’s center, to collect laser-induced fluorescence (LIF) light and direct it through the window in the baseplate to a PMT (Hamamatsu H8259) below the chamber. The remaining apertures

Figure 3.7: Internal Components of Ytterbium Atomic Beam Chamber



(a) Internal coils and spectroscopy box, viewed through the open upper flange of the spherical octagon. In this view, the atomic beam crosses the chamber from bottom to top and the pump and probe beams cross from left to right. The upper mirror housing visible in (b) has been removed from the spectroscopy box.

(b) Spectroscopy box viewed along the atomic beam axis; the collimating aperture in the front face is visible. Condenser lenses ($NA = 0.554$) are mounted inside for high-efficiency light collection. The top attachment redirects fluorescence through the bottom lens, forming a folded $4f$ system.

in the box are baffled with sections of lens tubing, to prevent ambient light and scattered laser light from reaching the PMT.

Shaped and discriminated pulses from the PMT head (2.2 V height, 30 ns width) are sent to a photon counter (Stanford Research Systems SR400), and read into a data acquisition computer (Windows XP) over an RS-232 interface. The computer interfaces with the photon counter through a MATLAB control script, which regulates most aspects of the experiment and performs online data analysis. Gate settings are entered into the control script at the beginning of the experiment, and automatically written to the photon counter when the script verifies equipment connections prior to recording data. When the photon counter is not triggered by an external device such as an optical chopper, the script also provides a trigger signal for each recorded data point.

The computer also has USB connections to a wavelength meter (HighFinesse/Ångstrom WS Ultimate), and the voltage controller for a liquid crystal retarder (Thorlabs LCR-1-NIR). Both are ultimately handled by the same control script; the waveplate is discussed later on. The wavemeter is calibrated by periodically referencing a frequency-stabilized HeNe laser (SIOS SL 02/1), which is fiber-coupled to a second port independent from the measurement port. The wavemeter displays two modes of frequency instability: a slow drift of several MHz per day which is observed by measuring the center frequency of the

same reference transition at 556 nm (^{171}Yb , $F = \frac{1}{2} \rightarrow F' = \frac{1}{2}$), and infrequent diabatic jumps of ~ 40 MHz that occur without a clear cause. It is possible that this is related to some intrinsic instability in the reference HeNe, and future experiments would benefit from a reference laser that is stabilized to an atomic or molecular resonance. Since the accuracy of the measured frequency also depends on its separation from the calibration frequency, a particularly attractive option is to use the same transition that is being studied as a frequency reference.¹

The laser used for optical pumping is a frequency-doubled, tunable diode laser (Toptica TA-SHG 110) which provides approximately 1 mW at 556 nm. The nominal linewidth is ~ 200 kHz, and the frequency can be tuned over a range of several hundred GHz. The fundamental light is supplied by an 1112 nm diode laser, which is line-narrowed by grating feedback and optically isolated from the frequency doubling stage. The doubler consists of a LBO crystal mounted in a resonant cavity, whose optical path length is locked by the Pound-Drever-Hall technique [76, 77]. Fine frequency adjustment is provided by a piezoelectric transducer, which scans the fundamental cavity. If the frequency change is not too large or too rapid, the cavity follows without losing its lock and the 556 nm frequency is also adjusted. For larger frequency changes, a coarse adjustment of the grating moves the center of the finely tunable dynamic range.

A small amount of the 556 nm light is picked off and fiber-coupled into the wavemeter to monitor the laser frequency. The wavemeter is controlled by a computer program that runs simultaneously with the MATLAB control script, and generates a PID error signal for laser stabilization if the measured frequency deviates from a prescribed value or time series. The error signal is converted to a voltage and sent to the piezoelectric transducer via an analog output board (National Instruments PCI-6713). The tuning sensitivity was calibrated by applying a known drive voltage and measuring the frequency response with the wavemeter; the sensitivity is entered as a scaling parameter in the control program. In practice, optimal frequency control is obtained by placing an RC filter and a 100 k Ω resistor between the data acquisition card and the laser, to smooth and scale the control voltage. The scaling due to the “voltage divider” is then included in the sensitivity calibration.

A typical measurement such as the fluorescence spectrum shown in figure 3.10 involves a sequential scan through a list of laser frequencies, where the laser is held for some time at each constant frequency as data is collected. In this case the control script sets the scan parameters by sending them to the wavemeter program before data acquisition begins,

¹We attempted to do this using saturated-absorption spectroscopy of a hollow-cathode ytterbium discharge. Due to the large magnetic fields applied in the atomic beam experiment, the atomic resonances in the beam are shifted by several MHz relative to those in the discharge. This approach therefore requires additional frequency-shifting elements, or an off-resonant measurement at low magnetic field

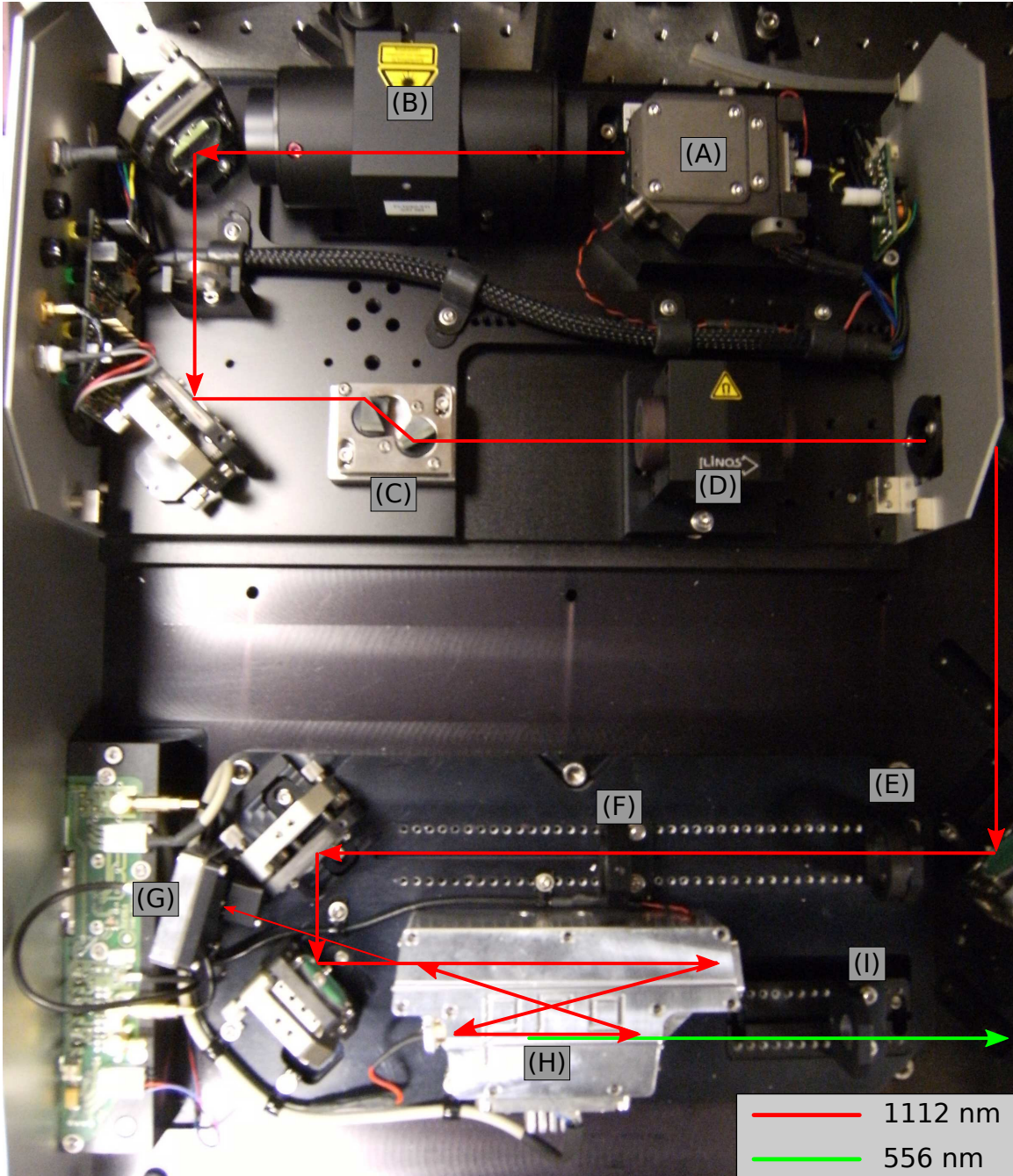


Figure 3.8: The Toptica TA-SHG 110 used to produce 556 nm light resonant with the $^1S_0 \rightarrow ^3P_1$ transition in ytterbium. The top half contains (A) the grating-feedback seed laser of 1112 nm wavelength, (B) and (D) optical isolators, and (C) anamorphic beam-shaping prisms. The lower half contains mode-matching optics (E) and (F), which prepare the beam for injection into the resonant doubling cavity (H). An optical error signal from the cavity is recorded on a photodiode (G) for Pound-Drever-Hall locking of the cavity resonance. The 556 nm beam produced by the BBO crystal in the cavity is coupled out and filtered (I) before being shaped with an additional set of anamorphic prisms (not shown).

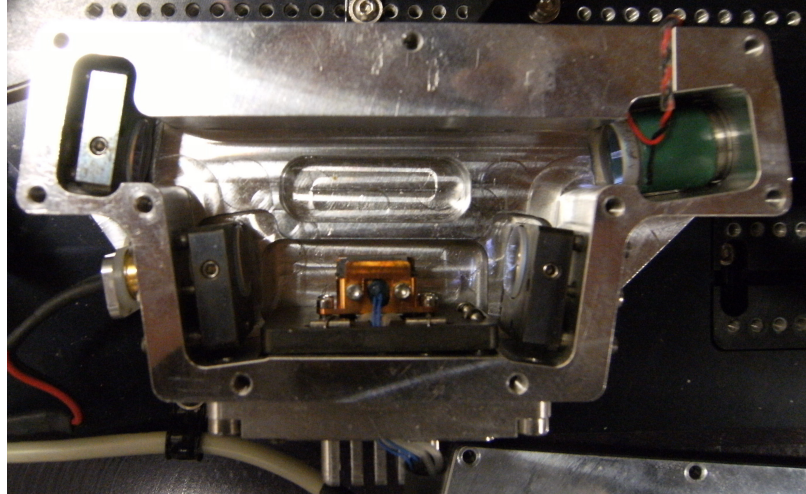


Figure 3.9: Detail of the resonant frequency doubling cavity. The four mirrors of the “bowtie” cavity are visible, and the doubling crystal is mounted in the small metallic temperature-stabilized platform between the lower two mirrors.

and verifies the frequency by querying the wavemeter before and after each data point is collected from the photon counter. For measurements at fixed frequency, or where the frequency is adjusted smoothly, a reference function (laser frequency as a function of time) is programmed into the wavemeter interface for PID feedback and similarly verified by online measurements as photon counting data is collected. With optimal PID settings, the measured frequency fluctuates by approximately 0.5 MHz when the reference function is a constant.

The two-photon probe laser is a cw Ti:sapphire oscillator (Coherent MBR-110), which is externally stabilized by a reference cavity and internally tunable via the error signal generated from an intracavity etalon. Under optimal operating conditions, the Ti:sapphire can supply 4 W at 808 nm, with sub-MHz linewidth and the ability to automatically scan the laser frequency over a specified range by tuning the reference cavity. In principle the wavemeter can simultaneously monitor several lasers by coupling them through an optical fiber switcher, but the loss in frequency resolution is considerable (a factor of five to ten). This is due to the duty cycle of the fiber switcher, and to the large-core fiber that is required to efficiently couple widely separated wavelengths through the same device. It is possible to simultaneously measure the frequencies from both lasers with the wavemeter, and to provide a control signal to one or both of them – but we found that in practice it is much more useful to scan the probe laser scan independently (without feedback from the wavemeter).

The liquid crystal variable waveplate is a transmissive optical element whose birefringence is adjustable by changing the amplitude of a 2 kHz square wave applied to it. When

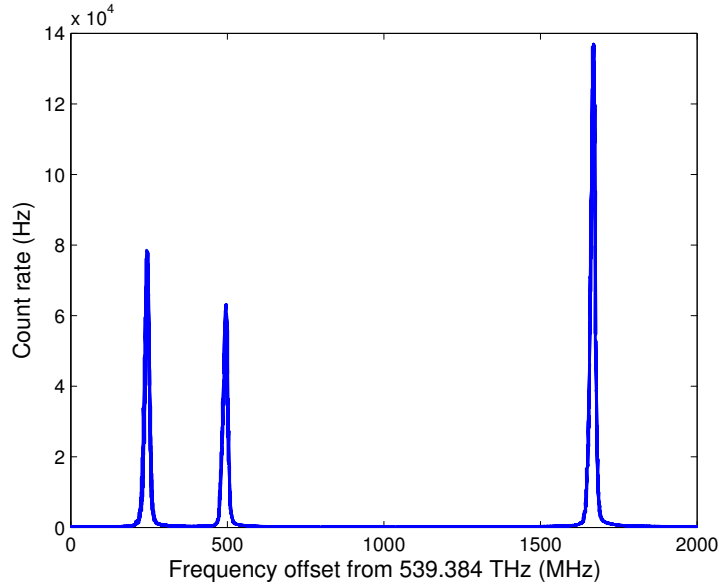


Figure 3.10: Typical fluorescence spectrum at 539.384 THz (~ 556 nm) as a function of probe frequency, showing resonance lines (from left to right) of ^{173}Yb , ^{171}Yb , and ^{176}Yb . Their relative spacing is due to hyperfine and isotope shifts.

the voltage is low the liquid crystal molecules have a preferred axis that is defined by an alignment layer on the substrates that confine them. The preferred axis at zero voltage is in the plane of the optical surface, so the birefringence (and thus retardance) is maximal when no voltage is applied. As the drive amplitude increases, the crystal axis is tilted into alignment with the surface normal and the retardance is reduced. At a drive amplitude of 25 V, the crystal saturates and the molecules (except those in contact with the alignment layer) are perfectly aligned with the optic axis; in this case birefringence disappears. A measured retardance curve for the device at 556 nm is shown in figure 3.11; although the coating is designed for near-infrared wavelengths, the transmission is quite high at 556 nm and we needed only to recalibrate the retardance curve.

The waveplate can be switched between two different drive amplitudes at a modulation frequency of up to 150 Hz, and a slew rate of 10 V/ms. When the crystal axis is oriented at 45° relative to an incident linear polarization, this allows us to switch between a $\frac{\lambda}{4}$ plate and a $\frac{3\lambda}{4}$ plate configuration, so that the transmitted polarization switches between $\hat{\sigma}^+$ and $\hat{\sigma}^-$ when the atomic quantization axis is aligned with the optical wave vector. Since this is done without physically moving any optics, the effect is highly reproducible and allows phase-sensitivity in the detection of optical pumping signals with polarization-modulated pump light.

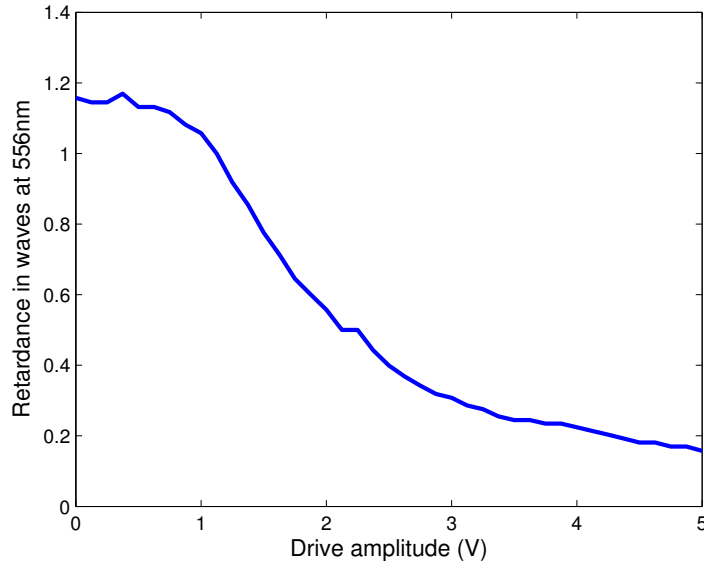


Figure 3.11: Measured retardance curve for liquid crystal variable waveplate at $\lambda = 556$ nm. The vertical axis shows the relative delay in wavelengths between linear polarization components along the fast and slow axes, i.e. $d\Delta n/\lambda$ where d is the waveplate thickness, Δn is the difference in index of refraction between the fast and slow axes, and λ is the wavelength. At drive voltages of 3.375 V and 1.5 V, the waveplate functions respectively as a quarter-wave plate and a three-quarter-wave plate. By switching between these values with a linearly polarized input beam, the sense of pump polarization can be changed from $\hat{\sigma}^-$ to $\hat{\sigma}^+$ without moving any optics.

3.2 Optical Pumping (One-Photon Transitions)

The simplest interesting experiment that can be done with the atomic beam is to produce and then measure static nuclear spin polarization using an E1 transition. The “green” 556 nm intercombination line is a natural starting place for both of these steps, since it is a good compromise between the strong transition from $6s^2\ ^1S_0$ to $6s6p\ ^1P_1$ and the weak two-photon transition to $5d6s\ ^3D_2$. The spin-orbit interaction that couples different eigenstates of **S** also serves as an analogue for the hyperfine interaction, which couples different eigenstates of **I**. (In each case, the interaction mixes eigenstates of a spin quantum number that are not directly coupled by the electric dipole operator.) The green transition thus serves as a baseline for the subsequent studies of two-photon excitation, and in fact measurements of this type revealed several limitations of the apparatus. These limitations include polarization losses on the original angled pump windows, and inhomogeneities of the applied magnetic field due to geometrical constraints within the chamber. These were respectively resolved by installing the normal-incidence adapters shown in figures 3.3 and 3.4, and by

applying a very homogeneous magnetic field with large externally mounted coils (see figures 3.3 and 3.13).

For these “one-photon” pump/probe experiments, both the pump and the probe beam are resonant with the 556 nm transition. The atoms interact first with a relatively intense pump beam, which propagates along the magnetic field axis and perpendicular to the mean atomic velocity vector. We can therefore produce any pump polarization that can be expressed as a superposition of $\hat{\sigma}^-$ and $\hat{\sigma}^+$; since we choose the quantization axis to be parallel with both the optical the wave vector and the magnetic field axis, there can be no $\hat{\pi}$ component. If the atoms are optically pumped into the $m_F = +\frac{1}{2}$ ground state and the field does not change too rapidly in their moving reference frame, then the atomic polarization adiabatically follows the magnetic field and the atoms remain polarized state until they are probed. Note that the 3P_1 excited state has a radiative lifetime of less than $1 \mu\text{s}$, which is approximately $1/250$ of the mean time of flight between the locations of the pump and probe beams. Thus, fluorescence due to the pump beam is completely negligible in the probe region.

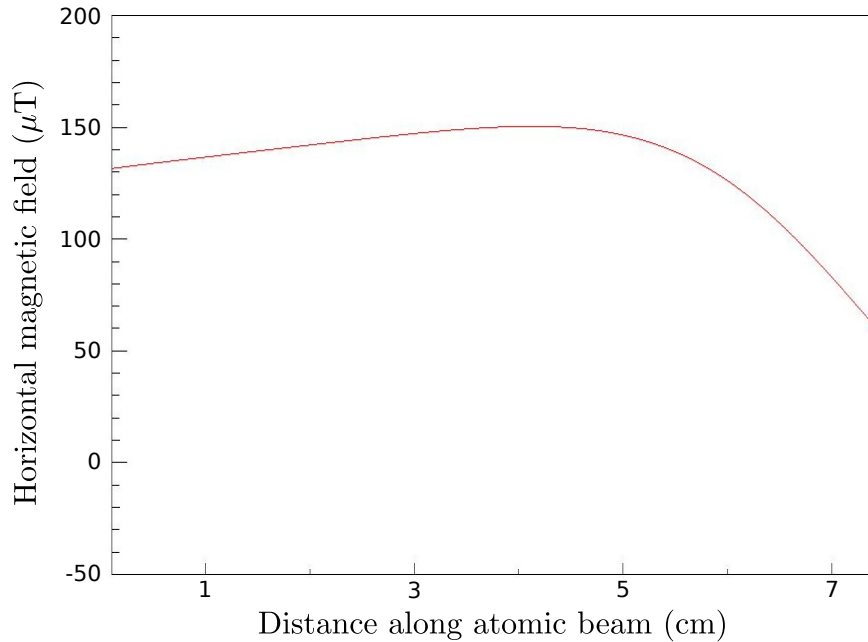


Figure 3.12: Magnetic field strength in the region between the pump beam (left limit) and the probe beam (right limit), calculated from a numerical model of the internal coils. Note that the field strength changes by roughly 50% between 5 cm and 7 cm (i.e., in $\sim 70 \mu\text{s}$ for an atom in the beam). The calculated field corresponds to 15 amp-turns applied to the coils shown in figure 3.7.

The field produced by the coils shown in figure 3.7 is actually quite inhomogeneous (see figure 3.12), in direction as well as magnitude. A characteristic timescale that defines the

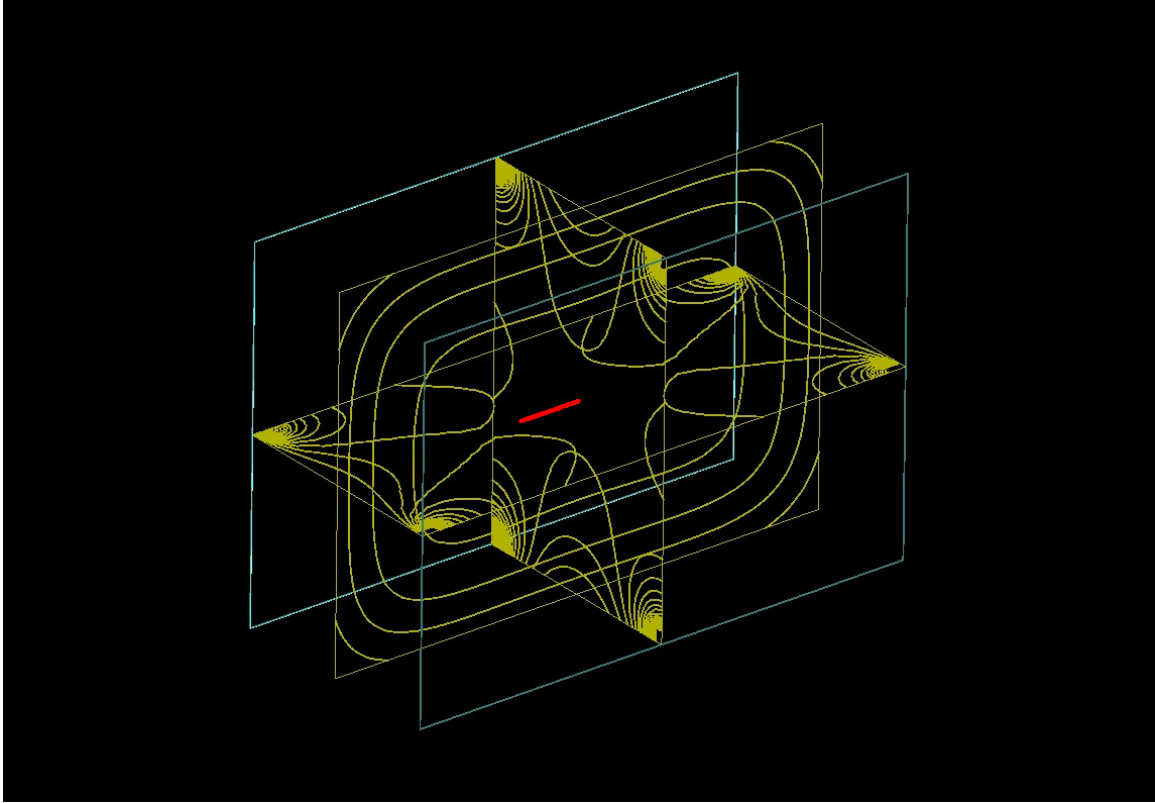


Figure 3.13: Calculated contours of magnetic field strength in the region around the atomic beam, which is represented by the red line. The field is produced by external coils visible in figure 3.3, shown here in blue. Field lines in each plane are spaced by $50 \mu\text{T}$.

adiabaticity criterion for the atoms is the Larmor precession period, which for the ground state of ^{171}Yb is $\sim 267 \text{ ns}$ in a 1 T magnetic field. We are concerned with fields of order 1 mT , and therefore with changes on a timescale of $\sim 267 \mu\text{s}$, which is comparable to the time of flight across the region where the field is changing. If the field changes by a significant fraction of 1 mT between the pump and probe regions, the spins may not be transported adiabatically. Indeed, numerical simulations of the magnetic field produced by the coils shown in figure 3.7 suggest that adiabaticity may be violated for moderate applied currents (see figure 3.12).

The spatial inhomogeneity of the magnetic field together with the use of narrow linewidth lasers also has an important consequence for these experiments, namely that in the pump and probe regions the Zeeman splittings are different by considerably more than the laser linewidth. Since both beams are produced by the same laser, we must then either detect an off-resonant interaction, or find some way of shifting the relative frequencies of the pump and probe beams to compensate for the difference in resonance frequencies. It turns out that the off-resonant interaction *is* detectable (see figure 3.14), although we could

also envision using acousto-optic modulators to shift a component of the laser light by the small frequency difference required to compensate for the shifted resonance.

We can understand this situation by realizing that the linewidth of the atomic transitions is dominated by residual Doppler broadening. Interaction with the pump and probe beams does not significantly affect the atomic velocity, since the momentum of a thermal atom (~ 40 au) is significantly larger than the recoil from absorbing or emitting a 556 nm photon ($\sim 6 \times 10^{-3}$ au). This decoupling of motional and internal states means that an atom whose resonance is Doppler-shifted by $\delta\omega$ from the central absorption resonance of the $m_F = \pm\frac{1}{2}$ ground state will have its new resonance shifted by the *same amount* from the central absorption resonance of the $m_F = \mp\frac{1}{2}$ ground state after being optically pumped by $\hat{\sigma}^\mp$ radiation. That is, independent of the value of $\delta\omega$, after optical pumping the atom's new resonance frequency will be shifted by the ground state Zeeman splitting $g_F\mu_N B$ from the original resonance frequency, (i.e., by a few MHz).

Unfortunately this means that when the Zeeman splitting exceeds the laser linewidth, an atom which was resonant with the pump beam will not be resonant with the probe beam, and vice versa. Detecting optical pumping in this situation requires an off-resonant measurement: we must detect a small change in nuclear spin polarization far away from the resonance frequency where it is most visible. Any signal results from the small but finite probability to absorb photons at large detunings from resonance, or from atoms that were resonantly excited by the weak tails of a narrow laser spectrum. The probability for single-photon absorption in a homogeneously broadened resonance is proportional to a normalized Lorentzian lineshape function

$$L(\delta, \gamma) = \left(\frac{\gamma}{2\pi}\right) \frac{1}{\delta^2 + \left(\frac{\gamma}{2}\right)^2}, \quad (3.6)$$

which falls off as δ^{-2} for $|\delta| \gg |\gamma|$. Estimating the laser linewidth to be ~ 200 kHz, we find that for a Zeeman splitting of a ~ 1 MHz the off-resonant transition probability is already reduced by two orders of magnitude. We must bear this in mind when interpreting the polarization signals in figure 3.14, since the apparent contrast corresponds to at most a few percent of the actual polarization.

This rough estimate indicates that the velocity class which is resonant with the pump beam is close to fully polarized, and remains so in the probe region. The small modulation depth of the signals in figure 3.14 (0.5%-1%) therefore results from a small overlap of the probe field spectrum with the resonance frequencies of the polarized atoms, not from low nuclear polarization. We have thus demonstrated that highly efficient detection is not required to observe nuclear spin polarization in a relatively weak E1 transition; the require-

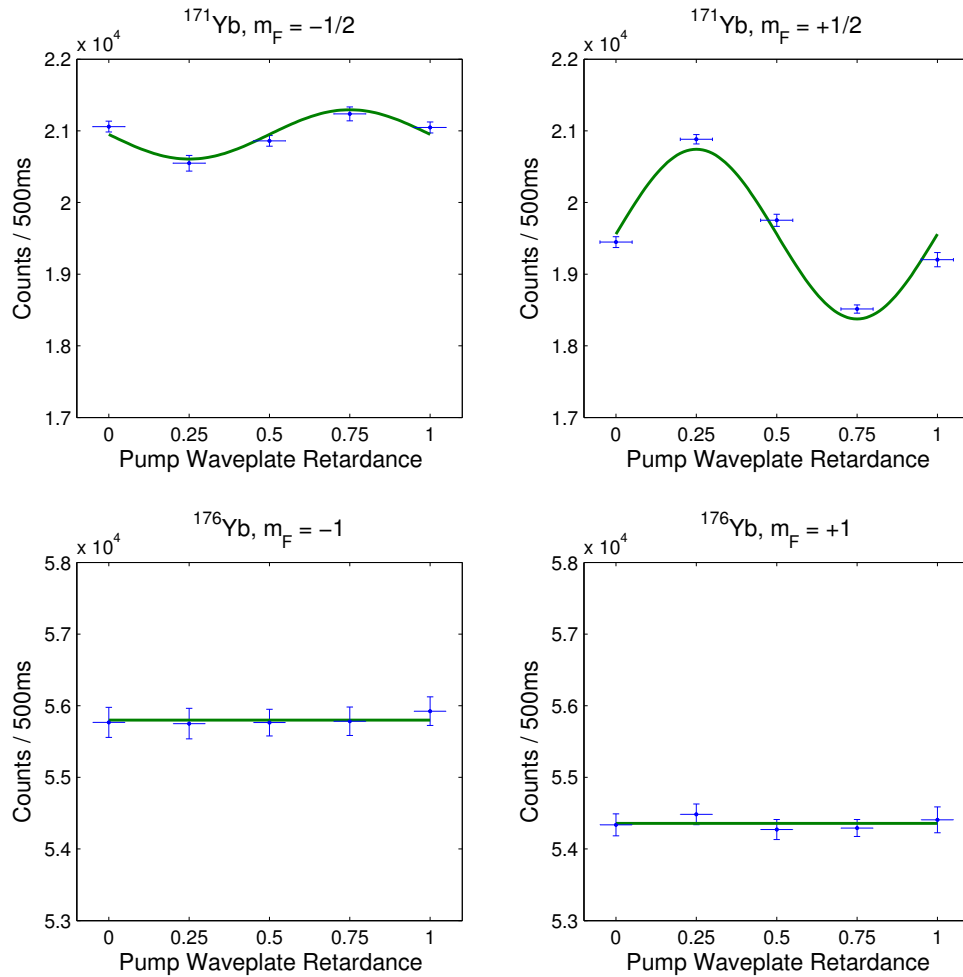


Figure 3.14: The upper two figures show the off-resonance effect of 556 nm optical pumping with various light polarizations on ^{171}Yb , as measured with a fixed probe polarization. The amplitude of the sinusoidal fit corresponds to the degree of measurable ground-state nuclear spin polarization. The bottom two figures show the same measurement performed on ^{176}Yb , which has no nuclear spin and therefore cannot be polarized in the $J=0$ ($F=0$) electronic ground state. The lack of a polarization signal in the $I=0$ isotopes provides an important systematic check in the two-photon case; in this case the fit function is a constant. (Note that for two-photon excitation there are significant qualitative differences in the Zeeman spectra of isotopes with and without nuclear spin. This phenomenon is illustrated in figure 3.19.)

ment to detect a small signal obscured by a large background is also characteristic of the two-photon experiments discussed later in this chapter.

3.2.1 Zeeman Splittings in a Homogeneous Field

In order to improve the detection contrast for ground state nuclear polarization, the internal field coils were replaced with large coils outside the vacuum chamber that produce a considerably more homogeneous field (see figures 3.3 and 3.13). This modification also provided the opportunity to quantitatively study the excited state Zeeman structure, and to perform basic measurements of the applied field strength (see figure 3.15). This was a crucial step towards studying polarization sensitivity using a the two-photon transition, since optimal contrast requires optical pumping at frequencies corresponding to velocity classes that are resonantly detected by the two-photon probe.

For the ^{171}Yb $F = \frac{1}{2} \rightarrow F' = \frac{1}{2}$ transition, only two Zeeman sublevels exist in the excited state. (Ground state Zeeman splitting is not resolved in the spectra presented here, since it arises due to a nuclear magnetic moment that is ~ 1800 times smaller than the excited state electronic magnetic moment.) When they are probed with equal efficiency, as for linear polarization, we can model the lineshape as

$$f_1(\omega) = A + \frac{B}{1 + \left(\frac{2\omega - 2\omega_0 + \Delta}{2\gamma}\right)^2} + \frac{B}{1 + \left(\frac{2\omega - 2\omega_0 - \Delta}{2\gamma}\right)^2}, \quad (3.7)$$

which is used as a fit function for the data shown in figure 3.15. The parameter values resulting from the fit lines shown in figure 3.15 are recorded in table 3.2. Note that the true lineshape for each transition is not a Lorentzian (due to residual Doppler broadening), but in the region of the spectrum near the peaks this lineshape is a quite reasonable approximation. Farther from resonance, it would be necessary to take more careful account of Doppler broadening in order to model the tails of the distribution.

When the atoms are optically pumped, or the probe polarization is not perfectly linear, the spectral peaks corresponding to $m'_F = \pm \frac{1}{2}$ have different amplitudes due to the modified scattering rates for $\hat{\sigma}^-$ and $\hat{\sigma}^+$ radiation. This is precisely the type of modulation that needs to be detected for a two-photon magnetometer, and it is therefore important to be able to distinguish the effect of imperfect probe polarization from that of optical pumping. A fit function appropriate to this task is

$$f_2(\omega) = A + \frac{B}{1 + \left(\frac{2\omega - 2\omega_0 + \Delta}{2\gamma}\right)^2} + \frac{(1 + \varepsilon)B}{1 + \left(\frac{2\omega - 2\omega_0 - \Delta}{2\gamma}\right)^2}, \quad (3.8)$$

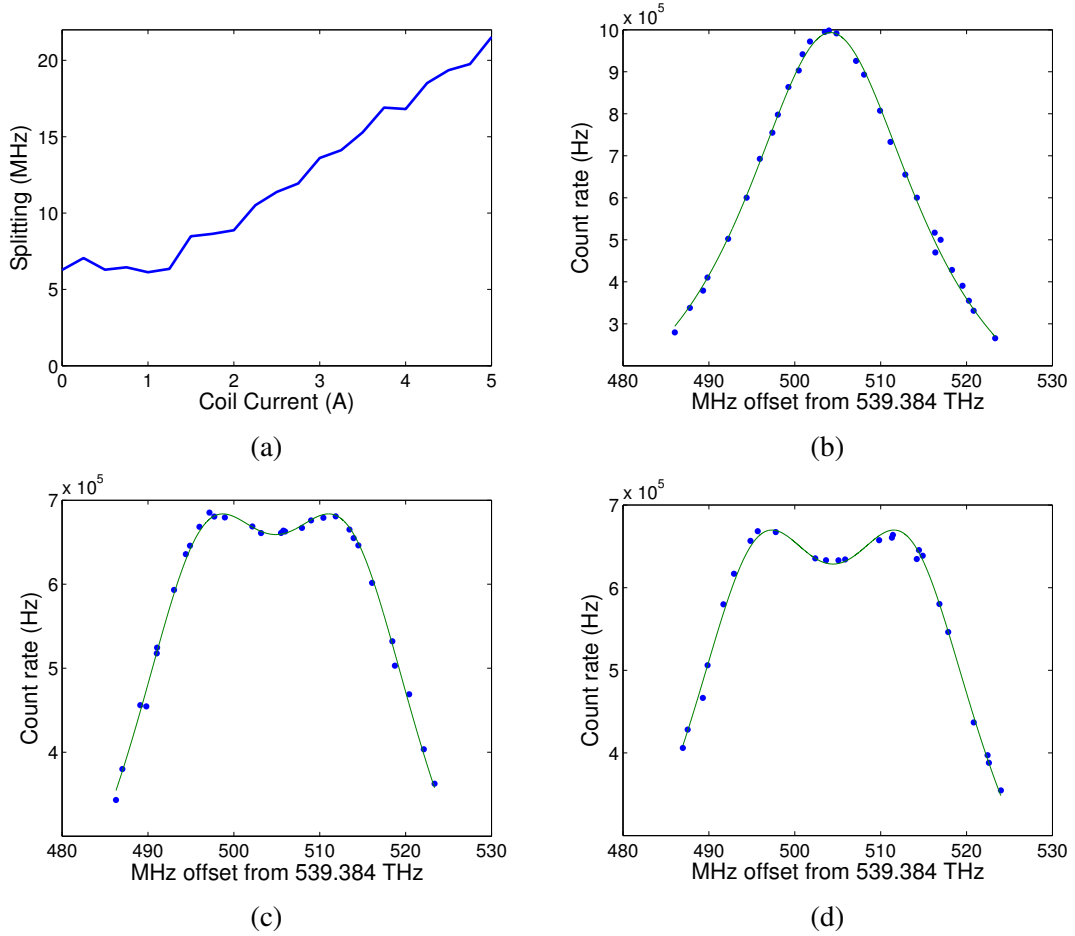
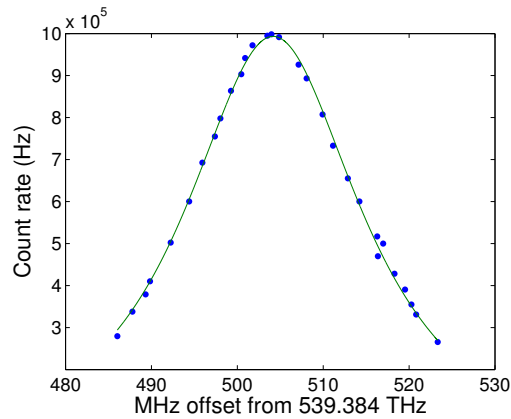
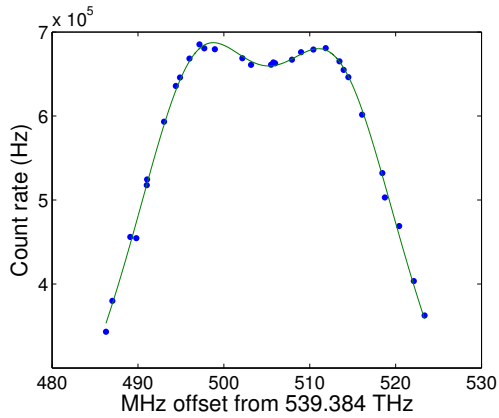


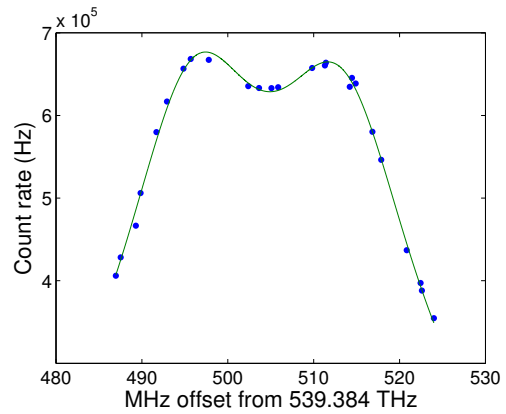
Figure 3.15: Zeeman splittings measured in a homogeneous external field. (a) Frequency splitting between the $m'_F = \pm \frac{1}{2}$ sublevels of $|^3P_1, F' = \frac{1}{2}\rangle$ as a function of coil current, measured by fitting a range of spectra like those shown in (b)-(d). The transition is probed with linear $\hat{\sigma}$ -polarized light, such that both peaks can be observed in the same dataset. The Zeeman splitting is extracted via a fit (see table 3.2) to the sum of two Lorentzian functions and a constant background (equation 3.7). The fit determines the individual line centers and the center of gravity. The two resonance peaks are constrained by the fit to have the same amplitudes and widths; see figure 3.16 for an alternative analysis with an additional free parameter. (b) Corresponds to the case of no applied field (and therefore no measurable splitting), while (c) and (d) illustrate the effect of slightly different applied fields on the measured spectra.



(a)



(b)



(c)

Figure 3.16: The same data sets shown in figure 3.15(b)-(d), now analyzed with the fit function equation 3.8. In this case the two peaks are allowed to have different amplitudes, which accommodates asymmetries due to optical pumping or elliptical probe polarization. See table 3.3 for the fit parameters; most of these agree well with the values in table 3.2. The most notable difference is in figure (c), which has a noticeable asymmetry of approximately 2% between the left- and right-hand peaks. Asymmetries of this magnitude correspond to a fraction of a degree in the alignment of the probe waveplate, and must be characterized in detail for optical pumping and magnetometry.

Sub-figure	A (Hz)	B (Hz)	Δ (MHz)	ω_0 (MHz)	2γ (MHz)
(b)	-4.9×10^4	9.93×10^5	2×10^{-3}	504.2	25.4
(c)	-1.6×10^4	6.69×10^5	16.9	504.9	22.9
(d)	3.4×10^4	6.60×10^5	17.7	504.4	21.9

Table 3.2: Fit parameters for the data shown in figure 3.15 (b)-(d). The fit constants are defined by the function $f_1(\omega)$ given in equation 3.7.

Sub-figure	A (Hz)	B (Hz)	ε	Δ (MHz)	ω_0 (MHz)	2γ (MHz)
(a)	-4.9×10^4	9.93×10^5	3×10^{-9}	2×10^{-3}	504.2	25.4
(b)	-2.0×10^4	6.73×10^5	1.3×10^{-2}	16.9	505.0	23.0
(c)	-3.3×10^4	6.68×10^5	2.0×10^{-2}	17.7	504.6	21.9

Table 3.3: Fit parameters for the data shown in figure 3.16 (a)-(c). The fit constants are defined by the function $f_2(\omega)$ given in equation 3.8.

and figure 3.16 shows the result of this fit applied to the same data that are shown in figure 3.15. The fit parameters for these data with the asymmetric fit function $f_2(\omega)$ are recorded in table 3.3, and the values for the fit parameters other than ε are largely consistent with the result of the “equal-amplitudes” fit to $f_1(\omega)$.

An asymmetry of approximately 2% is visible in figure 3.16(c), and confirmed by the fit to $f_2(\omega)$. Since no optical pumping was applied for these datasets (and the thermal Boltzmann polarization is many orders of magnitude smaller than the observed asymmetry), we can conclude that this is due to imperfect probe polarization. This asymmetry corresponds to a misalignment of a waveplate axis by considerably less than a degree; such a level of detection sensitivity is important for two-photon experiments where the signature of optical pumping may be considerably weaker, but also imposes stringent requirements on the alignment and stability of optical components.

We now turn our attention to similar studies using the 808 nm two-photon transition, and discuss the differences in apparatus and data analysis required to perform measurements of comparable precision.

3.3 Two-Photon Spectroscopy

Figure 3.17 shows fluorescence spectra recorded at 556 nm, following excitation of ^{174}Yb and ^{171}Yb using 808 nm cw radiation from a Coherent MBR-110 Ti:sapphire laser (see figure 3.5). These data show the effect of different probe polarizations and a relatively large applied magnetic field; the ^{171}Yb transition overlaps somewhat with various components of the ^{174}Yb transition, but the peaks are reasonably well separated when the probe polarization is $\hat{\sigma}^-$ or $\hat{\sigma}^+$ (red and green data series). The ^{171}Yb transition shown in figure 3.17 is the $F = \frac{1}{2} \rightarrow F'' = \frac{3}{2}$ hyperfine component, which is the transition relevant for two-photon magnetometry. This is the experimental configuration used in attempts to measure the effect of optical pumping on the two-photon scattering rate; leading up to that, we now discuss how the effects of probe polarization and Zeeman shifts can be disentangled for other probe polarizations and weaker magnetic fields.

An important feature of two-photon excitation is that selection rules occur which have no analogy in the single-photon case; these include the ‘‘Landau-Yang’’ selection rule that two-photon excitation with a total angular momentum change of unity is only possible with two photons of differing frequency and polarization [78]. For degenerate photons, only $|\Delta F| = 0, 2$ are therefore possible. In the case of linear $\hat{\sigma}$ polarization, which states can be excited depends on the multiplicity of the ground and excited state magnetic sub-levels: some levels may be inaccessible because they can only be reached via a $\Delta m_F = \pm 1$ transition, which cannot satisfy angular momentum conservation unless a photon with $\hat{\pi}$ polarization is involved. (Again, we ignore the possibility of $\hat{\pi}$ polarization in the probe beam, due to the alignment of the beam and magnetic field axes.)

This circumstance introduces a qualitative difference in the two-photon spectra of ytterbium isotopes with and without nuclear spin (see figure 3.19): those having a (total) spin zero ground state will have states ‘‘missing’’ from the distribution of observed lines. In the isotopes with finite nuclear spin, every excited state can be reached from some ground state by some combination of $\hat{\sigma}^-$ and $\hat{\sigma}^+$ polarizations, but the observed line strengths depend on the angular momentum coupling coefficients and the multiplicity of allowed excitation pathways. This makes it intuitively clear that the peak signal will be highest for $\hat{\sigma}^-$ or $\hat{\sigma}^+$ polarization, where the number of allowed Zeeman transitions is minimized – as experimentally verified in figure 3.17. This is because a larger fraction of the probe field is coherently driving the *same* resonance, rather than a lower amplitude of each polarization being split among several different resonances – adding atoms is not the same as adding photons. In some sense, this is the essential feature of nonlinear optics.

Sub-figure	A_0 (Hz)	A_1 (Hz)	A_2 (Hz)	A_3 (Hz)	ω_0 (MHz)	Δ (MHz)	2γ (MHz)
(a)	-2.5	165	156	131	604.9	16.6	9.5
(b)	-6.8	145	134	136	604.4	16.6	10.5
(c)	-5.5	128	142	167	604.3	16.4	9.7

Table 3.4: Fit parameters for the data shown in figure 3.18 (a)-(c). The fit constants are defined by the function $g(\omega)$ given in equation 3.9.

3.3.1 Probe Polarization and Allowed Transitions

Figure 3.18 shows a series of measurements using ^{172}Yb , which has no nuclear spin and therefore cannot be optically pumped. These data are used similarly to those presented in figures 3.15 and 3.16, to quantify the effects of slightly imperfect linear probe polarization on the fluorescence spectra that result from two-photon excitation. Due to angular momentum conservation, not all of the excited state magnetic sublevels can be probed with $\hat{\sigma}$ polarized light. The peaks in the fluorescence spectra of figure 3.18 correspond (from left to right) to $m''_j = -2, 0, 2$. Note that $m''_j = -2$ can only be excited by the $\hat{\sigma}^-$ component of the probe field, $m''_j = +2$ can only be excited by the $\hat{\sigma}^+$ component, and $m''_j = 0$ requires a contribution from both (allowed excitation channels are diagrammed in figure 3.19).

The ^{172}Yb spectra therefore provide a sensitive means of characterizing Zeeman shifts and effects due to probe polarization in the two-photon transition, which is a critical baseline for measurements of ^{171}Yb in which optical pumping can play a role (and which is the most useful test system for two-photon magnetometry). The fit function used for these spectra is

$$g(\omega) = A_0 + \frac{A_1}{1 + \left(\frac{\omega - \omega_0 - \Delta}{\gamma}\right)^2} + \frac{A_2}{1 + \left(\frac{\omega - \omega_0}{\gamma}\right)^2} + \frac{A_3}{1 + \left(\frac{\omega - \omega_0 + \Delta}{\gamma}\right)^2}, \quad (3.9)$$

where each term is allowed to have an independent amplitude but the widths are all the same. We could further constrain the A_2 to be a fixed linear combination of A_1 and A_3 , but leaving it independent allows us to characterize the degree to which $\hat{\pi}$ transitions occur due to pointing errors of the probe beam. Parameter values extracted from these fits are recorded in table 3.4. Note that we are able to plot an extrapolated fluorescence curve for any of the three allowed transitions by setting the amplitude parameters for the other two transitions equal to zero.

The observed Zeeman splitting in figure 3.18 is between the $m'_F = 0, \pm 2$ sublevels of the 3D_2 state; this splitting can be calibrated by the known Landé g -factor, and the relative amplitudes of the three sub-peaks are determined by Clebsch-Gordan coefficients and the

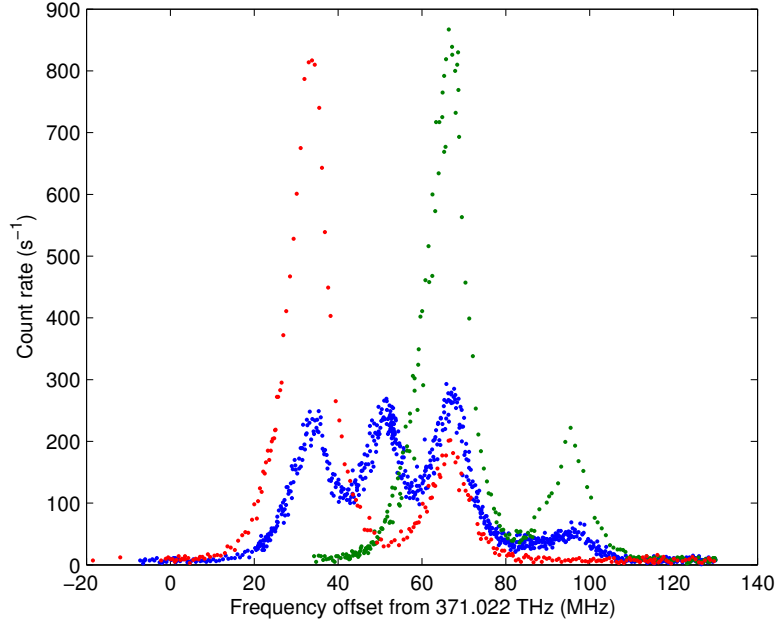


Figure 3.17: Raw data showing two-photon excitation of ^{174}Yb and the $F = \frac{1}{2} \rightarrow F'' = \frac{3}{2}$ hyperfine transition in ^{171}Yb , in a 1 mT magnetic field. **Blue:** A linearly polarized probe excites all allowed transitions in both isotopes (see figure 3.19). **Red:** A $\hat{\sigma}^-$ probe excites only $m_J = 0 \rightarrow m''_J = -2$ in ^{174}Yb and $m_F = +\frac{1}{2} \rightarrow m''_F = -\frac{3}{2}$ in ^{171}Yb . **Green:** A $\hat{\sigma}^+$ probe excites only $m_J = 0 \rightarrow m'_J = +2$ in ^{174}Yb and $m_F = -\frac{1}{2} \rightarrow m''_F = +\frac{3}{2}$ in ^{171}Yb . For each isotope the excited state Zeeman structure is clearly resolved, but note that at this magnetic field strength the peak for ^{171}Yb , $m''_F = -\frac{3}{2}$ overlaps with the one for ^{174}Yb , $m''_F = +2$. The relative line strengths (in the absence of optical pumping) are determined by the Clebsch-Gordan coefficients for each transition; these in turn are observed more or less efficiently according to the square of the optical intensity that satisfies the corresponding selection rules.

probe polarization. When the probe beam is weighted slightly towards $\hat{\sigma}^-$, the $m'_F = -2$ sublevel is probed more efficiently and we observe a slightly higher peak than for $m'_F = -2$; if instead the probe is weighted towards $\hat{\sigma}^+$, then the opposite situation obtains. Fits to this data provide a quantitative indication of how well the probe polarization must be known to identify a nuclear polarization signal of a given size.

3.3.2 Analysis of Overlapping Resonance Lines

The radiative lifetime of the 3D_2 state is roughly half that of the 3P_1 state, with the result that a Lorentzian function is an even better approximation than in the one-photon case. We now discuss the extraction of fit parameters when several resonance lines corresponding to different isotopes overlap, and the magnetic field and probe polarization are not adjusted

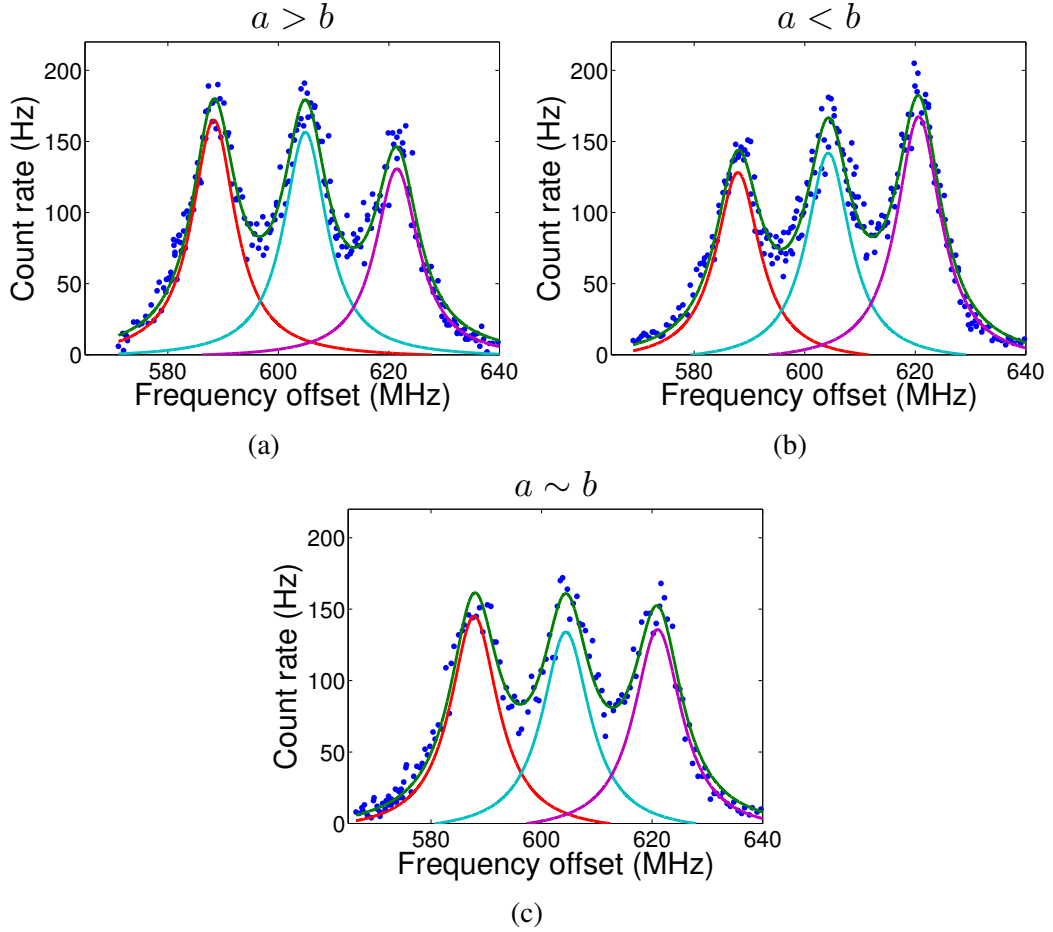


Figure 3.18: Zeeman structure of the $^{172}\text{Yb } 5d6s \ ^3D_2$ state in a magnetic field, where the probe polarization is $\hat{\epsilon} = a\hat{\sigma}^- + b\hat{\sigma}^+$: (a) nearly linear probe polarization with $a \gtrsim b$, (b) pure linear probe polarization ($a = b$ within experimental limitations), (c) nearly linear probe polarization with $a \lesssim b$. Only three of the five 3D_2 magnetic sublevels are excited, since angular momentum conservation cannot be satisfied for a $\Delta m = \pm 1$ transition where two circularly polarized photons are absorbed. When the probe polarization has no $\hat{\pi}$ component, there is no two-photon E1 amplitude that connects the state $m_J = 0$ with any of $m'_J = 0$ or $m'_J = \pm 1$ (see figure 3.19). Since the even isotopes of ytterbium have no nuclear spin, these spectra provide a reference baseline in which optical pumping has no effect on the ground state. As such, they are a sensitive means of calibrating the effects of imperfect probe polarization. Green lines show a fit to the function $g(\omega)$ defined in equation 3.9 (see table 3.4 for the fit parameters). Red lines show the $m_F'' = -2$ component, i.e. $g(\omega)|_{A_2=A_3=0}$. Blue lines show the $m_F'' = 0$ component, i.e. $g(\omega)|_{A_1=A_3=0}$. Pink lines show the $m_F'' = +2$ component, i.e. $g(\omega)|_{A_1=A_2=0}$. The horizontal-axis frequency offset is measured with respect to 371.022 THz.

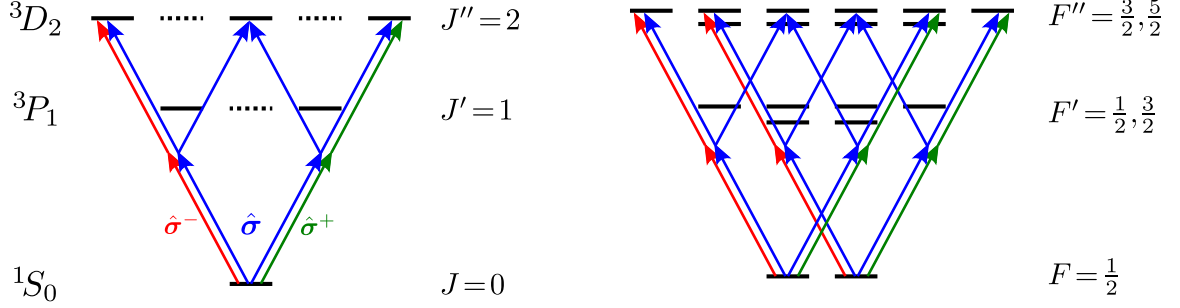


Figure 3.19: Two-photon excitation pathways in ytterbium from $6s^2 \ ^1S_0 \rightarrow 5d6s \ ^3D_2$ with light propagating along the quantization axis, in isotopes with (right) and without (left) nuclear spin. The transition can be driven driven by $\hat{\sigma}^-$ (red) or $\hat{\sigma}^+$ (green) polarization, or any superposition of the two – such as the linear polarization $\hat{\sigma} = (\hat{\sigma}^- + \hat{\sigma}^+)/\sqrt{2}$ shown in blue – but the polarization determines which Zeeman states can participate, through selection rules resulting from conservation of angular momentum. In the $I = 0$ isotope shown at left, the levels which do not participate in any of these pathways are dashed; to involve these requires a finite component of $\hat{\pi}$ polarization, which is impossible when the probe wave vector is parallel to the quantization axis. Note that all Zeeman sublevels can be involved when the nuclear spin is nonzero, but that each excited sublevel can only be reached from one ground state sublevel.

to isolate one component for each isotope. Figure 3.20 shows fluorescence spectra for the same transitions that are shown in figure 3.17, now with an elliptically polarized probe beam and smaller magnetic field. It is not possible by visual inspection to identify the different excited state Zeeman levels, but this can be accomplished within a certain range of magnetic fields and probe polarizations by using a fit function

$$h(\omega) = g(\omega) + \frac{B_1}{1 + \left(\frac{\omega - \omega'_0 - k\Delta/2}{\gamma'}\right)^2} + \frac{B_2}{1 + \left(\frac{\omega - \omega'_0 + k\Delta/2}{\gamma'}\right)^2}, \quad (3.10)$$

where $g(\omega)$ is given by equation 3.9, and $k = g_F/2g_J \approx 0.6$ is a fixed scaling factor that accounts for the different magnetic moments of the two isotopes. The scaling factor k is calculated a priori from a measured value of g_J for the 3D_2 levels [3] and the various quantum numbers that are coupled by the $F = \frac{1}{2} \rightarrow F'' = \frac{3}{2}$ hyperfine component of the ^{171}Yb transition. We also attempted an analysis using the fit function

Sub-figure	A_0 (Hz)	A_1 (Hz)	A_2 (Hz)	A_3 (Hz)	B_1 (Hz)	B_2 (MHz)	ω_0 (MHz)	$\omega'_0 - k\Delta$ (MHz)	Δ
(a)	19.5	14.2	129	397	2	78	52.6	84.2	10.1
(b)	20.1	143	357	803	0	159	49.7	73.3	14.7

Table 3.5: Fit parameters for the data shown in figure 3.20; the fit constants are defined by the function $h(\omega)$ given in equation 3.10. It should be noted that $\omega'_0 - k\Delta$ (not ω'_0) is the center of gravity for the ^{171}Yb transition, since only the $m_F = +\frac{1}{2}, +\frac{3}{2}$ components are included in the fit.

Sub-figure	A_0 (Hz)	A_1 (Hz)	A_2 (Hz)	A_3 (Hz)	B_1 (Hz)	B_2 (MHz)	ω_0 (MHz)	$\omega'_0 - k\Delta$ (MHz)	Δ
(a)	351	28	91	289	23	46	46.3	84.1	12.9
(b)	354	39	117	327	31	28	47.7	82.3	11.2

Table 3.6: Fit parameters for the data shown in figure 3.21; the fit constants are defined by the function $h(\omega)$ given in equation 3.10. It should be noted that $\omega'_0 - k\Delta$ (not ω'_0) is the center of gravity for the ^{171}Yb transition, since only the $m_F = +\frac{1}{2}, +\frac{3}{2}$ components are included in the fit.

$$\begin{aligned}
j(\omega) = g(\omega) &+ \frac{B_1}{1 + \left(\frac{\omega - \omega'_0 + 3k\Delta/2}{\gamma'}\right)^2} + \frac{B_2}{1 + \left(\frac{\omega - \omega'_0 + k\Delta/2}{\gamma'}\right)^2} \\
&+ \frac{B_3}{1 + \left(\frac{\omega - \omega'_0 - k\Delta/2}{\gamma'}\right)^2} + \frac{B_4}{1 + \left(\frac{\omega - \omega'_0 - 3k\Delta/2}{\gamma'}\right)^2}, \quad (3.11)
\end{aligned}$$

which includes all four excited levels of ^{171}Yb , but the extra degrees of freedom did not result in a better fit. This is because in these data, the contributions from $m_F'' = -\frac{1}{2}, -\frac{3}{2}$ are overwhelmed by the much stronger ^{174}Yb transitions at the same frequencies. We therefore proceed by using $h(\omega)$ to isolate the contribution from ^{171}Yb .

Figure 3.21 shows data obtained in a similar configuration, where a 556 nm pump beam was also applied. Even with normal-incidence windows, the background due to scattered pump light entering the PMT accounts for quite a large fraction of the recorded fluorescence spectrum. Although this background is not polarization-dependent, it does represent a major statistical limitation. No clear difference is apparent between the data sets with $\hat{\sigma}^-$ and $\hat{\sigma}^+$ pump beams, indicating a need to average data from multiple fluorescence spectra in each configuration to reduce the impact of statistical fluctuations.

Even with the pump background mitigated by beam shaping to reduce diffraction, the

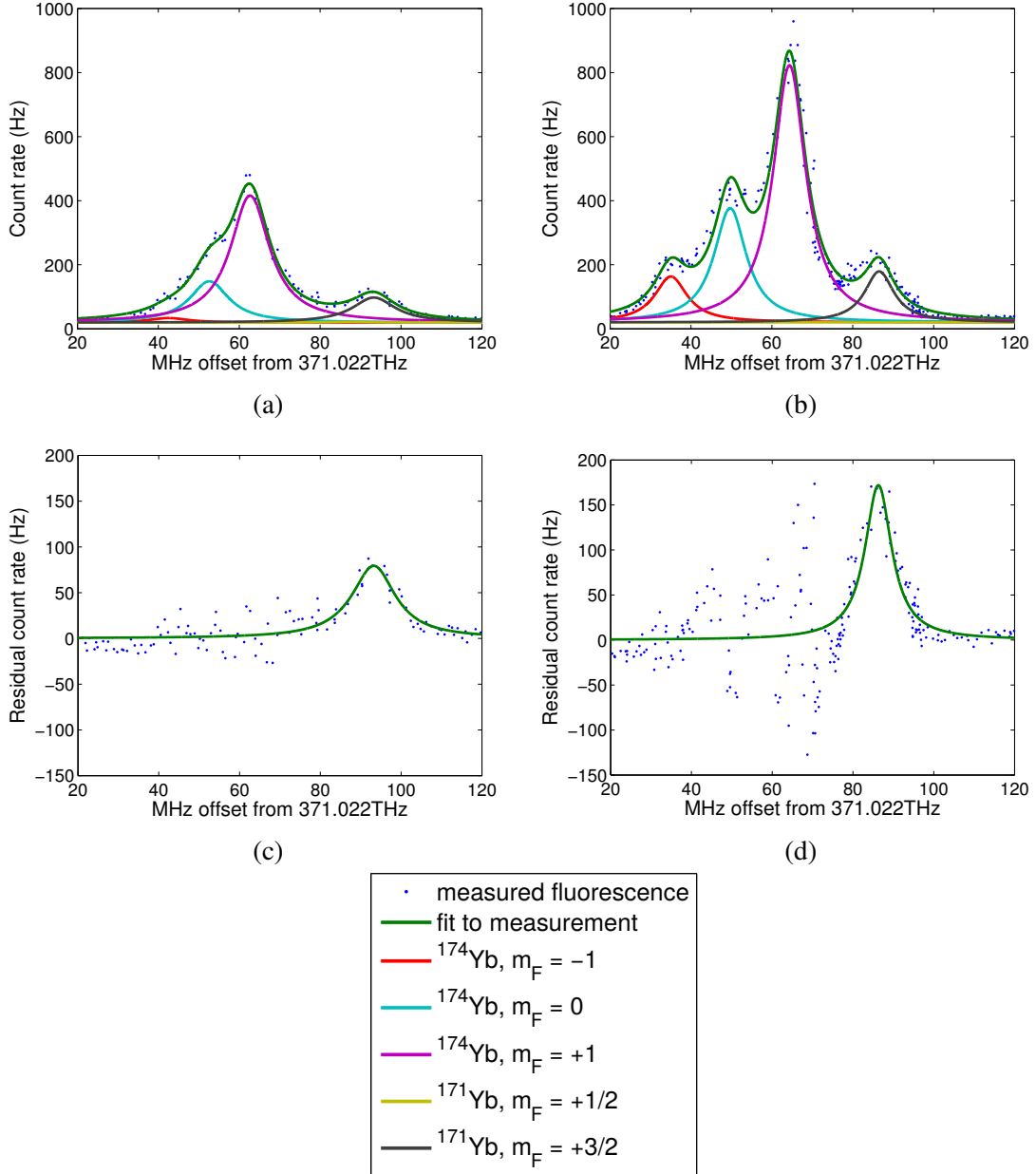


Figure 3.20: The upper figures (a) and (b) show fluorescence spectra in the absence of an optical pumping field, with an arbitrary probe polarization and at two relatively large (different) magnetic field strengths. The signal-to-noise ratio is high enough that the isotopes ^{174}Yb (compound peak between 30 MHz and 70 MHz) and ^{171}Yb (smaller peaks near 90 MHz) can be readily distinguished, and their Zeeman structure analyzed in some detail; the green line represents a fit to the function $h(\omega)$ defined in equation 3.10 (see table 3.5 for the fit parameters). The lower figures (c) and (d) show the same data, with the fit function for the ^{174}Yb peaks subtracted off; the green lines show $h(\omega)$ evaluated with $A_0 = A_1 = A_2 = A_3 = 0$, and the other parameters as in table 3.5.

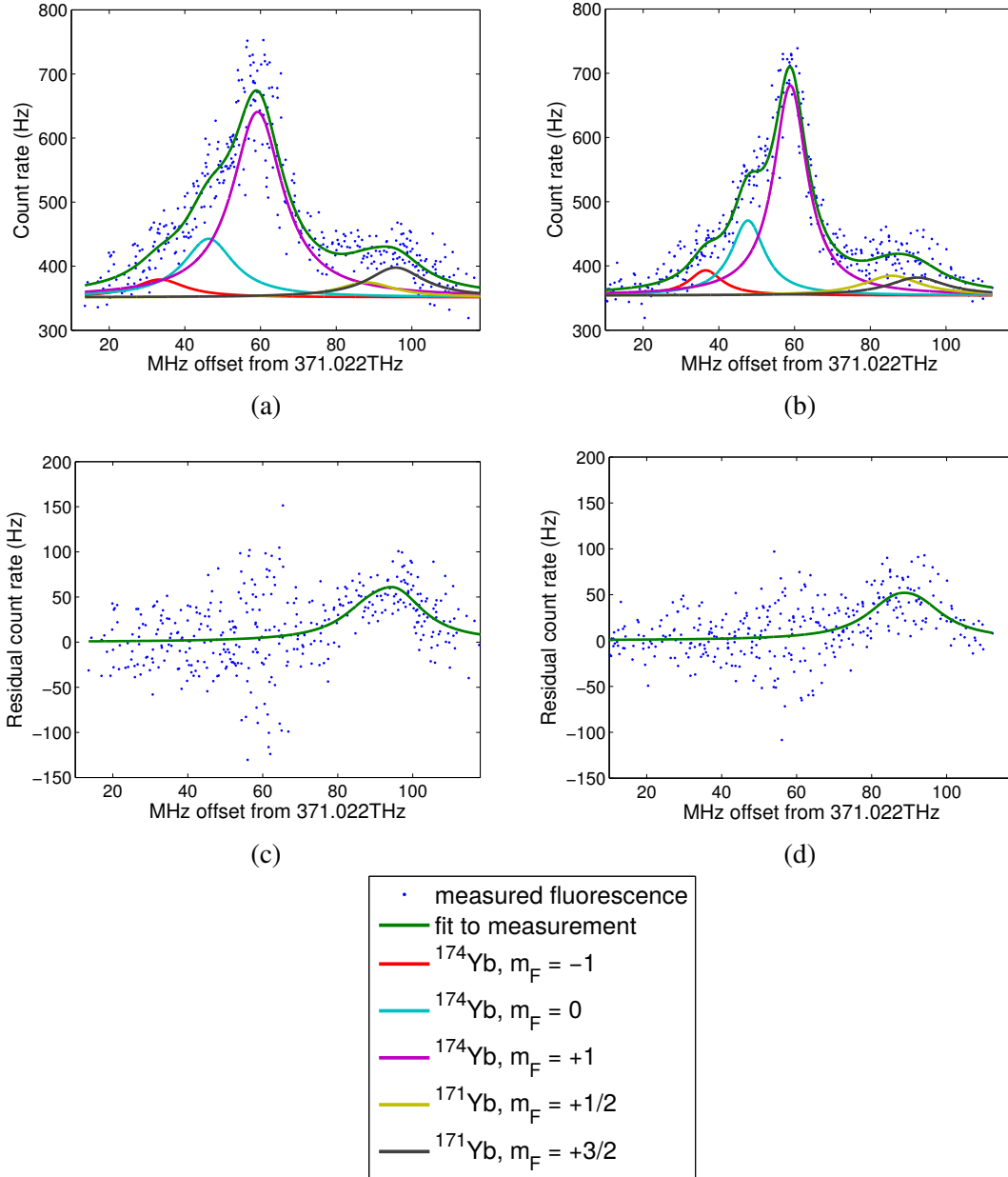


Figure 3.21: The upper figures show fluorescence spectra of ^{174}Yb and ^{171}Yb , with an optical pumping field of (a) $\hat{\sigma}^+$ polarization and (b) $\hat{\sigma}^-$ polarization applied to the atoms before they enter the probe region. The signal-to-noise ratio is considerably worse than in figure 3.20, owing largely to light from the pump beam entering the PMT. The lower figures (c) and (d) show the same data with the contribution from ^{174}Yb subtracted using the fit, as in figure 3.20. Fit parameters are given in table 3.6, according to the function $h(\omega)$ defined in equation 3.10.

available laser power at 808 nm and atomic beam number density result in a relatively low scattering rate. In order to correctly average data from multiple measurements, during and between which statistical fluctuations may be considerable, we take advantage of the nuclear spin zero isotope ^{174}Yb . Since only the isotopes with nuclear spin can be affected by optical pumping, we look for a modulation of the ^{171}Yb fluorescence amplitude that correlates with the pump polarization – normalized to the amplitude of the ^{174}Yb fluorescence that was measured in the same scan. The experiments with ^{172}Yb discussed earlier were critical to the interpretation of these data, since it is necessary to understand the influences of magnetic fields and probe polarization on the fluorescence spectra of a spin zero isotope independently, before effectively using one as a calibration standard.

Another limitation, which we have not yet discussed, is related to the precision with which the laser frequency can be controlled and measured. All of the data for two-photon fluorescence spectra with optical pumping were measured with the wavemeter, at the same time as it was measuring (and stabilizing) the 556 nm pump beam. This reduces the frequency with which each beam can be sampled, and the multimode fiber coupler used to switch between inputs is known to adversely affect the frequency resolution of the device. This complication adds significant frequency uncertainty (of order 5-10 MHz) to the measurement, which can be avoided if one of the lasers is independently measured or stabilized to a separate reference. It is presently unclear if the frequency resolution of the measurement, or the pump beam background, constitutes a more severe limitation.

3.3.3 Nuclear Polarization Dependence

Figure 3.22 shows the result of an attempt to measure nuclear polarization produced by 556 nm optical pumping of ^{171}Yb in the fluorescence spectra of the $F = \frac{1}{2} \rightarrow F' = \frac{3}{2}$ two-photon transition. This required averaging roughly 30 separate scans, with an independent normalization to the ^{174}Yb amplitude for each scan. The signal-to-noise is poor, but the relative positions of the data points for each pump polarization are consistent with nuclear spin polarization – unfortunately, the sign is the opposite of what would be expected given the applied pump polarization. With more data and improved laser stability, we might reasonably expect to see something like the signal shown in figure 3.14.

3.4 Further Thoughts and Improvements

A definitive demonstration of nuclear polarization dependence in the two-photon scattering rate would be radio-frequency quenching of the two-photon polarization signal. An exper-

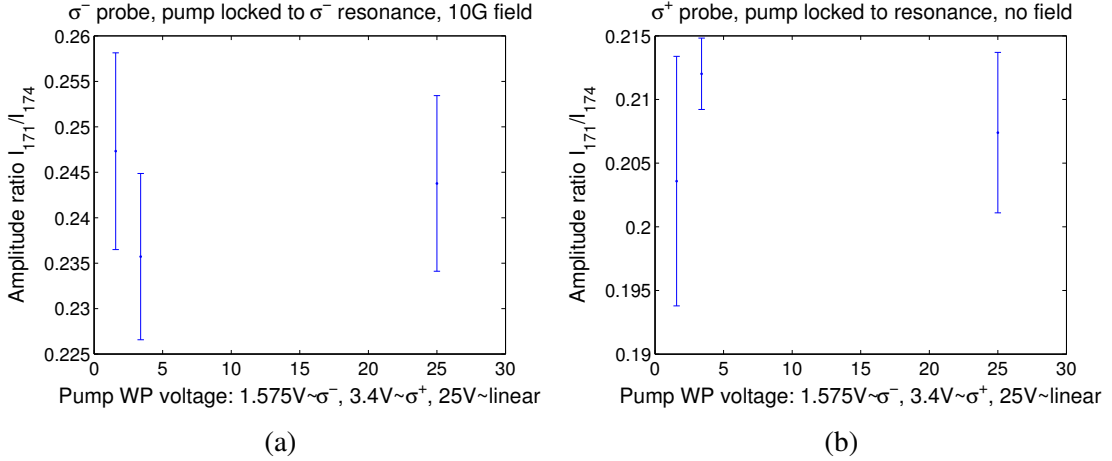


Figure 3.22: Normalized amplitude of the ^{171}Yb $F = \frac{1}{2} \rightarrow F' = \frac{3}{2}$ resonance peak, as a function of pump beam polarization (normalized to the amplitude of the neighboring ^{174}Yb resonance peak). (a) Probe polarization is $\hat{\sigma}^-$, corresponding to the red data series in figure 3.17, which is a good representation of the type of data sets that were averaged to produce the present plot. (b) Probe polarization is $\hat{\sigma}^+$, corresponding to the green data series in figure 3.17, which is a good representation of the type of data sets that were averaged to produce the present plot. The horizontal axes show the voltage applied to the liquid crystal waveplate in the pump beam (see figure 3.11). The three data points on each plot correspondingly show ($\hat{\sigma}^-$, $\hat{\sigma}^+$, $\hat{\sigma}$) pump polarizations from left to right.

iment attempted along these lines with pulsed lasers and rubidium (see chapter 4) indicates that magnetic shielding for the PMT may be required.

A significant advantage of two-photon spectroscopy is that the detected fluorescence wavelength can be different from the excitation wavelength; it follows that they can be separated by spectral bandpass filters, and background noise due to pump or probe light essentially eliminated. This advantage is not exploited in the experiments presented, largely as a matter of convenience; we could equally well envision an experiment in which optical pumping is done using the 399 nm $^1S_0 \rightarrow ^1P_1$ transition, with detection at 556 nm (or vice-versa). A future incarnation of this experiment could use a diode laser at 399 nm for optical pumping, with the existing detection apparatus. In practice, we were able to reduce the pump background to manageable levels by fiber-coupling the 556 nm pump beam and taking advantage of reduced diffraction from the resulting TEM_{00} spatial mode. In effect, we have replaced spectral filtering with spatial filtering: by eliminating extraneous optical paths to the PMT and reducing the intensity of scattered or diffracted pump light, the background can be reduced to manageable levels.

Note that radiative decays following two-photon excitation typically proceed in at least two cascaded steps, with the final steps involving E1 transitions that couple to the ground

state. In ytterbium the first cascade photons (~ 1479 nm) have too long a wavelength to be conveniently detectable, so we detect the final cascade photons, which radiate on the same transitions that are most convenient for optical pumping out of the ground-state. In the noble gases, the more convenient wavelength is the *first* emitted photon, since the strong E1 transitions coupling to the ground state are all in the vacuum ultraviolet. Thus, this particular limitation is generally avoidable and we do not expect to encounter it at all in noble gas magnetometry.

Two other versions of these experiments are possible with relatively minor modifications of the laser apparatus:

1. The pump and probe beams can be swapped, with the intention of detecting at 556 nm the signature of two-photon optical pumping (TPOP) at 808 nm. This is likely to be a weak effect, but the higher signal-to-background for the 556 nm probe / 808 nm pump combination may prove advantageous. It should also be noted that TPOP is expected to be a weak effect, but the polarization of either excited state produced by $\hat{\sigma}^{\pm}$ radiation ($F'' = \frac{3}{2}, m_F'' = \pm \frac{3}{2}$) is transferred to the ground state with unit efficiency due to angular momentum conservation.
2. If the 399 nm $^1S_0 - ^1P_1$ transition is used for optical pumping, the 556 nm pump background is no longer a limitation. Unfortunately, in our lab the only presently available source of 399 nm light is frequency-doubled Ti:sapphire, which is not compatible with using the Ti:sapphire laser to generate 808 nm light for the two-photon probe.

Figures 3.20 and 3.21 clearly illustrates the need for careful beam shaping and light blocking around the PMT; this becomes a more severe limitation in experiments with pulsed lasers where the signals obtained so far are smaller than in the cw case. The size of any apertures in the beam path must be chosen to minimize diffraction, and the spatial mode of the pump beam should be of high quality. Coupling the 556 nm beam through an optical fiber produces a significant improvement of the spatial mode, but additional measures may prove necessary if this remains a limitation. In chapter 4 we also present an example where the 808 nm probe light – although suppressed by at least six orders of magnitude – was still detectable through the 556 nm bandpass filter, at a level that overwhelmed the fluorescence signal until beam shaping was improved.

Table 3.7: Naturally occurring isotopes of mercury [4]

Isotope	Abundance (%)	Nuclear Spin	Nuclear Magnetic Moment (μ_N)
^{196}Hg	0.15	0+	
^{198}Hg	10.1	0+	
^{199}Hg	17.0	1/2-	+0.5059
^{200}Hg	23.1	0+	
^{201}Hg	13.2	3/2-	-0.5602
^{202}Hg	29.65	0+	
^{204}Hg	6.85	0+	

3.5 CW Lasers and Vapor Cell Spectroscopy

3.5.1 Mercury

Narrow-band diode lasers are commercially available to produce light for spectroscopy of the mercury intercombination line at 253.7 nm (Toptica TA-FHG pro). These are typically made by generating the fourth harmonic of a near-infrared seed laser in two successive resonant doubling cavities. The layout for such a laser is essentially the same as that shown in figure 3.8, with the components after the second isolator duplicated for fourth harmonic generation. The second doubling stage in such a system typically uses BBO, since phase matching with LBO is not possible at such short wavelengths. The temperature and humidity requirements for the second doubling stage are also stringent, and the crystal is prone to irreversible photodegradation from the ultraviolet light, with the result that it must be periodically moved to re-optimize output power using an undamaged region.

Mercury shares many of the interesting and useful features of ytterbium, and serves in some respects as a test system for deep-ultraviolet spectroscopy. The 253.7 nm intercombination line is analogous to the 556 nm transition in ytterbium (and is actually a stronger transition in mercury, due to more severe violations of LS coupling in the heavier atom). Conveniently, 253.7 nm also lies between two possible two-photon wavelengths in xenon; for this reason, our first attempts to find the xenon transition were based on modifications of the laser used for mercury spectroscopy.

In figures 3.23 and 3.24 we present a Doppler-free dichroic atomic vapor laser lock (Doppler-free DAVLL [79–81]) at 253.7 nm, based on spectroscopy of a thin mercury vapor cell. The fit function used to roughly model the error signal is a difference of Gaussians; since the actual frequency offset depends nonlinearly (and hysteretically) on the applied voltage V , it should not be surprising that the fit appears less than perfect. The stability

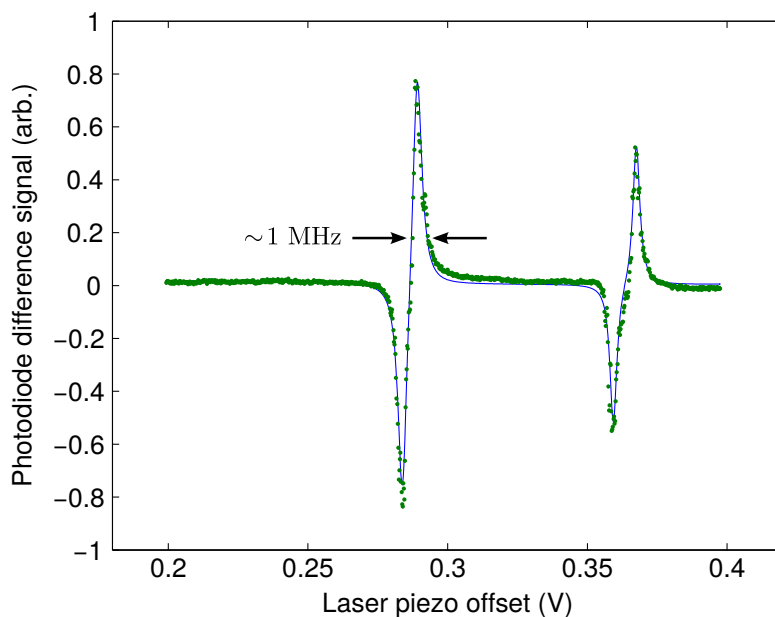


Figure 3.23: Error signal resulting from circular dichroism in ^{199}Hg (left) and ^{201}Hg (right) in a vapor cell, as a function of the offset voltage applied to an intracavity piezoelectric transducer. Two photodiodes are used to monitor the intensities of transmitted $\hat{\sigma}^+$ and $\hat{\sigma}^-$ light, which are normalized to the total power and subtracted. The ~ 1 MHz width results from an applied magnetic field along the probe axis; the dispersive lineshape arises from subtracting two nearly-overlapping absorption peaks. The laser frequency can be locked to either zero crossing, and the slope at the lock point determines the bandwidth of the lock. The blue curve is a fit that assumes Gaussian absorption lineshapes. (Data and figure produced in collaboration with Bernd Taubenheim.)

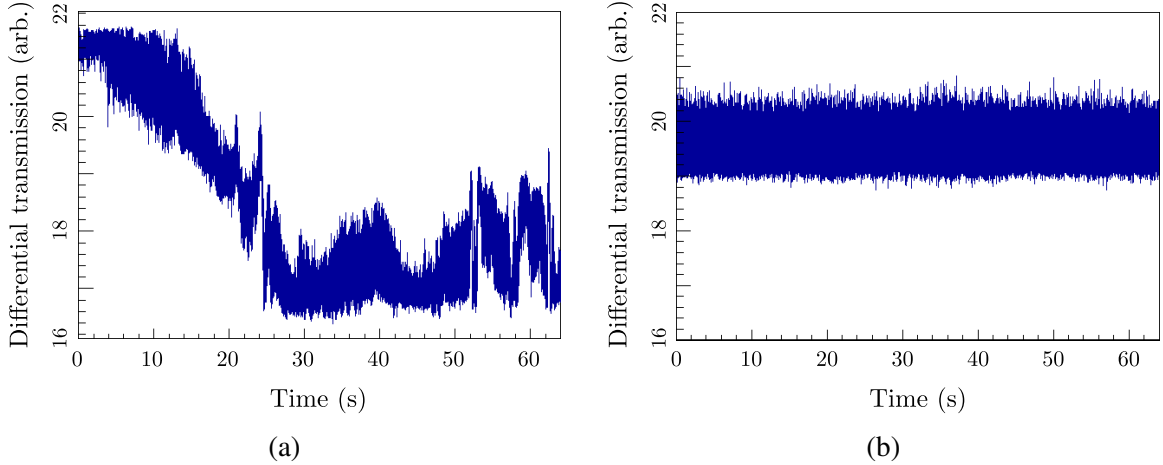


Figure 3.24: Differential transmission signal through a mercury vapor cell ($\hat{\sigma}^+$ compared to $\hat{\sigma}^-$): (a) without and (b) with a Doppler-free DAVLL system providing active frequency stabilization. The intensity modulation in (a) is a result of free-running frequency drift near resonance. (Data and figure produced in collaboration with Bernd Taubenheim.)

of the differential transmission signal in figure 3.24(b), in comparison to the free-running case, provides a good indication that the lock is effective. Based on the observed variation, we can roughly estimate that the laser frequency has a maximum excursion of less than 1 MHz from the line center.

3.5.2 Xenon

The $^1S_0 \rightarrow ^2[5/2]_2$ two-photon transition in xenon, which occurs at an optical wavelength of 256 nm, is a particularly attractive candidate for optical magnetometry. This is well outside the vacuum ultraviolet, but still not trivial to produce. We were able to obtain close to 1 mW of power at 256 nm by detuning the 253.7 nm laser discussed above, and then re-aligning and locking both doubling cavities at 256 nm. This output power is quite low in comparison to the several milliwatts produced at 253.7 nm, and the loss is attributable to the narrow design bandwidth of the commercial system. Figure 3.26 shows the output power in each doubling stage as a function of crystal temperature.

We ultimately found the 256 nm xenon transition by using a commercial Ti:sapphire system (M Squared SolsTiS) with external mixing and doubling modules (M Squared GRUVY and ECD-X-Q). The tunable Ti:sapphire output is mixed with fixed-wavelength 1550 nm light from a fiber laser, using a periodically-poled lithium niobate PPLN crystal cut for sum-frequency generation. The output of this mixing module is then frequency-doubled in a resonant cavity using BBO, to produce light at or near 256 nm. The 256 nm output is tunable via the Ti:sapphire, and can be broadly scanned without negatively affect-

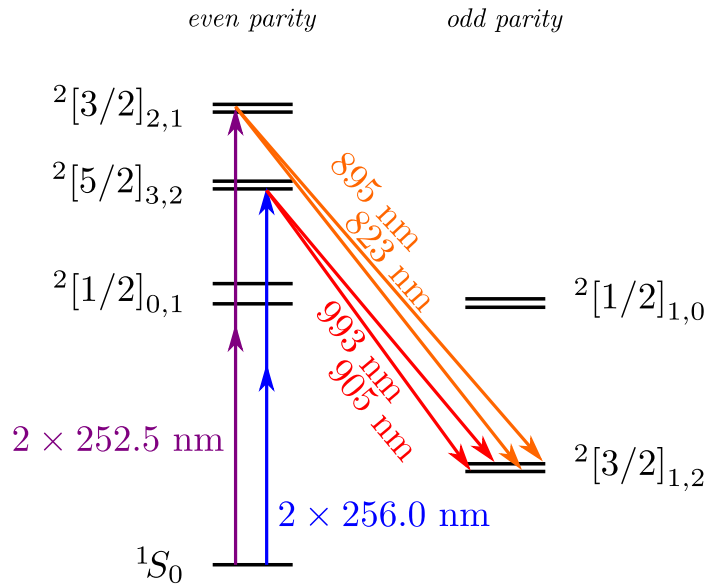


Figure 3.25: Level structure of atomic xenon, showing two possible two-photon transitions for magnetometry. The measurements reported here focus exclusively on the 256.0 nm transition and the 905 nm decay branch, but analogous measurements are possible using other wavelengths.

Table 3.8: Naturally occurring isotopes of xenon [4]

Isotope	Abundance (%)	Nuclear Spin	Nuclear Magnetic Moment (μ_N)
^{128}Xe	1.91	0+	
^{129}Xe	26.4	0+	
^{130}Xe	4.1	1/2+	-0.7768
^{131}Xe	21.2	0+	
^{132}Xe	26.9	3/2+	
^{134}Xe	10.4	0+	
^{136}Xe	8.9	0+	

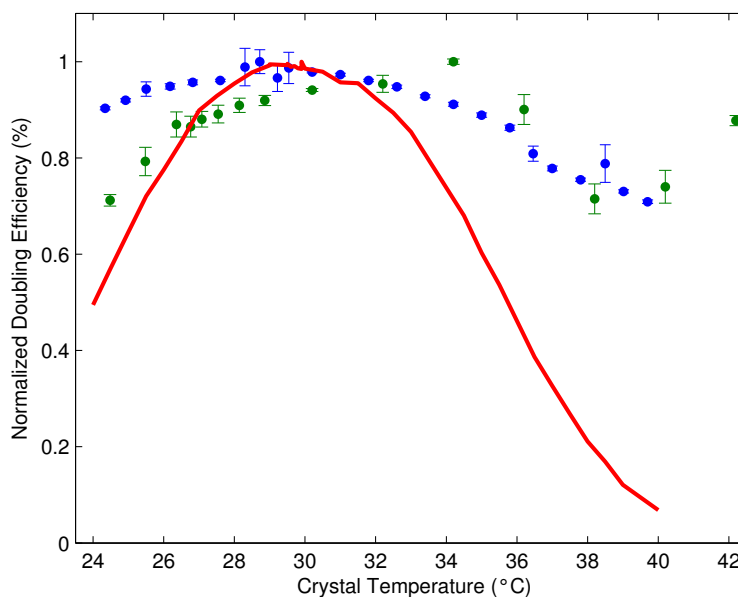


Figure 3.26: Measured doubling efficiencies as a function of temperature, in the second- and fourth-harmonic generation stages of a Toptica TA-FHG pro laser designed for mercury spectroscopy at 253.7 nm. For these data the laser is tuned to operate ~ 2 THz away from the design wavelength, in order to search for the 256 nm two-photon resonance in xenon. The red curve shows temperature dependence of the conversion efficiency in the first doubling stage, and the green data points show the same measurement performed on the second doubling stage (after optimizing the first doubler). For comparison, the blue curve shows a repeated measurement of the green data with the doubling cavity rapidly scanning; this averages out large fluctuations in the vicinity of certain problematic frequencies, and provides some indication of the phase-matching efficiency.

ing the cavity locks. It was necessary to purge the SolTiS module with dry nitrogen in order to obtain stable operation at 764.5 nm, which is the Ti:sapphire wavelength required to produce 256 nm in this scheme. The best results were obtained when the GRUVY module was also purged at the same time. Even so, the 256 nm output power is a strong function of wavelength due to the transferred effect of molecular oxygen resonances in the infrared.

The configuration of critical experimental components is shown in figure 3.27. The optical setup is very similar to the one used for the rubidium measurements described in chapter 4, with appropriate replacements for optical coatings, etc. In the present experiment, the chopper wheel is controlled by an external function generator, and this driving signal is also used to trigger photodiode measurements so that the 256 nm intensity monitor is synchronized with the photon counting data.

Despite using a fully blocked 905 nm bandpass filter with the PMT, nearly half of the detected photon counts on resonance are attributable to 256 nm laser light. We therefore

monitor the laser power with a photodiode, and use this data to normalize the fluorescence spectra point by point. The optical chopper wheel triggers the photon counter as well, and the “bright” and “dark” channels are subtracted to minimize the impact of non-laser background light. The photodiode’s output is recorded using a DAQ card (National Instruments M-Series USB DAQ), and the values during each trigger window are averaged and stored with the photon counting data. A representative, fully normalized spectrum is shown in figure 3.28.

We have verified to within 1% that the fluorescence intensity scales, as expected, with the square of the 256 nm intensity. Future work could improve the signal-to-noise ratio by reducing the laser background (and possibly replacing the PMT with a more sensitive InGaAs APD or other detector), characterize the effects of probe polarization and applied magnetic fields, and examine the transition at higher spectral resolution (e.g., at lower atomic densities or in a true Doppler-free configuration). We have also prepared cells containing ^{129}Xe and Rb, and a natural next step is to polarize the xenon using SEOP and investigate effects of nuclear spin polarization on the two-photon transition rate. If static longitudinal polarization can be detected using the two-photon probe, one can use pulsed NMR to initiate precession and employ the two-photon probe as a real-time monitor of the precession phase (as envisioned for EDM co-magnetometry). It may also be productive to investigate the 252.5 nm two-photon transition, which falls within the tuning range of the current laser configuration.

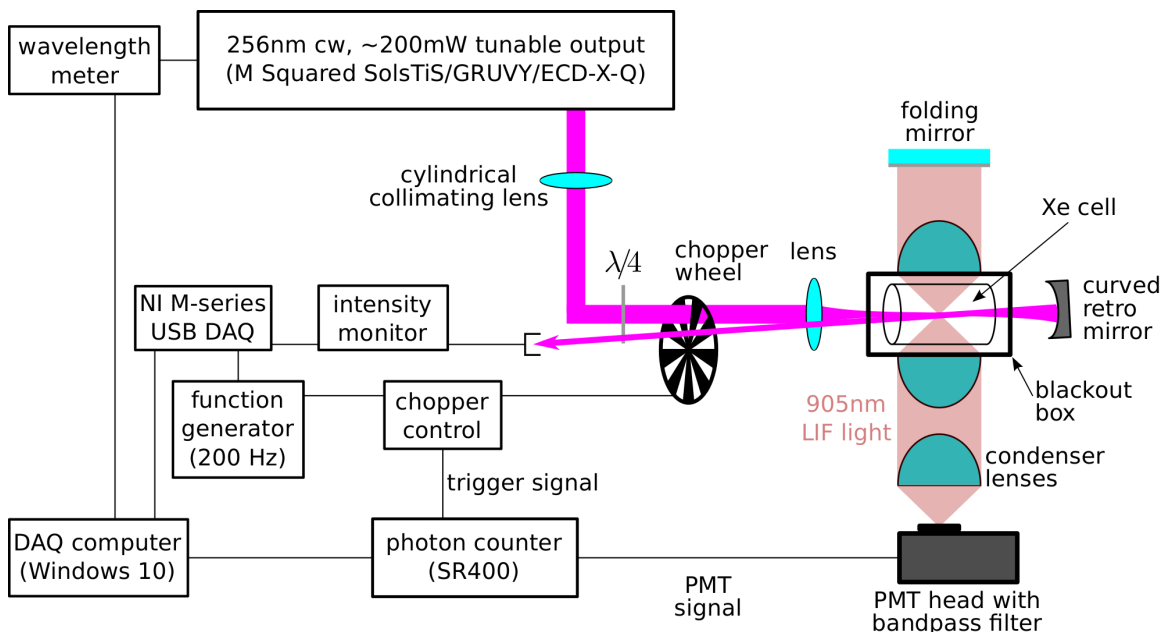


Figure 3.27: Simplified block diagram of the cw xenon experiment, in the configuration used to produce figure 3.28. Magnetic field coils (not shown) are mounted around the cell and blackout box.

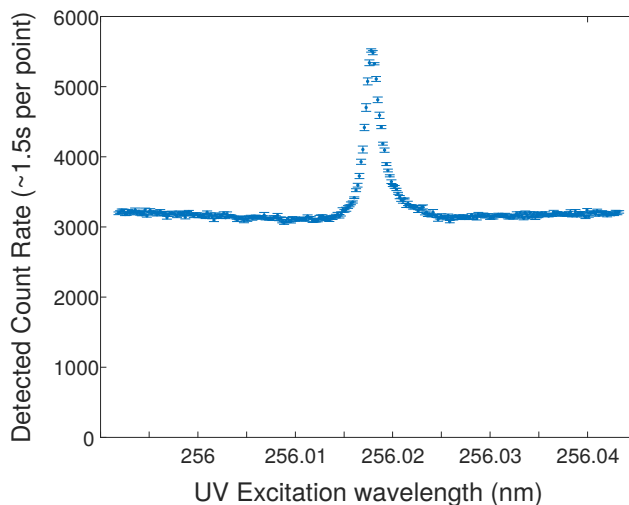


Figure 3.28: Xenon fluorescence signal at 905 nm, as a function of excitation wavelength. The cell used to obtain these data contained approximately 1.5 bar of natural xenon. Approximately 200 mW of power at 256 nm was used; the nearly constant background is due to laser light entering the PMT through the 905 nm bandpass filter. Weak modulation of the background is attributable to a molecular oxygen resonance at 764.5 nm, which reduces the Ti:sapphire power available to produce 256 nm light.

CHAPTER 4

Experiments with Pulsed Lasers

High spectral resolution and dispersion control are possible with ultrafast lasers, and the relative ease of producing high power ultraviolet probe light compensates for a moderate increase in technical complexity. The essential difficulty is that, while short optical pulses can have very high peak power (and thus high efficiencies for frequency conversion and multiphoton excitation), this comes at the cost of a corresponding increase in (frequency) bandwidth. For pulse lengths in the range of a few picoseconds to a few femtoseconds, the pulse bandwidth is between 100 GHz and 100 THz, with the result that most of the laser power lies outside the transition linewidth for degenerate photons.

We have nevertheless obtained two-photon fluorescence signals from atomic ytterbium (picosecond and femtosecond pulses) and rubidium (picosecond pulses only); these measurements are presented in the remainder of this chapter. The scattering rates are low compared to the cw experiment, and no sensitivity to ground state polarization was observed. However, we expect a considerable enhancement of the signal with additional laser stabilization (discussed in chapter 4.5.1) and a corresponding sensitivity to hyperfine structure (which was not resolved in the pulsed experiments reported here). Techniques for dispersion compensation are explored in the context of the femtosecond ytterbium experiment, and will be particularly relevant to future experiments where the nonlinear crystals used to produce ultraviolet pulses are expected to produce significant group delay dispersion.

We also survey some proposed improvements to the experiments discussed here, and extensions of the techniques to other atomic species and broader applications. Section 4.5.1 considers possible improvements to the pulsed ytterbium experiment, in particular methods for stabilizing the 808 nm picosecond laser. A similar method of stabilizing picosecond pulses for xenon spectroscopy is proposed in section 4.5.2, together with a frequency-tripling scheme to produce modelocked pulses at 256.0 nm using a Ti:sapphire oscillator. Section 4.5.3 discusses applications of two-photon magnetometry in experiments seeking to measure the nuclear EDM of certain radon isotopes; relatively little is known about the

optical spectrum of radon, and high resolution spectroscopy with a pulsed laser would be a powerful tool for investigating it.

4.1 Scaling of Excitation Efficiency with Pulse Parameters

Suppose we have a laser source whose spectral intensity distribution at the experiment is

$$I_\omega(\omega) = \frac{I_0}{\Gamma\sqrt{\pi}} e^{-\frac{(\omega-\omega_c)^2}{\Gamma^2}}, \quad (4.1)$$

i.e., one with a fixed total intensity I_0 . The power spectrum is a Gaussian centered at the carrier frequency ω_c , with full width at half maximum (FWHM) $2\sqrt{\ln 2}\Gamma$. A Lorentzian spectrum can be a better model when only a single axial mode of the laser is excited, but for broadband pulses a Gaussian or squared hyperbolic secant is typically more appropriate. Suppose also that the atomic density of states associated with absorption of two photons of frequency ω is

$$L(\omega) = \frac{N}{\gamma\sqrt{2\pi}} e^{-\frac{(\omega-\omega_0)^2}{2\gamma^2}}, \quad (4.2)$$

where N is the total number of atoms, ω_0 is the central resonance frequency, and the FWHM of the distribution is $2\sqrt{2\ln 2}\gamma$. We have chosen a Gaussian distribution of the density of states for computational simplicity, but we could also use the Lorentzian distribution

$$L'(\omega) = \frac{N\gamma}{2\pi} \frac{1}{(\omega - \omega_0)^2 + \frac{\gamma^2}{4}}. \quad (4.3)$$

The first case is more appropriate to inhomogeneous broadening mechanisms (e.g., Doppler broadening), whereas the second is better suited to homogeneous mechanisms (such as the natural radiative linewidth). A Voigt lineshape, obtained from a convolution of the two with different width parameters, is yet a better approximation (especially when $\Gamma \approx \gamma$).

The efficiency of the field at driving two-photon transitions is well characterized by the overlap integral S (which is proportional to the resulting excited state population):

$$S = \int_{-\infty}^{\infty} \int_{-\infty}^{\infty} I(\omega_1)I(\omega_2)L\left(\frac{\omega_1 + \omega_2}{2}\right) d\omega_1 d\omega_2 \quad (4.4)$$

$$= \int_{-\infty}^{\infty} L(\omega) \int_{-\infty}^{\infty} I(\omega - \Delta)I(\omega + \Delta) d\Delta d\omega \quad (4.5)$$

$$= \frac{NI_0^2}{\sqrt{2\pi}(\Gamma^2 + 4\gamma^2)} e^{-\frac{2(\omega_0 - \omega_c)^2}{\Gamma^2 + 4\gamma^2}}, \quad (4.6)$$

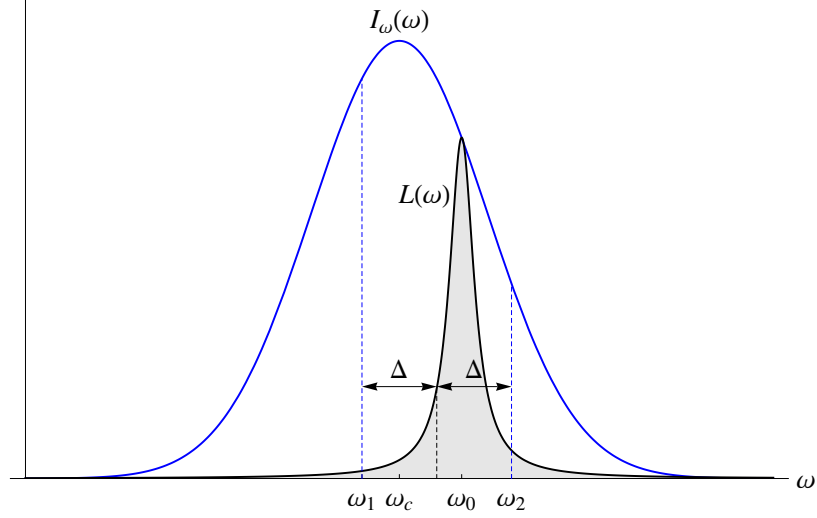


Figure 4.1: Intensity spectrum of the optical field, atomic absorption lineshape, and frequency parameters appearing in the overlap integral used to estimate the two-photon absorption rate. We can consider the integration parameters to be ω_1 and ω_2 , or (alternatively) ω and Δ .

where $\omega = (\omega_2 + \omega_1)/2$ and $\Delta = (\omega_2 - \omega_1)/2$. We have assumed that the intermediate detunings $\omega_i - \omega$ (where $\hbar\omega_i$ is the energy of a real atomic level) are large compared to either of the widths γ, Γ . Note that resonant excitation is possible whenever the *overall* detuning is close to zero; this accounts for the differing arguments between the first and second factors of intensity in either integral expression for S . Two relevant limits can be obtained from this result; they correspond to

$$\gamma \ll \Gamma \quad (\text{broad-line excitation field}) \quad (4.7)$$

$$\gamma \gg \Gamma \quad (\text{narrow-line excitation field}). \quad (4.8)$$

In either case, the excitation scales as

$$\frac{NI_0^2}{\gamma_{\max} \sqrt{2\pi}} e^{-\frac{(\omega_0 - \omega_c)^2}{\gamma_{\max}^2}}, \quad (4.9)$$

where γ_{\max} is the larger of Γ or 2γ . In particular, when the carrier frequency is tuned to resonance ($\omega_0 - \omega_c = 0$) we have

$$S \propto \begin{cases} \Gamma^{-1} & (\gamma \ll \Gamma) \\ \gamma^{-1} & (\gamma \gg \Gamma) \end{cases}, \quad (4.10)$$

which illustrates that in either case the excitation scales inversely with the largest width

parameter. For broad-line excitation, corresponding to most pulsed laser sources, we therefore expect the excitation from a single pulse to scale linearly with the pulse duration. The case of narrow-line pulsed excitation may be considered to include cw lasers, where the “pulse width” is really the transit-broadened field spectrum due to a finite interaction time.

Note that the peak squared spectral intensity is $I_0^2/\pi\Gamma^2$, so increasing the *total* intensity without changing the pulse width still achieves a quadratic gain with I_0 . However, the higher *peak* intensity achieved by shortening a temporal pulse with fixed energy does not, by itself, offset the loss in excitation due to increased spectral bandwidth. This loss can be recovered by preserving phase-coherence of the carrier wave between successive pulses, with the result that the excitation amplitudes from different pulses can interfere constructively. The time-domain picture of interpulse phase coherence corresponds to phase-locking the excited axial modes of the laser resonator in the frequency domain. Since in the coherent case we add amplitudes rather than probabilities to obtain the excited state population, a considerable enhancement of the excitation occurs if N phase-coherent pulses contribute before the excitation decays. The enhancement factor is N^2 when compared to a single pulse, or N when compared to an incoherent pulse train. Additionally, the characteristic “comb” spectrum associated with this periodic time dependence permits much higher frequency resolution than single-pulse excitation, since the limiting frequency scale is defined by the spacing between modes rather than the width of the entire spectrum (see section 2.3).

In many situations relevant to two-photon excitation, the absorption of one additional probe photon is sufficient to ionize the atom. It is often desirable (particularly in EDM experiments) to achieve a high two-photon excitation rate at the same time as a low ionization rate; we will suppose that the ionization probability is proportional to both the excited state population and the laser intensity I_0 . In this case, a single pulse with intensity I_0 produces roughly the same number of excited atoms as N phase-coherent pulses of intensity I_0/N . However, the single pulse produces a number of ions proportional to I_0^3 , while the scaling for the train of weaker pulses is approximately

$$n_{\text{ions}} \propto \frac{I_0^3}{N^2} \sum_{n=1}^N n^2 = I_0^3 \left[\frac{1}{3} + \frac{1}{2N} + \frac{1}{6N^2} \right], \quad (4.11)$$

approaching $I_0^3/3$ in the limit of many pulses. Moreover, the ions produced by the pulse train are spread out in time over a considerably longer interval – during which the ionization rate per pulse is significantly lower. In applications where a large number of simultaneous ionizations may cause problems (but a lower and more uniform ionization rate may not), this can be a crucial advantage.

In terms of the apparatus required for nonlinear frequency mixing, it is substantially easier to produce high optical power¹ with pulsed rather than cw lasers, owing to the high peak intensities available from short optical pulses. For this reason nonlinear frequency mixing of pulsed lasers is typically done without resonant cavity enhancement, which considerably simplifies the optical and electronics details of the apparatus. It also turns out that the dominant mechanisms for optical damage scale with the *average* laser intensity rather than peak intensity, and the situation concerning long-term deterioration of optics is not appreciably worse than in the cw case. Finally, pulsed excitation introduces new degrees of freedom (pulse timing, chirp, and overlap), which can be exploited experimentally to regulate different sensitivities in their application to magnetometry.

4.2 Ytterbium Atomic Beam: Picosecond Pulses

The atomic beam apparatus is the same one discussed in chapter 3 (see figures 3.3 to 3.7). The 556 nm pump laser for nuclear spin polarization also remains the same, although no sensitivity of the two-photon scattering rate to ground state nuclear spin polarization was ultimately observed with a pulsed probe. (The absence of a polarization signal is attributable to instability of the probe laser spectrum, resulting in a stochastic average over different isotopes and hyperfine transitions that reduces the visibility of population differences due to optical pumping.) The configurations for experiments with pulsed probe lasers are detailed in figures 4.2, 4.3, 4.9 and 4.11, and discussed below.

The picosecond pulsed laser is a Ti:sapphire oscillator (Spectra-Physics Tsunami 3960-X1BB), which in the configuration used here (see figure 4.3) produces 2 ps pulses with a repetition rate of ~ 80 MHz and an average power of 1-2 W. It is actively modelocked with an acousto-optic modulator (AOM) driven near the repetition rate, and the pulse length is controlled by a Gires-Tournois interferometer (GTI) at one end of the cavity, which introduces negative group velocity dispersion to compensate for the normal dispersion resulting from other cavity optics. Other pulse lengths can be achieved by using a GTI with a different dispersion profile. The cavity length and dispersion are not stabilized, with the result that the repetition rate and carrier-envelope offset phase are prone to drift. We will discuss schemes for stabilizing these degrees of freedom in section 4.5.1, since instability of these parameters appears to be the main limitation presently affecting the experiment.

The carrier frequency is tunable over a wide range via rotation of an intracavity birefringent filter. This, the position of the GTI, and the vertical alignment of the output coupler are the principal degrees of freedom available for frequency adjustments; all must currently

¹Both average and peak.

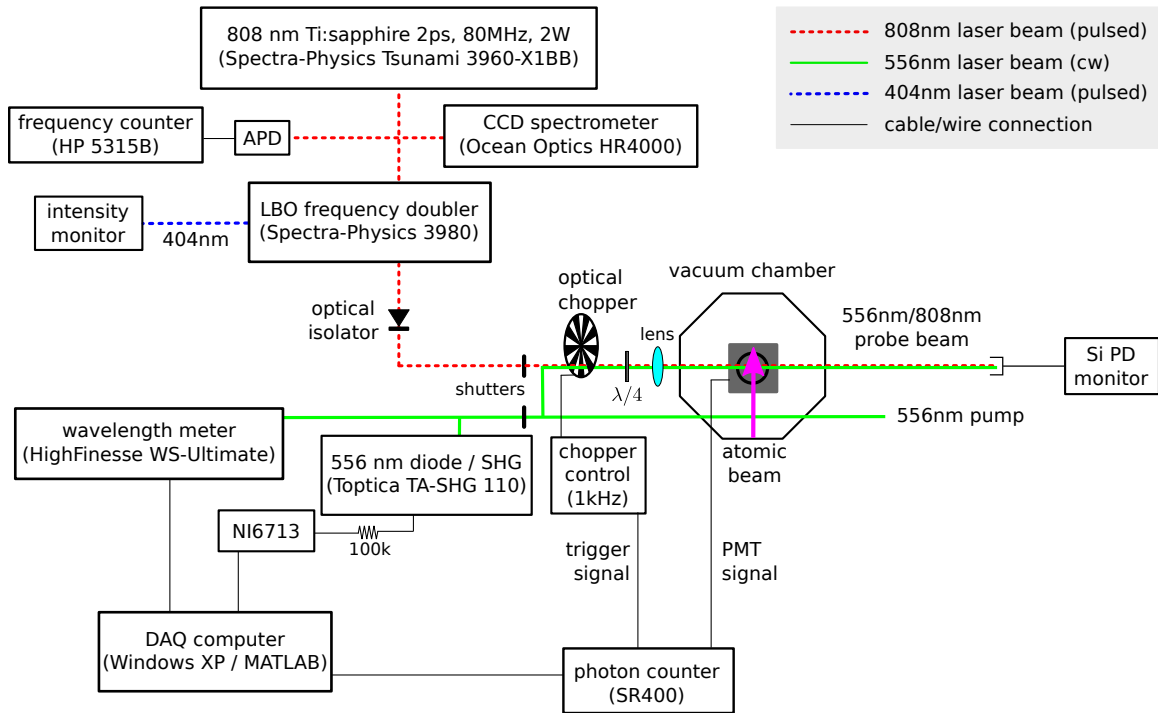


Figure 4.2: Block diagram of the experimental configuration used for picosecond two-photon spectroscopy of ytterbium; the atomic beam and 556 nm laser are discussed in chapter 3. The 808 nm probe beam is produced by a commercial Ti:sapphire oscillator (Spectra-Physics Tsunami), pumped by 10 W at 532 nm (Coherent Verdi V-12). The beam passes through a LBO frequency doubler, optical isolator, and optical chopper wheel. Pick-off beams are used to monitor the pulse train (on an APD) and the power spectrum (on a CCD spectrometer), while the intensity of the 404 nm second harmonic is used to evaluate modelocking stability. (Future experiments will use an error signal generated by the second harmonic beam to stabilize the fundamental frequency; see section 4.5.1). The optical isolator is required for stable modelocking since back-reflections from normal-incidence optics tend to destabilize the resonator. A monitor photodiode behind the chamber is used to track the phase of the optical chopper for gated photon counting, and a lens in front is used to increase the intensity incident on the atomic beam.

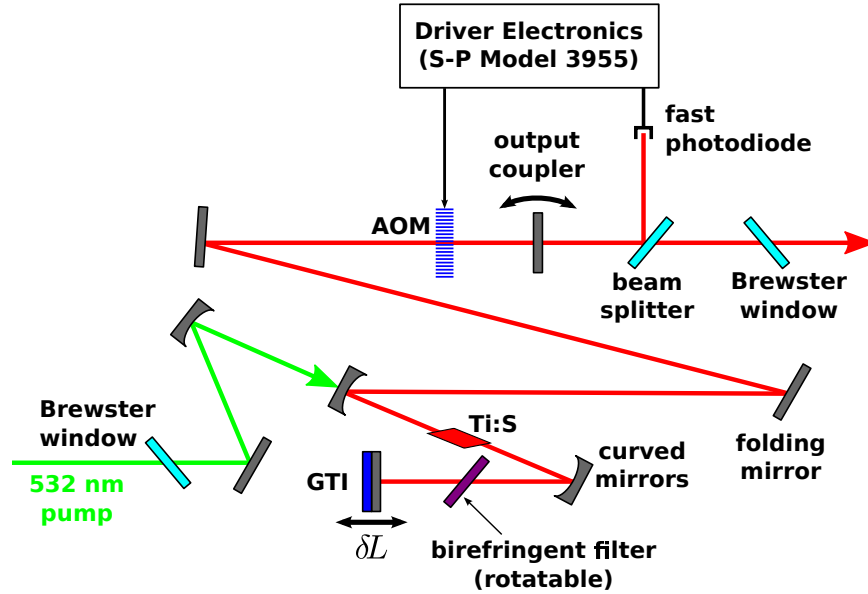


Figure 4.3: Schematic diagram of the Spectra-Physics Tsunami 3960-X1BB cavity. Pump light at 532 nm (9-10 W) is coupled into the cavity with a Brewster window and steering and focusing mirrors. The cavity is a folded linear configuration, with a Gires-Tournois interferometer (GTI) at one end and the output coupler mirror providing the second boundary. The GTI can be adjusted to change the amount of negative group velocity dispersion (GVD), thereby regulating the pulse length within approximately a factor of two. The carrier frequency is adjusted by rotating a three-plate birefringent filter about its optical axis. External adjustment knobs for the GTI, birefringent filter, and output coupler are provided for optimization without opening the cavity’s protective cover. Active modelocking is accomplished using an acousto-optic modulator driven near the repetition rate of ~ 80 MHz, and an error signal is produced using the output of a fast photodiode monitor whose alignment can be adjusted by opening the cavity. The control electronics is a Spectra-Physics Model 3955 driver, which provides coarse and fine adjustments of the modelocker phase (required for compensation when cable lengths are changed).

be tuned manually, although in future experiments we plan to introduce a piezoelectric transducer to modulate the cavity length (thereby stabilizing the repetition rate). The birefringent filter provides a coarse selection of the carrier frequency, which is finely tuned by position and orientation of the GTI and the output coupler. However, these three degrees of freedom must also coincide with a cavity alignment where modelocking occurs, and this is not a trivial requirement. An additional degree of freedom exists to regulate modelocking – the phase of reference signal driving the AOM – but is not especially useful as a tuning parameter, since it does not significantly affect the carrier frequency and is not strongly coupled to any other tunable degree of freedom.

Modelocking can be diagnosed in three ways: second-harmonic generation (SHG) efficiency, spectral bandwidth, and pulse train stability. Qualitatively the simplest is to measure

the output power of the doubler at the second harmonic frequency, since this increases by approximately two orders of magnitude when modelocking is established (with a corresponding decrease of the infrared power). When attempting to achieve modelocking it can also be sometimes easier to observe the transient bright flash of blue light, than to notice a similarly rapid variation of the intensity spectrum or pulse train. Once modelocking is achieved, it is typically necessary to fine tune the carrier frequency via small adjustments of the GTI and output coupler. The LBO frequency doubler (Spectra-Physics Model 3980) is a passive device operated in a single-pass configuration. Except for rotating the LBO crystal to re-optimize phase-matching when the output frequency of the Tsunami is changed significantly, no adjustments are required in the course of routine use.

Other diagnostics for modelocking include the shape of the power spectral envelope observed on the CCD spectrometer (Ocean Optics HR4000); see figure 4.6 for a similar spectrum at the resonance wavelength for a two-photon transition in rubidium. It appears roughly Gaussian with a width of ~ 0.5 nm when properly modelocked. The peak spectral intensity is substantially lower than in the cw regime, since the output power is roughly the same but the spectral bandwidth is considerably larger. We similarly observe the slowly-varying time-domain envelope of the pulse train by using an avalanche photodiode (APD), and measure the repetition rate by tracking the APD signal with a frequency counter (HP 51358). The pulse amplitude should not visibly fluctuate when monitored with an oscilloscope, and the measured repetition frequency should be stable below 1 ppm (a few tens of hertz at 80 MHz) on the frequency counter.

Figure 4.4 shows a typical fluorescence signal from the atomic beam, where the count rate detected by a photomultiplier tube (PMT) is correlated with the presence or absence of ~ 2 ps laser pulses at 808 nm. The signal appears when both the atomic beam and the probe laser are present, but vanishes when either is turned off or the probe laser is detuned from resonance. We extrapolate a Gaussian beam waist of approximately $100 \mu\text{m}$ at the atomic beam, meaning the thermal atoms interact with the probe field for approximately 330 ns (i.e., an average of 27 pulses). The associated transit-time broadening is 3 MHz, which also corresponds to the apparent resolution of an individual comb tooth in the frame of a moving atom. Since the inverse interaction time is roughly twice the excited state radiative linewidth of 2 MHz, it is a reasonable approximation to neglect atomic relaxation. (Alternatively, roughly 37 pulses are absorbed for every $1/e$ decay in the excited state population.) The dominant frequency scale – apart from the optical carrier frequency – is the bandwidth of the pulsed field (~ 250 GHz), followed by the Voigt linewidths of the individual isotopic and hyperfine transitions (tens of MHz mainly due to the residual Doppler effect, as inferred from cw experiments performed under similar conditions; see

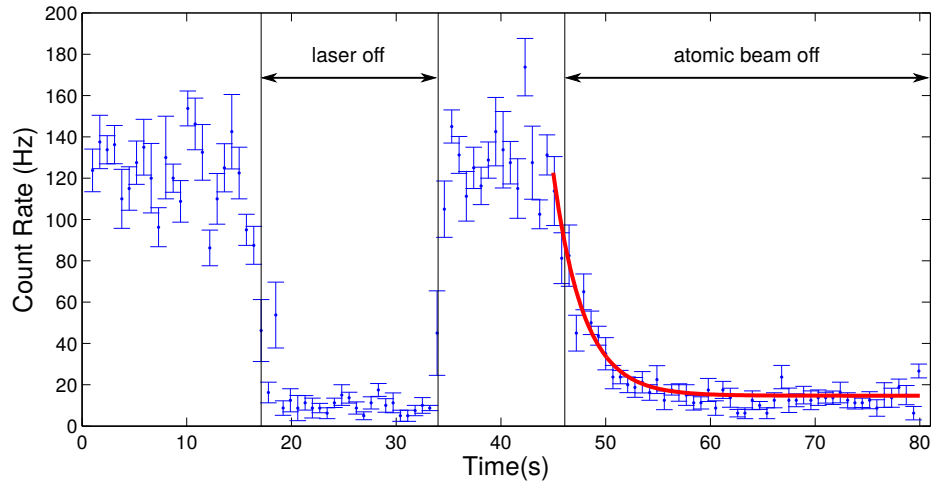


Figure 4.4: Two-photon fluorescence signal from the Yb atomic beam, excited by 2 ps pulses at 808 nm. Seven 100 ms bins are averaged for each data point, and the signal-to-background ratio is approximately 10. When the atomic beam current is switched off, exponential decay of the fluorescence signal due to the oven cooling down is observed with a time constant of $\tau \approx 2.9$ s (fit line to $f(t) = A + Be^{-(t-t_0)/\tau}$ shown in red). No chopper wheel was used for the measurement shown here, so the residual count rate during the “off” intervals is indicative of the level of background light entering the PMT.

chapter 3).

In principle, a sufficiently stable probe field could resolve isotopic and hyperfine structure – but since the carrier frequency is $f_c \approx 371$ THz, a change in repetition rate by 10 Hz corresponds to a change of ~ 46 MHz in f_c . This is already greater than $f_r/2 \approx 40$ MHz, which is all that is required to go from a “direct” resonance where a comb tooth overlaps an atomic transition to an “indirect” one where two teeth lie symmetrically on either side of the resonant transition frequency. Without better stabilization of the repetition rate, we cannot expect to resolve individual isotopes or hyperfine transitions.

4.3 Rubidium Vapor Cell

The rubidium picosecond experiment is technologically the closest to a noble gas nuclear spin magnetometer; it consists of a room-temperature vapor cell with natural-abundance rubidium in vacuum, probed by the picosecond laser discussed in section 4.2. Though not a nuclear spin system, the experiment provides an opportunity to explore some aspects of two-photon spectroscopy with vapor cells and pulsed lasers, and illustrates that some basic properties such as the dependence of excitation probability on probe field polarization carry over into pulsed systems more or less as expected.

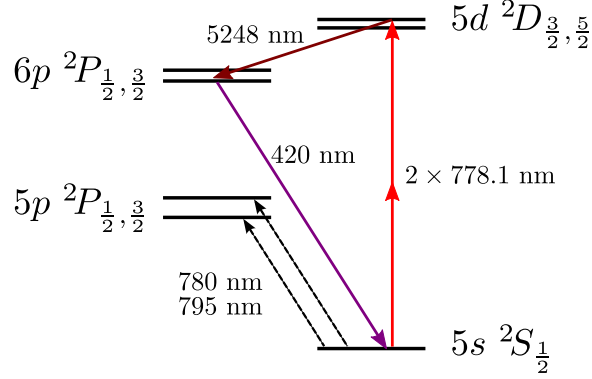


Figure 4.5: Level structure of the 778 nm $5s\ ^2S_{\frac{1}{2}} \rightarrow 5d\ ^2D_{\frac{5}{2}}$ two-photon transition, including the 420 nm fluorescence line used for detection.

The two-photon laser is nearly resonant with the strong D-line transitions from the $5s\ ^2S_{\frac{1}{2}}$ ground state to the $5p\ ^2P_{\frac{1}{2}, \frac{3}{2}}$ states at 795 nm and 780 nm (respectively). These transitions are not resonant with the picosecond probe field (due to the relatively narrow bandwidth of ~ 0.5 nm, but the small intermediate detunings contribute a large enhancement of the transition rate. It is relatively straightforward to obtain a 420 nm fluorescence signal even without heating the cell, and peak count rates above 10^6 Hz were achieved with moderate laser power (limited by PMT saturation).

The mean thermal velocity for atoms in the vapor cell is approximately 270 m/s, roughly comparable to ytterbium atoms in the atomic beam or xenon atoms under the same conditions. In this case (unlike the Yb beam, where Doppler broadening was minimized by the transverse excitation geometry) the Doppler broadening is about 0.5 GHz, considerably larger than the radiative linewidth of 4 MHz. Again assuming a beam waist of $100\ \mu\text{m}$, the atoms experience a transit broadening of just under 3 MHz, comparable to the radiative linewidth of the excited state. This means that on average each atom interacts with 30 pulses, 20 of which occur within a single radiative lifetime.

The laser configuration is the same as that shown in figures 4.2 and 4.3, with the birefringent filter tuned to select 778 nm instead of 808 nm. We attempted to observe a fluorescence signal with a CCD imaging system, but ultimately did not succeed. The imaging system was replaced with a PMT and ambient light shields. Only one fluorescence path is necessary to detect a signal from rubidium, but for xenon and other atoms where the intermediate detunings are large and less laser power is available, the folded $4f$ fluorescence collection system is expected to provide a factor of two signal enhancement. In principle, the recycling mirror can be aligned to produce a Doppler-free enhancement of the two-photon scattering rate (i.e. a factor of six accompanied by increased spectral resolution, rather than the existing factor of two that preserves Doppler broadening), but the interpulse

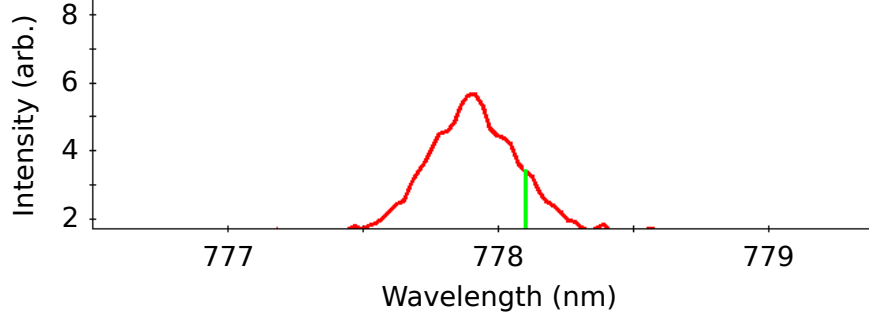


Figure 4.6: Spectrum of the picosecond Ti:sapphire oscillator, tuned to the 778 nm two-photon resonance in rubidium. The green line indicates the nominal transition wavelength, but the laser spectrum is centered at the observed fluorescence maximum (the discrepancy is likely due to error in the spectrometer calibration). The spectral bandwidth corresponds to approximately 0.5 nm or ~ 250 GHz, near the transform limit of 220 GHz for 2 ps Gaussian pulses.

distance is ~ 3.75 m, requiring a two-meter extension of the optical path to overlap successive pulses in the vapor cell. For this reason, we have not yet explored Doppler-free pulsed two-photon spectroscopy.

In figure 4.8 we show a $\sim 25\%$ modulation of the detected fluorescence intensity, as a function of probe polarization. The linear polarizations correspond to a maximal scattering rate, while the circular polarizations correspond to minima; this can be explained by the Clebsch-Gordan coefficients and respective line strengths that are allowed in each case (recall that this includes an average over both stable isotopes and all hyperfine components). The fit function (green line) is given by

$$q(\theta) = A + B \sin(C\theta + D), \quad (4.12)$$

where θ is the waveplate angle.

The rubidium experiment demonstrates two-photon excitation with modelocked picosecond pulse, detected by laser-induced fluorescence in a room-temperature vapor cell. Although the spectral stability of the laser is not presently adequate to resolve individual hyperfine transitions, we have verified that the scattering rate depends on the probe field polarization as expected – this is a crucial point for two-photon magnetometry, which (as demonstrated in chapter 3) relies on very fine control of the probe polarization. It remains to extend these studies to include the effects of optical pumping and magnetic resonance, for which a more stable laser spectrum is required.

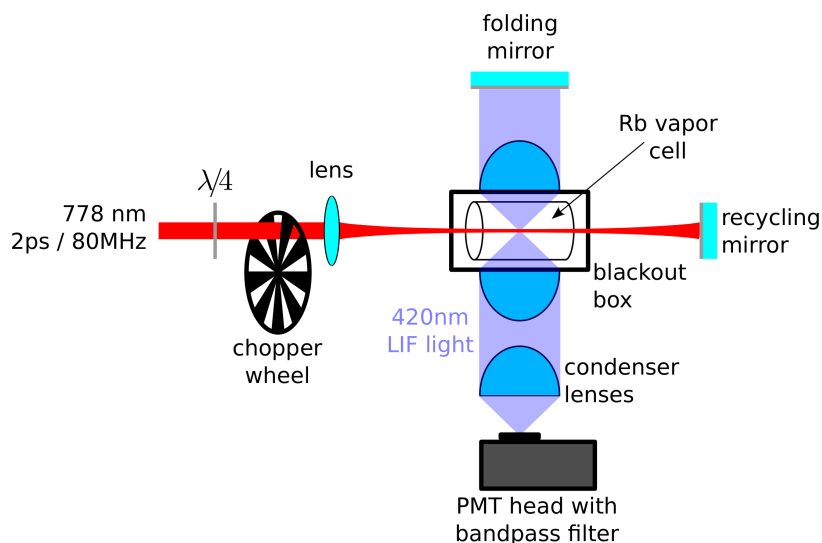


Figure 4.7: Diagram of the rubidium vapor cell experiment, in a configuration similar to that envisioned for noble gas vapor cells. A room-temperature rubidium vapor cell is mounted inside a light-blocked “blackout” box, and probed with a focused probe beam at 778 nm produced by the picosecond Ti:sapphire oscillator. A focusing lens and recycling mirror maximize the intensity at the center of the cell, which is also the focal point for the high-numerical-aperture collection optics for the 420 nm fluorescence light. Two antiparallel fluorescence paths are collected, and both are directed through a bandpass filter into a photon-counting PMT head, similar to that used for the ytterbium experiments. The fluorescence and excitation wavelengths are discriminated by a 420 nm bandpass filter, and detection is synchronized to an optical chopper wheel for background subtraction.

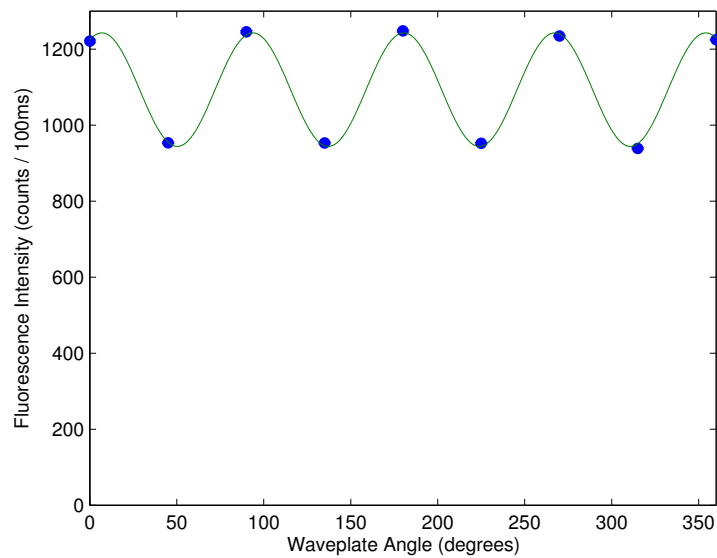


Figure 4.8: Modulation of fluorescence signal with probe polarization. The x -axis indicates the angular orientation of a quarter-waveplate's fast axis; the angles 0° , 90° , 180° , 270° , and 360° correspond to the same linear polarization. The angles 45° and 225° correspond to right-hand circular polarization, while 135° and 315° correspond to left-hand circular polarization. Note that the sense of circular polarization does not affect the signal, but the degree of ellipticity does. The green line is fit to the function $q(\theta)$ defined in equation 4.12; the period of the sinusoidal modulation is approximately 90° , as expected.

4.4 Ytterbium Atomic Beam: Femtosecond Pulses

The femtosecond laser used for pulsed spectroscopy of ytterbium is a homemade system diagrammed in figure 4.9. (We are indebted to Steve Cundiff’s research group, and in particular to Bachana Lomsadze for the loan of this equipment and assistance operating it). The cavity layout is relatively simple and standard for modelocked femtosecond Ti:sapphire oscillators (see figure 4.9 and [82, 83]). A ~ 5 W pump beam at 532 nm is coupled into the cavity through a dichroic coating on one of the curved focusing mirrors; it enters the Ti:sapphire crystal, which is Brewster-cut to minimize reflection losses. Intracavity dispersion compensation is provided by fused silica prisms, in a double-pass folded configuration. The end mirror of the prism compressor is mounted on a split piezo to provide a fine tuning degree of freedom for the cavity dispersion; this can also be adjusted via intensity modulation of the pump beam, using an AOM outside the cavity to redirect a small fraction of the incident power. Passive modelocking is provided by Kerr lensing in the Ti:sapphire crystal, whereby the intensity-dependent index of refraction is exploited to couple high-energy pulses into resonant spatial modes, and the lower-intensity wings of the pulse become attenuated on each round trip through the cavity. Since the pulsed frequency spectrum fills the gain bandwidth of the cavity, the carrier-envelope offset phase is less prone to drift than in picosecond oscillators. A small mechanical perturbation (such as tugging on a wire connected to one of the translation stages on which the prisms are mounted) is usually sufficient to establish modelocking when the cavity is well aligned. Once modelocking is established, the repetition rate can be finely adjusted by moving the output coupler with a piezoelectric transducer.

In the alignment configuration used for this experiment the laser produces 25-30 fs pulses with a center wavelength near 808 nm, at a repetition rate of ~ 93.2 MHz. The spectrum can be adjusted by spatially filtering the dispersed spectrum with apertures (razor blades) between the compressor prisms. The maximum average power is ~ 300 mW, so a broader frequency spectrum is typically characterized by a lower peak (spectral) intensity. Naively scaling the picosecond signal by this repetition rate and average power, and a linewidth of 15 THz, we would expect a femtosecond signal of ~ 0.2 counts per second – this is remarkably close to the detected signal of 0.5 counts per second, shown in figures 4.13 and 4.14.

The experimental configuration shown in figure 4.11 is similar to the one described in the picosecond experiment of the previous section. The major difference is that dispersive optics must be kept to an absolute minimum, in particular coated or transmissive optics such as lenses and windows that are not specifically designed for low group delay disper-

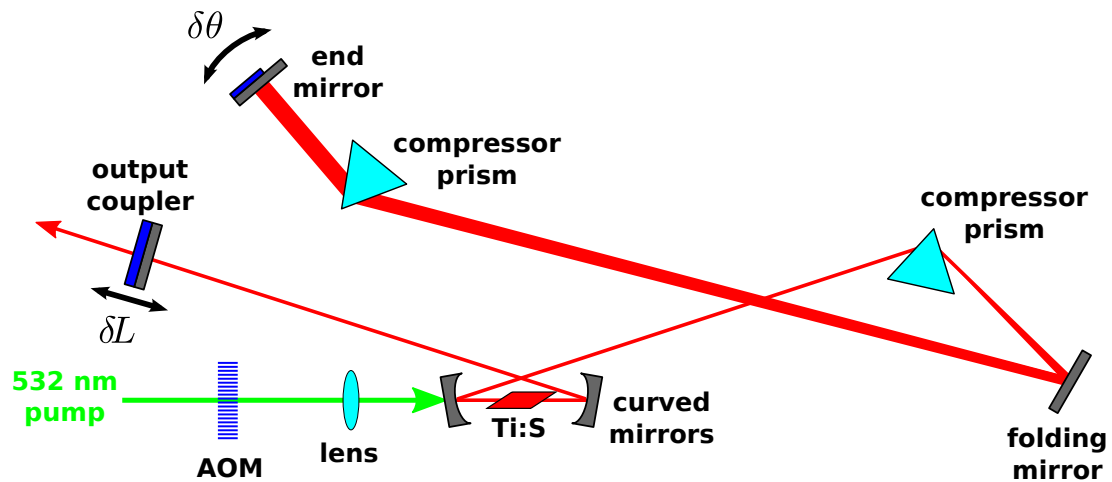


Figure 4.9: Diagram of the femtosecond Ti:sapphire (Ti:S) resonator, showing the tuning degrees of freedom δL and $\delta\theta$ that respectively stabilize the repetition rate f_r and the carrier-envelope offset frequency f_0 . The angular parameter θ is modulated by a split piezo-electric transducer mounted on the end mirror of the double-pass prism compressor, providing a fine adjustment of the cavity dispersion. The repetition rate is determined by the optical path length L of the cavity, and adjusted by translating the output coupler with another piezo. The prism compressor consists of two fused silica prisms in double pass configuration; the interprism distance, where the beam is diverging, determines the amount of negative dispersion introduced to compensate for normal dispersion in other cavity components. This regulates the pulse length, which can be as low as 15-20 fs at the output of the resonator. The acousto-optic modulator (AOM) is used to modulate the intensity of pump light entering the cavity, and can be used to tune the cavity dispersion via the intensity-dependent refractive index of the Ti:sapphire crystal. The curved cavity mirrors focus the beam into the Ti:sapphire crystal, increasing the intensity to further exploit the Kerr nonlinearity for modelocking.

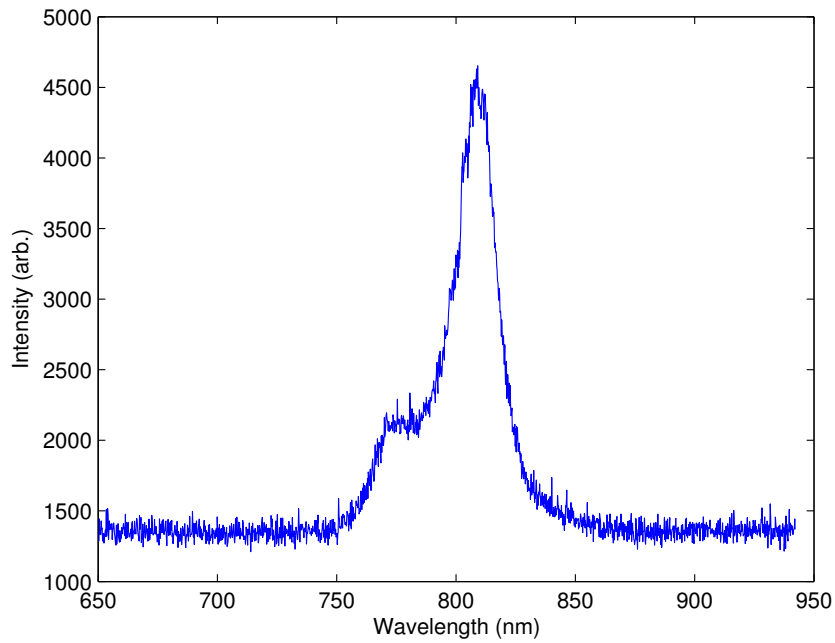


Figure 4.10: Representative spectrum of the femtosecond Ti:sapphire oscillator, with a center wavelength near 808 nm. The frequency bandwidth is approximately 15 THz, corresponding to a pulse length of ~ 30 fs for a transform-limited Gaussian pulse. The central frequency is $f_c \approx 371$ THz and the repetition rate is $f_r \approx 93.2$ MHz, so that an adjustment of f_r by 1 Hz produces a change of ~ 4 MHz in f_c .

sion (GDD). Protected silver and gold mirrors (metal coatings with a protective SiO₂ layer, e.g. Thorlabs PF10-03-P01) seem to adequately minimize the GDD introduced by reflective optics. (No signal was observed in earlier attempts, when multilayer dielectric mirrors were included in the beam path.) Transmissive dispersion due to unavoidable lenses and windows was partially precompensated using a prism compressor or chirped mirrors. Even without additional optics the pulse length increases to ~ 250 fs by the time it can be measured in an autocorrelator, and even after precompensation the shortest measured pulses were ~ 60 fs – at least a factor of two longer than the transform limit of 30 fs. Therefore, we expect that despite precompensation the pulses incident on the atomic beam are strongly chirped.

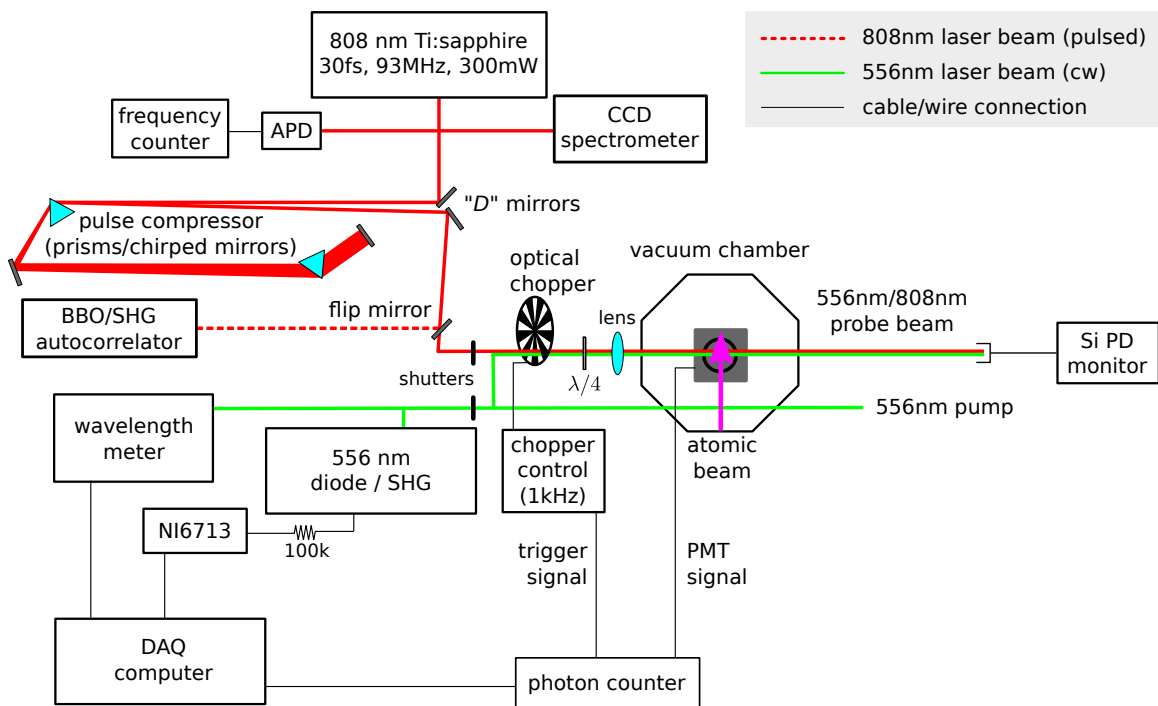


Figure 4.11: Diagram of the experimental configuration used for femtosecond two-photon spectroscopy of the ytterbium atomic beam. The picosecond oscillator shown in figure 4.2 has been replaced by the femtosecond oscillator shown in figure 4.9. The monitors for repetition rate and power spectrum are similar, but a pulse compressor and autocorrelator have been added in place of the LBO frequency doubler. The pulse length at the cavity output is 25-30 fs (inferred from the power spectrum), but this broadens to ~ 250 fs due to propagation through dispersive optical media. Prisms (shown) or chirped mirrors are used in the compression stage to precompensate for dispersion, and their effect can be measured by redirecting the beam into a BBO autocorrelator with a flip mirror. Pulses as short as 60 fs were observed in autocorrelation, using either chirped mirrors or fused silica prisms.

Both fused silica prisms and chirped mirrors were successfully used for pulse compression (see figure 4.12); of these, the prisms were more reliable. This is because their

dispersion relations are better known, and their degrees of freedom continuously tunable (chirped mirrors allow only integer multiples of the per-reflection negative GDD). In either case, the shortest achievable output pulse was approximately 60 fs as measured in a homemade BBO autocorrelator, where the beam path is arranged such that the probe beam can be switched between autocorrelator and experiment by raising or lowering a flip mirror (see figure 4.11). The autocorrelator measures the intensity of second-harmonic light produced in BBO, when the probe beam is divided and recombined on the crystal. By scanning the length of one path with a hollow corner cube on a translation stage, the relative delay between pulses in the two arms is adjusted through zero such that the pulses overlap and produce a measurable enhancement of the SHG intensity. The pulse width is measured by recording the SHG intensity as a function of the delay-stage position and converting the known optical path difference into a corresponding delay of propagation time. The autocorrelator beam paths require a focusing lens and a few other transmissive optics that produce a reasonable approximation of the amount of dispersive glass in the alternate beam path to the ytterbium experiment; we attempt to calibrate the pulse length in the experiment by this means, and expect that the pulses arriving at the atomic beam are between 60 and 80 fs in duration.

Unlike in the picosecond experiment, the optical chopper was necessary to see a signal. It was also crucial to turn off all lights in the lab, including the display panels of most electronics. Even with the chopper wheel for background subtraction, the statistical noise associated with residual ambient light was large enough to wash out the fluorescence signal. As in previous experiments, good beam shaping and minimal diffraction were required to avoid overwhelming the PMT with scattered laser light – in this case, laser light that was already suppressed by six orders of magnitude with a bandpass filter! The ultimately successful detection configuration involved chopping the probe beam at 1 kHz and subtracting back-to-back gated bins from the central 150 μs of each chopper window. The photon counter integrated for 100 s per data point in this configuration, and between 10 and 100 data points were collected between changes of experimental parameters. Signals showing modulation with laser and atomic beam intensity are presented in figure 4.13. The second maximum near 17 mm in figure 4.13(b) may be due to diffracted laser light entering the PMT, as the focusing lens is positioned differently with respect to apertures that were optimized for spatial filtering at 25 mm. Another possibility is that the atomic beam is spatially inhomogeneous (although this was not observed in cw two-photon data).

With optimized lens position and pulse compression, we attempted to measure the excited state spectrum by allowing the repetition rate to slowly drift. Smooth scans of the output coupler over a small range did not show significant modulation of the fluorescence

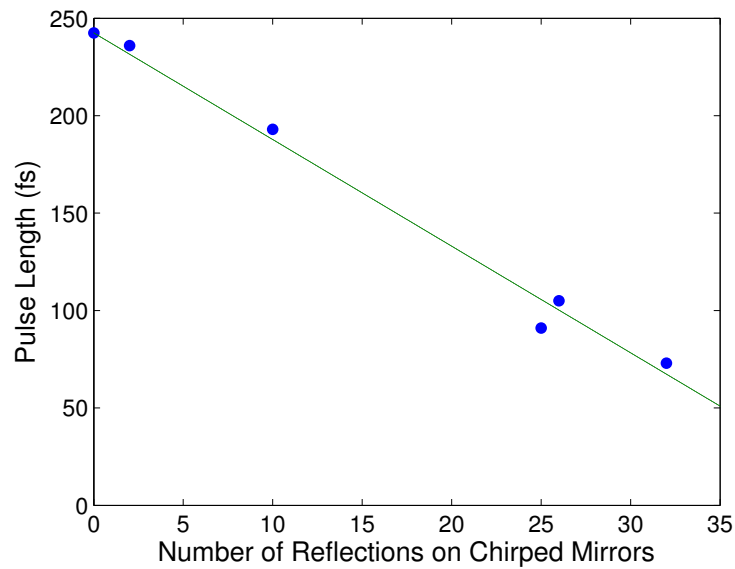


Figure 4.12: Pulse width measured by autocorrelation, as a function of the number of reflections on a set of chirped mirrors. Without chirped mirrors, the pulse width was measured to be 242.5 fs; blue points show measurements. The green line is a linear fit to these data, which indicates a reduction in pulse length by approximately 5.5 fs per reflection. The shortest pulse length achievable with chirped mirrors was 60 fs; additional reflections on the chirped mirrors seem to introduce higher-order dispersion that leads to pulse broadening.

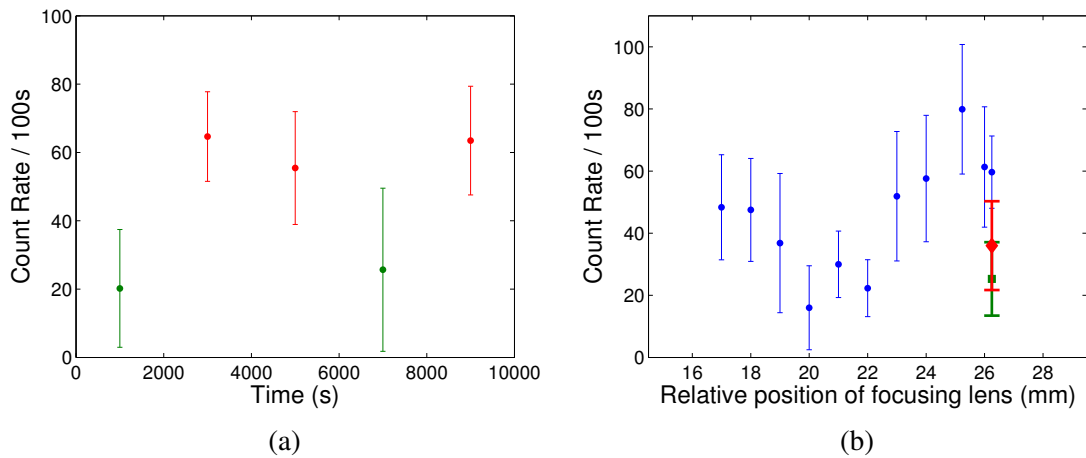


Figure 4.13: Fluorescence data showing the presence/absence of a femtosecond ytterbium signal, and its dependence on the position of a focusing lens for the probe beam. (a) Red data points correspond to both the probe laser and atomic beam on and intersecting; the first green data point has the laser blocked (atomic beam on) and the second has the atomic beam blocked (laser on). (b) Variation of the measured fluorescence intensity as the probe focusing lens is moved, thereby scanning the highest-intensity region through the atomic beam. The peak around 25 mm is the global maximum; the smaller maximum near 17 mm may result from a subsidiary density maximum in the atomic beam, or from diffracted laser light entering the PMT. The green data point on the right-hand plot was recorded with the lens in the same position as the corresponding blue data point, but with the atomic beam turned off. The red data point at the same position was recorded after the oven was turned back on, but not fully warmed up. The full signal, consistent with the blue data point, was recovered when the oven was allowed to warm up completely.

intensity, but figure 4.14 shows frequency-dependent structure in the fluorescence spectrum when the repetition rate was allowed to drift over a large range for an extended period of time. It is not possible to identify specific known transitions in this spectrum, but it is hoped that with an improved signal-to-noise ratio and finer control of the repetition rate it will be possible to perform high-resolution spectroscopy on specific hyperfine and isotopic transitions.

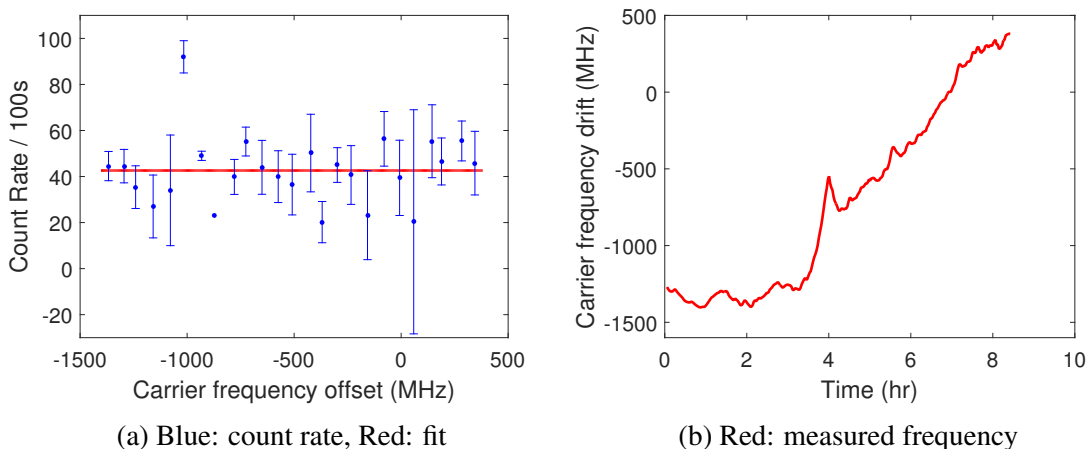


Figure 4.14: (a) Detected count rate as a function of carrier frequency (blue points), which is extrapolated from the measured repetition rate f_r under the assumption that drifts in the carrier-envelope offset frequency f_0 are negligible. The red line shows a fit to a constant “off-resonant” average signal of 43 Hz, corresponding to the situation where no single transition makes a dominant contribution to the measured count rate. The peak visible near -1000 MHz is a resonantly enhanced transition, but the signal-to-background ratio is not high enough to conclusively identify it. (b) Drift of the laser spectrum during the nine hours when the data in plot (a) were collected. Note that a majority of the recorded frequencies are in the range of -1500 MHz to -1000 MHz, so the error bars are correspondingly larger in the range of -500 MHz to 500 MHz.

4.5 Further Thoughts and Improvements

It was hoped that superior control of the repetition rate in the femtosecond system (via active stabilization of the cavity length) and carrier-envelope offset frequency (via a split piezo on the cavity end mirror, or intensity modulation of the pump beam with an AOM) would contribute to a more rapid characterization and optimization of the signal than in the picosecond system, but in fact it was quite laborious even to unambiguously detect a fluorescence signal using the femtosecond probe laser.

Proposed methods to stabilize the picosecond laser spectrum are discussed in section

4.5.1; the essential point is that the laser bandwidth is sufficiently narrow that the experimental effects of drift in f_0 and f_r are indistinguishable. Thus, one can feed back to correct an unknown combination of these independent drifts simply by shifting the entire spectrum with an AOM outside the laser cavity. The difficulty is to find a stable frequency reference within the bandwidth of the laser; fortunately this can be achieved for both xenon and ytterbium using a diode laser stabilized to an atomic potassium resonance. The dynamic range of the AOM technique is limited, and it is likely to require pre-stabilization of the repetition rate using an intracavity piezoelectric transducer. This can be accomplished with commercial (e.g., Spectra-Physics Lok-to-Clock) or homemade apparatus.

Dispersion due to the LBO doubling crystal is also a concern in the picosecond experiments, since any even-order spectral phase will reduce the two-photon excitation rate through interference of different excitation pathways. The configurations used so far all include the LBO crystal in the beam path from the Ti:sapphire cavity to the experiment. A useful diagnostic would be to repeat the picosecond experiments with the doubler removed (or placed behind the atomic beam or vapor cell), to see if the excitation rate is increased beyond what would be expected from the increased incident intensity. If dispersion from the doubling crystal is a limitation in the present experiments, dispersion compensation will likely be required for two-photon experiments with noble gases (which require an additional nonlinear frequency-mixing stage).

A picosecond or experiment with a higher signal-to-noise ratio could map out the excited state spectrum in detail by deliberately scanning the repetition rate; such measurements are envisioned for the determination of hyperfine structure and isotope shifts in radon.

As in the cw case, a magnetic resonance experiment with an RF quenching field is a desirable step toward a two-photon pulsed magnetometer; by inducing transitions between different ground state Zeeman sublevels (or hyperfine levels in the case of rubidium), it should be possible to observe a modulation of the two-photon scattering rate. This modulation will depend on the probe field polarization, even if individual hyperfine transitions are not resolved. This was attempted in the rubidium experiment, but a large baseline modulation was observed due to the presence of a time-varying magnetic field at the PMT location. Future efforts could magnetically shield the PMT, or spatially separate the RF region from the detection apparatus.

4.5.1 Stabilization of the Picosecond Pulsed Spectrum at 808nm

The principal limitation of the picosecond experiments described in chapter 4 is a lack of stability and fine control for the laser spectrum. Since the repetition rate is $f_r \approx 80$ MHz, a change of ~ 9 Hz in f_r is required to change f_c by 40 MHz, the amount required to scan the laser from a “direct” resonance to an “indirect” one (or vice versa). This corresponds to scanning a cavity mirror by approximately $0.25 \mu\text{m}$, which is well within the range of standard piezoelectric actuators. Since f_r is currently unstable at the level of a few tens of hertz, it may be most reasonable to use a stacked actuator with a large dynamic range of several microns for “coarse” stabilization. A harmonic of f_r , measured on an avalanche photodiode (APD), can be stabilized to a RF reference source. This is a standard technique for cavity stabilization of Ti:sapphire oscillators [84].

The difficulty is that even with f_r stabilized, drift of the carrier-envelope offset frequency f_0 in the picosecond system may still be significant. The challenging task of stabilizing f_0 has been overcome in femtosecond frequency combs via a variety of methods for self-referencing, but all such techniques require a spectral bandwidth that is reasonably large in comparison to the carrier frequency (i.e., only a factor of two or three smaller). In fact, any sufficiently stable cw laser can be used as a frequency reference for a modelocked laser, provided its frequency falls within the spectrum of the pulsed laser. A beat note between the modelocked and cw lasers can be measured on an APD and stabilized using standard techniques; the challenge then lies in obtaining a sufficiently stable cw laser at a useful frequency.

Fortunately, the 404.8 nm and 404.5 nm potassium transitions from the $3p^6 4s \ ^2S_{\frac{1}{2}}$ ground state to the $3p^6 5p \ ^2P_{\frac{1}{2}, \frac{3}{2}}$ excited states (sometimes referred to as the “second doublet”) fall nearly within the bandwidth of 2 ps pulses at 404.0 nm. The latter are already produced in our picosecond ytterbium experiment by passing the 808 nm probe beam through the LBO doubling stage; except for modelocking diagnostics, the resulting 404 nm light is not used in the experiment. We therefore envision a cw diode laser stabilized to a 404.5 nm potassium resonance by polarization spectroscopy, saturated absorption spectroscopy, a dichroic atomic vapor laser lock (DAVLL), or other standard technique. This is overlapped with the pulsed 404 nm beam on an APD, to produce a beat note for stabilization as shown in figure 4.15.

The spectral bandwidth of the picosecond oscillator can be tuned by roughly a factor of two using a single GTI. It may be that the frequency-doubled spectrum in the current configuration (FWHM ≈ 0.25 nm) has insufficient spectral intensity at 404.5 nm to produce a useful beat note with a potassium-stabilized diode laser; in this case the GTI should be

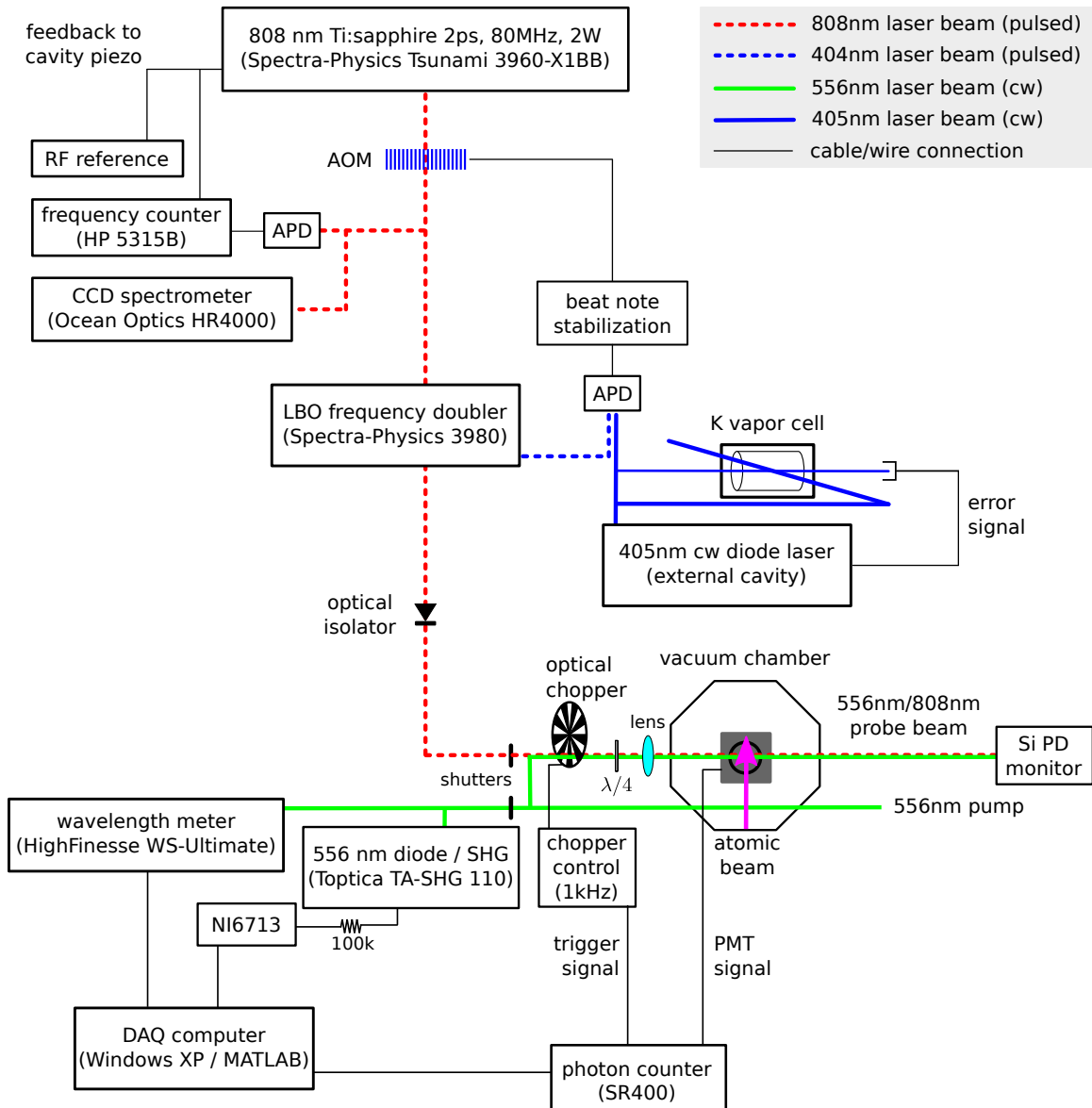


Figure 4.15: Stabilization scheme for the picosecond ytterbium experiment. A cw diode laser at 404.5 nm is locked to a potassium reference cell, and its heterodyne beat frequency with the second harmonic beam from the Ti:sapphire is measured with an avalanche photodiode (APD). The beat frequency is stabilized by adjusting the drive frequency of an acousto-optic modulator (AOM) in the original 808 nm beam. The cavity length can be separately stabilized with a piezoelectric transducer, by separately locking a harmonic of the repetition rate f_r to a RF reference oscillator. The AOM thus feeds back to a combination of f_0 and f_r , but the spectral bandwidth of a picosecond pulse is sufficiently narrow that this distinction is not important.

adjusted to broaden the spectrum, or replaced with one that allows slightly shorter pulses.

To transfer the lock to the 808 nm beam, the output of the cavity-stabilized Tsunami can be directed through an acousto-optic modulator (AOM), which acts as a common-mode frequency shifter for all axial modes in the pulsed laser spectrum. By changing the drive frequency of the AOM, the spectrum can be easily shifted by several times the inter-mode spacing of $f_r \approx 80$ MHz. This frequency shift is transferred to the 404 nm spectrum, and thus affects the beat note with the potassium-stabilized diode laser. Considering the potassium to be an absolute frequency reference, we need only adjust the AOM frequency to stabilize the beat note in order to transfer that stabilization to the picosecond oscillator. This can be accomplished with standard RF electronics and a relatively simple feedback circuit.

A remaining concern is what happens if the laser spectrum diabatically “jumps” by a full axial mode spacing, in which case the error signal from the potassium lock will transfer the locking point to a new axial mode and the Ti:sapphire spectrum will remain stabilized with an 80 MHz offset (or 160 MHz, etc.). This can in principle be prevented by modulating the repetition rate at a relatively slow frequency, such that the phase of the modulation is abruptly shifted by 180° in the event of such a jump. Once stabilized, the system can thus be prevented from locking to the “wrong” axial mode.

4.5.2 Modelocked Picosecond Pulses for Xenon

Figure 4.16 shows a scheme for pulsed two-photon spectroscopy of the 256 nm xenon transition, where the excitation light is produced by third-harmonic generation from the existing picosecond Ti:sapphire oscillator. This can be accomplished starting from 768 nm light (which is easily produced by the Ti:sapphire laser in its current configuration) and generating the second harmonic in LBO. We have produced over 200 mW of average power at 384 nm using the single-pass LBO doubler described in chapter 4, with approximately 1.5 W remaining in the residual 768 nm beam. The presently missing piece is a BBO sum-frequency generator that would combine the 384 nm and 768 nm pulses to produce 256 nm, hopefully resulting in an output beam with several milliwatts of average power.

A significant advantage of pulsed lasers, already mentioned in chapter 4, is that the relevant optical damage mechanisms scale with average intensity rather than peak intensity. At minimum, this means that the situation is not worse than for a cw laser of the same average power, but in fact it may be considerably better since resonant cavity enhancement is not typically required for pulsed frequency mixing (due to the much higher peak intensity). Single-pass frequency mixing also means that dispersion from the nonlinear crystal is not

compounded on successive round trips, and we can extrapolate the expected spectral phase profile using the Sellmeier equations for BBO (see [85] and references therein).

Modelocking is reliably transferred to the ultraviolet by nonlinear frequency conversion, but the fundamental oscillator must again be stabilized. Remarkably, there is again a conveniently located potassium doublet that can in principle be used as an absolute frequency standard. The potassium D-line transitions occur at 766.7 nm and 770.1 nm, and standard techniques developed by atomic physics laboratories over the last twenty years have made it routine to stabilize external-cavity diode lasers at these wavelengths. Since both D-lines are detuned from the 768 nm Ti:sapphire wavelength by more than two bandwidths of the pulsed spectrum, a different GTI is probably necessary to broaden the pulse spectrum in order that axial modes overlapping with the potassium resonance can be excited.

4.5.3 Radon EDM

An EDM search is planned using isotopes of radon, in which a nuclear octupole deformation is expected to significantly enhance sensitivity to CP -violating physics [21, 86]. All isotopes of radon are radioactive, and the isotopes that are relevant for EDM searches have half-lives on the order of 30 minutes. The experimental approach involves obtaining radon gas from a rare isotope beam facility and polarizing it using spin-exchange optical pumping. The polarized spins can then be manipulated with magnetic resonance pulses to initiate free precession in the presence of applied external electric and magnetic fields. The angular correlation of decay products with the instantaneous spin orientation would be used to read out Larmor precession, and the measured precession phase used to place a bound on the nuclear EDM in the usual way.

Such an experiment is extremely technically intensive, and direct optical magnetometry with radon is a desirable alternative to detailed characterization of the time-varying decay spectra. The precision available from gamma anisotropy measurements is limited by detector efficiency and the fact that only decay products are measured, whereas every radon atom in the cell can contribute to an optical magnetometry based method.

The longest E1 wavelength for one-photon excitation of radon is 179 nm, near the long-wavelength limit of the vacuum ultraviolet. On the other hand, two-photon transitions out of the ground state are available at wavelengths as long as 300 nm. In particular, a transition at 257 nm is very near the 256 nm xenon resonance, and in fact is even better suited to the stabilization scheme proposed in section 4.5.2 since the potassium resonance at 770.1 nm is closer to the center of the fundamental spectrum.

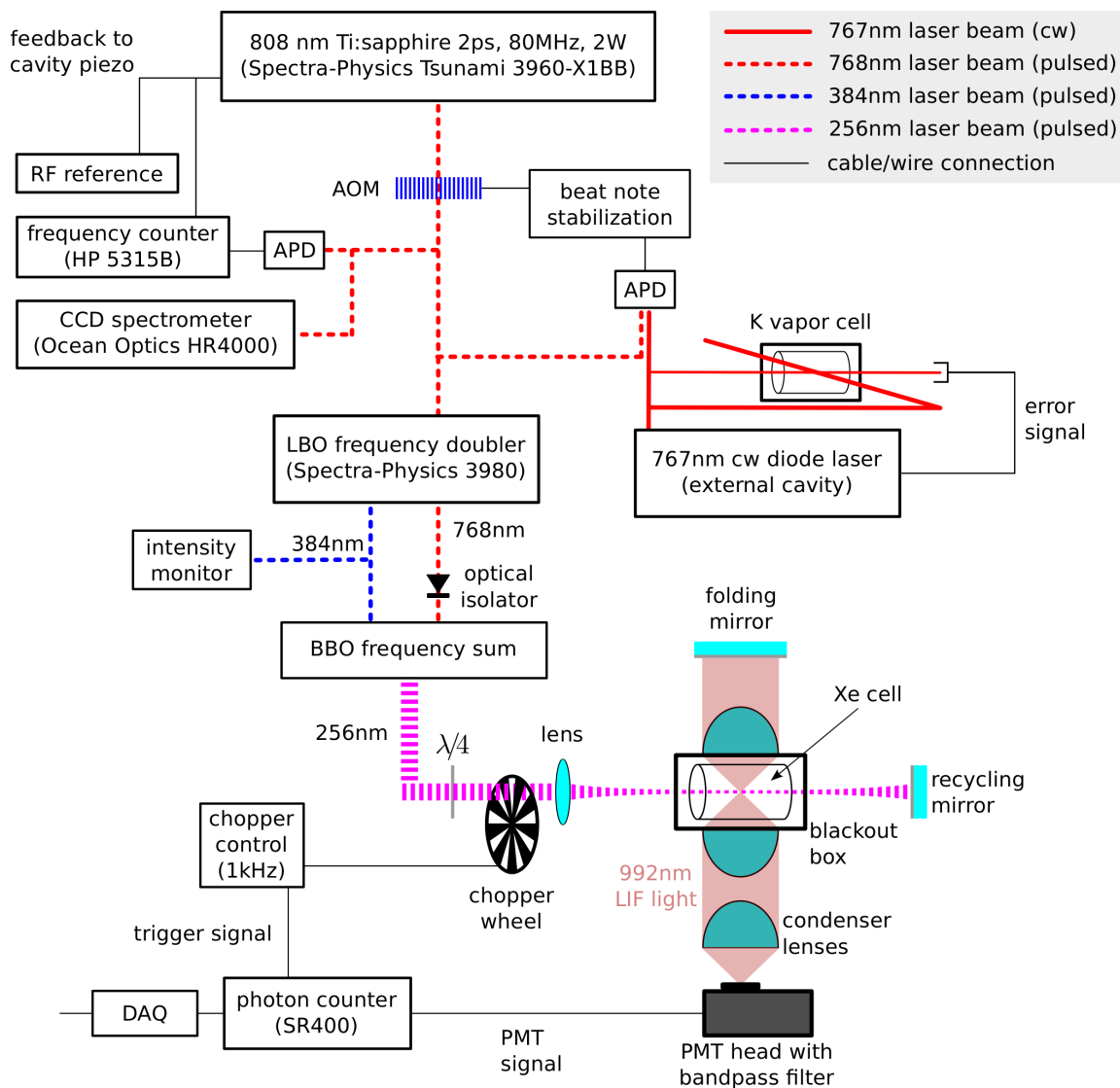


Figure 4.16: The scheme envisioned for producing stable picosecond pulses at 256 nm for two-photon spectroscopy of xenon. Most features of the laser stabilization are similar to those detailed in figure 4.15, with the difference that the potassium D-line resonance at 766.7 nm or 770.1 nm is used as an absolute reference to stabilize the 768 nm fundamental output of the Ti:sapphire. The stabilized 768 nm beam is frequency-doubled to produce 384 nm, followed by a sum-frequency stage in BBO to produce 256 nm. The experimental apparatus for xenon spectroscopy is similar to the one described for rubidium in section 4.3.

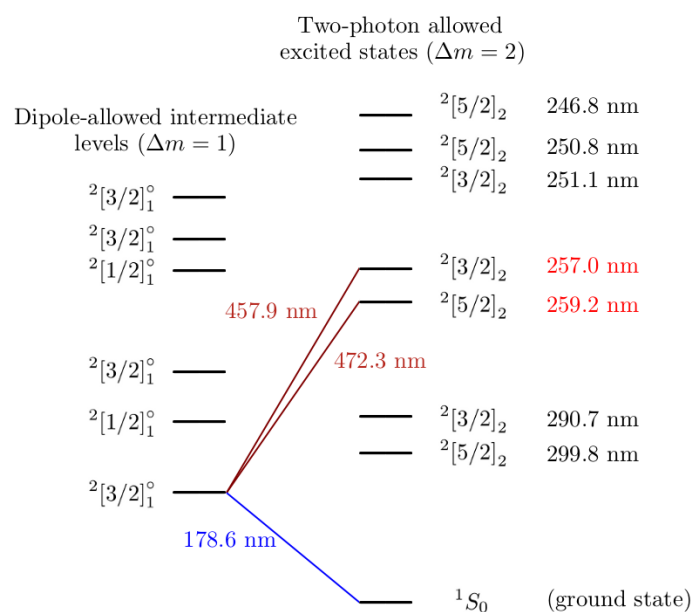


Figure 4.17: Some excited states and intermediate levels relevant to two-photon excitation of radon. The red wavelengths are close to the xenon transition at 256 nm and could therefore be obtained from a xenon experiment with minimal adjustments.

CHAPTER 5

Cells and EDM Applications

Optical magnetometry, searches for a permanent electric dipole moment (EDM), and other precision measurements involving polarized spin distributions very often rely on gaseous samples contained in sealed cells. The statistical precision of such measurements is limited by the number of polarized atoms or molecules in the cell and by their spin coherence time, both of which can be quite large in comparison to the values achievable in laser traps or storage rings. This chapter discusses the production and optimization of cells for optical magnetometry and EDM searches involving polarized ^3He and ^{129}Xe . We also briefly touch upon some related issues involving spin-exchange polarization, refillable valved cells, and stand-alone noble gas polarizers.

The technical requirements imposed on cells for hyperpolarized diamagnetic atoms depend on the type of measurement for which they are intended, and on which systematic effects are likely to limit it. The shape, size, material(s), cleaning and filling procedures, internal coating (if any), and filling pressure can all limit the achievable polarization amplitude and lifetime. Other effects that may enter the error budget of a precision measurement include shape-dependent frequency shifts, motional averaging in different regimes of number density and field strength, the rate of dimer formation and break-up, decoherence and frequency shifts due to magnetic impurities, and (especially in EDM experiments) effects related to the presence of electric fields inside the cell. The method of polarization and the precise mixture of different atomic and molecular species can modify these effects, and also place bounds on the maximum achievable signal.

Each degree of freedom in cell production has an optimal value or range; for example the filling pressure should be sufficiently high that the cell contains enough particles for the desired statistical precision, yet not so high that the spin coherence time is significantly reduced by the high collision rate. However, other degrees of freedom may conflict with that optimum. For example, in EDM experiments the final precision also depends on the applied electric field strength, with the result that dielectric breakdown may impose a high-pressure limit more stringent than the one due to collisional decoherence. The next section

summarizes the different limitations associated with optical magnetometer cells and EDM cells, and the following sections survey how these requirements can be satisfied in practice.

5.1 Requirements for Optical Magnetometry

The most obvious requirement for optical magnetometry is that the cell be optically transmissive at the relevant wavelengths. For ^{129}Xe , the excitation wavelength is 256 nm and the infrared fluorescence wavelengths are 904.8 nm and 992.6 nm (see chapter 3, figure 3.25). Pyrex and GE-180 have poor optical transmission at 256 nm, and materials with high ultraviolet transmission such as MgF_2 , LiF , and sapphire (Al_2O_3) cannot be worked with a torch like optical glasses (see section 5.4.1 for an alternative approach to cell construction using these materials). The most practical options remaining are quartz and fused silica, which can be worked with a torch and even welded to each other. In particular, a 1 cm thick window of uncoated ultraviolet-grade fused silica (UVFS) can transmit $> 90\%$ of the incident optical power at 256 nm (loss is dominated by Fresnel reflection).

It is also desirable that atomic polarization in a magnetometer should not relax too quickly. The walls of glass cells are known to generally contain spin-depolarizing paramagnetic impurities. The effect of these can be mitigated by the application of antirelaxation coatings such as octadecyltrichlorosilane (OTS) [87–90], and to some extent by proper cleaning protocol. The effect of antirelaxation coatings is two-fold: the “sticking time” during which the atom is transiently bound to the wall is reduced so that the depolarizing perturbation is applied for a shorter time, and the distance between the atom and the impurity is increased so that the perturbing magnetic field (usually modeled as a point dipole) is substantially reduced at the location of the polarized nucleus. Iron-free aluminosilicate glasses such as GE-180 and Corning 1720 have favorable noble gas relaxation properties even without wall coatings [91–97].

5.2 EDM Measurements: the HeXe Experiment

EDM experiments require the application of large static electric fields to the cell’s interior volume. The field must be applied in such a way that it is not screened from the interior by the electrostatic displacement of bound charges in the cell walls; in practice this means that electrodes must be located inside the cell. A simple way to accomplish this is to make a cylindrical cell whose end walls are also electrodes, with a glass cylindrical body providing an insulating barrier between them. We have developed such cells for EDM experiments using a modified hydroxide-catalysis bonding method [2], which is discussed

in section 5.6 below. This section briefly surveys experiments conducted by the HeXe collaboration, which has used those cells in developing a new approach to measuring the nuclear EDM of ^{129}Xe . Further details concerning these and related measurements are available in [2, 98, 99].

These measurements employ low T_c (LTc) SQUID gradiometers to measure the precession of polarized ^3He and ^{129}Xe nuclei in the presence of applied electric and magnetic fields. The noble gases are polarized using SEOP with rubidium, in an aluminosilicate optical pumping cell operated in a flow-through configuration. The evacuated optical pumping cell contains rubidium metal, and unpolarized gas is introduced from a separate gas handling system via manually actuated valves. The ratio of noble gas partial pressures is chosen to produce comparable magnetic field sensitivities when accounting for differences in gyromagnetic ratio and polarization efficiency between the two species [98]. The total pressure in the optical pumping cell is typically in the range of one bar, including 5-10% nitrogen buffer gas for collisional quenching of excited rubidium. The cell is contained within a calcium silicate oven, and maintained at a temperature of approximately 150°C using flowing air. A magnetic field around 4 mT is produced by external coils, and polarization build-up can be monitored using pulsed NMR at a resonance frequency of 40 kHz for ^{129}Xe (the field can be changed to bring the ^3He resonance down to the same frequency). Equilibrium polarization is typically achieved after several hours of optical pumping with a 100 W circularly polarized beam from a 795 nm laser diode array.

An EDM cell with silicon electrodes is evacuated and connected to the optical pumping cell, and then filled by opening a valve once equilibrium polarization has been reached. It is mounted in a cell holder with high voltage connections for the two electrodes, and mechanically transported into a magnetically shielded room (MSR) through a hole in the wall. The MSR has three layers of passive shielding: one aluminum layer for RF suppression, and two layers of μ -metal (Krupp Magnifer) for magnetic shielding [99]. At the center of the MSR, the residual magnetic field is below 1 nT and the residual gradient is below 300 pT/m. An internal static bias field of approximately $1.2 \mu\text{T}$ is supplied by three-axis Helmholtz coils inside the MSR, resulting in Larmor frequencies of approximately 40 Hz for ^3He and 14 Hz for ^{129}Xe .

The cell is placed under a grounded silicon wafer (see figure 5.1), which protects the SQUIDs from damage in case of a high voltage breakdown; the liquid helium dewar that contains the SQUIDs is positioned directly above this wafer. The pickup coils for the SQUID sensors are arranged on the faces of a 30 mm cube, such that two channels are available for each axis. The six channels are accordingly referred to as X1, Y1, Z1, X2, Y2, Z2 and are oriented such that these labels agree with the coordinate axes shown in figure 5.1

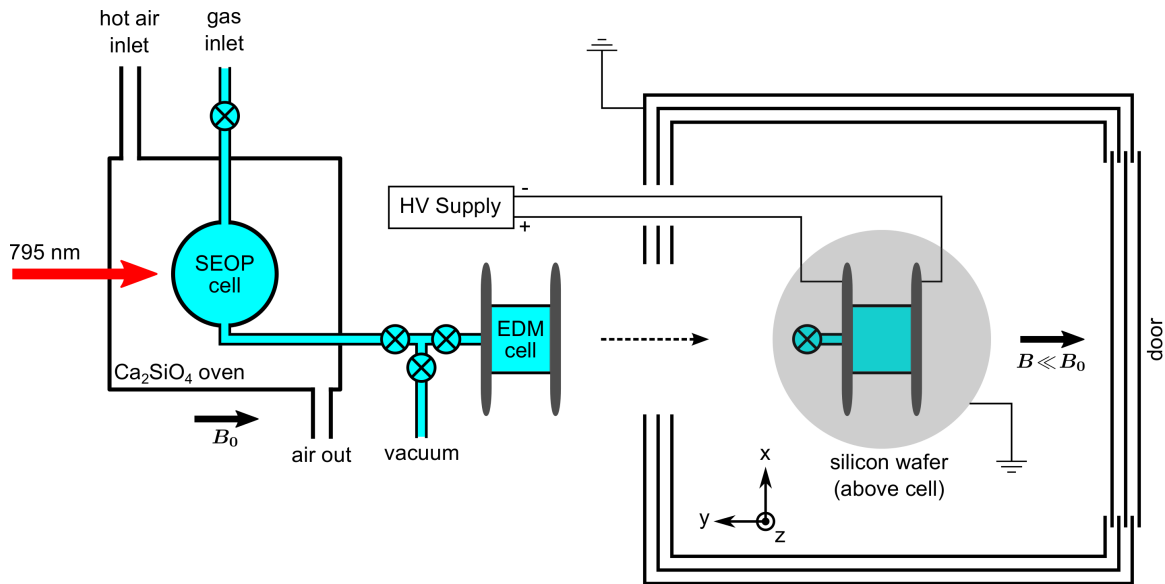


Figure 5.1: Block diagram of central components in the HeXe EDM experiment. A spin-exchange optical pumping cell containing rubidium, N_2 buffer gas, ^3He , and ^{129}Xe is contained in a calcium silicate oven and heated to 150°C by flowing air. A magnetic field along the beam axis of approximately 4 mT is produced by coils outside the oven (not shown). The rubidium vapor is maintained at nearly 100% polarization by D1 optical pumping using a 100 W circularly polarized beam (produced by a 795 nm laser diode array); this polarization is collisionally transferred to the noble gas nuclei over a period of several hours. The polarized gas is introduced to an evacuated EDM cell using manually actuated valves, and the cell is transported into a magnetically shielded room whose walls include an aluminum layer for RF shielding and two layers of μ -metal (Krupp Magnifer) for passive magnetic shielding. The cell's silicon electrodes are connected to high voltage leads to produce an internal electric field, and it is placed directly underneath a nonmagnetic liquid helium dewar containing a six-channel LTc SQUID sensor (not shown). The grounded silicon wafer serves as a protective barrier for the SQUIDs in case of high voltage breakdown. A magnetic field of approximately $1 \mu\text{T}$ is supplied by three-axis Helmholtz coils within the room (not shown), and spin precession is initiated either by rapidly changing the direction of this applied field, or by using one pair of coils to produce a resonant NMR pulse.

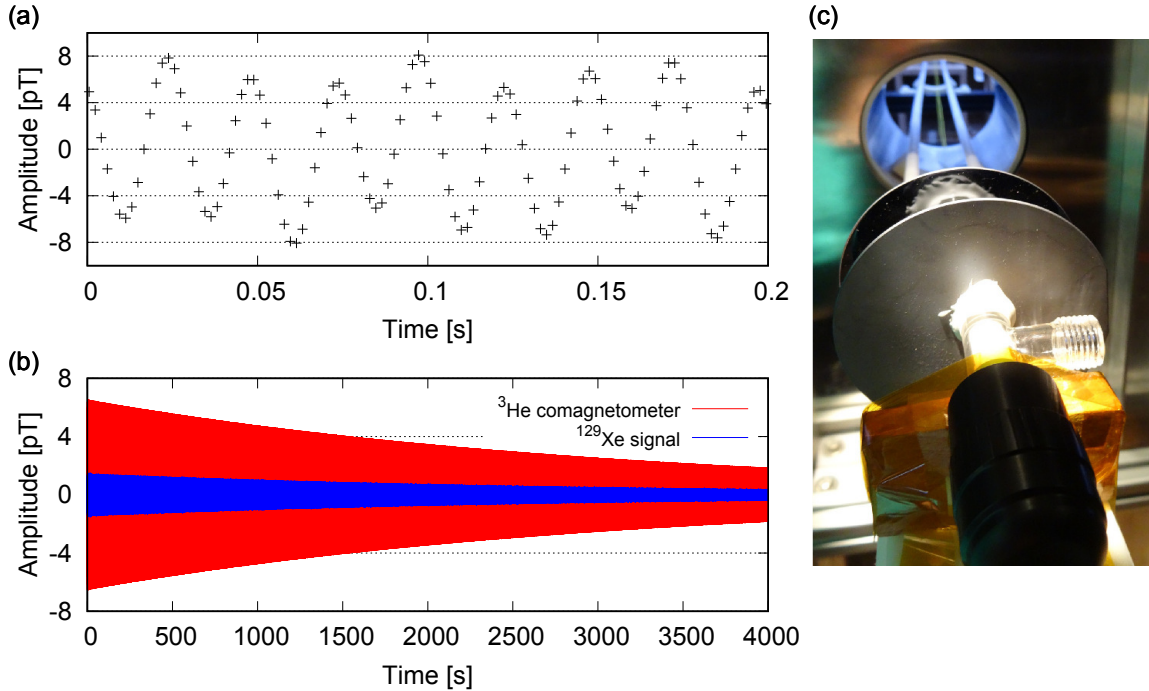


Figure 5.2: (a) Spin precession signals of ^3He and ^{129}Xe at frequencies of 40.8 Hz and 14.8 Hz, respectively, detected by the LTc SQUID sensor (Z1) at a distance of about 110 mm to the center of the EDM cell. (b) Free precession decays of ^3He (red) and ^{129}Xe (blue) (signals were filtered by a software FIR bandpass filter of 4 Hz width centered at the corresponding Larmor frequencies) (c) EDM cell mounted on the transport system. (Reproduced from [2] with permission of Springer; figure and caption © Springer International Publishing Switzerland 2016.)

(acceleration due to gravity is into the page, along $-\hat{z}$). Gradiometric measurements are performed by subtracting the signals for each pair of channels; the spin precession signal is typically measured using the $Z1-Z2$ gradiometer. For EDM measurements, the applied electric and magnetic fields should be parallel; the simplest configuration is to thus orient both along the \hat{y} axis, with the result that the spins precess in the xz plane. Gradiometry in this configuration has the significant advantage that it is only sensitive to magnetic fields that vary significantly over 30 mm (e.g. the spin precession signal, which has the strong spatial dependence of a magnetic dipole).

High voltage is applied to the cell's electrodes from a supply outside the MSR, using insulated leads and copper contacts. After proper conditioning, the cells can typically sustain electric fields of 4 kV/cm across a 2.5 cm electrode gap (we expect the ultimate limitation to be the dielectric strength of helium gas). The electric field and high voltage apparatus do not measurably affect the SQUID system.

Spin precession is initiated by a rapid change of the bias field direction, or by using one

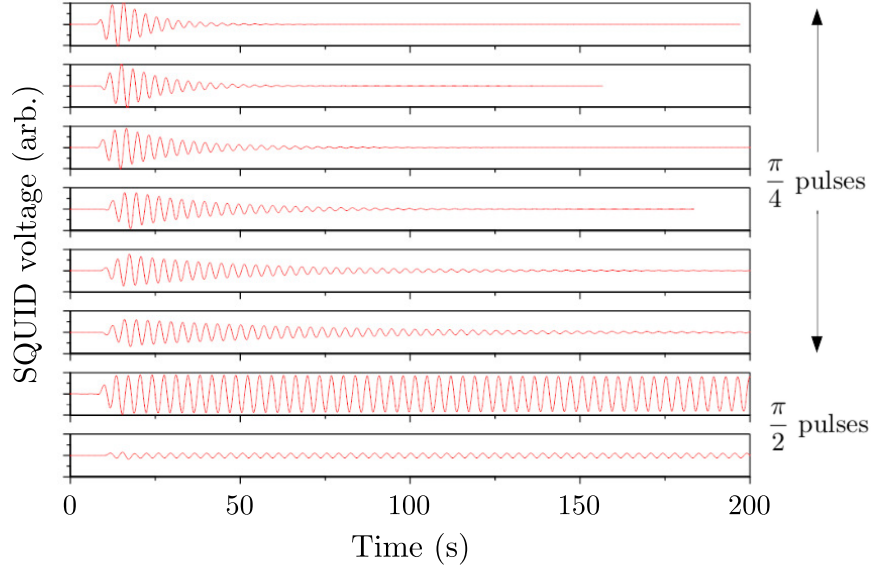


Figure 5.3: Gradiometer signals recorded from the SQUID sensor, following a series of NMR pulses (ordered in time from top to bottom). Note that the transverse relaxation time increases with each successive $\frac{\pi}{4}$ pulse; this effect may be due to the diminution of a large longitudinal magnetization component, which is assumed to produce rapid relaxation of the precessing spins. When a $\frac{\pi}{2}$ pulse is applied instead, most of this longitudinal magnetization is rotated into the precession plane and the transverse relaxation time increases substantially. The small signal resulting from application of a second $\frac{\pi}{2}$ pulse is consistent with the assumption that little longitudinal polarization remains after the first $\frac{\pi}{2}$ pulse.

set of Helmholtz coils to produce a $\frac{\pi}{2}$ pulse for both nuclei. The SQUID signal is the output voltage of a flux-locking circuit (flux-locked loop), provided by two custom electronics modules (Magnicon); this is recorded by a 24-bit USB DAQ system (Data Translation, DT 9826-16 USB). Reference [98] contains further details of the data acquisition system and experimental components.

Figure 5.2 shows a typical dataset, and figure 5.3 demonstrates some effects that result from successive application of multiple NMR pulses. We have observed transverse relaxation times exceeding 4500s for both species, simultaneously, in the presence of high voltage. (This indicates that noble gas relaxation due to interactions with the silicon walls will not be a limiting factor in this type of EDM search.) Together with the observed signal amplitudes (several pT) and noise densities ($15 \text{ fT}/\sqrt{\text{Hz}}$), this implies an achievable frequency resolution per measurement on the order of 1 nHz [2]. The equivalent EDM sensitivity can be estimated from this value; it may approach $10^{-27} e \text{ cm}$ per measurement, but we must consider that systematic effects (which have not yet been addressed) are expected to dominate the final error budget.

In addition to challenges associated with electrodes and cell construction, EDM cells

are often limited by breakdown and frequency shifts. This places limitations on the shape and filling pressure that can be accommodated in an EDM measurement, and EDM cells are typically designed around such practical limitations. Fortunately iron-free aluminosilicate glasses are characterized by high bulk resistivity and low helium permeability in addition to their intrinsically favorable magnetic and spin-relaxation qualities.

5.3 Glass Design and Vacuum Filling Station

Glass working to produce cells and cell components was done by Roy Wentz in the chemistry department's glass shop at the University of Michigan. A typical manifold with three cells is shown in figure 5.4. Most cells prepared in our lab conform to this general scheme, and are prepared and filled (after cleaning) on the vacuum and gas-filling system shown in figure 5.5. The attachment point to the vacuum station is a glass-to-metal Kovar joint, which couples the glass manifold to a standard 1-1/3" ConFlat flange. The sidearm for alkali loading and distillation is relevant only to cells containing alkali metal, but this is actually a majority of the cells considered here since rubidium is used for spin-exchange optical pumping (SEOP) of xenon and helium. In most cases the entire manifold is made of "pyrex" (really borosilicate, see below), with graded seals to match thermal expansion with other glass types if such are used for the cells themselves. We have also used quartz and aluminosilicate manifolds, but these present greater challenges to the glassblower and few significant advantages in cell preparation.

The process for preparing and filling cells can be roughly divided into four parts:

1. **Pre-cleaning (and coating):** The glass is cleaned with detergent, organic solvents, and corrosive piranha solution (see below) to remove surface contaminants. This is critical for cells containing reactive elements or intended for experiments that require long polarization lifetimes. Antirelaxation coatings, when used, are applied and cured after cleaning and before bake-out.
2. **Pump-down and bake-out:** The manifold is attached to the vacuum system and open ports (used for cleaning access) are sealed with an oxygen-propane torch. Alkali metal is often introduced at this point, by opening an ampoule and placing it in the sidearm immediately before sealing the top of the sidearm and pumping away atmospheric gas with the vacuum station. The exposed alkali invariably oxidizes during this process, and once the manifold is sealed and pumped out the ampoule is usually heated through the glass with a torch just until the alkali metal melts. Once the metal has melted, the oxide has also been eliminated (e.g. by dissociation, by

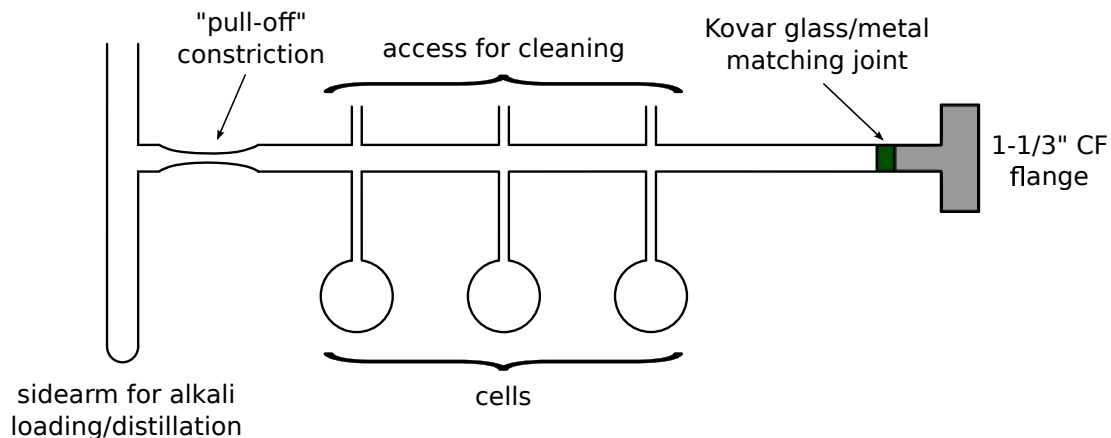


Figure 5.4: Typical layout of a three cell manifold prepared for filling on the vacuum system shown in figure 5.5. The connection to the vacuum system is made with a standard 1-1/3" ConFlat flange, which is attached to the glass manifold via a Kovar joint. The open apertures (including the sidearm for alkali-loading) are used for cleaning, and sealed with an oxygen-propane torch when the manifold is attached to the vacuum system. Virtually any cell with a glass stem can be attached to this type of manifold for filling, but a thermal-expansion-matching layer may be necessary for certain glass types. The manifold – apart from the cells – is almost always made of pyrex, or occasionally quartz.

pumping away volatile elements, or by submersion of the residual crust in the liquid metal). Part of the reason for having a separate sidearm is so that the contaminated alkali can be re-distilled into the rest of the manifold, thus increasing the purity of what is finally introduced to the cells.

The sealed manifold is then baked under vacuum, usually for 12-48 hours at a temperature between 80°C and 250°C. The base pressure of the system is monitored with an ion gauge during this time (see figure 5.5), and the chemical composition of background gas can be determined with a residual gas analyzer (RGA). A typical base pressure reached after bake-out is in the range of 10^{-7} - 10^{-8} Torr.

3. **Filling:** Alkali is “chased” from the sidearm into the cells using a propane-oxygen flame. Alternatively, the alkali can be slowly distilled into the cells by heating the entire manifold with the exception of the cells themselves and a section of glass tube leading up to the glass-metal joint. In this case, hot alkali vapor condenses on the unheated surfaces and is trapped there: atoms that enter the cells do not escape, and alkali is prevented from migrating out of the manifold by the barrier section of unheated tube. This may result in higher-purity alkali in the cells, but care should be taken to preserve an adequate length of unheated glass (or preferably, a section of tubing that includes a bend) between the cells and the pumps, in order that significant

quantities of alkali are not introduced to the rest of the vacuum system. Coated cells should be heated only gently in the presence of alkali, since OTS reacts with hot alkali vapor at temperatures above $\sim 200^{\circ}\text{C}$.

The desired gas mixture is flowed into the cell from pre-attached reservoir bottles, and partial pressures are measured with a 1000-Torr Baratron gauge. For this step, the gate valve connecting the manifold to the vacuum pumps should be closed, and only the valves leading from the gas source through the appropriate getter to the cell left open. If a super-atmospheric cell is required, the cell may be submerged in liquid nitrogen to reduce the internal pressure while it is filled and pulled off.

4. **Pull-off:** The thin glass tube (usually 0.25" or 6 mm) is sealed shut with a propane-oxygen flame, and the cell pulled off from the manifold while the glass is soft. For vacuum and sub-atmospheric pyrex cells, the glass has a tendency to collapse inward due to the pressure difference from atmosphere to vacuum. If a significant amount of gas is loaded inside the cell, one must work relatively quickly such that the cell can be pulled off before the gas inside heats up and expands, "blowing out" the pull-off point and ruining the cell. Liquid nitrogen can also be used to reduce the internal pressure, and since xenon freezes at liquid nitrogen temperature, cells with quite high xenon pressures can be made in this way. The pull-off point of the sealed cell should be annealed with a softer flame to remove thermal stress resulting from the high temperature gradient during pull-off.

Most cells prepared in our lab are cleaned according to a standard protocol, which was developed for the application of OTS antirelaxation coatings. The procedure is as follows:

1. **Alconox wash:** Wash with a warm solution of Alconox detergent in distilled water, especially if the glass received from the shop is particularly dirty. This removes grease and dirt, but can be skipped if the cells are reasonably clean.
2. **Organic solvents:** Rinse the cells with methanol and/or acetone if they seem particularly dirty. This step is also sometimes skipped, when the glass is already somewhat clean.
3. **DI water rinse:** Rinse three times with deionized water.
4. **Piranha clean:** Mix piranha solution (30% H_2O_2 and 97% H_2SO_4 in a 7:3 volume ratio), pour into the manifold, and allow to sit and work for one hour. If the geometry is such that part of the manifold cannot be submerged in piranha, it should be

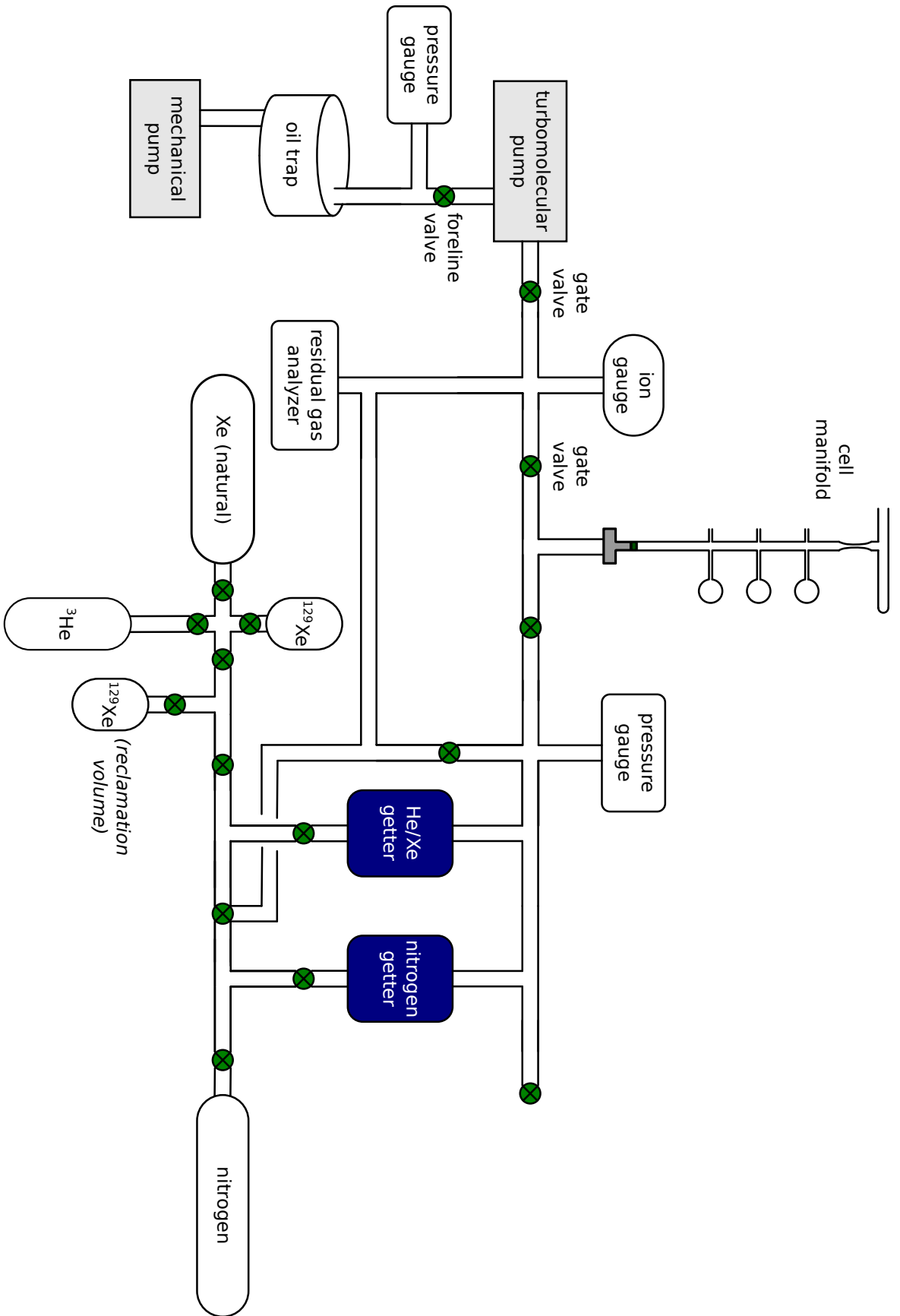


Figure 5.5: Layout of the vacuum system used for cell filling. All tubing is stainless steel.

repositioned periodically during this time to ensure that the entire interior surface is cleaned. This is a good idea anyway, since piranha produces bubbles of glass that easily become trapped inside the cells and should be encouraged to escape so that they do not shield part of the inner surface from the piranha itself. This step is the one most responsible for removing contaminants from the glass surface, and care should be taken after it is complete not to reintroduce any contamination.

5. **DI water rinse:** Rinse three times with deionized water.
6. **Methanol rinse:** Rinse three times with “clean” methanol, i.e. spectrophotometric grade. This removes any residual traces of the piranha mixture.
7. **DI water rinse:** Rinse three times with deionized water. By this point, the glass is usually clean enough that water interacts with the surface in a noticeably different way – surface tension makes it difficult to get water in and out of the cells. Small residual drops can be blown out with clean dry nitrogen gas, and if a large amount of water becomes trapped in a cell, a clean glass or teflon capillary can be used to introduce air and allow it to flow out. Care should be taken to use equally clean capillary, and to avoid brushing the interior surface of the cells.
8. **Dry and coat:** At this stage, the cells can be dried and coated (see [87] for details of the coating recipe).

5.4 Survey of Some Bonding Methods Relevant to Cell Fabrication

5.4.1 Hydroxide-Catalysis Bonding

When the materials desired for a cell cannot be worked by conventional glassblowing, do not have well-matched coefficients of thermal expansion, or include delicate components such as optical coatings that may be destroyed by glass working, it is possible to produce seals cells from pre-formed parts with various bonding techniques. Numerous methods of bonding glass to silicon, metals, glass, and other materials have been developed over years of extensive industrial research (especially wafer bonding in the context of nanofabrication), and we will not attempt to survey them. The silicate-assisted hydroxide catalysis bond described here was developed for space-based research instrumentation and gravitational wave interferometers [100–106]; to our knowledge this is the first application of the technique to fabrication of vapor cells.

Hydroxide-catalysis bonds are formed by successive hydration and dehydration of a silica surface, catalyzed by a hydroxide such as NaOH in aqueous solution. During the hydration process hydroxide ions in the bonding solution etch the surface and release silicate ions [107], which subsequently dissociate into the silanol $\text{Si}(\text{OH})_4$. As the hydroxide ions are used up, the pH of the solution lowers and the silanol gradually polymerizes into siloxane (Si-O-Si) chains. The polymerization process releases water, which evaporates, migrates, and diffuses away from the bond layer. When fully dehydrated, the surfaces are joined by a rigid network of siloxane bridges; the settling time increases with initial pH and decreases with annealing temperature.

The siloxane network that forms the final bond can also anchor to a surface oxide layer on silicon. Silicate-bearing substrates can be bonded to other oxygen-rich surfaces in this way, and bonds between two non-silica surfaces (e.g., alumina or silicon carbide) can be achieved by introducing a silicate bonding solution, provided that both surfaces contain sufficient oxygen to bond with the silicate. It appears that for silicon and silicon carbide, the presence of a surface oxide layer is extremely important to the success of the bond [106].

Hydroxide-catalysis bonding was developed for fused silica elements in Gravity Probe B, and is now used in the GEO600 gravitational wave detector to connect weight-bearing fibers to the interferometer's suspended mirrors [105, 106]. The bond's high mechanical strength (approaching that of bulk silica), stability, and resistance to temperature fluctuations were important factors in its selection for interferometric and space applications. For purposes of optical alignment, the settling time and strength of the bond can be adjusted via the concentration of the bonding solution. The settling time is an increasing function of initial pH (since a more basic solution takes longer to neutralize), and the ultimate bond strength depends on the silicate density since this affects the final density of siloxane bridges. The curing period may be reduced from a typical four weeks by annealing the bond above room temperature.

Typically only a few microliters (or less) of aqueous hydroxide solution are required to bond surfaces of a few cm^2 in area; the resulting bond layer is less than 100 nm thick, and the required global surface flatness is usually quoted as $\lambda/10$ (i.e., 60-100nm). This requirement may be relaxed to approximately $\lambda/4$ through use of a (few-percent) silicate bonding solution which extends the siloxane network across larger interstitial voids. Optical contact bonding (also known as "wringing" [108–110]) can occur when the bonding surfaces are locally flat and globally conformal on length scales of $\sim 1\text{nm}$. When the contact area is sufficiently large, the surfaces bind via van der Waals forces, hydrogen bonds, and dipole-dipole interactions. Hydroxide catalysis bonding also requires optical contact between the surfaces, but the use of liquid bonding catalysts or filler materials can some-

what relax the stringent flatness requirements. Elastic deformation of large pieces can also compensate for local roughness, but this is negligible on the millimeter to centimeter dimensions that are relevant for most cells. The contact area for vapor cell bonds is typically small (less than 1 cm²), with the result that optical wringing is noticeable during the bonding process but does not contribute substantially to the final bond strength. If the pieces do wring together during preparation, one should be careful not to let them rub or scrape against each other, since the resulting surface damage may reduce the final contact area and therefore the final bond strength. In a dirty environment, surface contaminants such as grease and dust particles disrupt the bond primarily by reducing the overall contact area; for this reason we found it necessary to work in a clean-room environment when bonding cells.

Hydroxide-catalysis bonding is a chemical process, and even in a clean environment residual surface contamination can easily prevent or weaken a bond. In many cases, the use of water or an aqueous bonding catalyst exploits a hydrophilic (or hydrophobic) surface which must be specially prepared. Some silicon-bonding techniques (e.g., hydroxide-catalysis bonding) require an oxide layer on the surface, while others (e.g., direct bonding) may require that native oxide layers be completely removed. In cases where the oxide layer forms part of the bond, the mechanical strength of bonded parts may depend on its thickness. In particular, thermal oxides can be grown on silicon substrates under controlled conditions in order to maximize bond strength [106]. Thin-film coatings of silicon oxides may also be deposited in vacuum to achieve the same effect.

A generic feature of most pre-bonding surface preparation for silicon substrates is the RCA cleaning protocol [111] (although it may subsequently be necessary to replace the removed oxide layers). Ultrasonic cleaning in solvent solutions, use of piranha solution, and flushing with deionized water are also common steps in surface preparation of both silicon and glasses. It is frequently desirable to work at a laminar flow bench, or in a cleanroom environment to prevent particle contamination.

5.4.2 Diffusion Bonding

Typically used for bonding metals, diffusion bonding relies on permanent modifications of the bonded surfaces under high temperature and pressure [112]. Plastic deformation should occur only on the scale of surface asperities, which by deforming increase the contact area during the welding process (this deformation is controlled by the applied interfacial pressure). At high temperature and pressure, the “cold flow” is accelerated such that voids are compensated and the contact area approaches 100%. The bonding mechanism is mutual

diffusion of material from each side across the boundary, which occurs at a useful rate only after the surfaces have deformed to match each other (unless the surface quality is initially very high). Diffusion bonding can result in very large residual thermal stresses when dissimilar materials are joined, since the bonding typically takes place at temperatures several hundred degrees above the intended operating temperature for the bonded part.

5.4.3 Anodic Bonding of Glass to Silicon

For glass containing a sufficient fraction of alkali, high temperature and high voltage can be applied to force cation drift away from the interface (into the glass and away from the silicon). This results in a thin depletion zone at the interface into which oxygen anions drift. A positive volume charge is induced in the silicon, resulting in electrostatic attraction. The electrochemical process which produces an irreversible bond also involves the formation of siloxane bridges at the interface [113]. Aluminosilicate glasses have been anodically bonded, typically by introducing an alkali such as lithium into the glass composition [114]. Anodic bonding of glass to metals and silicon oxide films has also been demonstrated [115–117].

5.5 Cell Materials

Three glass types were used for the bodies of various cells:

1. **Pyrex (Borosilicate)** This is often actually Kimble Kimax or Schott DURAN, but we follow common usage by referring to any of these borosilicate glasses as “pyrex”. (PYREX is the trademark of a borosilicate produced by Corning, and should not be confused with Pyrex – a tempered soda-lime glass used for kitchenware.) These all conform to the standards laid out in ASTM E438 [118], which include a relatively low softening point (815-820°C) and moderate thermal expansion coefficient (3.3 ppm/°C). This means that they are relatively forgiving to work with, and for this reason pyrex is the preferred material for components that must be worked with a torch in the lab. Pyrex is rich in sodium, and can be anodically bonded to silicon; we have also successfully bonded it to silicon and sapphire via silicate-assisted hydroxide catalysis. It is relatively impermeable to helium, and can be antirelaxation-coated with organic silanes such as OTS. Valves, stopcocks, and commercial components of any complexity are almost invariably made of pyrex, and it is necessary to provide a matching layer when these are used in apparatus constructed from a glass type with different thermal expansion properties. Pyrex does not transmit short-wavelength

ultraviolet light, but has relatively good optical properties in the visible and near-infrared.

Pyrex cells, including those containing close to an atmosphere of gas, can be sealed using an oxygen-propane torch with the cell body at room temperature. Super-atmospheric cells can be produced by submerging part of the cell in liquid nitrogen while the cell is “pulled off”, to increase the internal atomic/molecular number density without increasing the pressure. The pressure increases after the cell warms up, so it is important to properly anneal the pull-off point.

2. **Quartz (GE type 214 or similar)** Pure SiO_2 has a high softening point (1683°C) and very low thermal expansion ($0.55 \text{ ppm}/^\circ\text{C}$). Thermal expansion matching to pyrex requires several intermediate layers (a “graded seal”), but is routine. Quartz is quite permeable to helium, is fairly electrically resistive (though less so than GE-180), and has very low alkali content. Optical transmission is high from 200 nm into the infrared. Commercial quartz glass such as GE-214 can be welded to uncoated UVFS optical windows (such as Thorlabs WG41010).

Quartz cells can be sealed with some difficulty using an oxygen-propane flame. Due to the high softening point of the glass, even a low-pressure gas cell risks “blowing out” at the pull-off due to the substantial increase of internal pressure when the gas is heated. This can be avoided either by the cryogenic method described above, or by attaching a quartz cell to a pyrex stem and sealing the pyrex portion.

3. **GE type 180 (Iron-Free Aluminosilicate)** Available mainly in the form of stock tubing with 15mm diameter, is produced by General Electric as an automotive glass and used in that industry for lamp bulbs. It has a relatively high softening point (1015°C) and thermal expansion coefficient ($4.5 \text{ ppm}/^\circ\text{C}$), and is notoriously susceptible to reboil and thermal shock. These properties make it challenging to work, but it is nevertheless a preferred material in experiments that rely on polarized noble gas nuclei, since when properly cleaned it does not require an antirelaxation coating. (The reasons for this remarkable feature are somewhat unclear; we remark only that the few GE-180 cells made in our lab with OTS coatings did not significantly outperform the more typical uncoated ones.) GE-180 can be thermally matched to pyrex with uranium glass. GE-180 is additionally impermeable to helium, very electrically resistive, and low in alkali content. We were not able to anodically bond GE-180 to silicon (attributable to low alkali content), but the polished surface is sufficiently oxygen-rich to anchor siloxane bridges; GE-180 bonds well to silicon via silicate-

assisted hydroxide catalysis. It does not efficiently transmit short-wavelength ultraviolet light, but has relatively good optical properties in the visible and near-infrared. GE-180 cells can be sealed with an oxygen-propane torch, similarly to pyrex albeit at a somewhat higher temperature. The higher working temperature means that one must work rapidly to avoid a blow-out when sealing cells that contain gas; this occurs when hot gas inside the cell expands, producing a bubble of soft glass that can easily pop and expose the interior of the manifold to atmosphere. This time constraint leads to a somewhat awkward compromise when working with GE-180, since the glass should be gradually warmed and cooled to avoid thermal shock. The annealing process after the cell is sealed is critical, and improperly annealed cells often crack when cooled (or later, when temperature-cycled in an experiment). In practice, the cell is pulled off as rapidly as possible, and then annealed at a temperature below the softening point.

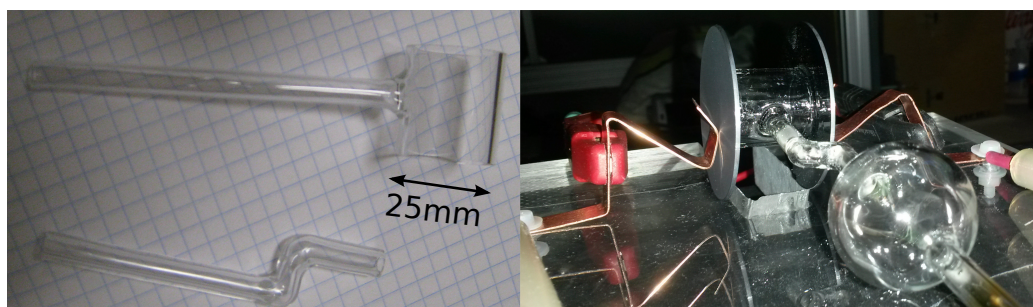


Figure 5.6: (Left) GE-180 components prepared for a sealed two-chamber EDM cell. The bent tube is intended to regulate diffusion between the chambers and prevent metallic rubidium from migrating into the cylindrical chamber where high voltage is applied. (Right) Finished cell installed in an experiment.

5.6 Silicate Assisted Hydroxide-Catalysis Bonding

This section describes the protocol we developed for silicate assisted hydroxide-catalysis bonding of cylindrical cells made from dissimilar materials. Most of our bonded cells were made with GE-180 cylindrical bodies, with test-grade (surplus) doped silicon wafers serving the combined function of end caps and electrodes in EDM measurements. We have also made pyrex/silicon cells while developing the bonding technique for GE-180/silicon cells. Pyrex/quartz and pyrex/sapphire cells were made for two-photon spectroscopy of xenon, in order that the cell body could be easily formed and still accommodate ultraviolet-transmitting windows on two perpendicular axes.

5.6.1 Polishing

The principal challenge associated with bonding flat end caps to a cylindrical cell body is polishing the annular edge of the cylinder sufficiently flat. All of the cells discussed here were polished by hand using silicon carbide and diamond; this proved adequate after some iterative optimization to determine an appropriate polishing recipe. GE-180 is slightly more brittle than pyrex, so greater care is required to prevent edge chipping, but otherwise the polishing recipe does not change for different glasses.

We obtain cylindrical cell bodies from the glass shop, after they are cut on a grinding wheel and rough-polished with wet 300 grit or 600 grit silicon carbide. In our lab, we iteratively fine-polish the edges using silicon carbide sanding sheets and water on a polishing flat. One must be careful to move the piece in a pseudo-random pattern, without catching an edge and damaging the sanding sheet. Starting with 300 grit, we move up to 2000 grit in steps of 200-300 and clean the polished edge with water and organic solvents after each step. At 2000 grit, the surface is visibly polished to a specular finish but may have residual fine scratches. These are removed with diamond polishing sheets of 2000 grit (1 μm particle size) and 2500 grit (0.1 μm particle size), and/or 2500 grit diamond lapping paste. Polishing is complete when no defects are visible on the surface under bright light, and no cloudiness is visible in the water on the polishing sheet. The polished edges are cleaned with optics-grade solvents and lens paper.

Most of the silicon wafers used for cell fabrication are single-side polished; for cells that required a second surface polish (e.g., to attach a valve over a hole in the wafer), a chemical mechanical planarization system (Strasbaugh 6EC) is used in the Lurie Nanofabrication facility at the University of Michigan.

5.6.2 Surface Cleaning and Wafer Preparation

In early attempts we were occasionally able to bond silicon/pyrex cells in a laminar flow hood in our lab, but complete silicon/GE-180 bonds were only achieved in a cleanroom at the University of Michigan Lurie Nanofabrication Facility. (Bonding is performed in a lab whose particle count is between Class 100 and Class 1000; the RCA clean and thermal oxidation are performed in a Class 100 lab.) So far, every attempt in the cleanroom has produced a mechanically strong and vacuum-tight bond; it appears that particle contamination was the most important limitation in our lab, and that (with adequate surface preparation) the technique is surprisingly robust.

Glass components are cleaned in our lab with organic solvents and piranha solution, then transported to the cleanroom in an evacuated plastic container. In the cleanroom they

are cleaned again with either piranha or a CO₂ snow jet [119], and surface-activated with O₂/Ar plasma in a commercial plasma cleaner (Glen 1000P). The cell is bonded within ~15 minutes of surface activation, since the effect is temporary and chemical reactions with the ambient environment will slowly restore the surface bonds and layers that were removed by plasma cleaning.

Bare silicon reacts immediately with oxygen and other atmospheric contaminants, with the result that silicon wafers invariably have a contaminated and oxidized surface unless specially prepared. The “native oxide” is actually sufficient in many cases to anchor hydroxide-catalysis bonds, and in most cases we simply cleaned the wafers in the same way that the glass was prepared. However, the best practice is to replace the native oxide with a good quality thermal oxide. Thermal oxidation of silicon requires meticulous cleaning in a pristine environment; we use the RCA cleaning protocol, which is the industry standard in semiconductor manufacturing [111]. It comprises three steps, which we summarize here:

1. **Organic clean and particle removal:** Wafers are submerged for 10-20 minutes in a hot (85°C) solution of deionized water, ammonium hydroxide, and hydrogen peroxide in 5:1:1 ratio by volume. This removes organic residues and particles adhered to the wafer surface.
2. **Oxide removal:** Wafers are etched for 30 seconds in dilute hydrofluoric acid (10:1 or 100:1) at room temperature. This step removes the oxide layer and some metallic contaminants.
3. **Ionic clean:** Wafers are submerged for 10-20 minutes in a hot (85°C) solution of deionized water, hydrochloric acid, and hydrogen peroxide in 6:1:1 ratio by volume. This removes residual metallic contamination and leaves a thin passivating layer that protects the cleaned surface from contamination.

The cleaned wafers are rinsed with flowing water and dried, then oxidized in a dry furnace tube at 1000°C for 125 minutes. This produces a 100 nm layer of SiO₂, which visibly changes the color of the wafer surface to a deep purple. After the oxide has grown and the wafer is cooled, the surface is activated by plasma cleaning simultaneously with the glass.

5.6.3 Bonding

The activated wafers and glass are brought to a wet bench, where a bonding solution of five parts distilled water and two parts aqueous sodium silicate (Sigma-Aldrich 338443) has

been pre-mixed in clean glassware. A micropipette is used to apply the bonding solution to the glass edge in the amount of $1 \mu\text{l}/\text{cm}^2$ of surface area to be bonded. (For most of our cylindrical cells, the surface area of the polished edge is approximately 1.5 cm^2 .) The glass is pressed onto the silicon wafer until whetting is observed (see figure 5.7), and left under weight to cure for three days. After three days the cell can be safely handled, and we typically allow two to three weeks before the bond is assumed to be fully cured (further investigation is required to quantify bond strength as a function of curing time). The second wafer can be bonded after a few days or (preferably) a week; if it is bonded sooner, water migrating inward from the bond interface becomes trapped inside the cell and cannot easily escape.

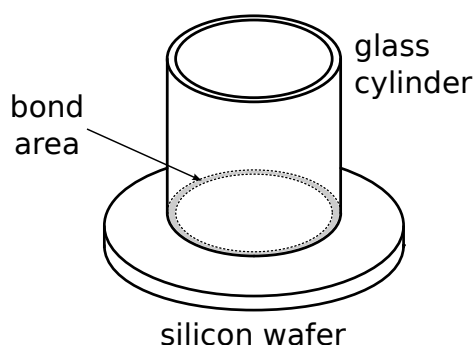


Figure 5.7: Schematic illustration of the first silicon wafer being bonded to an EDM cylinder. The bond area of about 1.5 cm^2 is determined by the wall thickness of the glass tubing, which is polished to an optical finish by hand. Whetting at the interface is visible through the glass when bonding solution is applied to the edge and the pieces are pressed together. Once pressed together, the pieces should not be allowed to move until the bond has cured, and may be weighted to maintain good contact.

Bond strength has not been systematically investigated for the geometries relevant here; in fact, we typically apply a layer of epoxy over the bond on the outside of the cell as a precautionary measure. The bonds tested to failure could be broken (with some difficulty) by hand. These do not usually fail at the bond itself, but damaged the silicon wafer and left a ring of silicon stuck to the glass edge. This seems to indicate that a good hydroxide-catalysis bond is stronger than bulk silicon.

5.6.4 Sapphire and Quartz Bonding for Spectroscopy Cells

Pyrex cells bonded with uncoated sapphire and quartz optical windows are also prepared according to the above protocol. The sapphire and quartz windows are cleaned and surface-activated in the same manner as the glass, and the bonding and curing process proceeds identically.

One caveat concerns the very different thermal expansion coefficients of pyrex (3.3 ppm per °C) and sapphire (5.3 ppm per °C, perpendicular to the optical axis). The cell with sapphire windows bonded successfully, and rapidly pumped out to a base pressure below 10^{-7} Torr (this is typical of a good-quality manifold on the vacuum station used for cell filling). However, subsequent baking appears to have broken the bond layer due to differential thermal expansion between the pyrex body and the sapphire windows. The cell was baked overnight at 245°C, after which it no longer held vacuum. Application of a high vacuum leak sealant (VACSEAL) to the sapphire-pyrex interface resulted in the sealant being visibly drawn into the cell: the leaks were too large to seal effectively. Future efforts in this direction may benefit from baking all surfaces before bonding them, and limiting the range of temperatures applied to the completed cell.

5.7 Further Thoughts and Improvements

It is possible to mount the glass cell body in a polishing jig for automated planarization, but we did not pursue this beyond designing an adapter for an existing jig, since hand-polishing does not appear to be a limiting factor in our bonding protocol. For studies involving higher-volume cell production or investigating the repeatability of the technique, automated polishing would be advisable.

A promising direction for further efforts is the development of cells whose components cannot be bonded at high temperatures. This includes materials with very different thermal expansion properties (since hydroxide-catalysis bonding occurs at room temperature, there is no residual thermal stress), and windows or coated components that would be damaged by glass working. When cleaning and bonding is performed in a cleanroom environment, it is possible to prepare good quality cells without baking under vacuum. (One must, however, ensure that the components are not re-contaminated after they have been cleaned.) A final possibility is the development of cells for fluorescence spectroscopy, in which the windows for excitation and fluorescence are made from different materials that are selected to enhance transmission or reject background for each path independently.

CHAPTER 6

Conclusions

In this dissertation, we have presented experimental and theoretical progress in the development of optical magnetometry using nuclear spins and multiphoton transitions. In particular we have demonstrated the feasibility of two-photon magnetometry using noble gases and cw or pulsed lasers; obtained fluorescence signals from two-photon excitation of ytterbium, rubidium, and xenon; and developed a new technique for cell fabrication that accommodates both deep-ultraviolet optical transmission and long nuclear spin polarization lifetimes. In this chapter we summarize the main contributions of this work, and place them in context with the next steps required for future developments.

6.1 Theoretical Material

The theoretical material presented mainly surveys or reformulates existing work. We have derived simple analytical expressions for two-photon excitation amplitudes involving one or several classical optical fields, in which the contributions from an arbitrary number of intermediate states are treated using first-order perturbation theory. Angular momentum coupling and selection rules were discussed, and a model presented to calculate the magnitude of a signal arising from paramagnetic rotation. The optical spectra of modelocked pulsed lasers were briefly considered to illustrate the experimental possibility of high spectral resolution with a reasonable signal size; a sum formula was also given, relating the power per mode to the total average power for transform-limited Gaussian pulses. Magnetometer sensitivity was discussed with respect to the spatial and temporal bandwidth of a measurement. The geometric phase arising from adiabatic evolution of parameters in the Hamiltonian was derived in a general form, and then discussed in the specific context of false EDM signals due to motional magnetic fields.

6.2 Experiments with CW Laser Sources

We have presented measurements of one-photon transitions in a ytterbium atomic beam, including measurements of excited state Zeeman splittings as a function of applied magnetic field strength. We have also reported optical pumping of the ^{171}Yb nuclear spin with optical detection far from resonance, and discussed the nuclear polarization signal's dependence on the polarization of both pump and probe beams.

Two-photon spectra of several ytterbium isotopes were presented, and methods developed to disentangle the contributions from overlapping resonance lines. We have discussed measurements of ytterbium isotopes with nuclear spin $I = 0$ as a comparative standard for measurements using ^{171}Yb ($I = \frac{1}{2}$). Measurements analogous to the one-photon case were presented and analyzed to determine the effect of various pump and probe polarizations.

One-photon Doppler-free spectroscopy of mercury was presented, in the context of laser frequency stabilization using an error signal generated by magnetically-induced dichroism. An unsuccessful attempt to detect a two-photon resonance in xenon was briefly mentioned, in which the the 253.7 nm laser from the mercury measurements was detuned to operate at 256.0 nm. We also reported the first signals from a separate experiment, which successfully probed the 256.0 nm xenon transition using a different laser with higher output power.

The methods developed to quantify asymmetries introduced by polarization errors in the pump or probe beam may be applied to the analysis of light shifts and Bloch-Siegert shifts, and to the determination of hyperfine and isotope structure in the spectra of atoms whose optical transitions have not been studied in detail. This is particularly important in the case of radon, for which detailed spectral data is lacking.

Further improvements to the cw ytterbium experiments will rely on improved stabilization of the probe laser frequency and power, without sacrificing the same qualities in the pump laser. Similar experiments using the 399 nm $^1S_0 \rightarrow ^1P_1$ transition for optical pumping, and/or using one-photon transitions to detect nuclear polarization due to TPOP, would then be possible. Improved magnetic shielding of the detection PMT would enable an RF resonance experiment to optically detect the quenching of nuclear polarization.

The xenon measurements would be most significantly improved by an increase of the signal-to-noise ratio. This could be accomplished by spatial and spectral filtering of the probe beam, and by additional spectral filtering in the fluorescence path. An experiment with improved signal-to-noise could be straightforwardly modified for optical detection of nuclear polarization in xenon, which is most easily produced by SEOP in a cell containing rubidium. Such an experiment could then incorporate an NMR component, for optical

detection of nuclear spin precession. Cells containing isotopically enriched ^{129}Xe will have simpler optical spectra and larger polarization signals than those containing xenon of natural isotopic abundance. Such experiments can be repeated using the $^1S_0 \rightarrow ^2[3/2]_2$ two-photon transition in xenon at a wavelength of 252.5 nm, which lies within the tunable range of the cw laser system.

6.3 Experiments with Pulsed Laser Sources

We have presented fluorescence measurements with ytterbium and rubidium, in which two-photon transitions were excited using picosecond pulses from a Ti:sapphire oscillator. These signals were discussed in terms of the RF parameters that constrain modelocked laser spectra, and the need for improved laser stabilization was established. Sinusoidal modulation of the rubidium fluorescence rate was demonstrated, as a function of the rotation angle of a quarter-wave plate in the probe beam.

We have also reported on similar measurements in ytterbium, for which the picosecond source was replaced by a femtosecond oscillator. Our analysis showed modulation of the fluorescence spectrum when the repetition rate of the laser was scanned. The signal size was consistent with rapid drift of the laser spectrum, which would average out the contributions from underlying resonance peaks (reducing spectral resolution).

Improvements to these experiments will rely on active laser stabilization, and (especially for femtosecond spectroscopy) also on chirp compensation. For the picosecond laser, a piezoelectric transducer should be installed behind a cavity mirror and used to actively stabilize the repetition rate. Residual spectral drift can be compensated by placing an AOM in the beam path outside the cavity, and modulating its drive frequency using an error signal generated from spectroscopy of a potassium resonance.

The scheme proposed for stabilization of the picosecond pulsed laser can also be applied to xenon spectroscopy with picosecond pulses. In this scenario the 256.0 nm light is generated by frequency tripling the 768 nm output of the Ti:sapphire oscillator; a different potassium resonance can be used as an absolute frequency reference for stabilization of the infrared spectrum. Experiments analogous to the cw case may be performed with xenon, given a sufficiently stable source of 256.0 nm pulsed light.

6.4 Cell Development and EDM Experiments

We have developed a method of producing cylindrical vapor cells from dissimilar materials, using silicate assisted hydroxide-catalysis bonding. We reported on construction and

testing of cells that consist of an open glass cylinder (aluminosilicate or pyrex) sealed by end caps made from silicon, sapphire, quartz, or pyrex. We have discussed the use of aluminosilicate/silicon cells in an experiment studying the nuclear EDM of ^{129}Xe , and observed that certain material combinations represent a favorable compromise among the requirements associated with nuclear polarization, high voltage, and optical transmission.

Future efforts in cell development would refine the silicate bonding protocol, and in particular investigate the role of surface oxides and doping on the bond strength of aluminosilicate joined to silicon. Automated polishing of the glass cylinders would enable significantly more rapid development and prototyping, and may also improve polarization lifetimes by reducing surface area. Improved cleaning recipes may also contribute to longer polarization lifetimes. The use of transparent conductive films such as indium tin oxide (ITO) has not been investigated in this context, but may be compatible with hydroxide-catalysis bonding.

APPENDIX A

The Two Level Problem

The evolution of a two-state quantum system in a time-harmonic potential is a classic calculation in time-dependent perturbation theory. It is the prototype for semiclassical treatments of the interaction between matter and electromagnetic radiation, and standard presentations are found in many textbooks [55, 120, 121] and research articles [122–124]. Our discussion here is motivated by the fact that harmonic perturbations applied to two-level systems accurately describe both magnetic resonance in spin- $\frac{1}{2}$ nuclei, and optical excitation of electronic states when only two levels are resonantly coupled. Moreover, when intermediate states can be adiabatically eliminated from the dynamics of two-photon excitation, this formalism also applies to the resulting *effective* two-level problem. Thus, all of the essential atom-field interactions that are relevant to optical magnetometers can be expressed as different particular cases of a general phenomenon.

We emphasize that many features of this problem have close analogies – or are completely equivalent – in the various particular cases. These include the role of field polarization in angular momentum coupling, and selection rules associated with the transition matrix elements that determine which transitions are allowed for a given field polarization and quantization axis. Off-resonant corrections, such as light shifts (AC Stark and Zeeman effects) and Ramsey-Bloch-Siegert shifts [124] also occur in a similar fashion when the rotating-wave or two-level approximations are not exact. (The precise form of such perturbative corrections depends on the structure of the transition matrix elements involved, which can vary substantially between particular cases.) Finally, effects associated with smooth variation of the field envelope and the inclusion of multiple oscillating perturbations at different frequencies (i.e., different field modes) are relevant in all cases, although certain unique features arise in the case of multiphoton transitions that have no counterpart in any single-quantum process.

Solutions are most readily obtained in the interaction picture. Suppose that we already know the eigenstates and eigenvalues for a time-independent Hamiltonian H_0 , and wish to know the effect of an additional time-dependent interaction $V(t)$, where H_0 and $V(t)$ may

also depend on position coordinates and other parameters. We can expand an arbitrary state vector $|\psi\rangle$ in Schrödinger-picture eigenstates $|n\rangle$ as

$$|\psi\rangle = \sum_n a_n(t) |n\rangle .$$

In the presence of H_0 alone the amplitudes a_n evolve according to the time-dependent Schrödinger equation as

$$i\hbar\dot{a}_n(t) = \hbar\omega_n a_n(t) ,$$

where $\hbar\omega_n$ is the energy eigenvalue associated with $|n\rangle$. The state amplitudes in the interaction picture are designated $c_n(t)$, and they obey the relation $c_n(t) = a_n(t)e^{i\omega_n t}$. This has the effect of removing the “energy term” from the equation of motion when we include the interaction potential $V(t)$:

$$i\hbar\dot{a}_n = \hbar\omega_n a_n + \sum_m V_{nm} a_m \tag{A.1}$$

$$i\hbar\dot{c}_n = \sum_m V_{nm} c_m e^{i\omega_{nm} t} , \tag{A.2}$$

where $V_{nm}(t) = \langle n| V(t) |m\rangle$ and $\omega_{nm} = \omega_n - \omega_m$. In the same way, we can absorb terms such as light shifts within the interaction picture; this amounts to a simple redefinition of the energy $\hbar\omega_n$ whenever the equation of motion for \dot{c}_n includes terms proportional to c_n . Note that the state populations are identical in the Schrödinger and interaction pictures, since $|c_n|^2 = |a_n|^2$.

The simplest case obtains when $V_{nm}(t) = A e^{i\omega t}$. For real and constant A we need only solve a second-order equation with constant coefficients, and the solution for all times is analytic. This well-known result is originally due to Rabi [123]; we will consider a more general case, where

$$V_{nm}(t) = \sum_j V_{nm}^{(j)}(t) A_j(t) + \text{c.c.} , \tag{A.3}$$

and the time- and space-dependence of each term is separated into “rapid” and “slow” factors. The rapid factors $V_{nm}^{(j)}(t)$ are assumed to vary harmonically, and we have

$$V_{nm}^{(j)}(t) \propto e^{i(\mathbf{k}_j \cdot \mathbf{r} - \omega_j t + \phi_j)} , \tag{A.4}$$

where the parameters \mathbf{k}_j and ω_j will usually correspond to the propagation vector and angular frequency of a plane-wave electromagnetic field, respectively. The variation of the envelope functions $A_j(t)$ is assumed to be slow compared to the carrier oscillations described by this exponential phase factor. The phases ϕ_j are constant in time, but may depend on other parameters such as position or static field strengths. To model magnetometers we will sometimes also allow slow time variations of the matrix elements $V_{nm}^{(j)}(t)$, corresponding to ground state Larmor precession.

For a system consisting of two atomic states, we now have

$$\hbar\dot{c}_1 = -i \sum_j \left(V_{12}^{(j)}(t) A_j(t) + \text{c.c.} \right) e^{-i\omega_0 t} c_2 = -i V_{12} e^{-i\omega_0 t} c_2 \quad (\text{A.5})$$

$$\hbar\dot{c}_2 = -i \sum_j \left(V_{21}^{(j)}(t) A_j(t) + \text{c.c.} \right) e^{i\omega_0 t} c_1 = -i V_{21} e^{i\omega_0 t} c_1, \quad (\text{A.6})$$

where we taken $\omega_0 \equiv \omega_{21} \geq 0$ without loss of generality. In general $V_{12} \neq V_{21}$, but we can force any single matrix element to be real by an appropriate choice of the relative phase between the electronic wavefunctions. (For electric dipole transitions, this has the consequence that V_{nm} can be symmetrized if every field mode in the sum A.3 has the same polarization. If not, then the phase choice that produces a real matrix element for one polarization generally requires a complex matrix element for any linearly independent polarization.)

At this point it is common to make the *rotating wave approximation* (RWA), which consists of dropping the terms proportional to $V_{12}^{(j)}$ in equation A.5 and those proportional to $V_{21}^{(j)*}$ in equation A.6. Since these terms oscillate at the frequencies $\omega_0 + \omega_j$, their average contribution on timescales much larger than an optical cycle can be neglected in what amounts to a coarse-grain time average. The residual lowest-order effect ignored by the RWA is a shift in the apparent energy of each state known as the Bloch-Siegert shift [124, 125], which to lowest nonvanishing order is

$$\mp \hbar \sum_j \frac{|A_j|^2 V_{12}^{(j)} V_{21}^{(j)*}}{\omega_0 + \omega_j}, \quad (\text{A.7})$$

where the upper (lower) sign is taken for state 1 (2) and we have assumed that terms oscillating at the difference frequencies $\omega_j - \omega_{j'}$ can be neglected.

By differentiating equation A.6 and substituting into equation A.5 (or vice-versa), we obtain separated second-order equations of motion for c_1 and c_2 :

$$\begin{aligned}
\ddot{c}_1 - \left[\frac{\dot{V}_{12}}{V_{12}} - i\omega_0 \right] \dot{c}_1 + \frac{V_{12}V_{21}}{\hbar^2} c_1 &= 0 \\
\ddot{c}_2 - \left[\frac{\dot{V}_{21}}{V_{21}} + i\omega_0 \right] \dot{c}_2 + \frac{V_{12}V_{21}}{\hbar^2} c_2 &= 0 .
\end{aligned} \tag{A.8}$$

These equations transform into each other under $(1 \leftrightarrow 2)$, if we are careful to recall that $\omega_0 = \omega_{21} = -\omega_{12}$. The terms that involve V_{21} may be quite complicated functions of time. However, it is sometimes possible to transform a second-order ordinary differential equation into a form where the coefficients are constant, and which is therefore easily solved in closed form. Given an equation

$$\frac{d^2y}{dx^2} + p(x) \frac{dy}{dx} + q(x)y = 0 , \tag{A.9}$$

such a transformation is possible if the quantity

$$P \equiv \frac{q'(x) + 2p(x)q(x)}{q(x)^{\frac{3}{2}}} \tag{A.10}$$

is independent of x . If this condition holds, then a change to the variable

$$z \equiv \int \sqrt{q(x)} dx \tag{A.11}$$

results in a constant-coefficient second-order equation for $y(z)$,

$$\frac{d^2y}{dz^2} + \frac{P}{2} \frac{dy}{dz} + y = 0 , \tag{A.12}$$

from which it is straightforward to extract a formal solution for $y(x)$.

Equation A.10 may be regarded as a constraint on the mathematical functions $V_{nm}(t)$ for which analytic solutions are easily obtainable; this in turn jointly constrains the quantities in each term of the sum A.3 that defines $V_{nm}(t)$. A full solution is not available in general, but some cases of interest are straightforward. Equation A.10 is clearly satisfied if $q'(x) + 2p(x)q(x) = 0$; for the two-level problem given by equations A.8, this constraint is equivalent to

$$V_{12}\dot{V}_{21} - \dot{V}_{12}V_{21} + 2i\omega_0 V_{12}V_{21} = 0 . \tag{A.13}$$

The constraint is identical for both equations, since the left-hand side differs only by an overall minus sign. We also note that the first two terms cancel in the case where $V_{12} = V_{21}$, i.e. when V is symmetric.

Assuming the phases ϕ_j are constants and the E_j are real functions of time, we have

$$V_{12} = \sum_j A_j(t) \left(V_{12}^{(j)} + V_{12}^{(j)*} \right) \quad (\text{A.14})$$

$$\dot{V}_{12} = \sum_j (-i\omega_j) A_j(t) \left(V_{12}^{(j)} - V_{12}^{(j)*} \right) + \sum_j \dot{A}_j(t) \left(V_{12}^{(j)} + V_{12}^{(j)*} \right), \quad (\text{A.15})$$

and similarly for V_{21} . Upon substitution into equation A.13, the constraint becomes

$$\begin{aligned} 0 = \sum_{j,k} \left[2i\omega_0 A_j A_k \left(V_{12}^{(j)} + V_{12}^{(j)*} \right) \left(V_{21}^{(k)} + V_{21}^{(k)*} \right) \right. \\ + i\omega_j A_j A_k \left(V_{12}^{(j)} - V_{12}^{(j)*} \right) \left(V_{21}^{(k)} + V_{21}^{(k)*} \right) \\ - \dot{A}_j A_k \left(V_{12}^{(j)} + V_{12}^{(j)*} \right) \left(V_{21}^{(k)} + V_{21}^{(k)*} \right) \\ - i\omega_j A_j A_k \left(V_{21}^{(j)} - V_{21}^{(j)*} \right) \left(V_{12}^{(k)} + V_{12}^{(k)*} \right) \\ \left. + \dot{A}_j A_k \left(V_{21}^{(j)} + V_{21}^{(j)*} \right) \left(V_{12}^{(k)} + V_{12}^{(k)*} \right) \right], \quad (\text{A.16}) \end{aligned}$$

in which the third and final lines evidently cancel if $V_{12}^{(j)} = V_{21}^{(j)}$ for every j , or vanish if none of the A_j depend on time. Supposing one of these to be true, rearranging indices, and collecting terms, we obtain:

$$\begin{aligned} 0 = \sum_{j,k} A_j A_k \left[2i\omega_0 \left(V_{12}^{(j)} V_{21}^{(k)} + V_{12}^{(j)*} V_{21}^{(k)} + V_{12}^{(j)} V_{21}^{(k)*} + V_{12}^{(j)*} V_{21}^{(k)*} \right) \right. \\ + i\omega_j \left(V_{12}^{(j)} V_{21}^{(k)} - V_{12}^{(j)*} V_{21}^{(k)} + V_{12}^{(j)} V_{21}^{(k)*} - V_{12}^{(j)*} V_{21}^{(k)*} \right) \\ \left. - i\omega_k \left(V_{12}^{(j)} V_{21}^{(k)} + V_{12}^{(j)*} V_{21}^{(k)} - V_{12}^{(j)} V_{21}^{(k)*} - V_{12}^{(j)*} V_{21}^{(k)*} \right) \right] \\ = i \sum_{j,k} A_j A_k \left[(2\omega_0 - \omega_j - \omega_k) V_{12}^{(j)*} V_{21}^{(k)} \right. \\ + (2\omega_0 + \omega_j + \omega_k) V_{12}^{(j)} V_{21}^{(k)*} \\ + (2\omega_0 + \omega_j - \omega_k) V_{12}^{(j)} V_{21}^{(k)} \\ \left. + (2\omega_0 - \omega_j + \omega_k) V_{12}^{(j)*} V_{21}^{(k)*} \right]. \quad (\text{A.17}) \end{aligned}$$

A.1 Rotating Wave Approximation

We now apply the RWA, with the result that the condition A.17 reduces to

$$0 = i \sum_{j,k} A_j A_k (2\omega_0 - \omega_j - \omega_k) V_{12}^{(j)*} V_{21}^{(k)}, \quad (\text{A.18})$$

which is easily satisfied if $\omega_j = \omega_0$ for every j . This restricted solution allows us to develop a useful time-domain model of pulsed excitation, including timing and phase fluctuations. The interaction matrix elements then have the form

$$V_{12} = e^{i\omega_0 t} \sum_j \chi_j^* A_j(t) \quad (\text{A.19})$$

$$V_{21} = e^{-i\omega_0 t} \sum_j \chi_j A_j(t), \quad (\text{A.20})$$

where $\chi_j = V_{12}^{(j)} e^{-i\omega_0 t}$ is the “leftover” part of $V_{12}^{(j)}$ when the rapid time-dependence is factored out. Thus,

$$V_{12} V_{21} = \sum_{j,k} \chi_j \chi_k^* A_j(t) A_k(t), \quad (\text{A.21})$$

and we can transform to the variable

$$z = \frac{1}{\hbar} \int dt \sqrt{V_{12} V_{21}} \quad (\text{A.22})$$

to arrive at the equation of motion

$$c_2''(z) + c_2(z) = 0. \quad (\text{A.23})$$

The solution is

$$c_2(z) = A \cos(z) + B \sin(z), \quad (\text{A.24})$$

and thus $c_2(t)$ is trivially determined when we have an explicit expression for $z(t)$.

A.2 Time-Separated Resonant Pulses

A case of particular interest occurs when the envelope functions in equation A.20 do not overlap in time. In that case only diagonal terms in the sum survive in equation A.21, since $A_j(t)A_k(t) \approx \delta_{jk}A_k^2(t)$, and the integrand $V_{12}V_{21}$ may be simplified by bringing the square root inside the sum. Thus, we have

$$z = \frac{1}{\hbar} \sum_j \int dt |\chi_j A_j(t)|, \quad (\text{A.25})$$

and formally,

$$c_2(t) = A \cos \left[\frac{1}{\hbar} \sum_j \int^t dt' |\chi_j A_j(t')| \right] + B \sin \left[\frac{1}{\hbar} \sum_j \int^t dt' |\chi_j A_j(t')| \right]. \quad (\text{A.26})$$

If we now model the interaction as a series of time-separated pulses,

$$\int^t dt' |\chi_j A_j(t')| = \hbar A(t - T_j), \quad (\text{A.27})$$

then

$$c_2(t) = A \cos \left[\sum_j A(t - T_j) \right] + B \sin \left[\sum_j A(t - T_j) \right]. \quad (\text{A.28})$$

The constants A, B can be determined if the values of c_1 and c_2 are known at some instant t_0 , together with the values of their derivatives $\dot{c}_1(t_0), \dot{c}_2(t_0)$ (from equations (A.5) and (A.6)).

A.3 Monochromatic Field with Constant Amplitude

The other situation in which the equations of motion can be easily solved is when only one field contributes to the excitation; this is the classic solution originally due to Rabi [123]. We retain the RWA, but now the constraint A.13 cannot be satisfied and we must show instead that

$$P = \hbar \frac{V_{12}\dot{V}_{21} - \dot{V}_{12}V_{21} + 2i\omega_0 V_{12}V_{21}}{(V_{12}V_{21})^{\frac{3}{2}}} = \text{constant}, \quad (\text{A.29})$$

where now

$$V_{12} = \frac{\hbar\Omega^*}{2}e^{i\omega t} \quad (\text{A.30})$$

$$V_{21} = \frac{\hbar\Omega}{2}e^{-i\omega t}, \quad (\text{A.31})$$

and we do not assume $\omega = \omega_0$. The quantity Ω is known as the Rabi frequency, here assumed to be a complex constant. We also define the frequency detuning from exact resonance, $\delta = \omega_0 - \omega$. With these definitions, equation A.29 reduces to

$$P = \frac{4i\delta}{|\Omega|}, \quad (\text{A.32})$$

which is constant by assumption. We again transform to an auxiliary variable,

$$z = \hbar^{-1} \int dt \sqrt{V_{12}V_{21}} = \frac{|\Omega|t}{2}, \quad (\text{A.33})$$

and obtain the constant-coefficient equations of motion

$$c_1''(z) + \frac{P}{2}c_1'(z) + c_1(z) = 0 \quad (\text{A.34})$$

$$c_2''(z) - \frac{P}{2}c_2'(z) + c_2(z) = 0. \quad (\text{A.35})$$

The roots of the associated characteristic equations are

$$\text{for } c_1: \quad \lambda_1^{(\pm)} = -\frac{i\delta}{|\Omega|} \pm \frac{i\tilde{\Omega}}{|\Omega|} \quad (\text{A.36})$$

$$\text{for } c_2: \quad \lambda_2^{(\pm)} = \frac{i\delta}{|\Omega|} \pm \frac{i\tilde{\Omega}}{|\Omega|}, \quad (\text{A.37})$$

where we have defined the *generalized Rabi frequency* $\tilde{\Omega} = \sqrt{\delta^2 + |\Omega|^2}$. The solutions as functions of time are then

$$c_1(t) = e^{-i\frac{\delta t}{2}} \left\{ c_1(0) \left[\cos \frac{\tilde{\Omega}t}{2} + \frac{i\delta}{\tilde{\Omega}} \sin \frac{\tilde{\Omega}t}{2} \right] - c_2(0) \frac{i\Omega^*}{\tilde{\Omega}} \sin \frac{\tilde{\Omega}t}{2} \right\} \quad (\text{A.38})$$

$$c_2(t) = e^{i\frac{\delta t}{2}} \left\{ -c_1(0) \frac{i\Omega}{\tilde{\Omega}} \sin \frac{\tilde{\Omega}t}{2} + c_2(0) \left[\cos \frac{\tilde{\Omega}t}{2} - \frac{i\delta}{\tilde{\Omega}} \sin \frac{\tilde{\Omega}t}{2} \right] \right\}, \quad (\text{A.39})$$

where we assume that the amplitudes are known at $t=0$.

APPENDIX B

Ramsey Interferometry

This section closely follows the famous theoretical treatments of Ramsey [122] and Rabi [123], for the time evolution of a two-level system subjected to resonant or near-resonant harmonic perturbations. In contrast to appendix A (where the solution is established for all times), we solve for certain values of several parameters in the equations of motion, and then allow these parameters to take on different values at various times. In this way, the two oscillating fields of Ramsey's model can be readily generalized to accommodate multiple pulses and phase fluctuations; smooth pulse envelopes are considered in appendix A. We again emphasize that the solution, originally envisioned for NMR in molecular beams, applies equally well to any effective two-level system. In particular it provides an excellent description of two-photon excitation by pulsed optical fields, when the intermediate states are eliminated from the equations of motion and the RWA has been made.

In this section, we work in the Schrödinger picture and parameterize the Rabi frequency as a real amplitude multiplied by a complex phase factor. Radiative decay is neglected.

B.1 Two Square Pulses

Suppose we have a two-level system in a pure state, whose wavefunction is

$$\Psi(t) = a_1(t)\psi_1 + a_2(t)\psi_2, \quad (\text{B.1})$$

where the energy eigenvalues are $E_1 = \hbar\omega_1$ and $E_2 = \hbar\omega_2$. Let these levels be coupled by the interaction $V(t)$, which has the matrix elements

$$\begin{aligned}
V_{11} &= V_{22} = 0 \\
V_{12} &= \hbar b e^{i(\omega t + \phi)} \\
V_{21} &= \hbar b e^{-i(\omega t + \phi)}.
\end{aligned} \tag{B.2}$$

We interpret $b = \Omega/2$ as one-half of the (real and constant) Rabi frequency Ω , ω as the oscillation frequency, and ϕ as the phase of the field at $t = 0$. The Schrödinger equations of motion are thus

$$i\hbar\dot{a}_1 = \hbar\omega_1 a_1 + \hbar b e^{i(\omega t + \phi)} a_2 \tag{B.3}$$

$$i\hbar\dot{a}_2 = \hbar b e^{-i(\omega t + \phi)} a_1 + \hbar\omega_2 a_2, \tag{B.4}$$

which we differentiate again to obtain two independent equations of motion:

$$\ddot{a}_1 - i(\omega - \omega_1 - \omega_2)\dot{a}_1 + (b^2 + \omega_1\omega - \omega_1\omega_2)a_1 = 0 \tag{B.5}$$

$$\ddot{a}_2 + i(\omega + \omega_1 + \omega_2)\dot{a}_1 + (b^2 - \omega_2\omega - \omega_1\omega_2)a_1 = 0. \tag{B.6}$$

We now define some auxiliary parameters to simplify notation: the resonance frequency is $\omega_0 = \omega_2 - \omega_1$, the detuning from resonance is $\delta = \omega_0 - \omega$, the generalized Rabi frequency is $\tilde{\Omega} = \sqrt{\delta^2 + 4b^2}$, and we denote the sum of the two eigenfrequencies by $\omega' = \omega_1 + \omega_2$. In terms of these quantities, the roots of the characteristic equations associated with B.5 and B.6 are

$$\lambda_{\pm}^{(1)} = \frac{i}{2} \left[(\omega - \omega') \pm \tilde{\Omega} \right] \tag{B.7}$$

$$\lambda_{\pm}^{(2)} = \frac{i}{2} \left[-(\omega + \omega') \pm \tilde{\Omega} \right], \tag{B.8}$$

so that the solutions take the form

$$a_1(t) = e^{i(\omega - \omega')t/2} \left[A e^{i\frac{\tilde{\Omega}t}{2}} + B e^{-i\frac{\tilde{\Omega}t}{2}} \right] \tag{B.9}$$

$$a_2(t) = e^{-i(\omega + \omega')t/2} \left[C e^{i\frac{\tilde{\Omega}t}{2}} + D e^{-i\frac{\tilde{\Omega}t}{2}} \right] \tag{B.10}$$

The constants A, B, C, D are related to the initial values of a_1 and a_2 ; to determine their explicit dependence, we suppose that $a_1(t_1)$ and $a_2(t_1)$ are known at some time t_1 . We can write these initial values in terms of the above constants by letting $t \rightarrow t_1$ in equations (B.9) and (B.10) above. Two more constraints are required, and these come from the derivatives $\dot{a}_1(t_1)$ and $\dot{a}_2(t_1)$. They can be determined by equating the derivatives of equations (B.9) and (B.10) to the corresponding quantities in the equations of motion (B.3) and (B.4):

$$\begin{aligned}\dot{a}_1(t_1) &= e^{i(\omega-\omega')t_1/2} \left[\frac{i}{2} \left[(\omega - \omega') + \tilde{\Omega} \right] A e^{i\frac{\tilde{\Omega}t_1}{2}} \right. \\ &\quad \left. + \frac{i}{2} \left[(\omega - \omega') - \tilde{\Omega} \right] B e^{-i\frac{\tilde{\Omega}t_1}{2}} \right] \\ &= -i\omega_1 a_1(t_1) - i b e^{i(\omega t_1 + \phi)} a_2(t_1),\end{aligned}\tag{B.11}$$

and

$$\begin{aligned}\dot{a}_2(t_1) &= e^{-i(\omega+\omega')t_1/2} \left[\frac{i}{2} \left[-(\omega + \omega') + \tilde{\Omega} \right] C e^{i\frac{\tilde{\Omega}t_1}{2}} \right. \\ &\quad \left. + \frac{i}{2} \left[-(\omega + \omega') - \tilde{\Omega} \right] D e^{-i\frac{\tilde{\Omega}t_1}{2}} \right] \\ &= -i b e^{-i(\omega t_1 + \phi)} a_1(t_1) - i\omega_2 a_2(t_1).\end{aligned}\tag{B.12}$$

Solving for A, B, C, D , we find

$$A = e^{-i(\omega-\omega')t_1/2} e^{-i\tilde{\Omega}t_1/2} \left[\frac{\tilde{\Omega} + \delta}{2\tilde{\Omega}} a_1(t_1) - e^{i(\omega t_1 + \phi)} \frac{b}{\tilde{\Omega}} a_2(t_1) \right]\tag{B.13}$$

$$B = e^{-i(\omega-\omega')t_1/2} e^{i\tilde{\Omega}t_1/2} \left[\frac{\tilde{\Omega} - \delta}{2\tilde{\Omega}} a_1(t_1) + e^{i(\omega t_1 + \phi)} \frac{b}{\tilde{\Omega}} a_2(t_1) \right]\tag{B.14}$$

$$C = e^{i(\omega-\omega')t_1/2} e^{-i\tilde{\Omega}t_1/2} \left[-e^{-i(\omega t_1 + \phi)} \frac{b}{\tilde{\Omega}} a_1(t_1) + \frac{\tilde{\Omega} - \delta}{2\tilde{\Omega}} a_2(t_1) \right]\tag{B.15}$$

$$D = e^{i(\omega-\omega')t_1/2} e^{i\tilde{\Omega}t_1/2} \left[e^{-i(\omega t_1 + \phi)} \frac{b}{\tilde{\Omega}} a_1(t_1) + \frac{\tilde{\Omega} + \delta}{2\tilde{\Omega}} a_2(t_1) \right],\tag{B.16}$$

and so we obtain solutions for $a_1(t)$ and $a_2(t)$:

$$a_1(t) = e^{\frac{i}{2}(\omega-\omega')(t-t_1)} \left[\left(i \frac{\delta}{\tilde{\Omega}} \sin \frac{\tilde{\Omega}(t-t_1)}{2} + \cos \frac{\tilde{\Omega}(t-t_1)}{2} \right) a_1(t_1) - i e^{i(\omega t_1 + \phi)} \frac{2b}{\tilde{\Omega}} \sin \frac{\tilde{\Omega}(t-t_1)}{2} a_2(t_1) \right] \quad (\text{B.17})$$

$$a_2(t) = e^{-\frac{i}{2}(\omega+\omega')(t-t_1)} \left[-i e^{-i(\omega t_1 + \phi)} \frac{2b}{\tilde{\Omega}} \sin \frac{\tilde{\Omega}(t-t_1)}{2} a_1(t_1) + \left(-i \frac{\delta}{\tilde{\Omega}} \sin \frac{\tilde{\Omega}(t-t_1)}{2} + \cos \frac{\tilde{\Omega}(t-t_1)}{2} \right) a_2(t_1) \right]. \quad (\text{B.18})$$

Ramsey notes that this solution is equally valid at times when there is no field present (i.e., when $b=0$) [122]. In this case, the equations reduce to

$$a_1(t) = e^{-i\omega_1(t-t_1)} a_1(t_1) \quad (\text{B.19})$$

$$a_2(t) = e^{-i\omega_2(t-t_1)} a_2(t_1), \quad (\text{B.20})$$

which is the ordinary dynamical evolution in the absence of interactions. Neglecting some subtleties associated with how rapidly the fields are turned on and off (which relate to the validity of the RWA and the two-level approximation, see [55]), we can use equations (B.17) to (B.20) to describe the system's evolution before, after, and during pulses. We need only know the system's initial state (say at $t=0$ or $t=-\infty$) to obtain the state at some later time $t=t_1$; the state at $t=t_1$ being known, we can then obtain the state at $t=t_2 > t_1$ in a similar fashion. For each step we simply carry out the evolution as prescribed by our solutions, with the appropriate values of b , ω , and ϕ for the field that acts during that interval. We also mention that the state of the system can be extrapolated *backward* in time from an instant where it is known, simply by taking $t < t_1$ in place of $t > t_1$ above.

The prototypical experiment with two square pulses is illustrated in figure B.1. We suppose that two pulses of equal duration τ are applied to the system, with a time T separating the falling edge of the first pulse from the rising edge of the second. If the first pulse turns on at $t=0$, when the amplitudes are known to be $a_i = \delta_{i1}$, then the amplitudes at $t=2\tau + T$ are

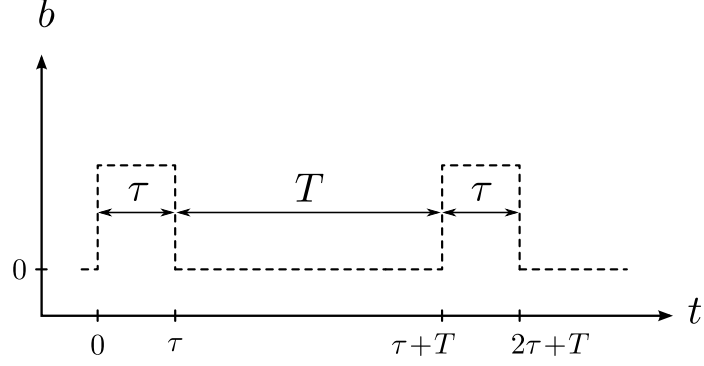


Figure B.1: Two pulse resonance experiment, where a constant-amplitude oscillating field acts for a duration τ starting at $t=0$ and again at $t=\tau+T$.

$$\begin{aligned}
a_1(2\tau+T) &= e^{\frac{i}{2}(\omega-\omega')(2\tau+T)} e^{\frac{-i}{2}(\bar{\omega}_1-\omega_1+\bar{\omega}_2-\omega_2)T} e^{-i\frac{\Delta\phi}{2}} \\
&\times \left[\left(\cos \tilde{\Omega}\tau + i \cos \theta \sin \tilde{\Omega}\tau \right) \cos \frac{\lambda T + \Delta\phi}{2} \right. \\
&\quad \left. + \left(i \cos \tilde{\Omega}\tau \cos^2 \theta + i \sin^2 \theta - \sin \tilde{\Omega}\tau \cos \theta \right) \sin \frac{\lambda T + \Delta\phi}{2} \right] \quad (\text{B.21})
\end{aligned}$$

$$\begin{aligned}
a_2(2\tau+T) &= 2i \sin \theta \sin \frac{\tilde{\Omega}\tau}{2} e^{\frac{i}{2}(\omega+\omega')(2\tau+T)} e^{\frac{-i}{2}(\bar{\omega}_1-\omega_1+\bar{\omega}_2-\omega_2)T} e^{\frac{-i}{2}(\phi+\phi')} \\
&\times \left[\cos \theta \sin \frac{\tilde{\Omega}\tau}{2} \sin \frac{\lambda T + \Delta\phi}{2} - \cos \frac{\tilde{\Omega}\tau}{2} \cos \frac{\lambda T + \Delta\phi}{2} \right], \quad (\text{B.22})
\end{aligned}$$

where we have followed Ramsey by defining $\sin \theta = 2b/\tilde{\Omega}$, and $\cos \theta = \delta/\tilde{\Omega}$ (note that $\sin^2 \theta + \cos^2 \theta = 1$). We have also allowed for the possibility that the eigenfrequencies ω_1, ω_2 may drift during the interval between pulses, and defined their average values over that interval by $\bar{\omega}_1, \bar{\omega}_2$ respectively. The quantity $\lambda \equiv \bar{\omega}_2 - \bar{\omega}_1 - \omega$ is the mean detuning over the same interval, and we have allowed the second oscillating field to have a phase offset ϕ' independent from the phase offset ϕ of first field. The relative phase between the two fields (which are still assumed to have the same amplitude) is $\Delta\phi \equiv \phi - \phi'$.

B.2 Multiple Pulses

The solutions derived in the previous section for two-pulse interferometry have relatively compact expressions, but for more pulses the time-evolution is more readily handled with matrices. In matrix form, we can write equations (B.17) to (B.20) as

$$\begin{pmatrix} a_1(t) \\ a_2(t) \end{pmatrix} = \begin{pmatrix} \alpha E_1 & \beta E_1 \\ -\beta^* E_2 & \alpha^* E_2 \end{pmatrix} \begin{pmatrix} a_1(t_1) \\ a_2(t_1) \end{pmatrix} \quad (\text{B.23})$$

in general, or

$$\begin{pmatrix} a_1(t) \\ a_2(t) \end{pmatrix} = \begin{pmatrix} \epsilon_1 & 0 \\ 0 & \epsilon_2 \end{pmatrix} \begin{pmatrix} a_1(t_1) \\ a_2(t_1) \end{pmatrix} \quad (\text{B.24})$$

when $b = 0$. We have defined the auxiliary quantities

$$\alpha = i \frac{\delta}{\tilde{\Omega}} \sin \frac{\tilde{\Omega}(t-t_1)}{2} + \cos \frac{\tilde{\Omega}(t-t_1)}{2} \quad (\text{B.25})$$

$$\beta = -i e^{i(\omega t_1 + \phi)} \frac{2b}{\tilde{\Omega}} \sin \frac{\tilde{\Omega}(t-t_1)}{2} \quad (\text{B.26})$$

$$E_1 = e^{\frac{i}{2}(\omega - \omega')(t-t_1)} \quad (\text{B.27})$$

$$E_2 = e^{-\frac{i}{2}(\omega + \omega')(t-t_1)} \quad (\text{B.28})$$

$$\epsilon_1 = e^{-i\tilde{\omega}_1(t-t_1)} \quad (\text{B.29})$$

$$\epsilon_2 = e^{-i\tilde{\omega}_2(t-t_1)} , \quad (\text{B.30})$$

and we will for now allow the field to have different parameters each time it acts. Rewriting equation B.23 as

$$\mathbf{a}(t + \tau) = \mathbf{M}(t, \tau) \cdot \mathbf{a}(t) , \quad (\text{B.31})$$

and equation B.24 as

$$\mathbf{a}(t + T) = \mathbf{m}(T) \cdot \mathbf{a}(t) , \quad (\text{B.32})$$

we obtain the state after an equal number of pulses and delays as

$$\mathbf{a} \left(t + \sum_j \tau_j + \sum_j T_j \right) = \prod_j (Q_j \mathbb{1} + \mathbf{R}_j \cdot \boldsymbol{\sigma}) \cdot \mathbf{a}(t) , \quad (\text{B.33})$$

where $\mathbb{1}$ is the identity matrix, $\boldsymbol{\sigma}$ is the vector of Pauli matrices, and the matrices Q_j and $\mathbf{R}_j = R_{j,x} \hat{\mathbf{x}} + R_{j,y} \hat{\mathbf{y}} + R_{j,z} \hat{\mathbf{z}}$ are implicitly defined functions of the auxiliary quantities $\alpha, \beta, E_1, E_2, \epsilon_1, \epsilon_2$.

BIBLIOGRAPHY

- [1] C. Alcock, V. Itkin, and M. Horrigan, “Vapour pressure equations for the metallic elements: 298–2500K,” *Canadian Metallurgical Quarterly*, vol. 23, no. 3, pp. 309–313, 1984.
- [2] F. Kuchler, E. Babcock, M. Burghoff, T. Chupp, S. Degenkolb, I. Fan, P. Fierlinger, F. Gong, E. Kraegeloh, W. Kilian, *et al.*, “A new search for the atomic EDM of ^{129}Xe at FRM-II,” *Hyperfine Interactions*, vol. 237, no. 1, pp. 1–5, 2016.
- [3] A. Kramida, Yu. Ralchenko, J. Reader, and NIST ASD Team. NIST Atomic Spectra Database (ver. 5.3), [Online]. Available: <http://physics.nist.gov/asd> [2016, July 14]. National Institute of Standards and Technology, Gaithersburg, MD., 2015.
- [4] J. Emsley, “The elements, Oxford chemistry guides,” 1995.
- [5] C. S. Wood, S. C. Bennett, D. Cho, B. P. Masterson, J. L. Roberts, C. E. Tanner, and C. E. Wieman, “Measurement of parity nonconservation and an anapole moment in cesium,” *Science*, vol. 275, no. 5307, pp. 1759–1763, 1997.
- [6] D. Hanneke, S. Fogwell, and G. Gabrielse, “New measurement of the electron magnetic moment and the fine structure constant,” *Phys. Rev. Lett.*, vol. 100, p. 120801, Mar 2008.
- [7] M. Pospelov and A. Ritz, “Electric dipole moments as probes of new physics,” *Annals of Physics*, vol. 318, no. 1, pp. 119 – 169, 2005. Special Issue.
- [8] V. Cirigliano and M. J. Ramsey-Musolf, “Low energy probes of physics beyond the standard model,” *Progress in Particle and Nuclear Physics*, vol. 71, pp. 2 – 20, 2013. Fundamental Symmetries in the Era of the LHC.
- [9] C. A. Baker, D. D. Doyle, P. Geltenbort, K. Green, M. G. D. van der Grinten, P. G. Harris, P. Iaydjiev, S. N. Ivanov, D. J. R. May, J. M. Pendlebury, J. D. Richardson, D. Shiers, and K. F. Smith, “Improved experimental limit on the electric dipole moment of the neutron,” *Phys. Rev. Lett.*, vol. 97, p. 131801, Sep 2006.
- [10] B. Graner, Y. Chen, E. G. Lindahl, and B. R. Heckel, “Reduced limit on the permanent electric dipole moment of ^{199}Hg ,” *Phys. Rev. Lett.*, vol. 116, p. 161601, Apr 2016.

- [11] J. Baron, W. C. Campbell, D. DeMille, J. M. Doyle, G. Gabrielse, Y. V. Gurevich, P. W. Hess, N. R. Hutzler, E. Kirilov, I. Kozyryev, *et al.*, “Order of magnitude smaller limit on the electric dipole moment of the electron,” *Science*, vol. 343, no. 6168, pp. 269–272, 2014.
- [12] R. Pohl, A. Antognini, F. Nez, F. D. Amaro, F. Biraben, J. M. Cardoso, D. S. Covita, A. Dax, S. Dhawan, L. M. Fernandes, *et al.*, “The size of the proton,” *Nature*, vol. 466, no. 7303, pp. 213–216, 2010.
- [13] G. W. Bennett, B. Bousquet, H. N. Brown, G. Bunce, R. M. Carey, P. Cushman, G. T. Danby, P. T. Debevec, M. Deile, H. Deng, W. Deninger, S. K. Dhawan, V. P. Druzhinin, L. Duong, E. Efsthadiadis, F. J. M. Farley, G. V. Fedotovitch, S. Giron, F. E. Gray, D. Grigoriev, M. Grosse-Perdekamp, A. Grossmann, M. F. Hare, D. W. Hertzog, X. Huang, V. W. Hughes, M. Iwasaki, K. Jungmann, D. Kawall, M. Kawamura, B. I. Khazin, J. Kindem, F. Krienen, I. Kronkvist, A. Lam, R. Larsen, Y. Y. Lee, I. Logashenko, R. McNabb, W. Meng, J. Mi, J. P. Miller, Y. Mizumachi, W. M. Morse, D. Nikas, C. J. G. Onderwater, Y. Orlov, C. S. Özben, J. M. Paley, Q. Peng, C. C. Polly, J. Pretz, R. Prigl, G. zu Putlitz, T. Qian, S. I. Redin, O. Rind, B. L. Roberts, N. Ryskulov, S. Sedykh, Y. K. Semertzidis, P. Shagin, Y. M. Shatunov, E. P. Sichtermann, E. Solodov, M. Sossong, A. Steinmetz, L. R. Sulak, C. Timmermans, A. Trofimov, D. Urner, P. von Walter, D. Warburton, D. Winn, A. Yamamoto, and D. Zimmerman, “Final report of the E821 muon anomalous magnetic moment measurement at BNL,” *Phys. Rev. D*, vol. 73, p. 072003, Apr 2006.
- [14] S. Arzumanov, L. Bondarenko, S. Chernyavsky, P. Geltenbort, V. Morozov, V. Nesvizhevsky, Y. Panin, and A. Strepetov, “A measurement of the neutron lifetime using the method of storage of ultracold neutrons and detection of inelastically up-scattered neutrons,” *Physics Letters B*, vol. 745, pp. 79 – 89, 2015.
- [15] T. Chupp and M. Ramsey-Musolf, “Electric dipole moments: A global analysis,” *Phys. Rev. C*, vol. 91, p. 035502, Mar 2015.
- [16] E. A. Cornell and C. E. Wieman, “Nobel lecture: Bose-Einstein condensation in a dilute gas, the first 70 years and some recent experiments,” *Rev. Mod. Phys.*, vol. 74, pp. 875–893, Aug 2002.
- [17] D. Budker and D. F. J. Kimball, eds., *Optical magnetometry*. Cambridge: Cambridge University Press, 2013.
- [18] H. B. Dang, A. C. Maloof, and M. V. Romalis, “Ultrahigh sensitivity magnetic field and magnetization measurements with an atomic magnetometer,” *Applied Physics Letters*, vol. 97, no. 15, 2010.
- [19] M. A. Bouchiat, T. R. Carver, and C. M. Varnum, “Nuclear polarization in He³ gas induced by optical pumping and dipolar exchange,” *Phys. Rev. Lett.*, vol. 5, pp. 373–375, Oct 1960.

- [20] E. A. and J. Kitching, “Nuclear magnetic resonance gyroscopes,” in Budker and Kimball [17], ch. 19, pp. 369–386.
- [21] T. Chupp, “Permanent electric dipole moments of atoms and molecules,” in *Advances in Atomic, Molecular, and Optical Physics* (P. B. E. Arimondo and C. Lin, eds.), vol. 59 of *Advances In Atomic, Molecular, and Optical Physics*, pp. 129 – 174, Academic Press, 2010.
- [22] B. C. Grover, “Noble-gas NMR detection through noble-gas-rubidium hyperfine contact interaction,” *Phys. Rev. Lett.*, vol. 40, pp. 391–392, Feb 1978.
- [23] T. W. Kornack, R. K. Ghosh, and M. V. Romalis, “Nuclear spin gyroscope based on an atomic comagnetometer,” *Phys. Rev. Lett.*, vol. 95, p. 230801, Nov 2005.
- [24] I. M. Savukov and M. V. Romalis, “NMR detection with an atomic magnetometer,” *Phys. Rev. Lett.*, vol. 94, p. 123001, Mar 2005.
- [25] M. Scheid, D. Kolbe, F. Markert, T. W. Hänsch, and J. Walz, “Continuous-wave Lyman- α generation with solid-state lasers,” *Opt. Express*, vol. 17, pp. 11274–11280, Jul 2009.
- [26] R. W. Boyd, *Nonlinear Optics*, ch. 12. Academic press, 2003.
- [27] M. Balabas, D. Budker, J. Kitching, P. Schwindt, and J. Stalnaker, “Magnetometry with millimeter-scale antirelaxation-coated alkali-metal vapor cells,” *JOSA B*, vol. 23, no. 6, pp. 1001–1006, 2006.
- [28] M. Balabas, T. Karaulanov, M. Ledbetter, and D. Budker, “Polarized alkali-metal vapor with minute-long transverse spin-relaxation time,” *Physical review letters*, vol. 105, no. 7, p. 070801, 2010.
- [29] W. Happer, “Optical pumping,” *Reviews of Modern Physics*, vol. 44, no. 2, p. 169, 1972.
- [30] J. C. Allred, R. N. Lyman, T. W. Kornack, and M. V. Romalis, “High-sensitivity atomic magnetometer unaffected by spin-exchange relaxation,” *Phys. Rev. Lett.*, vol. 89, p. 130801, Sep 2002.
- [31] A. Gozzini, F. Mango, J. Xu, G. Alzetta, F. Maccarrone, and R. Bernheim, “Light-induced ejection of alkali atoms in polysiloxane coated cells,” *Il Nuovo Cimento D*, vol. 15, no. 5, pp. 709–722, 1993.
- [32] M. Meucci, E. Mariotti, P. Bicchi, C. Marinelli, and L. Moi, “Light-induced atom desorption,” *EPL (Europhysics Letters)*, vol. 25, no. 9, p. 639, 1994.
- [33] I. Savukov, S.-K. Lee, and M. Romalis, “Optical detection of liquid-state NMR,” *Nature*, vol. 442, no. 7106, pp. 1021–1024, 2006.
- [34] B. Patton, *NMR studies of angular momentum transfer and nuclear spin relaxation*. PhD thesis, Princeton University, 2007.

- [35] M. J. Bales, P. Fierlinger, and R. Golub, “Nonextensive statistics in spin precession,” *arXiv preprint arXiv:1602.01082*, 2016.
- [36] M. Auzinsh, D. Budker, and S. Rochester, *Optically polarized atoms: understanding light-atom interactions*. Oxford University Press, 2010.
- [37] H. A. Bethe and E. E. Salpeter, *Quantum mechanics of one-and two-electron atoms*, ch. IV. Dover Publications, Inc., 2008.
- [38] W. C. Griffith, S. Knappe, and J. Kitching, “Femtotesla atomic magnetometry in a microfabricated vapor cell,” *Optics express*, vol. 18, no. 26, pp. 27167–27172, 2010.
- [39] S. Knappe and J. Kitching, “Microfabricated atomic magnetometers,” in Budker and Kimball [17], ch. 7, pp. 125–141.
- [40] I. Kominis, T. Kornack, J. Allred, and M. Romalis, “A subfemtotesla multichannel atomic magnetometer,” *Nature*, vol. 422, no. 6932, pp. 596–599, 2003.
- [41] W. Gawlik and J. M. Higbie, “Magnetometry with cold atoms,” in Budker and Kimball [17], ch. 9, pp. 167–189.
- [42] A. Kastler, “Quelques suggestions concernant la production optique et la détection optique d’une inégalité de population des niveaux de quantification spatiale des atomes. application à l’expérience de stern et gerlach et à la résonance magnétique,” *J. Phys. Radium*, vol. 11, no. 6, pp. 255–265, 1950.
- [43] W. Happer, “Optical pumping,” *Reviews of Modern Physics*, vol. 44, no. 2, p. 169, 1972.
- [44] S. Appelt, A. B.-A. Baranga, C. Erickson, M. Romalis, A. Young, and W. Happer, “Theory of spin-exchange optical pumping of ^3He and ^{129}Xe ,” *Physical Review A*, vol. 58, no. 2, p. 1412, 1998.
- [45] T. G. Walker and W. Happer, “Spin-exchange optical pumping of noble-gas nuclei,” *Reviews of Modern Physics*, vol. 69, no. 2, p. 629, 1997.
- [46] E. E. Robertson, R. W. Eason, Y. Yokoo, and P. J. Chandler, “Photorefractive damage removal in annealed-proton-exchanged LiNbO_3 channel waveguides,” *Applied Physics Letters*, vol. 70, no. 16, pp. 2094–2096, 1997.
- [47] Y. Colombe, D. H. Slichter, A. C. Wilson, D. Leibfried, and D. J. Wineland, “Single-mode optical fiber for high-power, low-loss UV transmission,” *Optics express*, vol. 22, no. 16, pp. 19783–19793, 2014.
- [48] J. Paul, Y. Kaneda, T.-L. Wang, C. Lytle, J. V. Moloney, and J. Jones, “Precision spectroscopy of atomic mercury in the deep ultraviolet based on fourth-harmonic generation from an optically pumped external-cavity semiconductor laser,” in *Conference on Lasers and Electro-Optics*, p. CTuS6, Optical Society of America, 2010.

- [49] J. Paul, Y. Kaneda, T.-L. Wang, C. Lytle, J. V. Moloney, and R. J. Jones, “Doppler-free spectroscopy of mercury at 253.7 nm using a high-power, frequency-quadrupled, optically pumped external-cavity semiconductor laser,” *Optics letters*, vol. 36, no. 1, pp. 61–63, 2011.
- [50] M. Scheid, F. Markert, J. Walz, J. Wang, M. Kirchner, and T. W. Hänsch, “750 mW continuous-wave solid-state deep ultraviolet laser source at the 253.7 nm transition in mercury,” *Optics letters*, vol. 32, no. 8, pp. 955–957, 2007.
- [51] I. B. Khriplovich and S. Lamoreaux, *CP violation without strangeness: electric dipole moments of particles, atoms, and molecules*. Springer Science & Business Media, 2012.
- [52] B. A. Capron, *Two-Photon Multiwave Mixing*. PhD thesis, The University of Arizona., 1986.
- [53] M. Sargent III, S. Ovakia, and M. H. Lu, “Theory of two-photon multiwave mixing,” *Physical Review A*, vol. 32, no. 3, p. 1596, 1985.
- [54] A. R. Edmonds, *Angular momentum in quantum mechanics*. Princeton University Press, 1996.
- [55] P. R. Berman and V. S. Malinovsky, *Principles of laser spectroscopy and quantum optics*. Princeton University Press, 2010.
- [56] R. N. Zare, *Angular Momentum: Understanding spatial aspects in chemistry and physics*. New York: John Wiley & Sons, Inc., 1988.
- [57] R. Loudon, *The Quantum Theory of Light*. Oxford: Clarendon Press, 1973.
- [58] L. D. Landau and E. M. Lifshitz, *Quantum mechanics, non-relativistic theory*. Butterworth-Heineman, 1977.
- [59] E. U. Condon and G. H. Shortley, *The Theory of Atomic Spectra*. Cambridge University Press, 1935.
- [60] U. Fano and G. Racah, *Irreducible Tensorial Sets*. Academic Press, Inc., 1959.
- [61] G. Lindblad, “On the generators of quantum dynamical semigroups,” *Communications in Mathematical Physics*, vol. 48, no. 2, pp. 119–130, 1976.
- [62] D. Budker, W. Gawlik, D. Kimball, S. Rochester, V. Yashchuk, and A. Weis, “Resonant nonlinear magneto-optical effects in atoms,” *Reviews of Modern Physics*, vol. 74, no. 4, p. 1153, 2002.
- [63] W. L. Peticolas, “Multiphoton spectroscopy,” *Annual Review of Physical Chemistry*, vol. 18, no. 1, pp. 233–260, 1967.
- [64] G. Grynberg and B. Cagnac, “Doppler-free multiphotonic spectroscopy,” *Reports on Progress in Physics*, vol. 40, no. 7, p. 791, 1977.

- [65] K. D. Bonin and T. J. McIlrath, “Two-photon electric-dipole selection rules,” *JOSA B*, vol. 1, no. 1, pp. 52–55, 1984.
- [66] A. Siegman, *Lasers*, ch. 27. University Science Books, 1986.
- [67] M. C. Stowe, M. J. Thorpe, A. Pe’er, J. Ye, J. E. Stalnaker, V. Gerginov, and S. A. Diddams, “Direct frequency comb spectroscopy,” *Advances in Atomic, Molecular, and Optical Physics*, vol. 55, pp. 1–60, 2008.
- [68] M. V. Berry, “Quantal phase factors accompanying adiabatic changes,” in *Proceedings of the Royal Society of London A: Mathematical, Physical and Engineering Sciences*, vol. 392, pp. 45–57, The Royal Society, 1984.
- [69] J. Pendlebury, W. Heil, Y. Sobolev, P. Harris, J. Richardson, R. Baskin, D. Doyle, P. Geltenbort, K. Green, M. Van Der Grinten, *et al.*, “Geometric-phase-induced false electric dipole moment signals for particles in traps,” *Physical Review A*, vol. 70, no. 3, p. 032102, 2004.
- [70] A. Steyerl, C. Kaufman, G. Müller, S. S. Malik, A. Desai, and R. Golub, “Calculation of geometric phases in electric dipole searches with trapped spin-1/2 particles based on direct solution of the Schrödinger equation,” *Physical Review A*, vol. 89, no. 5, p. 052129, 2014.
- [71] Y. Masuda, K. Asahi, K. Hatanaka, S.-C. Jeong, S. Kawasaki, R. Matsumiya, K. Matsuta, M. Mihara, and Y. Watanabe, “Neutron electric dipole moment measurement with a buffer gas comagnetometer,” *Physics Letters A*, vol. 376, no. 16, pp. 1347–1351, 2012.
- [72] M. Mihara, Y. Masuda, K. Matsuta, S. Kawasaki, Y. Watanabe, K. Hatanaka, and R. Matsumiya, “Present status of the ^{129}Xe comagnetometer development for neutron EDM measurement,” *Hyperfine Interactions*, vol. 237, no. 1, p. 122, 2016.
- [73] K. Blagoev and V. Komarovskii, “Lifetimes of levels of neutral and singly ionized lanthanide atoms,” *Atomic Data and Nuclear Data Tables*, vol. 56, no. 1, pp. 1 – 40, 1994.
- [74] M. Baumann and G. Wandel, “Lifetimes of the excited states $(6s6p) ^1P_1$ and $(6s6p) ^3P_1$ of ytterbium,” *Physics Letters*, vol. 22, no. 3, pp. 283–285, 1966.
- [75] C. Bowers, *Experimental investigation of the $6s^2 ^1S_0 \rightarrow 5d6s ^3D_{1,2}$ forbidden transitions in atomic ytterbium*. PhD thesis, University of California, Berkeley, 1998.
- [76] R. Drever, J. L. Hall, F. Kowalski, J. Hough, G. Ford, A. Munley, and H. Ward, “Laser phase and frequency stabilization using an optical resonator,” *Applied Physics B*, vol. 31, no. 2, pp. 97–105, 1983.
- [77] R. V. Pound, “Electronic frequency stabilization of microwave oscillators,” *Review of Scientific Instruments*, vol. 17, no. 11, pp. 490–505, 1946.

- [78] D. DeMille, D. Budker, N. Derr, and E. Deveney, “Search for exchange-antisymmetric two-photon states,” *Phys. Rev. Lett.*, vol. 83, pp. 3978–3981, Nov 1999.
- [79] G. Wasik, W. Gawlik, J. Zachorowski, and W. Zawadzki, “Laser frequency stabilization by Doppler-free magnetic dichroism,” *Applied Physics B*, vol. 75, no. 6-7, pp. 613–619, 2002.
- [80] T. Petelski, M. Fattori, G. Lamporesi, J. Stuhler, and G. Tino, “Doppler-free spectroscopy using magnetically induced dichroism of atomic vapor: a new scheme for laser frequency locking,” *The European Physical Journal D-Atomic, Molecular, Optical and Plasma Physics*, vol. 22, no. 2, pp. 279–283, 2003.
- [81] H. Liu, S. Yin, J. Qian, Z. Xu, and Y. Wang, “Optimization of Doppler-free magnetically induced dichroic locking spectroscopy on the 1S_0 – 3P_1 transition of a neutral mercury atom,” *Journal of Physics B: Atomic, Molecular and Optical Physics*, vol. 46, no. 8, p. 085005, 2013.
- [82] T. M. Fortier, D. J. Jones, J. Ye, S. T. Cundiff, and R. S. Windeler, “Long-term carrier-envelope phase coherence,” *Optics letters*, vol. 27, no. 16, pp. 1436–1438, 2002.
- [83] A. Marian, *Direct Frequency Comb Spectroscopy for Optical Frequency Metrology and Coherent Interactions*. PhD thesis, University of Colorado, 2005.
- [84] S. T. Cundiff and J. Ye, “Colloquium: Femtosecond optical frequency combs,” *Reviews of Modern Physics*, vol. 75, no. 1, p. 325, 2003.
- [85] D. Nikogosyan, “Beta barium borate (BBO),” *Applied Physics A*, vol. 52, no. 6, pp. 359–368, 1991.
- [86] L. P. Gaffney, P. A. Butler, M. Scheck, A. B. Hayes, F. Wenander, M. Albers, B. Bastin, C. Bauer, A. Blazhev, S. Bönig, *et al.*, “Studies of pear-shaped nuclei using accelerated radioactive beams,” *Nature*, vol. 497, no. 7448, pp. 199–204, 2013.
- [87] M. S. Rosen, *Laser-polarized ^{129}Xe magnetic resonance spectroscopy and imaging; The development of a method for in vivo perfusion measurement*. PhD thesis, The University of Michigan, 2001.
- [88] M. Rosenberry and T. Chupp, “Atomic electric dipole moment measurement using spin exchange pumped masers of ^{129}Xe and ^3He ,” *Physical review letters*, vol. 86, no. 1, p. 22, 2001.
- [89] S. J. Seltzer, *Developments in alkali-metal atomic magnetometry*. PhD thesis, Princeton University, 2008.
- [90] S. J. Seltzer and M. V. Romalis, “High-temperature alkali vapor cells with antirelaxation surface coatings,” *Journal of Applied Physics*, vol. 106, no. 11, 2009.

- [91] M. Repetto, E. Babcock, P. Blmler, W. Heil, S. Karpuk, and K. Tullney, “Systematic T_1 improvement for hyperpolarized ^{129}Xe ,” *Journal of Magnetic Resonance*, vol. 252, pp. 163 – 169, 2015.
- [92] M. Repetto, S. Zimmer, F. Allmendinger, P. Blmler, M. Doll, J. Grasdijk, W. Heil, K. Jungmann, S. Karpuk, H.-J. Krause, A. Offenhuser, U. Schmidt, Y. Sobolev, and L. Willmann, “HP-Xe to go: Storage and transportation of hyperpolarized ^{129}Xe ,” *Journal of Magnetic Resonance*, vol. 265, pp. 197 – 199, 2016.
- [93] J. Schmiedeskamp, W. Heil, E. W. Otten, R. K. Kremer, A. Simon, and J. Zimmer, “Paramagnetic relaxation of spin polarized ^3He at bare glass surfaces,” *The European Physical Journal D - Atomic, Molecular, Optical and Plasma Physics*, vol. 38, no. 3, pp. 427–438, 2006.
- [94] A. Deninger, W. Heil, E. W. Otten, M. Wolf, R. K. Kremer, and A. Simon, “Paramagnetic relaxation of spin polarized ^3He at coated glass walls,” *The European Physical Journal D - Atomic, Molecular, Optical and Plasma Physics*, vol. 38, no. 3, pp. 439–443, 2006.
- [95] J. Schmiedeskamp, H.-J. Elmers, W. Heil, E. W. Otten, Y. Sobolev, W. Kilian, H. Rinneberg, T. Sander-Thömmes, F. Seifert, and J. Zimmer, “Relaxation of spin polarized ^3He by magnetized ferromagnetic contaminants,” *The European Physical Journal D - Atomic, Molecular, Optical and Plasma Physics*, vol. 38, no. 3, pp. 445–454, 2006.
- [96] A. G. Glenday, *Progress in Tests of Fundamental Physics Using a ^3He and ^{129}Xe Zeeman Maser*. PhD thesis, Harvard University, 2010.
- [97] T. Gentile, “Overview of polarized neutron sources,” in *Proceedings of the Ninth International Workshop Polarized Sources and Targets: Nashville, Indiana, USA, 30 September-4 October 2001*, p. 233, World Scientific, 2002.
- [98] F. Kuchler, *Electric dipole moment searches using the isotope ^{129}Xe* . PhD thesis, Technische Universität München, 2014.
- [99] I. Altarev, E. Babcock, D. Beck, M. Burghoff, S. Chesnevskaya, T. Chupp, S. Degenkolb, I. Fan, P. Fierlinger, A. Frei, *et al.*, “A magnetically shielded room with ultra low residual field and gradient,” *Review of scientific instruments*, vol. 85, no. 7, p. 075106, 2014.
- [100] E. Elliffe, J. Bogenstahl, A. Deshpande, J. Hough, C. Killow, S. Reid, D. Robertson, S. Rowan, H. Ward, and G. Cagnoli, “Hydroxide-catalysis bonding for stable optical systems for space,” *Classical and Quantum Gravity*, vol. 22, no. 10, p. S257, 2005.
- [101] K. Haughian, R. Douglas, A. van Veggel, J. Hough, A. Khalaidovski, S. Rowan, T. Suzuki, and K. Yamamoto, “The effect of crystal orientation on the cryogenic strength of hydroxide catalysis bonded sapphire,” *Classical and Quantum Gravity*, vol. 32, no. 7, p. 075013, 2015.

- [102] A.-M. A. van Veggel and C. J. Killow, “Hydroxide catalysis bonding for astronomical instruments,” *Advanced Optical Technologies*, vol. 3, no. 3, pp. 293–307, 2014.
- [103] R. Douglas, A. A. van Veggel, L. Cunningham, K. Haughian, J. Hough, and S. Rowan, “Cryogenic and room temperature strength of sapphire jointed by hydroxide-catalysis bonding,” *Classical and Quantum Gravity*, vol. 31, no. 4, p. 045001, 2014.
- [104] N. Beveridge, A. Van Veggel, L. Cunningham, J. Hough, I. Martin, R. Nawrodt, S. Reid, and S. Rowan, “Dependence of cryogenic strength of hydroxide catalysis bonded silicon on type of surface oxide,” *Classical and Quantum Gravity*, vol. 30, no. 2, p. 025003, 2012.
- [105] S. Rowan, S. Twyford, J. Hough, D.-H. Gwo, and R. Route, “Mechanical losses associated with the technique of hydroxide-catalysis bonding of fused silica,” *Physics Letters A*, vol. 246, no. 6, pp. 471–478, 1998.
- [106] N. L. Beveridge, *Characterisation of silicon-silicon hydroxide catalysis bonds for future gravitational wave detectors*. PhD thesis, University of Glasgow, 2012.
- [107] E. Elliffe, J. Bogenstahl, A. Deshpande, J. Hough, C. Killow, S. Reid, D. Robertson, S. Rowan, H. Ward, and G. Cagnoli, “Hydroxide-catalysis bonding for stable optical systems for space,” *Classical and Quantum Gravity*, vol. 22, no. 10, p. S257, 2005.
- [108] A. Plößl and G. Kräuter, “Wafer direct bonding: tailoring adhesion between brittle materials,” *Materials Science and Engineering: R: Reports*, vol. 25, no. 1, pp. 1–88, 1999.
- [109] R. Schödel, “Length and size,” in *Handbook of optical metrology: Principles and Applications* (T. Yoshizawa, ed.), ch. 15, pp. 405–432, CRC Press, 2009.
- [110] G. Siddall and P. Willey, “Flat-surface wringing and contact error variability,” *Journal of Physics D: Applied Physics*, vol. 3, no. 1, p. 8, 1970.
- [111] W. Kern, “The evolution of silicon wafer cleaning technology,” *Journal of the Electrochemical Society*, vol. 137, no. 6, pp. 1887–1892, 1990.
- [112] B. Derby and E. Wallach, “Theoretical model for diffusion bonding,” *Metal Science*, vol. 16, no. 1, pp. 49–56, 1982.
- [113] G. Wallis and D. I. Pomerantz, “Field assisted glass-metal sealing,” *Journal of Applied Physics*, vol. 40, no. 10, pp. 3946–3949, 2003.
- [114] S. Shoji, H. Kikuchi, and H. Torigoe, “Low-temperature anodic bonding using lithium aluminosilicate- β -quartz glass ceramic,” *Sensors and Actuators A: Physical*, vol. 64, no. 1, pp. 95–100, 1998.
- [115] K. M. Knowles and A. T. J. van Helvoort, “Anodic bonding,” *International Materials Reviews*, vol. 51, no. 5, pp. 273–311, 2006.

- [116] U. Kreissig, S. Grigull, K. Lange, P. Nitzsche, and B. Schmidt, “In situ ERDA studies of ion drift processes during anodic bonding of alkali-borosilicate glass to metal,” *Nuclear Instruments and Methods in Physics Research Section B: Beam Interactions with Materials and Atoms*, vol. 136, pp. 674–679, 1998.
- [117] M. Nese and A. Hanneborg, “Anodic bonding of silicon to silicon wafers coated with aluminium, silicon oxide, polysilicon or silicon nitride,” *Sensors and Actuators A: Physical*, vol. 37, pp. 61 – 67, 1993.
- [118] “ASTM E438-92(2011): Specification for glasses in laboratory apparatus,” 2011.
- [119] R. Sherman, D. Hirt, and R. Vane, “Surface cleaning with the carbon dioxide snow jet,” *Journal of Vacuum Science & Technology A*, vol. 12, no. 4, pp. 1876–1881, 1994.
- [120] J. J. Sakurai, *Modern Quantum Mechanics*. Addison-Wesley Publishing Company, 1994.
- [121] B. W. Shore, “The theory of coherent atomic excitation, 2 volume set,” *The Theory of Coherent Atomic Excitation, 2 Volume Set, by Bruce W. Shore, pp. 2509. ISBN 0-471-52417-4. Wiley-VCH, January 1996.*, vol. 1, 1996.
- [122] N. F. Ramsey, “A molecular beam resonance method with separated oscillating fields,” *Physical Review*, vol. 78, no. 6, p. 695, 1950.
- [123] I. I. Rabi, “Space quantization in a gyrating magnetic field,” *Phys. Rev.*, vol. 51, pp. 652–654, Apr 1937.
- [124] N. F. Ramsey, “Resonance transitions induced by perturbations at two or more different frequencies,” *Phys. Rev.*, vol. 100, pp. 1191–1194, Nov 1955.
- [125] F. Bloch and A. Siegert, “Magnetic resonance for nonrotating fields,” *Physical Review*, vol. 57, no. 6, p. 522, 1940.